ABSTRACT

CAO, WEI. Experimental and Analytical Investigations of Permanent Deformation Behavior of Asphalt Mixtures under Confining Pressure. (Under the direction of Dr. Y. Richard Kim.)

This dissertation is devoted to understanding and phenomenologically characterizing the mechanisms underlying permanent deformation in asphalt concrete. To capture the combined effect of both deviatoric stress and confining pressure, a series of cyclic creep and recovery tests are performed with 3 deviatoric stress levels (70, 100, 130 psi) and 4 confining pressures (0, 10, 20, 30 psi). Experimental observations and hypotheses are made regarding the variation in material's hardening/softening state and time dependence of viscoplastic deformation.

The previous viscoplastic models developed at NC State University and their concepts are revisited and evaluated against the obtained experimental data. Focus has been put on the convolution-type model proposed by Subramanian (2011) and the incremental-shift model developed by Choi (2013). The convolution-type model features a rather complex structure and a highly computational demand. It is first simplified through mathematical speculations based on experimental evidences and then the additional variable is introduced to account for effects of the confining pressure on permanent deformation. The improved model is able to represent the permanent deformation phenomenon through a single viscoplastic relaxation spectrum and a stress state dependent parameter. The incremental-shift model is also extended to incorporate the confinement effect so that eventually it can serve as a feasible material evaluation tool in the laboratory and also as a convenient model in the finite element analysis of pavement structures. Both models are successfully verified through random loading tests.

The rutting predictions on the two full-scale pavement tracks (FHWA ALF and NCAT) using the in-house developed finite element program Layered ViscoElastic pavement analysis for Critical Distresses (LVECD) reveal the importance of incorporating the shear effect in pavement performance simulations. The inadequacy of representing the field shear mechanisms via triaxial testing is pointed out. An exploratory study using the WesTrack

shear based transfer function is conducted, which further emphasizes the necessity and enhances the confidence of taking the shear contribution into account.

Experimental and Analytical Investigations of Permanent Deformation Behavior of Asphalt Mixtures under Confining Pressure

by
Wei Cao

A dissertation submitted to the Graduate Faculty of
North Carolina State University
in partial fulfillment of the
requirements for the degree of
Doctor of Philosophy

Civil Engineering

Raleigh, North Carolina

2015

APPROVED BY:

_____	_____
Dr. Y. Richard Kim Committee Chair	Dr. Murthy Guddati
_____	_____
Dr. Cassandra Castorena	Dr. Tasnim Hassan

BIOGRAPHY

Wei Cao was born in Nanjing, China in December 1987. He entered the Southeast University in Nanjing in September 2005 as a student in the department of transportation engineering, where he was first exposed to traffic theories, bridge designs and pavement materials and structures. He earned his Bachelor's degree in 2009 and then continued his one year graduate study with the focus on pavement engineering under the direction of Dr. Huang Xiaoming. With a thirst for advanced modeling theories and mathematical techniques, he made a decision to pursue his PhD degree in the United States. He then moved to North Carolina and started his exploration under the guidance of Dr. Y. Richard Kim in NC State University in July 2010.

ACKNOWLEDGEMENTS

I would like to first express heartfelt gratitude to my advisor Dr. Y. Richard Kim for his guidance and patience not only on my research but also on my life and mental growth. I would also like to thank Dr. Murthy N. Guddati for his insights on my harsh journey of model development. I very much appreciate the help from my colleague Dr. Yeong-tae Choi who introduced me to the real world of triaxial testing with MTS and plastic modeling. Special thanks go to Dr. Cheolmin "Charlie" Baek who trained me in specimen fabrication, dynamic modulus test and fatigue test. He is really patient and nice and his smile has helped me quickly get involved into the big group when I first came here. I also thank Dr. Andrew T. LaCroix for his kindness in showing me the use of the core drill machine, the UTM and the AMPT. He is ready for help whenever I encountered problems in the laboratory. I also want to express thanks to Dr. B. Shane Underwood, who is very intelligent and rigorous on research and experiments, for his guidance on my early research. I also feel grateful to work with all my other colleagues: Hong-joon Park, Jongsub "Jay" Lee, Jeonghyuk "JK" Im, Dahae Kim, Seong Hwan Cho, Morteza Ashouri, Mohammad Sabouri, Amirhossein Norouzi, Shayan Safavizadeh, Joseph Jones, Gledi Softa, Andrew Wargo, Nasrin Sumee, Mohammad Ilias, Jing Jin, Yizhuang "David" Wang, Luis Nascimento, and Diane Gilmore. Mehran Eslamina and Behrooz helped me in understanding details and principles in LVECD and making necessary modifications when requested.

TABLE OF CONTENTS

LIST OF TABLES ..... **viii**

LIST OF FIGURES ..... **ix**

CHAPTER 1 INTRODUCTION **1**

1.1 Background 1

1.2 Objective 3

1.3 Methodology 3

1.4 Organization 3

CHAPTER 2 THEORETICAL BACKGROUND AND LITERATURE REVIEW **5**

2.1 Introduction 5

2.2 Linear Viscoelasticity 5

2.2.1 Boltzmann superposition principle 5

2.2.2 Characterization of viscoelastic kernel functions 6

2.2.2.1 Discrete models 7

2.2.2.2 Continuous models 10

2.2.3 Fractional viscoelasticity 14

2.2.3.1 Fractional integrals and derivatives 14

2.2.3.2 Fractional dashpot and the fractional Maxwell model 15

2.2.3.3 Application to asphalt concrete 18

2.2.3.4 Relationship with conventional Prony models 20

2.2.3.5 Final comments 21

2.3 Nonlinear Viscoelasticity 21

2.3.1 Single integral form 22

2.3.1.1 Nonlinear superposition method 22

2.3.1.2 Schapery's theory 23

2.3.2 Multiple integral form 24

2.3.3 Comments 25

2.4 Viscoelasticity under Confinement 26

2.5 Classical Plasticity and Viscoplasticity 28

2.5.1 Plasticity 28

2.5.2 Viscoplasticity 29

2.5.3 Pressure dependent yield criteria 30

2.5.3.1 The Haigh-Westergaard stress space 30

2.5.3.2 Mohr-Coulomb criterion 32

2.5.3.3 Drucker-Prager criterion 35
2.6 Viscoplastic Modeling of Asphalt Mixtures at NCSU 37
2.6.1 A classical viscoplastic model with rate-dependent yield surface 37
2.6.2 A convolution-type viscoplastic model with rate-dependent hardening 41
2.6.3 Incremental-shift model 45
CHAPTER 3 MATERIAL TESTING 49
3.1 Materials 49
3.2 Specimen Fabrication 50
3.3 Specimen Preparation and Test Setup 50
3.4 Test Protocols 53
3.4.1 Stress condition 53
3.4.2 Test temperature 59
3.4.3 Pulse time and rest period 60
CHAPTER 4 EXPERIMENTAL OBSERVATIONS AND PHENOMENOLOGICAL HYPOTHESES 62
4.1 Variation in Material Time Dependence 62
4.2 Hypotheses Regarding Hardening, Softening, and Recovery 67
4.3 Viscoelastic Hardening due to Plastic Straining 71
4.4 Difficulties in Interpreting Tests with Large Deformations 76
CHAPTER 5 ANALYTICAL INVESTIGATIONS 79
5.1 Evaluation of the Incremental Model 79
5.2 Extension of the Incremental-Shift Model 87
5.2.1 Extended model form and experimental protocol 87
5.2.2 Verification using the random loading test 97
5.3 Improvement on the Convolution-type Viscoplastic Model 98
5.3.1 Improvement on the compliance-like functions 99
5.3.2 Simplification on the stress terms and hardening 102
5.4 Understanding the Improved Model 104
5.4.1 Parameter analysis for the linear viscoelastic model 104
5.4.1.1 Sensitivity with D_0 105
5.4.1.2 Sensitivity with ΔD 106
5.4.1.3 Sensitivity with β 108
5.4.1.4 Sensitivity with τ_m 109
5.4.1.5 Summary 110
5.4.2 Parameter analysis for the improved viscoplastic model 111
5.5 Evaluation of the Improved Model 118

5.5.1 Conversion of the retardation spectra to relaxation spectra 123
5.5.2 Final model form 128
5.6 Parameter Calibration of the Improved Viscoplastic Model 129
5.7 Verification of the Convolution-type Viscoplastic Model 131
5.7.1 Model Calibration and Verification on a Different Mix 132
CHAPTER 6 SHEAR RELATED TRANSFER FUNCTION AND FIELD PREDICTION IMPROVEMENTS 138
6.1 Finite Element Implementation and Numerical Examples 138
6.1.1 Implementation of rigorous viscoplastic models 138
6.1.2 Implementation of the extended incremental-shift model 139
6.2 LVECD Rut Predictions on Field Sections 148
6.2.1 FHWA ALF test sections 148
6.2.1.1 Project overview 148
6.2.1.2 LVECD predictions 149
6.2.2 NCAT test sections 152
6.2.2.1 Project overview 152
6.2.2.2 LVECD predictions 154
6.2.3 Summary 155
6.3 Understanding the Shear Behavior of Asphalt Concrete 156
6.3.1 General Deformation Mechanisms of Granular Materials 156
6.3.2 Determination of Angle of Internal Friction and Angle of Dilation 160
6.3.3 Application to CCR and TSS Tests 162
6.3.4 Comparative Study: Application to Monotonic Compression Tests 165
6.3.5 Summary 174
6.4 Review of Shear Based Transfer Functions 175
6.4.1 Simple power law by Selvaraj 176
6.4.2 WesTrack transfer function 176
6.4.3 Transfer function based on shear stress to strength ratio by Li *et al.* 177
6.5 Implementation of the WesTrack Shear Based Transfer Function 178
6.5.1 Maximum shear stress and strain 178
6.5.2 Application on FHWA ALF test sections 184
6.5.3 Application on NCAT test sections 188
CHAPTER 7 SUMMARY AND RECOMENDATIONS 193
7.1 Summary 193
7.2 Recommendations for Future Work 194
REFERENCES 196

APPENDICES 204
APPENDIX A. Proof of the Cauchy Formula..... 205
APPENDIX B. Numerical Implementation of the Improved Convolution-type Viscoplastic Model 206
APPENDIX C. Calibration of the Extended Incremental-Shift Model using Other Temperature-Confinement Combinations 211
APPENDIX D. Conversion of the Relaxation Spectra to Retardation Spectra..... 215

LIST OF TABLES

Table 3-1 Summary of Mixture Information 49
Table 3-2 Case Matrix for Stress Analysis 54
Table 5-1 Optimized Coefficients of the Incremental Model for Different Stress Conditions 83
Table 5-2 Calibrated Parameters of the Extended Incremental-Shift Model 93
Table 5-3 Parameters of the Compliance Function Used in Sensitivity Analysis 105
Table 5-4 Calibrated Parameters for All Stress Conditions 129
Table 5-5 Calibrated Parameter E_∞ for Each Stress Condition 129
Table 6-1 Time-Temperature Shift Factor Function and Parameters for VTa0% (SI) 139
Table 6-2 Parameters of the Prony Series for VTa0% (SI) 140
Table 6-3 Calibrated Parameters of the Original Incremental-Shift Model (SI) 140
Table 6-4 Selected FHWA ALF Test Sections for LVECD Rut Simulations 149
Table 6-5 Description of NCAT Test Sections (LaCroix 2013) 153
Table 6-6 Angle of Dilation for All Monotonic Compression Tests 171
Table 6-7 *K*-values for the WesTrack Transfer Function 177
Table 6-8 Maximum Shear Stresses and Strains Extracted for FHWA ALF Sections 185
Table 6-9 The Optimized Coefficients of the Transfer Function for FHWA ALF Sections 185

LIST OF FIGURES

Figure 2-1 Mechanical analogs for Prony-type viscoelastic kernel functions: (a) relaxation modulus $E(t)$, and (b) creep compliance $D(t)$. 8

Figure 2-2 Mechanical analogs for (a) fractional dashpot, and (b) fractional Maxwell element. 17

Figure 2-3 Generalized fractional Maxwell model with (a) 4 parameters, and (b) 7 parameters (a spring is put in parallel with the fractional Maxwell elements to provide a non-zero equilibrium modulus for viscoelastic solids). 19

Figure 2-4 Networks of springs and dashpots equivalent to fractional models: (a) a tree structure, and (b) a ladder structure. 20

Figure 2-5 The Haigh-Westergaard stress coordinate of a point in the principal stress space. 32

Figure 2-6 The Mohr-Coulomb criterion: (a) the principal stress space, (b) the π-plane, and (c) the meridian plane. 34

Figure 2-7 Yield surface in the π-plane for cohesionless soils (Lewis 2004). 35

Figure 2-8 Drucker-Prager and Mohr-Coulomb yield loci in the π-plane. 37

Figure 2-9 A cyclic creep and recovery test with square-shaped pulse for the illustration of the evolution of yield stress G. 39

Figure 2-10 The evolution of the compliance-like functions used in the calculation of yield stress G during hardening and softening. 40

Figure 2-11 Mechanical analog for the convolution-type viscoplastic model. 42

Figure 2-12 Modified stress and the evolution of the back stress illustrated for either one of the convolution integrals in Equation (2.6.5). 44

Figure 2-13 Similarity between the back stress in the convolution-type model and the yield surface concept in a classical plasticity or viscoplasticity model. 44

Figure 3-1 Aggregate gradation of the mix VT0%. 49

Figure 3-2 Sample prepared for the triaxial tests. 52

Figure 3-3 Annual temperature history at the pavement surface for Vermont State generated by EICM (note that the starting date is not prescribed). 55

Figure 3-4 High and low temperature profiles used in response analysis. 55

Figure 3-5 Horizontal and vertical stresses calculated with different vehicle speeds and temperature profiles for: (a) and (b) a thin 4-in. pavement, and (c) and (d) a thick 18-in. pavement. 56

Figure 3-6 Stress ratio along the depth for thin and thick pavement cases..... 58

Figure 3-7 Deviatoric stress and confinement calculated from stress invariants..... 59

Figure 3-8 Cumulative distribution of temperature to total deformation throughout one year. 60

Figure 4-1 Load history used in a CCR test by Yun (2008). 62

Figure 4-2 Permanent strain (axial strain collected at the end of rest period in each cycle) of the test corresponding to the loading history depicted in Figure 4-1 (Yun 2008). 63

Figure 4-3 Averaged axial strain response for selected cycles (Yun 2008). 63

Figure 4-4 Recoverable axial strain for selected cycles (Yun 2008). 64

Figure 4-5 Permanent strain and the cyclic increment for an unconfined cyclic creep and recovery test (Test-38) with peak deviatoric stress of 100 psi and TH = 48°C. 65

Figure 4-6 Recoverable axial strain for selected cycles in the unconfined creep and recovery test with haversine-shaped pulse. 66

Figure 4-7 Volumetric deformation history for two replicates at different confinement levels: (a) 0 psi, (b) 10 psi, (c) 20 psi, and (d) 30 psi, with one deviatoric stress of 100psi. 68

Figure 4-8 Strain decomposition for the first cycle in an unconfined creep and recovery test (Test-7) by the use of the linear viscoelasticity theory. 72

Figure 4-9 Strain decomposition in an unconfined creep and recovery test (Test-7) by the use of the linear viscoelasticity theory for (a) cycle #3, and (b) cycle #10; for both cycles the material remains in the primary deformation region. 75

Figure 4-10 Significant reduction in Cauchy stress at the end of the test for several combinations of deviatoric stress and confinement: (a) 70-0 psi, (b) 100-0 psi, (c) 130-0 psi, and (d) 130-10 psi. 77

Figure 5-1 Application of the incremental model to CCR tests with 70 psi deviatoric stress and 3 confinement levels: 10, 20, and 30 psi. 80

Figure 5-2 Application of the incremental model to CCR tests with 100 psi deviatoric stress and 3 confinement levels: 10, 20, and 30 psi. 81

Figure 5-3 Application of the incremental model to CCR tests with 130 psi deviatoric stress and 3 confinement levels: 10, 20, and 30 psi. 82

Figure 5-4 Relation between incremental model coefficients and confining pressure. 84

Figure 5-5 Relation between incremental model coefficients and deviatoric stress..... 85

Figure 5-6 Relation between (1-α) and the triaxiality ratio..... 87

Figure 5-7 Reference tests and the incremental model fit using the first block of TSS tests at 48°C and 10 psi confinement..... 91

Figure 5-8 Fitted total shift factors versus the calculated ones from all TSS data with 6 blocks: (a) with the linear terms of deviatoric stress and confinement in the total shift factor function Equation (5.2.4), and (b) with the power-law terms Equation (5.2.5)..... 92

Figure 5-9 Predicted strain histories for TSS tests at 10 psi confinement (TL = 28°C, TI = 38°C, and TH = 48°C). 94

Figure 5-10 Predicted strain histories for TSS tests at 20 psi confinement (TL = 28°C, TI = 38°C, and TH = 48°C). 95

Figure 5-11 Predicted strain histories for TSS tests at 30 psi confinement (TL = 28°C, TI = 38°C, and TH = 48°C). 96

Figure 5-12 Stress history used in the random loading tests for model verification. 97

Figure 5-13 Measured and predicted strain histories by the extended incremental-shift model for random loading tests..... 98

Figure 5-14 The linear viscoelastic retardation time distribution of mix VTa0% from experiments and the log-normal fitting function. 101

Figure 5-15 Discrete points selected from the continuous log-normal distribution of retardation for the compliance-like functions..... 102

Figure 5-16 Stress input for the sensitivity analysis..... 105

Figure 5-17 Change of the linear viscoelastic strain response with variation in D_0: (a) the elastic component, and (b) the total viscoelastic strain..... 106

Figure 5-18 Change of the linear viscoelastic strain response with variation in ΔD: (a) the viscous component, and (b) the total viscoelastic strain..... 107

Figure 5-19 Change of the linear viscoelastic strain response with variation in β: (a) the viscous component, and (b) the total viscoelastic strain..... 109

Figure 5-20 Change of the linear viscoelastic strain response with variation in ln(τ_m): (a) the viscous component, and (b) the total viscoelastic strain..... 110

Figure 5-21 Change in permanent strain and back stress with variations in D_0: (a) permanent strain in normal scale, (b) permanent strain in semi-log scale, and (c) back stress evolution. 112

Figure 5-22 Change in permanent strain and back stress with variations in ΔD: (a) permanent strain in normal scale, (b) permanent strain in semi-log scale, and (c) back stress evolution. 113

Figure 5-23 Change in permanent strain and back stress with variations in β: (a) permanent strain in normal scale, (b) permanent strain in semi-log scale, and (c) back stress evolution. 114

Figure 5-24 Change in permanent strain and back stress with variations in ln(τ_m): (a) permanent strain in normal scale, (b) permanent strain in semi-log scale, and (c) back stress. 115

Figure 5-25 Illustration of the mechanisms behind the evolution of back stress..... 118

Figure 5-26 The optimized parameter D_0 of the improved model with respect to confining pressure at different deviatoric stress levels. 120

Figure 5-27 The optimized retardation spectrum for the improved model at different deviatoric stress levels: (a) 70 psi, (b) 100 psi, and (c) 130 psi. 121

Figure 5-28 The optimized retardation spectrum for the improved model at different confinement levels: (a) 10 psi, (b) 20 psi, and (c) 30 psi. 122

Figure 5-29 Converted long-term modulus from the optimized viscoplastic compliance functions for all stress conditions. 127

Figure 5-30 Converted relaxation spectra from the optimized viscoplastic compliance functions for all stress conditions (70-10 #1 indicates 70 psi deviatoric stress, 10 psi confinement, and replicate #1). 127

Figure 5-31 Relation of E_∞ versus the ratio of first stress invariant and von Mises stress for all stress conditions. 131

Figure 5-32 Measured and predicted strain history by the improved convolution-type viscoplastic model for random loading tests at 48°C..... 132

Figure 5-33 Aggregate gradation of the FHWA ALF Control mix compared to the VT0% mix. 133

Figure 5-34 Model calibration on the FHWA ALF Control mix using CCR test data at 54C and 20 psi confinement with different deviatoric stress levels. 134

Figure 5-35 Measured and predicted strain histories of CCR tests on FHWA ALF Control mix with 0.1s and 1.6s pulse durations at different deviatoric stress levels. 135

Figure 5-36 Frequency of occurrence of test conditions in the random loading test on the FHWA ALF Control mix. 136

Figure 5-37 Measured and predicted strain histories in the random loading tests on the FHWA ALF Control mix. 137

Figure 6-1 Normal stresses calculated from LVECD for the 4 and 15 in. asphalt pavements (compressive treated as positive): (a) horizontal stresses, and (b) vertical stress. 141

Figure 6-2 Rut depth evolutions in the asphalt layer using three methods for the two cases investigated: (a) 4 in., and (b) 15 in. 143

Figure 6-3 Variables calculated for the 4 in. pavement at selected depths (cm) for: (a) total shift factor, (b) reduced pulse time, (c) vertical stress, and (d) confinement. 145

Figure 6-4 Individual contributions to the total shift factor at pavement surface from the first six terms in the extended function expressed in Equation (5.2.6). 146

Figure 6-5 The total shift factor at pavement surface and the individual contributions from the vertical stress and reduced pulse time in the improved function in Equation (5.2.1). 147

Figure 6-6 LVECD predicted and field measured rut depth in asphalt layers for FHWA ALF mixes: (a) Control, and (b) SBS-LG. 150

Figure 6-7 LVECD predicted and field measured rut depth in asphalt layers for FHWA ALF mixes: (a) CR-TB, and (b) Terpolymer. 151

Figure 6-8 The two year temperature history at pavement surface used in NCAT test track simulation. 154

Figure 6-9 LVECD predicted (with the improved form of the original incremental-shift model) and field measured rut depth in asphalt layers after two years for NCAT sections. 155

Figure 6-10 Representative stress and strain relations in monotonic tests for: (a) viscousless materials, and (b) viscous materials. 157

Figure 6-11 Calculation of the dilation angle based on the relation between volumetric strain and axial strain. 162

Figure 6-12 Relations of volumetric strain versus axial strain for CCR tests on VTa0% mix at 48°C and 130 psi deviatoric stress with various confinement levels. 164

Figure 6-13 Relations of volumetric strain versus axial strain for TSS tests on VTa0% mix at 10 psi confinement with various test temperatures. 165

Figure 6-14 Aggregate gradation curve of the FHWA ALF mix. 166

Figure 6-15 One batch of the total aggregate (including lime) for half a specimen. 168

Figure 6-16 Test specimens for the River Gravel mix (left) and FHWA ALF mix (right). . 168

Figure 6-17 Monotonic compression test results for FHWA ALF mix: (a) stress versus axial strain, and (b) expansive volumetric strain versus axial strain. 170

Figure 6-18 Monotonic compression test results for River Gravel mix: (a) stress versus axial strain, and (b) expansive volumetric strain versus axial strain. 171

Figure 6-19 Specimens fractured after the monotonic compression tests. 172

Figure 6-20 Stress and strain relations for all the monotonic compression tests. 172

Figure 6-21 Shear stress and strain beneath the tire edge responsible for the lateral upheavals. 179

Figure 6-22 Shear response under wheel loading for FHWA-4 in. structure: (a) shear stress σ_{zx} in kPa, and (b) shear strain ε_{zx}. 180

Figure 6-23 Shear response under wheel loading for FHWA-6 in. structure: (a) shear stress σ_{zx} in kPa, and (b) shear strain ε_{zx}. 181

Figure 6-24 Shear response under wheel loading for NCAT-7 in. structure: (a) shear stress σ_{zx} in kPa, and (b) shear strain ε_{zx}. 182

Figure 6-25 Calculated and field measured rutting histories for FHWA ALF sections with: (a) Control mix, and (b) SBS-LG mix. 186

Figure 6-26 Calculated and field measured rutting histories for FHWA ALF sections with: (a) CR-TB mix, and (b) Terpolymer mix. 187

Figure 6-27 The two year histories of maximum shear responses as a result of temperature fluctuation for the NCAT C section: (a) shear stress, and (b) shear strain. 189

Figure 6-28 Measured and predicted rut depths for NCAT test sections after two years: (a) simulation considering both densification and shear effects, and (b) prediction from the shear transfer function alone. 191

CHAPTER 1 INTRODUCTION

1.1 Background

Pavement, as one of the most basic and common infrastructure in the world, in fact can date back over two thousand years. Asphalt pavement was first implemented around two centuries ago. Compared to this long history, fundamental researches specifically on pavement materials and structures have been conducted for less than a century. Pavement construction has been for long heavily relied on field experience and considerable, perhaps excessive, economic investments to guarantee the service sustainability. On the other hand fundamental research in itself proceeds slowly and therefore requires patient and continuing support. Naturally and admittedly the paving industry is tempted to allocate more assets on field practice, which yields immediately apparent results.

However, an increasing number of professionals and even outsiders have realized, and it should be emphasized here, that, although pavement may be considered as a low-technology product compared to other modern civilizations, it happens to be one of the areas that require fundamental research. There are so many unpredictable factors in the field affecting the pavement behaviors, such as temperature variation, precipitation, and traffic loading. In addition, the composite materials used in construction like asphalt concrete and cement concrete further complicate the situation. Weak materials, poor design and construction, and harsh environments may cause material and/or structure failures out of which rutting and fatigue cracking have been the two most common and severe distress types for asphalt pavement.

Therefore, it is of critical importance to understand how pavement will behave under different loading and environmental conditions. To this end, a reasonable material constitutive relationship shall come as a first priority. This dissertation research is thus focused on one of the well-known and most challenging tasks in pavement research – constitutive modeling on permanent deformation behavior of asphalt mixtures. The specific loading history in the cyclic creep and recovery tests used in material characterization is unique for pavement in that it simulates the field traffic loading on pavements in service.

Understanding the mechanisms behind permanent deformation has been always remaining as a daunting task even only on the material level since asphalt mixtures exhibit strongly nonlinear and time dependent behaviors especially at high temperatures when the permanent deformation accumulates fast. Furthermore, in the field rutting can usually be accompanied with other distresses such as cracking. If water is trapped in the rut, it then may penetrate into underlying unbound layers through cracks to soften the materials underneath and consequently the pavement may lose its structural integrity. With such different physics interacting with each other, the mechanisms behind rutting could be extraordinarily complex and thus significant research efforts should be poured on to both material and structure levels. This current research serves as the exploration into the permanent deformation mechanisms on the material level.

Researchers have been for long borrowing concepts and modeling techniques developed for other materials (e.g., soils, steel, and polymers) with the attempt to model the viscoplastic behaviors of asphalt concrete. Very limited success has been seen so far due to the complexities involving the complicated traffic loading, material viscoelastic-viscoplastic coupling, softening, and pressure dependence.

In the meanwhile, material viscoplastic characterization work on asphalt concrete has been continued at NC State University (NCSU) for over ten years and multiple models have been developed. Yet, one common limitation associated with them lies in their one-dimensional nature. In other words, these models do not take the confining pressure explicitly in the expression while the behavior of asphalt concrete is fairly sensitive to the confinement level. On the other hand, the shear effect is absent in most existing models while it tends to be a more or at least equally important factor for pavements in-service with significant lateral upheavals observed beside the wheel paths.

This dissertation research is thus devoted to incorporating the pressure dependence through meticulously designed experiments and developing analytical modeling techniques based on proposed hypotheses and existing work to characterize the material's permanent deformation behavior. The shear effect will also be explored with the data from two full-scale pavement tracks, the FHWA ALF and NCAT test sections.

1.2 Objective

The main objective of this research is to propose an analytical model to account for the material nonlinearity with respect to deviatoric stress and confining pressure in viscoplastic deformation with reasonable amounts of experimental and computational efforts. The shear contributions relative to material densification are also investigated.

1.3 Methodology

Experimental programs are designed based on the previously developed concepts and modeling techniques at NCSU. The test type is the triaxial compression test with a constant confining pressure during loading. Previous models are evaluated using the experimental data for each confinement level and then simplified through certain practical assumptions by examining the model behaviors. The relations between model parameters and confinement levels are then established as the way to incorporate the confining pressure effect into the viscoplastic model. Regarding the addition of shear effect in performance prediction, shear based transfer functions are reviewed and a selected function is then applied to the prediction of permanent deformation in FHWA ALF and NCAT test sections. The predictions are then compared and qualitatively verified against the field measurements.

1.4 Organization

The dissertation is organized as follows. Theories and literature related to viscoelasticity and viscoplasticity are reviewed in Chapter 2. Different forms of linear and nonlinear viscoelastic models are briefly described. The focus is also placed on the historical development of each viscoplastic model at NCSU. Chapter 3 provides the details on how the experimental programs are designed in terms of stress condition, temperature, and test set-up. Chapter 4 is devoted to experimental observations and hypotheses regarding variation in material status due to viscoplastic straining. In Chapter 5, two recent models developed at NCSU are evaluated using the experimental data, and then improved and extended to incorporate the

material's pressure dependence. Random loading tests are finally employed in the model verifications. In Chapter 6 the predictions from the finite element program Layered ViscoElastic pavement analysis for Critical Distresses (LVECD) are compared to field measurements from FHWA ALF and NCAT test sections. The importance of considering shear contributions is revealed. A shear based transfer function is thus selected to supplement the LVECD predictions. In the last chapter, the general findings from the research are summarized, the limitations in current modeling and experimental framework are pointed out, and accordingly some future research directions are recommended.

CHAPTER 2 THEORETICAL BACKGROUND AND LITERATURE REVIEW

2.1 Introduction

Asphalt concrete is a composite of aggregate, asphalt binder, and air void. While aggregate can be simply treated as elastic materials, asphalt binder is a mixture of numerous types of high polymer, which features long and flexible chains in the molecules. Fundamentally, it is these molecular segments of different lengths not being able to reorient or distort immediately and simultaneously under external forces that endows asphalt binder with the attribute named delayed response or simply, viscosity. It is generally known that under low or intermediate temperatures asphalt binder and mixture are dominated by viscoelasticity whereas under high temperatures viscoplasticity will become a considerable component in response. Given this, some widely used models in theories of viscoelasticity and viscoplasticity will be briefly reviewed in subsequent sections.

2.2 Linear Viscoelasticity

2.2.1 Boltzmann superposition principle

Boltzmann superposition principle is one of the simplest but most powerful principles in polymer science. It basically relates the one dimensional tensile/compressive stress and strain through the following two expressions:

$$\sigma = \int_{0^-}^{t} E(t-\tau)\frac{d\varepsilon(\tau)}{d\tau}d\tau \tag{2.2.1}$$

$$\varepsilon = \int_{0^-}^{t} D(t-\tau)\frac{d\sigma(\tau)}{d\tau}d\tau \tag{2.2.2}$$

where $E(t)$ is the relaxation modulus and $D(t)$ is the creep compliance; τ is the time-like integration variable. Note that the lower limit of the integration is taken as 0^- by assuming the loading starts at time zero with minus sign suggesting integrating right before the loading in order to incorporate the initial jump, if any, in the input. The upper limit is t, the time of

observation, since obviously the input applied after t has no effect on the observed response. From the form of the two equations shown above, it is clear that the response (strain or stress) is proportional to the input (stress or strain). While the input history is given, the critical task remaining in linear viscoelasticity is to determine the kernel functions $E(t)$ and $D(t)$, also known as unit response functions, in these two convolution integrals.

2.2.2 Characterization of viscoelastic kernel functions

Generally the constraints imposed on the kernel functions are non-negative definiteness and strict monotonicity in order to represent the material's fading memory of previous loading. There are three common approaches in the laboratory to characterize these material functions: relaxation test by subjecting the specimen instantly to a constant strain while monitoring the stress, creep test by subjecting the specimen instantly to a constant stress while monitoring the strain, and dynamic test where a harmonically oscillating excitation is applied. For asphalt concrete specimens the first two types of tests may experience experimental difficulties involving machine capacity, robustness, compliance, and even safety issues. In addition, material information under transient loading may be hidden or even lost due to the difficulty in obtaining an accurate short-time response. Consequently dynamic modulus test in which the strain response is maintained within an appropriate viscoelastic range is chosen as the routine test for material characterization.

In the dynamic modulus test, frequency sweep applied at different temperatures will in the end give dynamic modulus data as a function of both physical frequency and temperature. Considering the well-proven applicability of time-temperature superposition principle from polymer science to both asphalt binder and mixture, the physical frequency (or time) and temperature can be combined through an important concept namely shift factor into one single variable called reduced frequency (or time). Shift factors, as a function of temperature only for thermorheologically simple materials, can be graphically perceived as the amount of horizontal shift of modulus data points from different temperatures in the plot of (logarithm of) modulus versus logarithm of physical frequency to form a smooth and continuous curve, termed master curve.

With dynamic modulus test data and shift factors at hand, the above-mentioned two unit response kernel functions can be obtained by means of some existing analytical/numerical techniques. These conversion methods generally vary with respect to the specific functional forms to be chosen for $E(t)$ and $D(t)$. In the following, two categories, discrete versus continuous models, will be briefly reviewed and compared.

2.2.2.1 Discrete models

Compared to sigmoidal functions, power functions and exponential functions have their own inherent mathematical advantages of being simple in differentiation and integration, and were initially chosen as the form for the kernel functions. However, the lack of prediction accuracy was later on realized to be resulting from the fact that the relaxation/retardation does not occur at a single time, but at a distribution of times. On the molecular level, this can be explained by the molecular segments of different lengths with different amount of contributions (Aklonis and MacKnight 1972). Taking this fact into consideration, it has been now commonly adopted to have as many exponential terms as necessary to accurately represent this time distribution. Here the mechanical analogs are presented in Figure 2-1 to facilitate the understanding of the model expressed in Prony series in Equations (2.2.3) and (2.2.4).

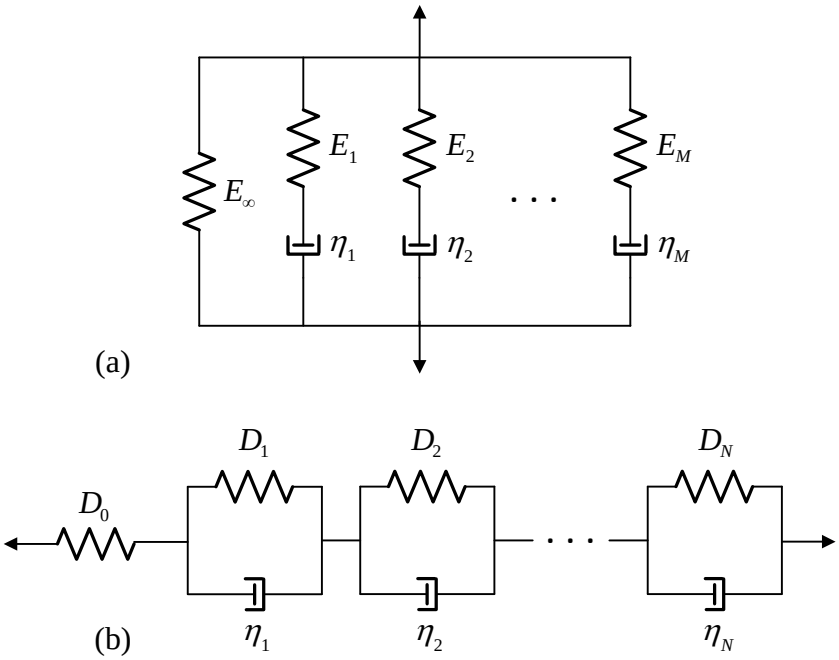

Figure 2-1 Mechanical analogs for Prony-type viscoelastic kernel functions: (a) relaxation modulus $E(t)$, and (b) creep compliance $D(t)$.

$$E(t) = E_\infty + \sum_{i=1}^{M} E_i e^{-t/\rho_i} \tag{2.2.3}$$

$$D(t) = D_0 + \sum_{i=1}^{N} D_i (1 - e^{-t/\tau_i}) \tag{2.2.4}$$

where the physical meaning of each symbol can be easily perceived when Figure 2-1 is referred to; $\rho_i = \eta_i/E_i$ is the relaxation time associated with each Maxwell element (a spring and a dashpot connected in series); $\tau_i = \eta_i \cdot D_i$ is the retardation time associated with each Voigt element (a spring and a dashpot connected in parallel).

A practical numerical technique converting dynamic modulus to the two transient kernel functions is detailed in Park and Schapery (1999). Basically the method is able to reduce the conversion into solving a system of linear algebraic equations for unknown Prony series coefficients (E_i and D_i) by specifying the time constants ρ_i and τ_i appropriately as a prior. However, it is also well-known that the determination of these coefficients is an ill-

posed problem using the linear regression method (Honerkamp and Weese 1989). That is, the resulting E_i or D_i strongly depends on the choices of time constants and the number of terms and thus the solution is not unique. Certain choices may even lead to negative values of E_i or D_i, which may cause certain theoretical difficulties and unrealistic predictions (such as oscillations in predicted curves). And as the number of terms increases, the number of negative coefficients also increases. Besides, the method should also be evaluated by examining the standard errors of these coefficients. The standard errors increases with the number of terms and can easily become as large as or even greater than the coefficients themselves.

An adjustment of the location or range of the pre-specified time constants may help but this is not that efficient for practical use. Realizing the high sensibility of the calculation with respect to scatter in the source experimental data, Park and Kim (2001) proposed a pre-smoothing method using one or multiple functions to provide smooth and continuous data points for subsequent fitting. This method proves to substantially enhance the quality but cannot completely eliminate the possibility of negative coefficients.

Despite the advantages in mathematical manipulation, another shortcoming associated with discrete models involves a large number of parameters to be identified in order to cover the broad transition zone, which together with the lack of a unique solution apparently harms the understanding of model dependency and sensitivity upon each parameter. In addition, it also discourages the attempt to correlate the material property changes, for example, due to differences in confining pressure or aging period, with the parameter variations. First, it is hardly reasonable or practical to find and establish a dependency function on material conditions for each of those many parameters. Secondly, a certain number of elements in a discrete model may give a perfect fitting quality, but this very model, seemingly quite accurate, may in turn distort and thus hide the true material information because of the error in experimental data.

As a compromise or more of an improvement in certain aspects, continuous models representing the distribution of relaxation/retardation times are used to express the viscoelastic kernel functions. It is an improvement because of the possible elimination of

certain ill-posedness and that much less parameters will be present and thus an easier and clearer correlation of model parameters with material behaviors will be promised. It may be also a compromise since instead of letting the experimental data and fitting techniques tell the overall shape of the distribution of relaxation/retardation times, this distribution is now specified with certain assumptions (and thus with potential errors) prior to determining the model coefficients. The continuous models, which are adopted in the present dissertation, are now reviewed in the following.

2.2.2.2 Continuous models

Considering a viscoelastic system where there are very many Maxwell elements used in the model, that is, M in Equation (2.2.3) is very large, it often becomes convenient to replace the summation by an integration as shown in Equation (2.2.5) below.

$$E(t) = E_\infty + \int_0^\infty E(u) e^{-t/u} du \tag{2.2.5}$$

Clearly the various E_i's are here replaced by a continuous function of the relaxation time $E(u)$, which is thus called a distribution of relaxation times. Instead of $E(u)$, one often encounters $H(u)$, which is simply defined as

$$H(u) = uE(u) \tag{2.2.6}$$

Therefore, in terms of $H(u)$, the relaxation modulus Equation (2.2.5) becomes

$$E(t) = E_\infty + \int_0^\infty \frac{H(u)}{u} e^{-t/u} du = E_\infty + \int_{\ln u=-\infty}^{\ln u=+\infty} H(u) e^{-t/u} d\ln u \tag{2.2.7}$$

Then, the dynamic modulus functions $E'(\omega)$ and $E''(\omega)$ are given as

$$E'(\omega) = E_\infty + \int_{\ln u=-\infty}^{\ln u=+\infty} H(u) \frac{u^2\omega^2}{1+u^2\omega^2} d\ln u \tag{2.2.8}$$

$$E''(\omega) = \int_{\ln u=-\infty}^{\ln u=+\infty} H(u) \frac{u\omega}{1+u^2\omega^2} d\ln u \tag{2.2.9}$$

Similarly the compliance function Equation (2.2.4) can be expressed in terms of a distribution of retardation times $L(u)$ as

$$D(t) = D_0 + \int_{\ln u=-\infty}^{\ln u=+\infty} L(u)\left(1-e^{-t/u}\right) d\ln u \tag{2.2.10}$$

And we have for the dynamic response functions as

$$D'(\omega) = D_0 + \int_{\ln u=-\infty}^{\ln u=+\infty} L(u)\frac{1}{1+u^2\omega^2} d\ln u \tag{2.2.11}$$

$$D''(\omega) = \int_{\ln u=-\infty}^{\ln u=+\infty} L(u)\frac{u\omega}{1+u^2\omega^2} d\ln u \tag{2.2.12}$$

In these equations, $H(u)d\ln u$ or $L(u)d\ln u$ is the corresponding amount of contributing processes for which the logarithm of the relaxation/retardation times fall in the range between $\ln u$ and $\ln u+d\ln u$. It is also necessary to note that although $H(u)$ and $L(u)$ are inherently related, their exact quantitative relationship is particularly intricate.

An effective approach using dynamic modulus data of asphalt concrete to obtain continuous relaxation/retardation spectra is detailed in the paper by Bhattacharjee *et al.* (2012). Basically the forms of $H(u)$ and $L(u)$ are determined from respectively storage modulus and storage compliance functions readily available from experimental data by fitting master curves. The solution for the parameters is unique. The authors also compared the discrete models with continuous ones and verified that the continuous spectra are the limiting case of the discrete spectra as the number of Maxwell/Voigt elements increased. The use of a continuous time distribution also makes the statistical analysis possible. Statistical properties such as mean, variance, and skewness can be easily acquired to quantify the change in the shape of the spectrum due to variation in experimental modulus data.

The derivation and characterization approach described above follows the rigorous viscoelasticity theories in Tschoegl (1989). Despite the uniqueness in characterization and ease in rational correlation with material behaviors, however, the obtained model forms are quite complex and mathematically inconvenient for the convolution integrals in Equations (2.2.1) and (2.2.2) especially when a long time history is required. Hence, as an alternative the shape of the time distributions can be assumed prior to subsequent characterization by experimental data. This way, certain rigorousness is sacrificed but still a satisfactory

engineering accuracy can be guaranteed and more importantly, mathematical manipulation can be a lot less demanding.

Some early functional forms of time distribution include the symmetric log-normal relaxation spectrum assumed by Jongepier *et al*. (1969) for asphalt binders, although experimental data in other contemporary literature (Dickinson and Witt 1974, Brodnyan *et al.* 1960) demonstrated a skewed distribution. Numerous other functional forms have been tried in the literature usually only on empirical grounds. For a compilation of these distributions, readers are referred to Gross (1953). After the SHRP project, notable models such as the CA (Christensen and Anderson 1992) and CAM models (Marasteanu and Anderson 1999) are proposed to predict the dynamic behaviors of asphalt binder.

Log-normal function

A log-normal distribution can be completely specified by only three parameters: the mean relaxation/retardation time, the width and the peak of the distribution (Nowick and Berry 1961). Take the relaxation function (2.2.7) as an example, the integration form implies that it would be most convenient to define the distribution function in terms of the variable ln$u$, rather than u itself. We first introduce the normalized distribution function $\Phi(\ln u)$ which is defined in such a way that

$$\int_{-\infty}^{+\infty} \Phi(\ln u) d \ln u = 1 \tag{2.2.13}$$

Then, Equations (2.2.7)-(2.2.9) become

$$E(t) = E_{\infty} + \Delta E \int_{-\infty}^{+\infty} \Phi(\ln u) e^{-t/u} d \ln u \tag{2.2.14}$$

$$E'(\omega) = E_{\infty} + \Delta E \int_{-\infty}^{+\infty} \Phi(\ln u) \frac{u^2\omega^2}{1+u^2\omega^2} d \ln u \tag{2.2.15}$$

$$E''(\omega) = \Delta E \int_{-\infty}^{+\infty} \Phi(\ln u) \frac{u\omega}{1+u^2\omega^2} d \ln u \tag{2.2.16}$$

where ΔE is the constant multiplier to the distribution and thus is a measure of the magnitude of the relaxation effect.

If we introduce a variable

$$z = \ln(u / u_m) \tag{2.2.17}$$

where u_m is the mean retardation time which locates the position of the peak, then the normalized distribution function $\Phi(\ln u)$ can be written as

$$\Phi(z) = \frac{1}{\beta\sqrt{\pi}} e^{-(z/\beta)^2} \tag{2.2.18}$$

where β is half of the width of the distribution measured between two points where $\Phi(\ln u)$ falls to $1/e$ of its maximum value $\Phi(0)$. In fact, it can be easily shown that β is equal to $\sqrt{2}$ multiplying the standard deviation of the log-normal distribution. Introducing the following variables

$$\begin{aligned} x &= \ln \omega u_m \\ y &= \ln(t / u_m) \end{aligned} \tag{2.2.19}$$

and substituting Equation (2.2.18) into (2.2.14)-(2.2.16), we obtain the following expressions for the static and dynamic response functions

$$E(y) = E_\infty + \frac{\Delta E}{\sqrt{\pi}} \int_{-\infty}^{+\infty} \exp(-r^2) \exp[-e^{(y-\beta r)}] dr \tag{2.2.20}$$

$$E'(x) = E_\infty + \frac{\Delta E}{\sqrt{\pi}} \int_{-\infty}^{+\infty} \exp(-r^2) \frac{1}{1+\exp[-2(x+\beta r)]} dr \tag{2.2.21}$$

$$E''(x) = \frac{\Delta E}{2\sqrt{\pi}} \int_{-\infty}^{+\infty} \exp(-r^2) \operatorname{sech}(x+\beta r) dr \tag{2.2.22}$$

where sech$x$ is the hyperbolic secant function defined as sech$x = 2/(e^x + e^{-x})$. Using static and/or dynamic experimental data, the four parameters can be identified and the validity of the log-normal assumption can be checked. Note that in the above, the case of a single relaxation time will be realized when $\beta = 0$.

Regarding the application to asphalt binder, a strong correlation between β and the type/composition of binder has been reported, and relatively low accuracy has been observed for binder with greater β values as compared to those with smaller β values (Anderson *et al.* 1994).

In the above final equations the expression inside the integrals are still complicated and numerical computation is thus required. Except the complexity in numerical computation which is also shared by other continuous models, one major drawback of this model lies in the assumption that the relaxation/retardation spectrum follows a log-normal distribution while it has been confirmed that both asphalt binder and mixtures demonstrate skewed distributions of relaxation/retardation spectrum (Dickinson and Witt 1974, and Bhattacharjee *et al*. 2012).

2.2.3 Fractional viscoelasticity

Constitutive models based on fractional derivatives were initially proposed as an empirical approach to viscoelasticity, and it is Bagley and Torvik (1983) that established a link between the then empirical method and the molecular theory which was developed by Rouse (1953) for dilute polymer solutions and later on modified by Ferry, Landel, and Williams (1955) for concentrated polymer solutions and polymer solids. Before presenting some simple fractional model forms, the definition of fractional integrals and derivatives should be first introduced. Then some preliminary applications to asphalt concrete is described, followed by the intrinsic relationship between the fractional models and the conventional Prony models.

2.2.3.1 Fractional integrals and derivatives

First the Cauchy formula for repeated integration is introduced. Let $f(x)$ be a continuous function defined in the domain $[a, +\infty)$ where a is a real number. The definite integral from a to x can be written using the operator I as

$$If(x) = \int_a^x f(t)dt \tag{2.2.23}$$

Repeating this process once yields

$$I^2 f(x) = \int_a^x If(t)dt = \int_a^x \left(\int_a^t f(s)ds \right) dt \tag{2.2.24}$$

and the same process can be repeated for an arbitrary number of times. For a positive integer number of repetition, the Cauchy formula states

$$I^n f(x) = \int_a^x \int_a^{x_1} \dots \int_a^{x_{n-1}} f(x_n) dx_n \dots dx_2 dx_1 = \frac{1}{(n-1)!} \int_a^x (x-t)^{n-1} f(t) dt \qquad (2.2.25)$$

The proof using mathematical induction is given in APPENDIX A. By generalizing the above formula for a real number α and using the Gamma function to replace the discrete factorial function, we can arrive at the following definition of fractional integration:

$$I^\alpha f(x) = \frac{1}{\Gamma(\alpha)} \int_a^x (x-t)^{\alpha-1} f(t) dt \qquad (2.2.26)$$

This expression sets the basis for the well-known Riemann-Liouville fractional integral: for a real function defined by the mapping from one real set to another real set, its integral $D^{-\alpha}$ of order $\alpha > 0$ is defined as

$$D^{-\alpha} f(x) = I^\alpha f(x) = \frac{1}{\Gamma(\alpha)} \int_a^x (x-t)^{\alpha-1} f(t) dt \qquad (2.2.27)$$

If, instead, the α order derivative is desired, it can be obtained by computing the n-th order derivative over the integral of order $(n-\alpha)$. In this case it is important to remember that n is the nearest integral greater than α. Hence, the corresponding Riemann-Liouville fractional derivative is given by

$$D^\alpha f(x) = \frac{d^n}{dx^n} \left(D^{-(n-\alpha)} f(x) \right) = \frac{d^n}{dx^n} \left(I^{n-\alpha} f(x) \right) \qquad (2.2.28)$$

Or, if the reverse order is used,

$$D^\alpha f(x) = D^{-(n-\alpha)} \left(\frac{d^n}{dx^n} f(x) \right) = I^{n-\alpha} \left(\frac{d^n}{dx^n} f(x) \right) \qquad (2.2.29)$$

2.2.3.2 Fractional dashpot and the fractional Maxwell model

The basic element named “fractional dashpot” or “springpot” (Koeller 1984) in the mechanical analogs for fractional models is introduced. From a mathematical point of view, for a purely elastic body (e.g., a spring) the stress response is proportional to the zeroth order derivative of the strain input, while for a purely viscous body (e.g., a dashpot) the stress

response is proportional to the first order derivative of the strain input. Similarly, for a fractional dashpot the stress is proportional to $\alpha \in (0, 1)$ order derivative of the strain, and thus a fractional model can be deemed as an interpolation between a purely elastic behavior and a purely viscous behavior. The stress-strain relationship for a fractional dashpot (Figure 2-2a) is therefore given by

$$\sigma(t) = E\tau^{\alpha} D^{\alpha} \varepsilon(t) \quad 0 \le \alpha \le 1 \tag{2.2.30}$$

Or,

$$\varepsilon(t) = \frac{D^{-\alpha}\sigma(t)}{E\tau^{\alpha}} \tag{2.2.31}$$

where $\tau = \eta/E$ is the characteristic time, E and η can be physically interpreted respectively as the elastic modulus and viscosity associated with the element. $D^{\alpha}\varepsilon(t)$ can be expressed by substituting $n = 1$ into Equation (2.2.29) and using Equation (2.2.26) as

$$D^{\alpha}\varepsilon(t) = \frac{1}{\Gamma(1-\alpha)} \int_{0^-}^{t} \frac{\dot{\varepsilon}(\tau)}{(t-\tau)^{\alpha}} d\tau \tag{2.2.32}$$

which is consistent with Caputo's definition of the fractional derivative (Caputo 1967).

To characterize the frequency dependent properties of materials, the Fourier transform is needed:

$$x^*(\omega) \equiv F\{x(t)\} = \int_{-\infty}^{+\infty} x(t) e^{-i\omega t} dt \tag{2.2.33}$$

The transform of the fractional derivative defined in Equation (2.2.32) produces a useful relation:

$$F\left\{D^{\alpha}\varepsilon(t)\right\} = (i\omega)^{\alpha} \varepsilon^*(\omega) \tag{2.2.34}$$

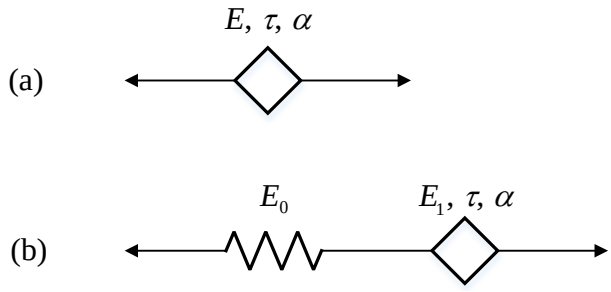

Figure 2-2 Mechanical analogs for (a) fractional dashpot, and (b) fractional Maxwell element.

Generally, to represent the behavior of a viscoelastic solid realistically, at least one elastic element should be added to Equation (2.2.30) or (2.2.31), which gives the fractional Maxwell model (Figure 2-2b) as the simplest case:

$$\varepsilon(t) = \frac{\sigma(t)}{E_0} + \frac{D^{-\alpha}\sigma(t)}{E_1 \tau^{\alpha}} \tag{2.2.35}$$

The Fourier transform of the fractional Maxwell model is

$$\varepsilon^*(\omega) = \frac{\sigma^*(\omega)}{E_0} + \frac{\sigma^*(\omega)}{E_1 (i\omega\tau)^{\alpha}} \tag{2.2.36}$$

with the frequency dependent complex modulus given by

$$E^*(\omega) = E'(\omega) + iE''(\omega) = \left[\frac{1}{E_0} + \frac{1}{E_1 (i\omega\tau)^{\alpha}} \right]^{-1} \tag{2.2.37}$$

By some mathematical manipulation and noting that $i^{\alpha} = \cos(\alpha\pi/2) + i\sin(\alpha\pi/2)$, we finally arrive at the expressions for the storage and loss modulus

$$E'(\omega) = E_0 E_1 \frac{E_1 (\omega\tau)^{\alpha} + E_0 \cos(\alpha\pi/2)}{E_1^2 (\omega\tau)^{\alpha} + 2E_0 E_1 \cos(\alpha\pi/2) + E_0^2 (\omega\tau)^{-\alpha}} \tag{2.2.38}$$

$$E''(\omega) = E_0 E_1 \frac{E_0 \sin(\alpha\pi/2)}{E_1^2 (\omega\tau)^{\alpha} + 2E_0 E_1 \cos(\alpha\pi/2) + E_0^2 (\omega\tau)^{-\alpha}} \tag{2.2.39}$$

It can be easily verified that the modulus expressions for a Maxwell element can be recovered simply by substituting $\alpha = 1$ into above two functions. With the storage and loss moduli at hand, the phase angle can be easily expressed as a function of frequency and α:

$$\tan\varphi = \frac{E''(\omega)}{E'(\omega)} = \frac{E_0 \sin(\alpha\pi/2)}{E_1(\omega\tau)^{\alpha} + E_0 \cos(\alpha\pi/2)} \tag{2.2.40}$$

2.2.3.3 Application to asphalt concrete

Here the application of fractional viscoelastic models to asphalt concrete is illustrated first using the research work described in Katicha and Flintsch (2011). By applying both the 4- and 7-parameter generalized fractional Maxwell models (Figure 2-3) to the modulus data of asphalt concrete, the authors concluded that the 4-parameter fractional model with only one relaxation stage (since only one fractional dashpot is present) worked practically similarly to the conventional 4-parameter sigmoidal function in terms of fitting quality and model behaviors. However, the 7-parameter model, which has two relaxation stages corresponding to the two different mechanisms dominating the material behavior at low and high temperature as argued in the paper, fitted quite well the material viscoelastic quantities (storage modulus, loss modulus, and phase angle) in addition to dynamic modulus.

Similar to the sigmoidal function, parameters in fractional models can be also associated with physical meanings. Take the simple 4-parameter model as an example (Figure 2-3a). E_0 and ($E_0 + E$) characterize respectively the low and high asymptotes of dynamic modulus, τ describes the horizontal location, and α depicts the slope or the width of the transition zone. The sigmoidal function, however, cannot provide other viscoelastic information except dynamic modulus. Classical Prony-type models that can be represented by mechanical analogs are also able to offer detailed viscoelastic information, but the previously mentioned disadvantages (a large number of parameters, ill-posedness) have precluded a consistent and reliable correlation between model parameters and material properties.

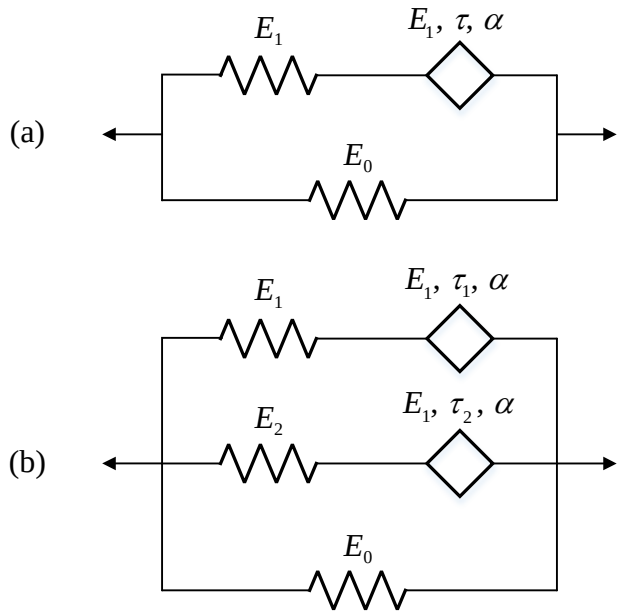

Figure 2-3 Generalized fractional Maxwell model with (a) 4 parameters, and (b) 7 parameters (a spring is put in parallel with the fractional Maxwell elements to provide a non-zero equilibrium modulus for viscoelastic solids).

Considering that the α-value in a fractional dashpot controls the extent to which the material behaves like a viscous fluid or an elastic solid, Oeser *et al.* (2008) explored the correlation between α and material hardening/softening state in the test. It is pointed out by the authors that initial compressive loading causes the material densification resulting into increased particle contacts, and thus the material exhibit less viscous and more solid-like behavior. During later part of the testing dilation may occur, which reduces the particle contacts and softens the material, and therefore the viscous binder will contribute more than earlier to the internal load transfer, and consequently an overall viscous-like behavior can be observed. Mathematically, the authors used a changing α-value to indicate the material evolving from solid-like to viscous-like state by correlating α with the volumetric strain, and their results show a satisfactory agreement in modeling creep and recovery tests.

2.2.3.4 Relationship with conventional Prony models

Given the mathematical soundness and practical advantages, fractional models are hard to visualize compared to models based on integer order derivatives (e.g. Prony series based models). However, it has already been demonstrated (Schiessel and Blumen 1993 and 1995, Schiessel *et al.* 1995, Heymans and Bauwens 1994, Hu and Zhu 2009) that a fractional model can be realized physically through hierarchical arrangements of springs and dashpots in structures such as trees and ladders (Figure 2-4). More recently, Adolfsson *et al.* (2005) and Papoulia *et al.* (2010) have shown that fractional models can be approximated as a limiting case from the classical generalized Maxwell and generalized Voigt models when the number of corresponding elements tends to infinity. These relations have provided a physical interpretation for fractional models with a link to classical ones.

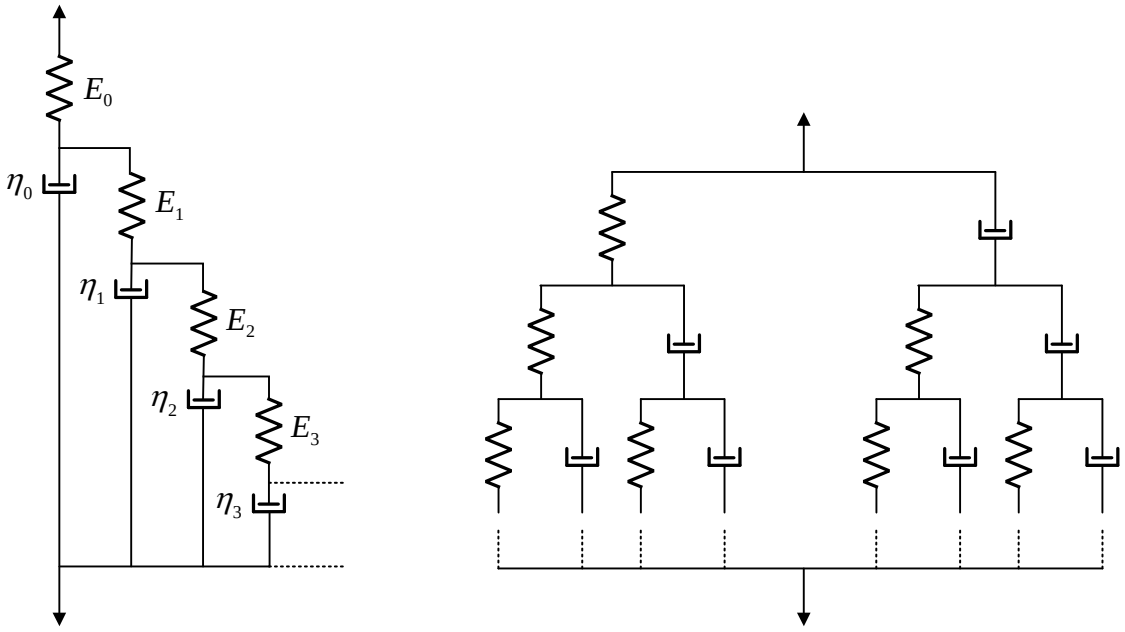

Figure 2-4 Networks of springs and dashpots equivalent to fractional models: (a) a tree structure, and (b) a ladder structure.

2.2.3.5 Final comments

The model expressions for frequency dependent viscoelastic quantities derived previously for the fractional Maxwell element have demonstrated the amenability to analysis and to the fitting of experimental data due to the simple form. However, for creep and relaxation tests, special functions such as the Mittag-Leffler (Erdélyi *et al.* 1954) function is required for the analysis in time domain. Thus, once robust numerical techniques can be developed to evaluate the special functions, the curve fitting to experimental data is easy to accomplish using standard methods.

Similar to the Prony-type model, higher model accuracy can be achieved by adding more fractional elements. However, in doing so the model complexity may become too mathematically cumbersome to be applicable, and also the closed form of one static function may not be available from the other given static function although the two are inherently correlated (Welch *et al.* 1999). Given the above-mentioned numerical and analytical difficulties, it is still comfortable to conclude that the role of fractional models in viscoelasticity will be continued considering the model ability to represent material behaviors over so many decades of time/frequency range with so few parameters.

2.3 Nonlinear Viscoelasticity

Nonlinear viscoelasticity has been explored for long for materials such as plastics (Lai and Bakker 1995), rubber (Ha and Schapery 1998), and biological materials (Fung 1993). The nonlinearities may originate from intrinsic atomic or molecular levels, or may be a result of the combined effect of distributed microcracks or dislocations, defects that are significant enough to be described using local continuum mechanics (Schapery 2000). For asphalt binder and mixture, it is usually considered that as long as the temperature, loading rate and/or magnitude are maintained within certain ranges material bulk behaviors may be well explained by linear viscoelasticity alone. However, nonlinearities may enter when it comes to large straining, microcracking, rutting and/or other mechanisms such as healing and aging.

2.3.1 Single integral form

2.3.1.1 Nonlinear superposition method

Viscoelasticity has been studied in numerous biological materials and Thornton *et al.* (1997) are among the first to observe experimentally that stress relaxation proceeds faster than creep in medical collateral ligaments, and that the linear viscoelasticity theory fails to phenomenologically describe both behaviors with correlated constitutive coefficients (Provenzano *et al.* 2001). In their study, Provenzano *et al.* (2001) examined the commonly used quasilinear viscoelastic theory (Fung 1972) which assumed a separable dependence on time and strain level regarding the relaxation function, and realized its incapability to admit the phenomena of load-level dependent creep rate and strain-level dependent relaxation rate as seen in experiments in addition to the above faster relaxation process than creep. On the other hand, analytical study also pointed out the inconsistance that a separable creep function would give rise to a non-seprable relaxation function (Lake and Vanderby 1999).

As an improvement on the quasilinear viscoelastic theory, the single integral formulation of the nonlinear (modified) superposition method (Findley *et al*. 1976) again allows for a strain-level dependent relaxation function which yet may now be chosen as a non-separable strain-dependent power-law form (Provenzano *et al*. 2002):

$$\sigma(\varepsilon,t)=\int_{0^-}^{t} E\left(t-\tau,\varepsilon(\tau)\right)\frac{d\varepsilon(\tau)}{d\tau}d\tau \tag{2.3.1}$$

$$E(\varepsilon,t)=A(\varepsilon)t^{B(\varepsilon)} \tag{2.3.2}$$

A stress-dependent compliance function may be used to formulate the load-controlled counterpart. In the above expression, the time dependence and strain-level dependence are coupled with the function $A(\varepsilon)$ representing the initial modulus and $B(\varepsilon)$ describing the strain dependence of the relaxation rate.

Provenzano *et al.* (2002) demonstrated using the rat ligament data the capability of the model to describe a decreasing rate of stress relaxation with an increase in the strain level (a phenomenon opposite to those in metals and geomaterials). Oza *et al.* (2003) investigated the analytical interconversion of creep and relaxation functions within the framework of non-

separable kernels. In the power-law expression of the relaxation function, owing to the clear interpretation of the relation between model parameters and mechanical behaviors, both the initial modulus and the exponent can be easily obtained from relaxation test with multiple strain levels. Despite the preliminary success and the convenience in characterization, the model still remains to be verified through comprehensive experiments with larger ranges of load magnitude and rate, and longer times.

2.3.1.2 Schapery's theory

The application of Schapery's nonlinear viscoelastic model can be found in many researches on polymer, biological tissues, and asphalt materials. Based on irreversible thermodynamic theory, Schapery initially proposed the nonlinear model in which stress was expressed as a function of strain and temperature histories (Schapery 1966). Then he reformulated it so that stress entered as the independent variable (Schapery 1969) since stress-controlled creep test is easier to perform on hard materials given machine flexibility and capacity for the characterization of viscoelastic properties. For the uniaxial case, the model is expressed as

$$\varepsilon^t = g_0{}^t D_0 \sigma^t + g_1{}^t \int_{0^-}^{t} \Delta D\left(\psi(t) - \psi(\tau)\right) \frac{d(g_2{}^\tau \sigma^\tau)}{d\tau} d\tau \tag{2.3.3}$$

where D_0 and $\Delta D(\psi)$ are instantaneous and transient components of creep compliance, respectively, in linear viscoelastic range; ψ is the reduced time defined by

$$\psi(t) = \int_{0^-}^{t} \frac{ds}{a_{\sigma^s,T}} \tag{2.3.4}$$

where $a_{\sigma^s,T}$ is the shift factor dependent on current stress state σ, temperature T, and possibly the aging time; and g_0, g_1, and g_2 are nonlinear functions of stress variables (e.g. octahedral shear stress and hydrostatic stress) and equal to one for small stress magnitudes (i.e. material exhibits linear viscoelasticity).

Compared to the nonlinear superposition model, the above Schapery's form provides higher flexibility in terms of model parameters thus making it more adaptable to the degree of nonlinearity observed in experiment. The parameter g_0, which is usually assumed to be

unity due to practical considerations (Rahmani *et al.* 2013), measures the increase or reduction in the instantaneous elastic compliance; g_1 describes the nonlinear effect of stress level in the transient compliance; g_2 accounts for the nonlinear effect of loading rate. It is worth noting that while these parameters bring about the versatility of the model, they may also suggest a less direct interpretative relation to material behaviors.

2.3.2 Multiple integral form

The basic idea behind the multiple integral formulation can be illustrated in a multi-step creep test. A linear viscoelasticity theory is brought about if the strain response is mathematically equal to the summation of each independent component generated by its corresponding stress step with no interactions. So naturally, if the cross effect between stress steps is considered in terms of, for example, higher order terms, then the multiple integral form of the nonlinear viscoelasticity theory can be formulated (Findley *et al.* 1976):

$$\begin{aligned}\varepsilon(t) = &\int_{0^-}^{t} \varphi_1(t-\xi_1)\dot{\sigma}(\xi_1)d\xi_1 + \int_{0^-}^{t}\int_{0^-}^{t} \varphi_2(t-\xi_1, t-\xi_2)\dot{\sigma}(\xi_1)\dot{\sigma}(\xi_2)d\xi_1 d\xi_2 \\ &+ \int_{0^-}^{t}\int_{0^-}^{t}\int_{0^-}^{t} \varphi_3(t-\xi_1, t-\xi_2, t-\xi_3)\dot{\sigma}(\xi_1)\dot{\sigma}(\xi_2)\dot{\sigma}(\xi_3)d\xi_1 d\xi_2 d\xi_3 + \cdots\end{aligned} \tag{2.3.5}$$

The above form somehow implies that the multiple integral theory may be understood as a generalization of the linear superposition principle by introducing the high order stress terms. Another implication, yet seemingly to make the interpretation more intricate, is that a linear response of a material under a single constant stress (i.e., φ_2 and φ_3 *etc*. vanish) is not a guarantee that the material follows the linear viscoelasticity theory in that terms like φ_2 *etc*. may still exist indicating a nonlinear material. For examples of application, interested readers may refer to Onaran and Findley (1965) for polymers and Adeyeri *et al.* (1970) for clay soils and the references therein.

Multiple integral formulation is complicated and less amenable for practical characterization or computation. However, it is inherently more robust and allows for more complex stress conditions such as the 3-D state of stress and more realistic load histories

containing multiple steps such as a creep and recovery test (Findley *et al.* 1976). On the contrary, the 1-D single integral formulation is able to describe only a subset of viscoelastic phenomena (Provenzano *et al.* 2002) and carries an inherent deficiency when expanded to multiaxial states.

2.3.3 Comments

To date, the linear viscoelasticity theory has been heavily relied on to characterize asphalt materials due to its advantages in the required experimental and computational efforts. However, the application of the linear assumption may render a poor prediction if the material goes beyond the linear range. For asphalt concrete, Monismith *et al*. (1966) put 0.1% as the upper strain limit for the linear range. Consequently, the material is mostly nonlinear during the normal service of pavements.

To the author's knowledge, the reason why nonlinear viscoelasticity has not seen its prosperity for now in the application to asphalt materials lies in three aspects. First, thresholds or appropriate ranges regarding temperature, load/deformation magnitude and rate are missing, which means we have no conclusive clue as to when plasticity or microcracks start to develop within the material. Secondly, it is quite difficult to discriminate the material intrinsic (if any) nonlinearities from the loading-induced nonlinearities. For example, in the strain decomposition assumption as commonly used in constitutive modeling, the (visco)plastic straining history may alter the viscoelastic properties, a phenomenon named as viscoelasticity-(visco)plasticity coupling. Thirdly, viscoelasticity theories are primarily developed for materials either homogeneous or for which tensile loading is of major interest, such as polymers, metals, and biological materials. Asphalt concrete may basically follow the same rationale when loaded in tension during which asphalt binder dominates the overall response. However, when it comes to compression the aggregate structure plays an ever increasingly decisive role in resisting the external loads as time goes and temperature increases, a mechanism that apparently cannot be covered by viscoelasticity theories.

2.4 Viscoelasticity under Confinement

Generally, as to dense materials like polymers and metals the existence of confinement does not exert a significant influence on material mechanical response. However, for porous materials such as soil, cement concrete, and asphalt mixtures, the presence or absence of confinement can make a big difference in response and the long term performance especially in the compressive loading mode. Here asphalt concrete is used as the medium whose viscoelastic properties are to be investigated under different confinements.

Pellinen and Witczak (2002) are among the first to examine the stress dependence of dynamic modulus of asphalt concrete. By assuming a linear behavior (thus stress independent) at low temperatures, they proposed that stress levels change only the moduli values at intermediate and high temperatures in terms of the equilibrium modulus value being a function of stress; meanwhile the time-temperature shift factors are maintained as opposed to being stress/strain dependent in Schapery's nonlinear theory (Schapery 1966 and 1969). The "universal material model" (Witczak and Uzan 1988) initially proposed for unbound materials was employed to describe the stress dependence of the equilibrium modulus:

$$\delta = \left(k_1 P_a\right)\left(\frac{\theta}{P_a}\right)^{k_2}\left(\frac{\tau_{oct}}{P_a}\right)^{k_3} \tag{2.4.1}$$

where P_a is the atmospheric pressure, θ is the bulk stress (first stress variant I_1), and τ_{oct} is the octahedral shear stress, and $k_{1\text{-}3}$ are the regression coefficients. It is worth mentioning that during the model characterization procedures the experimental data basically indicated an independence of the equilibrium modulus on the octahedral shear stress (Pellinen and Witczak 2002). Other modified forms are also available such as those in Lytton *et al*. (1993) and Kim *et al*. (2009). It should be pointed out that the assumption of time-temperature shift factors not being affected by confinement levels has been experimentally verified for limited mixes in Zhao *et al*. (2013), while LaCroix *et al.* (2011) and Underwood *et al*. (2011) observed additionally that the viscoelastic relaxation properties were similar at different confinements for a few mixes by comparing the distribution of relaxation spectrum.

By presenting the isobaric storage modulus master curves from different confinements, Zhao *et al*. (2013) realized, in addition to the traditional horizontal shift, the need of a vertical shift to collapse all the master curves with shift factors dependent on loading frequency and temperature, or the reduced frequency. The calculated vertical shift factors based on experimental data followed a sigmoidal function, and for the lower asymptote of the storage modulus an exponential function was used to express the pressure dependence:

$$\ln E'_{\min,P} = C_1\left(1-e^{-C_2 P}\right)+\ln E'_{\min,0} \tag{2.4.2}$$

where P is the confining pressure, $E'_{\min,0}$ is the minimum storage modulus without confinement, $E'_{\min,P}$ is the minimum storage modulus at confining pressure P, and $C_{1\text{-}2}$ are regression coefficients.

Under the framework of Schapery's nonlinear viscoelasticity theory described earlier, Rahmani *et al*. (2013) investigated quantitatively the combined effects of deviatoric stress and confining pressure through establishing relations of model nonlinear parameters (g_1, g_2) with the triaxiality ratio, which is defined as the ratio of mean stress to the von Mises equivalent stress:

$$\eta = \frac{\sigma_m}{\sigma_{vM}} \tag{2.4.3}$$

with

$$\begin{aligned} \sigma_m &= I_1/3 = \left(\sigma_{11}+\sigma_{22}+\sigma_{33}\right)/3 \\ \sigma_{vM} &= \sqrt{3J_2} \\ &= 1/\sqrt{2}\sqrt{\left(\sigma_{11}-\sigma_{22}\right)^2+\left(\sigma_{22}-\sigma_{33}\right)^2+\left(\sigma_{11}-\sigma_{33}\right)^2+6\left(\sigma_{23}^2+\sigma_{13}^2+\sigma_{12}^2\right)} \end{aligned} \tag{2.4.4}$$

After analyzing the confined multi-step creep tests, a relatively high variation of nonlinear parameters was seen for small triaxiality ratios, which implied a considerable nonlinearity associated with the deviatoric stress when the confinement level was low. Conversely, the increase of deviatoric stress at high confining levels tended to cause negligible nonlinearity on the material response. Based on the trend of the nonlinear parameters, the authors were also able to conclude that less time dependent and thus more

elastic-like behaviors were expected at high confinements presumably due to the reduced mobility of aggregates and asphalt binder in between.

2.5 Classical Plasticity and Viscoplasticity

2.5.1 Plasticity

Plasticity theory is developed to depict the irreversible or permanent deformation caused by the external loading. If the plastic strain is rate-dependent, viscoplasticity theory is then necessitated. Despite being initially formulated for metals, plasticity has seen its need and application in most materials including geomaterials (soils, rocks, concrete) and biological materials (bone, skin). It should be mentioned, however, that the physical mechanisms behind plastic deformation may vary greatly for different materials, from dislocation for metals to the formation of microcracks and slipping for rocks and concrete.

Mathematical descriptions of plasticity start with the deformation theory, in which the total stress is expressed as a function of the total strain. Despite its simplicity, this approach loses its accuracy when complex loading histories are considered such as non-proportional loading and load reversals.

The hypothesis of dislocations for ductile materials gave birth to the flow (incremental) plasticity theory. It is then assumed that the total strain in a body could be decomposed additively (or multiplicatively) into an elastic part and a plastic part. The plastic part of the deformation is to be specified by a flow rule that is expressed as the strain increment being a function of stress. The magnitude of the strain increment is dictated by the so-called plastic multiplier that can be determined from the consistency condition forcing the stress to stay on the evolving yield surface during plastic straining. The direction of the strain increment is described by the gradient of the plastic potential in the stress space. If the plastic potential function is assumed the same as the yield function, an associated flow rule is degenerated; otherwise, as in the most general case, we will have a non-associated flow rule. As just mentioned, the yield surface develops, symbolizing a growth in material resistance to plastic straining, for which a hardening law has to be specified in terms of, for example,

internal state variables expressed as functions of plastic work (work hardening) or plastic strain increment (strain hardening).

2.5.2 Viscoplasticity

It is already seen that flow rule, yield criterion, and hardening law constitute the three central ingredients of the classical plasticity theory. As a modification and extension of the plasticity theory to accommodate the rate-dependent plastic deformation, the consistency condition is abandoned indicating that a stress state beyond the yield surface is permitted, and the corresponding viscoplastic multiplier is now obtained through a selected expression of the yield function. The commonly used Perzyna type viscoplasticity model is presented below as an example:

$$\dot{\varepsilon}_{vp} = \dot{\lambda}\frac{\partial Q}{\partial \sigma} = \gamma\, \Phi(F)\frac{\partial Q}{\partial \sigma} \tag{2.5.1}$$

where $\dot{\lambda}$ is the viscoplastic multiplier, F is the yield function, Q is the viscoplastic potential function, γ is the material fluidity constant, and for the function Φ the following power law is usually adopted:

$$\Phi(F) = \left\langle \frac{\sigma_o}{\sigma_Y} \right\rangle^n \tag{2.5.2}$$

where σ_o is the overstress related to the yield function F, σ_Y is the uniaxial yield stress used to non-dimensionalize the overstress function, and n is a material constant. The Macaulay brackets $\langle \cdot \rangle$ are used to implement the theory hypothesis that the plastic strain increases only under a non-zero overstress. If we choose $F = Q$, then an associated viscoplasticity model is degenerated. Note that the above formulation is able to incorporate the rate-independent plasticity as the limiting case of the classical viscoplasticity for infinitely slow loading processes. Most viscoplasticity models available in the literature fit into this Perzyna type framework with differences mainly lie in the choices of functions Φ, F, and Q, and the hardening rules specifying the evolution laws of the internal state variables.

Owing to the negligible pressure dependence, metal plasticity and viscoplasticity have been using yield criteria that are independent of the mean stress I_1 since the first application. However, when this concept was borrowed to the application on geomaterials like soils and cement/asphalt concrete, the pressure dependence brought by the material porosity necessitated the presence of mean stress in the yield function. Two well-known examples are Mohr-Coulomb criterion and Drucker-Prager criterion.

2.5.3 Pressure dependent yield criteria

2.5.3.1 The Haigh-Westergaard stress space

In order to eliminate the dependence on specific coordinate system chosen for analysis, yield criteria, such as Tresca and von Mises criteria, have been commonly described in terms of stress invariants for isotropic materials in the 3-D space of principal stresses (σ_1, σ_2, σ_3). Nevertheless, it is particularly convenient to work with the Haigh-Westergaard coordinates (ρ, s, θ) for their superior capability in depicting and visualizing geometrically pressure dependent yield criteria. For this purpose, the Haigh-Westergaard stress space is first introduced here.

As illustrated in Figure 2-5, given any stress point A in the principal stress space, the stress vector can always be decomposed into a hydrostatic part $\boldsymbol{\rho} = (\sigma_m, \sigma_m, \sigma_m)$ and a deviatoric part $\boldsymbol{s} = (s_1, s_2, s_3)$:

$$\left(\sigma_1, \sigma_2, \sigma_3\right) = \left(\sigma_1 - \sigma_m, \sigma_2 - \sigma_m, \sigma_3 - \sigma_m\right) + \left(\sigma_m, \sigma_m, \sigma_m\right) \tag{2.5.3}$$

where the hydrostatic stress component is $\sigma_m = I_1 / 3$, and the deviatoric component lies on the π-plane, a stress surface defined by $\sigma_1 + \sigma_2 + \sigma_3 = 0$. Also in the figure, s_1 denotes the projection of the first principal axis σ_1 on to the π-plane by looking down at the coordinate system along the hydrostatic axis. The Lode angle θ, ranging from 0 to 60 degrees, is measured counterclockwise from s_1 axis to the deviatoric stress component in the π-plane.

The expression for θ can be found by the use of the unit vector along s_1 axis: $\mathbf{e} = \left(\sqrt{2}/\sqrt{3}, -1/\sqrt{6}, -1/\sqrt{6}\right)$. Considering the dot product $\boldsymbol{s} \cdot \mathbf{e} = s\cos\theta$ where $s = \sqrt{2J_2}$, we can easily arrive at

$$\cos\theta = \frac{\sqrt{3}s_1}{2\sqrt{J_2}} \tag{2.5.4}$$

Further manipulations may also give the expression in terms of stress invariants:

$$\cos 3\theta = \frac{3\sqrt{3}}{2}\frac{J_3}{J_2^{3/2}} \tag{2.5.5}$$

It is thus obvious that $\cos 3\theta$ is also an invariant.

From the above analysis, any stress point in the principal stress space can be rewritten in terms of Haigh-Westergaard coordinates as

$$\begin{Bmatrix}\sigma_1\\ \sigma_2\\ \sigma_3\end{Bmatrix} = \frac{1}{\sqrt{3}}\begin{Bmatrix}\rho\\ \rho\\ \rho\end{Bmatrix} + \sqrt{\frac{2}{3}}s\begin{Bmatrix}\cos\theta\\ \cos\left(\theta - 2\pi/3\right)\\ \cos\left(\theta + 2\pi/3\right)\end{Bmatrix} \tag{2.5.6}$$

where the magnitude of the hydrostatic stress component is $\rho = \sqrt{3}\sigma_m$. Therefore, by making the above substitution, any yield criterion represented by principal stresses can now be recast into the Haigh-Westergaard stress space.

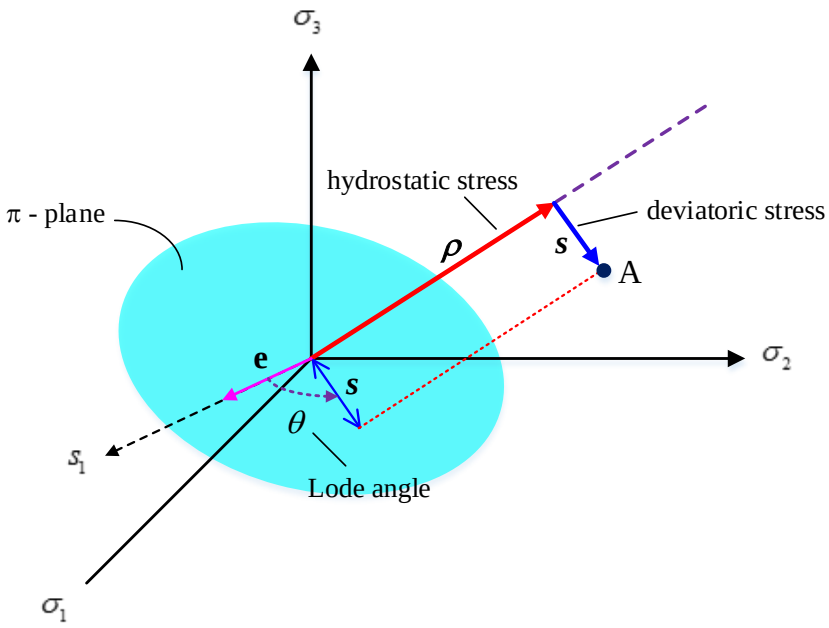

Figure 2-5 The Haigh-Westergaard stress coordinate of a point in the principal stress space.

2.5.3.2 Mohr-Coulomb criterion

Mohr-Coulomb theory proposed a linear failure envelope that is interpreted as the critical state of the combination of normal and shear stress in the 2-D case. The criterion is represented as

$$\tau = \sigma \tan\phi + c \tag{2.5.7}$$

where τ is the shear strength, σ is the normal stress, c is interpreted as the material cohesion and ϕ the angle of internal friction. Geometrically, c is the intercept of the linear envelope with the τ axis and ϕ is the slope of the envelope in the τ-ϕ space. As initially developed for geomaterials, the sign convention commonly uses compression as positive. Note that when ϕ = 0 the Mohr-Coulomb criterion reduces to the Tresca criterion.

When it comes to the 3-D case, if we assume the order for the principal stresses as $\sigma_1 > \sigma_2 > \sigma_3$, then the Mohr-Coulomb criterion can be expressed as

$$\frac{\sigma_1 - \sigma_3}{2} = \frac{\sigma_1 + \sigma_3}{2}\sin\phi + c\cos\phi \tag{2.5.8}$$

When the above relation is reduced to the uniaxial case, the strength of the Mohr-Coulomb material in tension f_{YT}, and in compression f_{YC} can be obtained as

$$f_{YT} = \frac{2c\cos\phi}{1+\sin\phi}, \quad f_{YC} = \frac{2c\cos\phi}{1-\sin\phi} \tag{2.5.9}$$

Therefore, the model coefficients c and ϕ can be fully determined if both uniaxial tension and compression tests can be performed on the material. As an alternative, given the popularity of triaxial shear test equipment, two triaxial compression tests at different confining pressure can be conducted to identify the model coefficients.

Substitution of Equation (2.5.6) into (2.5.8) yields the expression in terms of the Haigh-Westergaard coordinates:

$$K(\theta)s - \sqrt{2}\rho\sin\phi = \sqrt{6}c\cos\phi \quad \text{with} \quad K(\theta) = \sqrt{3}\sin\left(\theta+\frac{\pi}{3}\right) - \sin\phi\cos\left(\theta+\frac{\pi}{3}\right) \tag{2.5.10}$$

Obviously, the presence of the hydrostatic stress ρ brings the pressure dependence of the Mohr-Coulomb criterion.

The graphical representation of the Mohr-Coulomb yield criterion is given in Figure 2-6 in respectively the principal stress space, the π-plane, and the meridian plane. In the π-plane the yield locus appears as an irregular hexagon featuring two lengths: the magnitude of the deviatoric stress at failure in uniaxial tension s_{t0}, and that in compression s_{c0}, given by:

$$s_{t0} = \frac{\sqrt{6}f_{YC}(1-\sin\phi)}{3+\sin\phi}, \quad s_{c0} = \frac{\sqrt{6}f_{YC}(1-\sin\phi)}{3-\sin\phi} \tag{2.5.11}$$

In the meridian plane, the yield surface intercepts the hydrostatic axis at $\rho = \sqrt{3}c\cot\phi$.

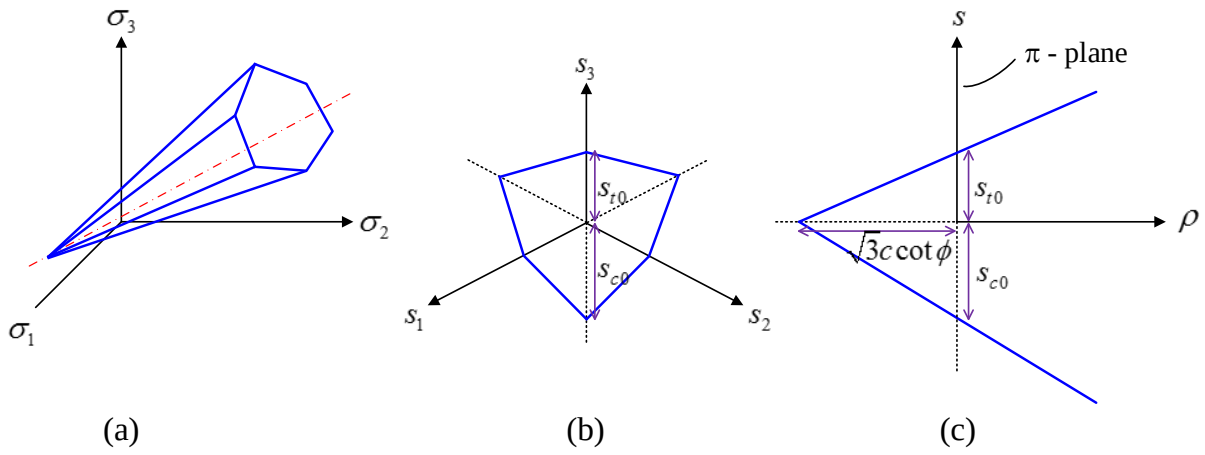

Figure 2-6 The Mohr-Coulomb criterion: (a) the principal stress space, (b) the π-plane, and (c) the meridian plane.

Due to its analytical simplicity and the clear physical significance associated with model parameters, the Mohr-coulomb yield criterion has received general academic acceptance and wide practical application. However, the model has been always suffering from two numerical deficiencies in implementation and thus may lose its robustness and accuracy. First, as described previously, the gradient of the (visco)plastic potential function in the stress space is to be calculated to provide the information regarding the strain increment. However, due to the presence of the corners on the yield locus as seen in Figure 2-6(b), if a Mohr-Coulomb type potential function is chosen, at the vertices of the yield locus the gradient is indeterminable and thus numerical instabilities and errors will occur. Secondly, as shown in Figure 2-6(c) the yield surface comes to a singular point at the hydrostatic axis with zero shear strength. This singularity can cause both numerical and efficiency problems in the algorithm implementation.

Regarding the above-mentioned deficiencies, some remedies have been explored to establish a smooth approximation to the standard Mohr-Coulomb model with a focus on modifying the function $K(\theta)$. Sloan and Booker (1986) proposed a round-off technique using trigonometric approximations to smooth the vicinity of vertices in the π-plane, so that a differentiable yield surface and thus a continuously varying gradient without jumps were

accomplished for all values of stresses. Abbo and Sloan (1995) used a hyperbola function to asymptotically approximate the straight line in the meridian plane so that the singular point was able to be replaced by a smooth surface around the area with zero shear strength. Lewis (Lewis 2004) proposed a new $K(\theta)$ function, different than the one specified in Equation (2.5.10) for the standard Mohr-Coulomb criterion, to account for the experimental phenomenon for cohesionless soil that the yield locus takes a triangular shape in the π-plane at low hydrostatic pressures (Figure 2-7).

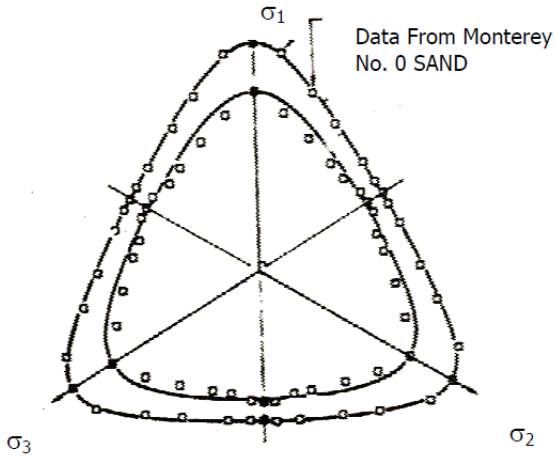

Figure 2-7 Yield surface in the π-plane for cohesionless soils (Lewis 2004).

2.5.3.3 Drucker-Prager criterion

The Drucker-Prager yield criterion has the following form

$$\sqrt{J_2} = A + B\, I_1 \tag{2.5.12}$$

The above expression can be interpreted as an improvement from the classical von Mises yield criterion ($\sqrt{J_2} = A$) by adding the mean stress term to account for the increased shear strength with the hydrostatic pressure. In terms of the Haigh-Westergaard coordinates, the Drucker-Prager criterion can be represented as

$$\frac{s}{\sqrt{2}} - \sqrt{3}B\rho = A \tag{2.5.13}$$

From the above Equation (2.5.13) it is readily visualized that the yield locus in the π-plane is a circle. Similar to the Mohr-Coulomb criterion, the model coefficients *A* and *B* also have clear physical significance. In the case of uniaxial tension with yield stress denoted as f_{YT}, the criterion gives $f_{YT} / \sqrt{3} = A - f_{YT}B$. When applied to the uniaxial compression with yield stress f_{YC}, the criterion yields $f_{YC} / \sqrt{3} = A + f_{YC}B$. These two equations can be solved to obtain the model coefficients:

$$A = \frac{2}{\sqrt{3}} \frac{f_{YC} f_{YT}}{f_{YC} + f_{YT}}, \quad B = \frac{1}{\sqrt{3}} \frac{f_{YC} - f_{YT}}{f_{YC} + f_{YT}} \tag{2.5.14}$$

Again here compressive stress is dealt with as positive. Note that as is the case for Mohr-Coulomb criterion, the Drucker-Prager criterion is also able to predict different uniaxial yield stresses in tension and in compression. The uniaxial asymmetry ratio, which is defined as the ratio of the yield stress in compression to that in tension, can be easily calculated as

$$\zeta = \frac{f_{YC}}{f_{YT}} = \frac{1 + \sqrt{3}B}{1 - \sqrt{3}B} \tag{2.5.15}$$

If the yield locus from Drucker-Prager criterion is compared to that of Mohr-Coulomb criterion in the π-plane, the Drucker-Prager circle can go through either the three major vertices of the Mohr-Coulomb hexagon (hence circumscription), or the three minor vertices (hence inscription), as illustrated in Figure 2-8. In both cases, relationships can be readily established between the model parameters from the two criteria. For the circumscription case, the expression for *A* and *B* are

$$A = \frac{6c\cos\phi}{\sqrt{3}(3 + \sin\phi)}, \quad B = \frac{2\sin\phi}{\sqrt{3}(3 + \sin\phi)} \tag{2.5.16}$$

And for the inscription case, we have

$$A = \frac{6c\cos\phi}{\sqrt{3}(3 - \sin\phi)}, \quad B = \frac{2\sin\phi}{\sqrt{3}(3 - \sin\phi)} \tag{2.5.17}$$

Therefore, the model parameters of the Drucker-Prager criterion can now be directly obtained from the two material constants: cohesion and angle of internal friction.

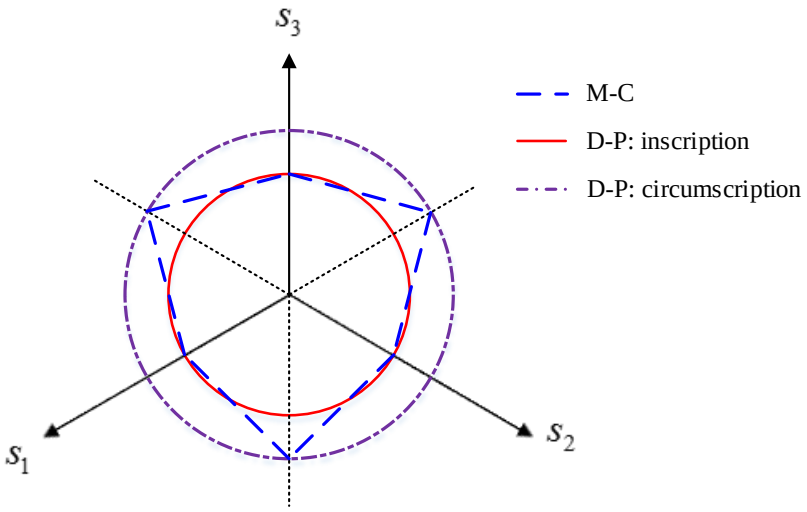

Figure 2-8 Drucker-Prager and Mohr-Coulomb yield loci in the π-plane.

2.6 Viscoplastic Modeling of Asphalt Mixtures at NCSU

2.6.1 A classical viscoplastic model with rate-dependent yield surface

Experimental and analytical explorations in plastic deformation of asphalt concrete have been performed at NCSU for over ten years. Yun (2008) conducted a series of creep and recovery test (with square-shape pulse) with different stress levels, temperatures, and complex loading history in which the pulse time and rest period change with cycle number. Even though in some tests the loading history is deemed as too complicated to be used directly in model development, these experiments provide an important appreciation of material complexity and guidelines for subsequent researches.

Observing the inadequacy of classical viscoplastic models for polymers and metals, Yun proposed a 1-D model with rate-dependent yield criterion within the framework of

classical viscoplasticity based on the time dependence of material hardening and recovery during the test. In Equation (2.5.1) as associated flow rule is assumed:

$$\dot{\varepsilon}_{vp} = \dot{\lambda}\frac{\partial F}{\partial \sigma} \tag{2.6.1}$$

with the viscoplastic multiplier given in a power form:

$$\dot{\lambda} = \left\langle \frac{\sigma_v}{D} \right\rangle^m = \left\langle \frac{f(\sigma-\alpha)-\gamma}{D} \right\rangle^m \tag{2.6.2}$$

where α is the kinematic hardening variable, γ is the isotropic hardening variable, the drag stress D is a material constant used to normalize the overstress σ_v, m is a material constant governing the rate dependence, and $F = f(\sigma - \alpha) - \gamma = 0$ defines the yield surface. In the simplest 1-D case the kinematic and isotropic hardening variable can be combined into a single variable G, and Equation (2.6.1) can be reduced to a power law relation:

$$\dot{\varepsilon}_{vp} = \left\langle \frac{\sigma - G}{D} \right\rangle^m \tag{2.6.3}$$

In the above expression, the yield stress G becomes the most critical variable to be characterized. Yun believed that material hardened during the creep loading. For the rest period, based on the observed phenomenon that longer rest period yields larger deformation in the subsequent cycle (which seemingly indicates that material softens due to rest), he claimed that the yield stress would decrease after load removal.

It is assumed that the yield stress G evolves in a viscoelastic-like fashion (see Equation (2.2.2)). That is, for one load cycle with creep pulse time t_p and rest period t_r shown in Figure 2-9, the yield stress is given by

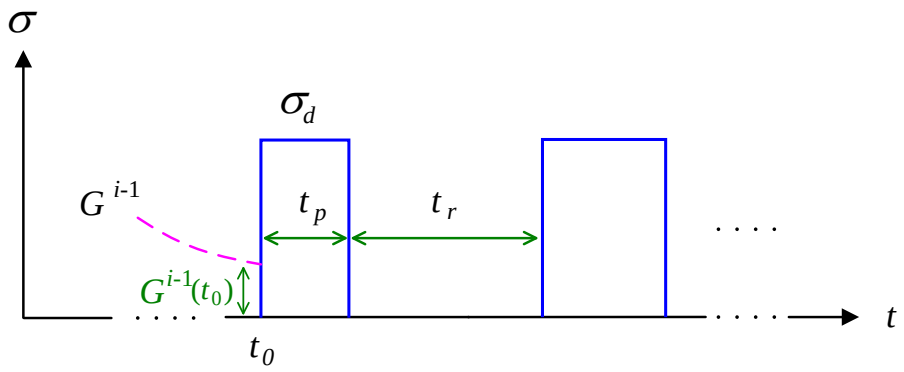

Figure 2-9 A cyclic creep and recovery test with square-shaped pulse for the illustration of the evolution of yield stress G.

$$
\begin{aligned}
G^i(t) &= G^{i-1}(t_0) + g_L^i(t-t_0)\left[\sigma_d - G^{i-1}(t_0)\right] && \text{for} \quad t \in \left(t_0, t_0 + t_p\right) \\
G^i(t) &= G^{i-1}(t_0) + g_L^i(t-t_0)\left[\sigma_d - G^{i-1}(t_0)\right] - g_R^i(t-t_0-t_p)\sigma_d && \text{for} \quad t \in \left(t_0 + t_p, t_0 + t_p + t_r\right)
\end{aligned}
\tag{2.6.4}
$$

where $G^{i-1}(t_0)$ indicates the yield stress value at the end of previous rest period, and both $g_L(t)$ and $g_R(t)$ are compliance-like functions representing different time dependence of the yield stress evolution during creep loading and recovery. It is assumed that both functions takes a sigmoidal shape in the space of $g(t)$ versus $\log(t)$ just like the linear viscoelastic creep function, and the softening function is located at the left of the hardening function which implies a higher rate of reduction in G during softening than increase in the hardening (see Figure 2-10). Since in Equation (2.6.4) the yield stress is not explicitly expressed as a function of deformation/loading history dependent state variable, $g(t)$ functions themselves have to vary, and they are assumed to vary only through horizontal shift in the space of $g(t)$ versus $\log(t)$ in order to reduce the number of parameters to be identified. Therefore, hardening or the increase of yield stress G is accomplished by shifting $g_L(t)$ toward left side, and the softening or reduction in the yield stress is achieved by shifting $g_R(t)$ to the right.

It is understandable to use right shifting $g_L(t)$ to represent hardening since higher values of yield stress can be resulted as cycle number increases, and thus less plastic strain will be generated. However, regarding the function $g_R(t)$, even though the softening

hypothesis is assumed correct, there is no physical or mathematical rationale to make it shift to right in order to describe a reduced yield stress since G will always decline after the load removal regardless of the horizontal location of $g_R(t)$. By shifting the $g_R(t)$ function only the rate of the reduction of yield stress G is affected.

This model generally agrees well with the experimental data considering the complex loading history used. The major limitation is due to its uniaxial nature in that the confining pressure does not enter the model explicitly but rather through changing the model parameters for different confinement levels. Besides, even for a single confinement level considerable experimental efforts are required to characterize the $g(t)$ functions. In addition, the model capability of accounting for the material nonlinearity due to deviatoric stress variations has not been explored or verified. Finally, tremendous difficulties lie in the process of optimizing 12 model parameters (including 6 for the internal state variables), none of which has clear interpretive relation with material response or property.

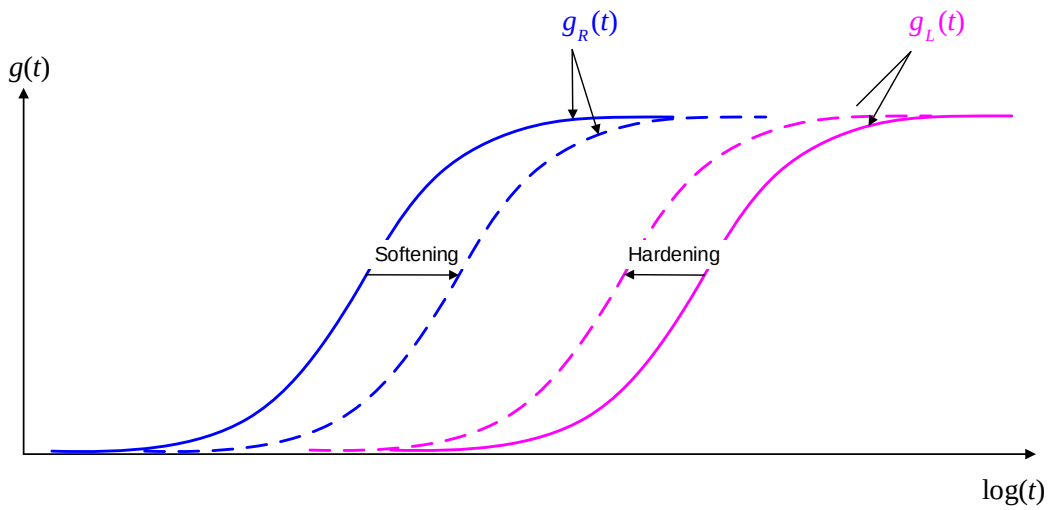

Figure 2-10 The evolution of the compliance-like functions used in the calculation of yield stress G during hardening and softening.

2.6.2 A convolution-type viscoplastic model with rate-dependent hardening

Following Yun's work and observing that in the 1-D case the plastic strain alone does not carry adequate historical loading or deformation information to serve as the state variable to track the material state, Subramanian (2011) proposed a new 1-D model form in which the whole loading history is fully and explicitly incorporated:

$$\begin{aligned} H(t) &= H_0 + \left\langle \int_{0^-}^{t} D_2(t-\tau)\frac{d\sigma(\tau)_H}{d\tau}d\tau \right\rangle \\ \varepsilon_{vp}(t) &= \left\langle \int_{0^-}^{t} D_1(t-\tau)\frac{d\sigma(\tau)_{vp}}{d\tau}d\tau \right\rangle \end{aligned} \tag{2.6.5}$$

In the above expressions, the material hardening state as well as the viscoplastic strain has been explicitly expressed as a function of the deviatoric stress through the convolution integral which takes the whole loading history into account. The Macaulay brackets, redefined in Equation (2.6.6), are added to guarantee the irreversibility of both hardening state and plastic deformation:

$$\begin{aligned} \left\langle \dot{\Psi} \right\rangle &= \dot{\Psi}, \quad \text{if } \dot{\Psi} \geq 0 \\ \left\langle \dot{\Psi} \right\rangle &= 0, \quad \text{if } \dot{\Psi} < 0 \end{aligned} \tag{2.6.6}$$

Two compliance-like functions $D_1(t)$ and $D_2(t)$ represent respectively the time-dependence of mechanisms behind hardening and plastic deformation. The parameter H_0 is primary introduced for numerical regularization purposes and literally can assume any positive value, which only affect the internal scale of the model while in the meantime it can also physically represent the initial hardening state of the material. For the stress terms in the convolution integrals, power laws are used to modify the actual stress to introduce the nonlinearity regarding the deviatoric stress:

$$\begin{aligned} \sigma(t)_H &= H_1\left(\sigma(t)\right)^q \\ \sigma(t)_{vp} &= \frac{\left(G_1\sigma(t)\right)^{p_1} + \left(G_2\sigma(t)\right)^{p_2}}{H(t)^{\alpha}} \end{aligned} \tag{2.6.7}$$

where H_1, q, G_1, G_2, p_1, p_2, and α are model parameters to be obtained from optimization. Note that these two stress functions only apply for the whole square-shaped loading pulse or

the first half of the haversine-shaped pulse. During the unloading (when stress is nonzero but decreasing) and rest period (when the stress is zero), material state and plastic deformation are assumed constant so that mathematically in Equation (2.6.5) the two stress terms have to be modified. For this purpose, Equation (2.6.5) is used in a reversed way to back calculate the "correct" stress values so that the results from the two convolution integrals do not reduce during unloading or after load removal.

Subramanian used a mechanical analog shown in Figure 2-11 to physically explain the behavior of a convolution integral enclosed in the Macaulay brackets. In the mechanical analog a linear viscoelastic device is connected in parallel with a slip device. The slip device features a non-decreasing deformation, which means whenever the viscoelastic device has the tendency to recover the strain the slip device locks forbidding the recovery. At this time, the resisting force (i.e. the back stress) is generated in the viscoelastic device in a direction opposite to the previous loading. Yet, due to viscoelastic relaxation this resisting force decreases with time. On the other hand, when the external force rises beyond the resisting force in the viscoelastic device the slip device is unlocked and becomes frictionless, and then the overall viscoplastic deformation develops in a viscoelastic fashion.

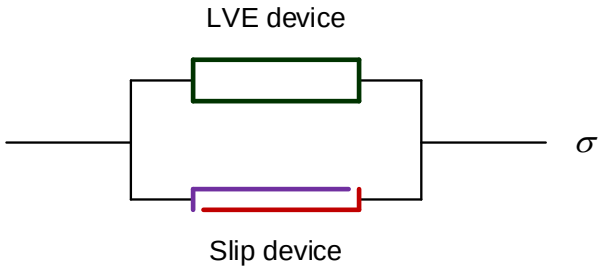

Figure 2-11 Mechanical analog for the convolution-type viscoplastic model.

In the following, compared to Subramanian's original dissertation a slightly different interpretation of the model mechanisms are presented as illustrated in Figure 2-12 and it is

believed that this provides an alternative approach to mathematically further understanding the model.

As just mentioned, during the unloading and rest period, the two stress terms in Equation (2.6.5) are not specified by Equation (2.6.7) but rather back calculated, and the resulting stresses are termed as back stresses. Note that the back stress here is different from the back stress commonly used to denote the center of yield surfaces in classical plasticity and viscoplasticity theories. The back stress can be understood as material internal stress developed during plastic straining in order to resist the external loading and thus it is fully determined by the loading portion of a stress pulse. How the back stress evolves during loading is not specified by the proposed model; it is only assumed to be equal to the modified peak stress obtained by substituting the actual peak stress into Equation (2.6.7). The back stress is only used after the peak modified stress and appears as a decreasing function. When the next cycle begins the current back stress still preserves certain magnitude and further hardening or plastic deformation does not occur until the corresponding modified stress increases beyond the back stress. At the time when the modified stress becomes larger than the back stress, this stress difference makes the convolution integrals in Equation (2.6.5) to increase. Note that since 100s is not long enough to relax all the back stress and it builds up over cycles, it has an increased value (denoted as $\sigma_{b,0}$ in Figure 2-12) at the time when hardening and viscoplastic strain starts to develop in the initial portion of each pulse, which leaves a reduced portion of loading to generate hardening and deformation, and this helps to account for the experimental observation that the net amount of material hardening and deformation decline with the cycle number. Regarding the back stress, it is also found that it acts like the yield surface concept in classical plasticity or viscoplasticity models since no change in the results of the two back stresses as well as respective convolution integrals can be made for any stress paths during unloading as long as they lie within the envelope of the back stress. See Figure 2-13.

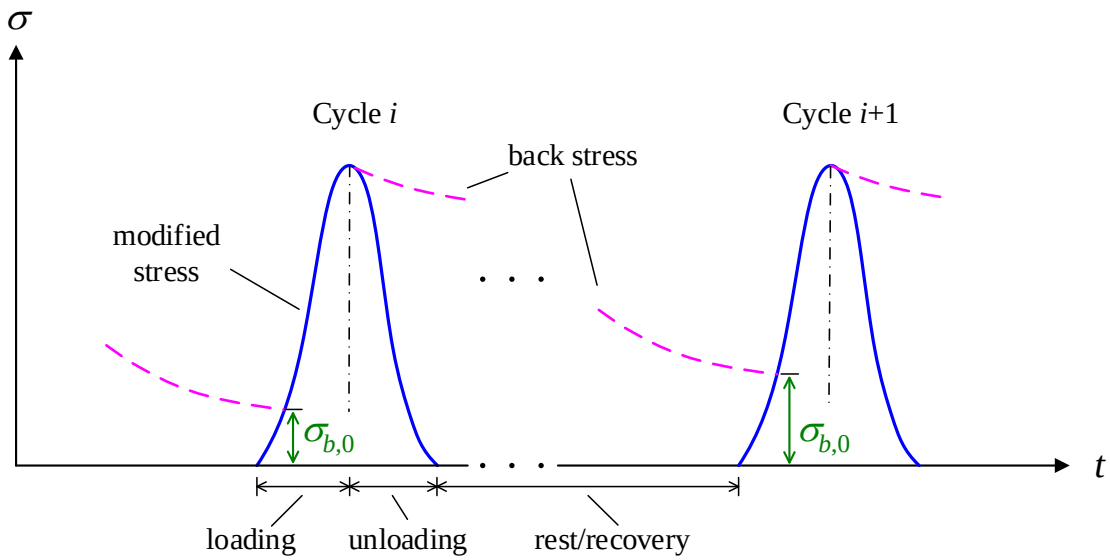

Figure 2-12 Modified stress and the evolution of the back stress illustrated for either one of the convolution integrals in Equation (2.6.5).

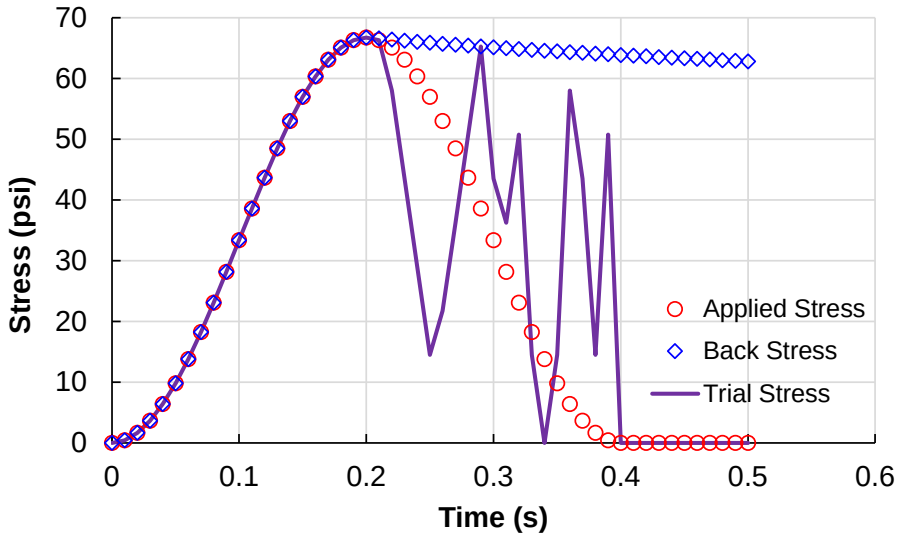

Figure 2-13 Similarity between the back stress in the convolution-type model and the yield surface concept in a classical plasticity or viscoplasticity model.

For the two compliance-like functions, two Prony terms are used in each giving totally 8 parameters. Combined with other others, finally we have 16 parameters, and to identify them experimental data from 9 different conditions, i.e., combinations of 3 deviatoric stress levels and 3 load pulse times, are required. In the optimization process, parallel programming techniques have to be used since 18 (for 2 replicates in each condition) or 27 (for 3 replicates in each condition) sets of test data are involved.

In the practical implementation, the process of convolution integral is expensive especially when the time spans up to for example 30 hours for long tests. In addition, it is formidable to optimize 16 parameters, none of which has direct physical significance, using totally 18 or 27 sets of experimental data at one time. In the theory side, the model presents a new framework to characterize material hardening and rate-dependent plastic deformation. It combines some features from both viscoelasticity and classical viscoplasticity theories, and thus many of the related assumptions remain for further investigations and verification. This convolution-type model seems to be able to capture the nonlinearities regarding stress levels and pulse time length based on limited application. It is worth pointing out that based on the characteristics of the evolution of back stress the model is expected to also capture the rest period effect but is proved otherwise when compared against the experimental data. Some of the model characteristics will be further discussed in CHAPTER 5.

2.6.3 Incremental-shift model

After the development of the convolution-type model Subramanian worked to simplify the form for easier engineering implementation. Through some simplifications including the steady state assumption (i.e., the calculated cyclic increments due to the two convolution integrals remain unchanged with cycle number), he finally arrived at an empirical function, named the incremental model, which relates the uniaxial plastic strain with the cycle number as shown in below:

$$\varepsilon_{vp} = \frac{A + BN}{(C + N)^{\alpha}} \tag{2.6.8}$$

where *A*, *B*, *C*, and α are regression coefficients. Even though the assumptions are believed to be very rough, Equation (2.6.8) works for any conventional creep and recovery tests as long as the test condition is maintained the same throughout. The incremental model can be deemed as an extension of the classical power-law relation by introducing the additional parameters *A* and *C*. The parameter *C* is used to adjust the model behavior for initial cycles while *A* can be literally set to zero since no permanent deformation exists before the load applies. When the permanent strain is plotted in the log-log scale versus cycle number *N*, (1-α) is approximately the slope of the curve at large *N* values. As will be discussed later in CHAPTER 4, due to its empirical nature the model coefficients are found to have no direct relation with test conditions, and for each different condition, a new set of coefficients have to be established.

By plotting all permanent strain curves from tests with various deviatoric stresses and pulse times, Choi (2013) realized that a single master curve could be constructed by horizontal shift along the log(*N*) axis. Discrepancies between different curves exist in the initial portion of the master curve but it is the later part with higher strain levels that we are generally interested. With the help of the verified applicability of time-temperature superposition principle under considerable plastic deformation (Yun 2008), Choi was able to combine the pulse time and test temperature into one single variable named reduced pulse time (ξ_p). Then a quantitative relationship between the amount of horizontal shift and reduced pulse time as well as the deviatoric stress was explored. By assuming a separable formulation for the total shift factor in terms of reduced pulse time and deviatoric stress, it was found that each one can be roughly expressed by a power function. The final model is termed the incremental-shift model which is able to account for the nonlinear effects due to pulse time and deviatoric stress. The model equations are presented below:

$$\varepsilon_{vp} = \frac{A + B \cdot N_{red}}{\left(C + N_{red}\right)^{\alpha}} \quad \text{with} \quad N_{red} = N \times 10^{a_{total}}$$

$$a_{total} = a_{\xi_p} + a_{\sigma_v} \quad \text{with} \quad a_{\xi_p} = p_1 \xi_p^{\,p_2} + p_3 \quad \text{and} \quad a_{\sigma_d} = b_1 \left(\frac{\sigma_v}{P_a}\right)^{b_2} + b_3 \tag{2.6.9}$$

where A, B, C, and α are the coefficients for the permanent deformation master curve, N is the physical cycle number, N_{red} is the reduced cycle number after shift, a_{total} denotes the total shift factor which is the sum of the reduced pulse time shift factor $a_{\xi p}$ and the vertical stress shift factor $a_{\sigma v}$, both of which are expressed as power functions of respective variables. Since the confinement is fixed at 10 psi, vertical stress has been used for easier finite element implementation.

Generally, the incremental-shift model can be characterized by running one reference CCR test to obtain A, B, C, and α, and then a few additional CCR tests with different stress levels, and reduced pulse times to identify the shift factor functions. Apparently this approach still involves a considerable amount of experimental work. Given this, Choi further investigated the characteristics of the model and by assuming again the plastic strain as the material state variable tracking the deformation history, he was able to reduce the required experiments down to 4 tests each with 2 replicates if necessary. One serves as the reference test run at a high temperature, and the other three with different test temperatures use composite loading history with varying deviatoric stress levels among loading blocks. This material test protocol is called TSS (triaxial stress sweep), and 10 psi is used as the single confining pressure.

By shifting all permanent strain curves along the log(N) axis, one underlying mathematical assumption is that the α values for all the individual curves are the same. This may not be an unfair approximation if the same confining pressure is used as for the experimental data based on which the model is developed. However, as will be seen in CHAPTER 5 the parameter α does have a significant variation with different deviatoric stress-confinement combinations. Another deficiency is related to the use of the plastic strain as the material state variable. As discussed previously, the axial plastic strain is inadequate in a uniaxial model to represent material state or store the loading/deformation history. In addition, the incremental-shift model is not a constitutive relation in that it does not give a complete viscoplastic strain history, and therefore it cannot be implemented in the finite element structure analysis in a rigorous way. Nevertheless, the model is proved to have

satisfactory capability to simulate laboratory CCR and random loading tests and qualitatively agree with field rut measurements (LaCroix 2013, Choi 2013).

The major merit of the incremental-shift model lies in its reduced experimental work and much easier parameter identification procedures. Besides, it also brings the temperature as a variable into the model. Certain improvements on the model accuracy can be made by exploring other possibilities in the functional form of shift factors. Besides, like the previous two models, the incremental-shift model does not incorporate the confining stress effect which may result into unrealistic predictions in pavement rut depth when implemented in the pavement structure analysis.

CHAPTER 3 MATERIAL TESTING

3.1 Materials

The loose mixture used in material testing is produced from the batch plant of Pike Industries, Inc. in Williston in the state of Vermont. The asphalt binder is of PG 52-34 and has 0% RAP (reclaimed asphalt pavement), hence designated as VT0%. The mixture information is given in Table 3-1, and the aggregate gradation plotted in Figure 3-1 below.

Table 3-1 Summary of Mixture Information

Mixture Designation	Nominal Maximum Aggregate Size (mm)	Binder PG Grade	RAP Content (% of total aggregate)
VT0%	9.5	52-34	0

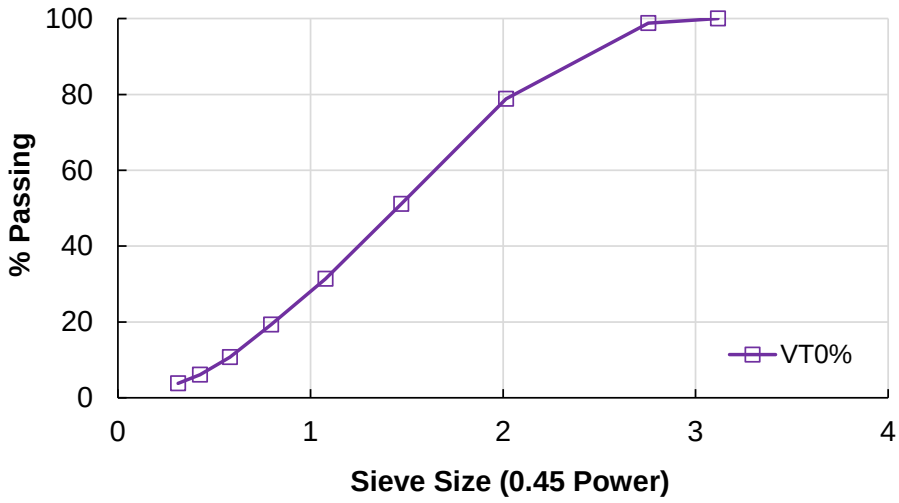

Figure 3-1 Aggregate gradation of the mix VT0%.

3.2 Specimen Fabrication

The Superpave Gyratory Compactor was utilized to compact all materials into cylinder specimens of 178 mm in height and 150 mm in diameter. To achieve a relatively uniform distribution of air void, all specimens were cored to a diameter of 100 mm and then cut to a height of 150 mm for compression testing. Afterwards, specimens were vacuum dried using the CoreDry equipment from InstroTek Inc., and then air void measurements were performed via the CoreLok method. The air void contents of specimens for both mixtures were maintained between 5.5 and 6.5 percent.

3.3 Specimen Preparation and Test Setup

The MTS 810 material testing system with a closed-loop servo-hydraulic load frame was used for all tests. In order to control, monitor and maintain the desired test temperatures an environmental chamber, equipped with liquid nitrogen coolant, electrical heating elements, and a temperature controller, was set between the two solid steel columns. During the test, crosshead displacement, load, axial and radial on-specimen deformation, and triaxial cell pressure data were collected via National Instruments® data acquisition hardware and recorded using LabView™ software.

During the material testing both axial and radial deformation were to be measured. For the axial measurement, four sets of loose-core linear variable differential transformers (LVDTs) were mounted to the brass studs glued circumferentially on the specimen with 90-degree intervals. The measurement was taken over the middle 70 mm of the specimen to minimize any end effect. It is worth mentioning here that 70 mm gauge length was chosen over the conventional 100 mm because of the availability of the gluing jigs and more importantly the fact that a greater measurable displacement range can be obtained for a shorter gauge length.

For radial measurements, first four studs were glued around the middle cross section of the specimen. Then during the test four sets of spring-loaded LVDTs were fixed on the triaxial cell with their tips contacting these studs. This way, the variations in diameters along

two perpendicular directions can be captured and then the two measurements can be averaged to give the radial strain history. However, from first few trial tests it was observed that this setup usually yielded non-smooth plots of permanent radial strain history, and this abnormality was then attributed partly to the non-negligible friction existing between the contact tip of the LVDTs and the studs because of some glue residual on and deformation of the stud surface and especially the presence of the bolt hole. Moreover, when large deformation occurred the studs kept moving downward and finally the contact between the stud surface and LVDT tips might be lost. To eliminate these adverse effects, rivets made of aluminum with smooth flat cap were machined to screw into the studs while providing a reduced friction and extended surface for the radial LVDT tips to move on. See Figure 3-2(a).

The specimen preparation processes are now briefly described. First totally twelve studs were glued on the specimen with specially manufactured gluing jigs. After about 30-minute curing time the sharp tips of the glue, if any, were filed off before encasing the specimen in a latex membrane. The membrane was then punctured at the center of each stud and was then stretched around the stud. Afterwards, effort and care was taken to slowly push the membrane around each stud back in contact with the specimen surface to remove any air pocket that might later build up when confining pressure was supplied. Then acrylic latex caulk was applied to seal the area around the studs. Usually three hours was needed for the caulk to harden. Finally all mounting brackets, rivets, and loose-core LVDTs were attached to the specimen. It can be seen that the preparation of specimens tested under confining pressure is non-trivial and time-consuming, but following the above general procedures is a guarantee that it is the specimen deformation that is to be measured, the deformation of the membrane itself not incorporated.

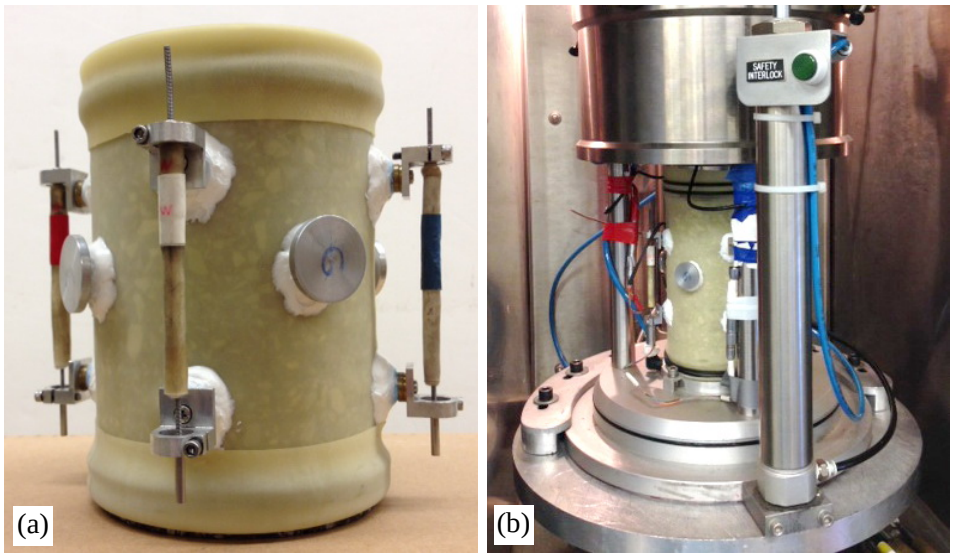

Figure 3-2 Sample prepared for the triaxial tests.

An aluminum top end plate was used in the compression test in order to minimize the undesired creep effect caused by the self-weight of the plate. A cast iron bottom end plate was built in the triaxial cell. A pair of latex sheet membrane of 100 mm in diameter, with grease applied in between as lubricant, was placed between the specimen and each end plate to avoid friction and thus end effects. It is important to point out that for the membrane between the specimen and the bottom end plate, a hole approximately of 10 mm in diameter was made in the center to ensure a proper drainage of excess pressure inside the membrane during a confined test. Correspondingly, the bottom end plate was also manufactured with a hole drilled in the center to drain the excess pressure outside of the triaxial cell. After transporting the specimen into the triaxial cell and connecting all LVDT cables and pressure gauges, the specimen was slightly rotated through trial and error to make sure that each rivet was faced with a channel where a radial LVDT was to be placed. And then the alignment between the loading rod and the top end plate on the specimen was checked to minimize the possibility of any horizontal sliding when the load started. It was learned that the specimen horizontal movement might easily result into a loss of contact between LVDT tips and rivets, and/or a reduction in the measurable range of deformation. Afterwards, the membrane ends

were sealed by means of O-rings which were received into circumferential grooves in the end plates.

An illustration of a specimen ready in the triaxial cell is provided in Figure 3-2(b). Temperature conditioning is initiated at this time. Note that during this stage, the triaxial cell was maintained open with the aim to achieve a fast thermal equilibrium at the desired temperature. After about three hours, the cell was first closed, and then the LVDTs for radial measurements were installed and fixed on the cell wall through four channels. Then approximately half an hour was needed for the temperature inside the chamber to re-stabilize before applying the confining pressure and starting axial loading.

3.4 Test Protocols

The material experiments here serve two purposes: to qualitatively appreciate the mechanisms behind material behaviors and to quantitatively represent the reduced observations in mathematics. For these purposes, representative test conditions have to be determined considering field situations, lab limitations, and computational possibilities.

3.4.1 Stress condition

Due to experimental limitations, true triaxial (three dimensional) testing with prismatic samples are more realistic but too overwhelming. Therefore, conventional triaxial test using cylindrical specimens is resorted to with existing testing systems (MTS & AMPT). Since a direct stress measurement in the pavement structure is not possible, researchers have been seeking to acquire the knowledge from numerical simulation which, however, requires the end of all our current efforts – the stress-strain constitutive relationship. As a compromise, simpler case scenarios such as elastic or viscoelastic layered material systems are studied and from this investigation we make further estimations.

Here the analysis tool serving the above role is called LVECD (Layered ViscoElastic pavement analysis for Critical Distresses) developed at NCSU (Eslaminia *et al.* 2012, Choi 2013). The LVECD package is able to handle different material types (viscoelastic/elastic),

moving wheel loading, and temperature gradient within the pavement structure. Performance analysis functions such as viscoelastic fatigue damage and healing (Ashouri 2014), and permanent deformation (incremental-shift model, Choi 2013) have been incorporated. For our purpose here, the stress response analysis is of interest. To grasp the effect of vehicle speed, temperature, and pavement thickness, totally 8 cases as shown below in Table 3-2 were investigated. For the temperature gradient, first the environmental temperature data from a history year of the location where the material was used were extracted using the Enhanced Integrated Climate Model (EICM), and then were converted into the hourly temperature profile within the pavement structure (see Figure 3-3 for the calculated temperature at the pavement surface). With a depth interval of 0.5 in., the average nodal temperature for the top 4 in. was calculated and compared to obtain a maximum and minimum which correspond respectively to the high and low hourly profile. The resulting hourly temperature profiles for each case are plotted in Figure 3-4.

Table 3-2 Case Matrix for Stress Analysis

Asphalt Layer Thickness (in.)	Vehicle Speed (mph)	Temperature Profile
4	25 & 45	high & low
18	45 & 60	high & low

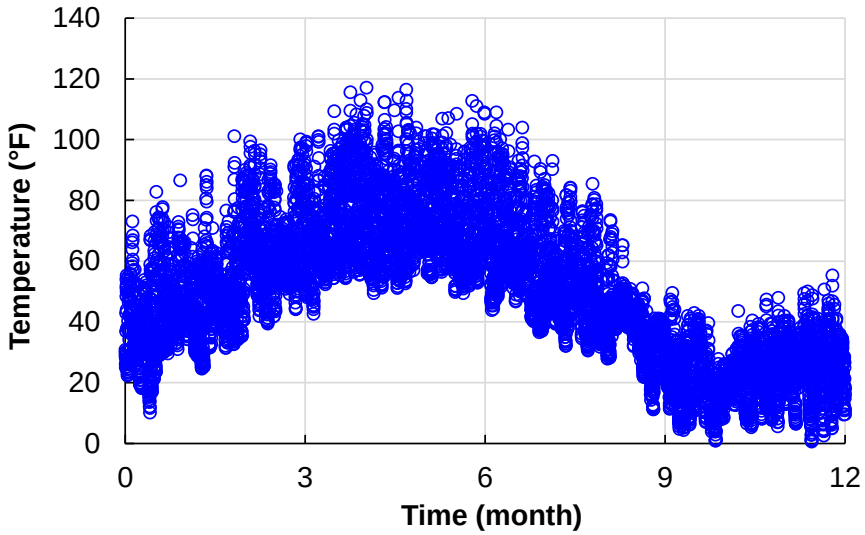

Figure 3-3 Annual temperature history at the pavement surface for Vermont State generated by EICM (note that the starting date is not prescribed).

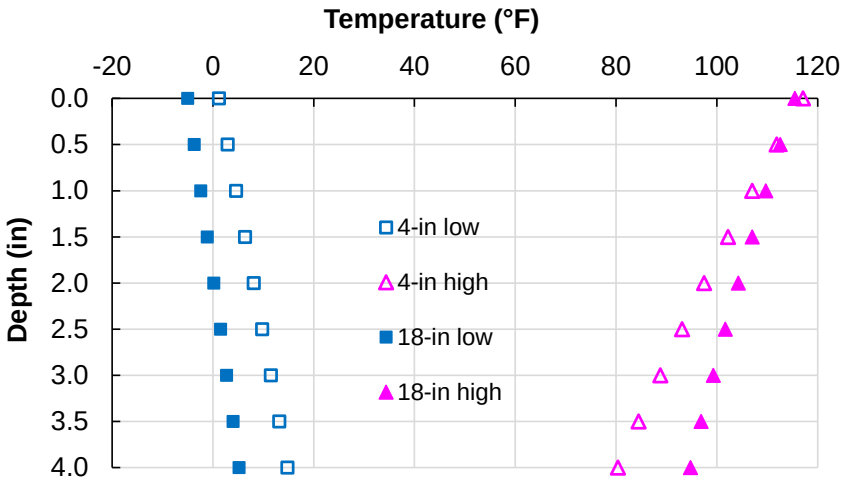

Figure 3-4 High and low temperature profiles used in response analysis.

The single axle single tire with standard 4500 lb wheel load was applied at the speed specified in Table 3-2. With one pass of the wheel, the maximum horizontal normal stresses

were extracted along the depth to acquire a concept regarding the confining stress to be used in lab testing. The stress results are shown in Figure 3-5 below.

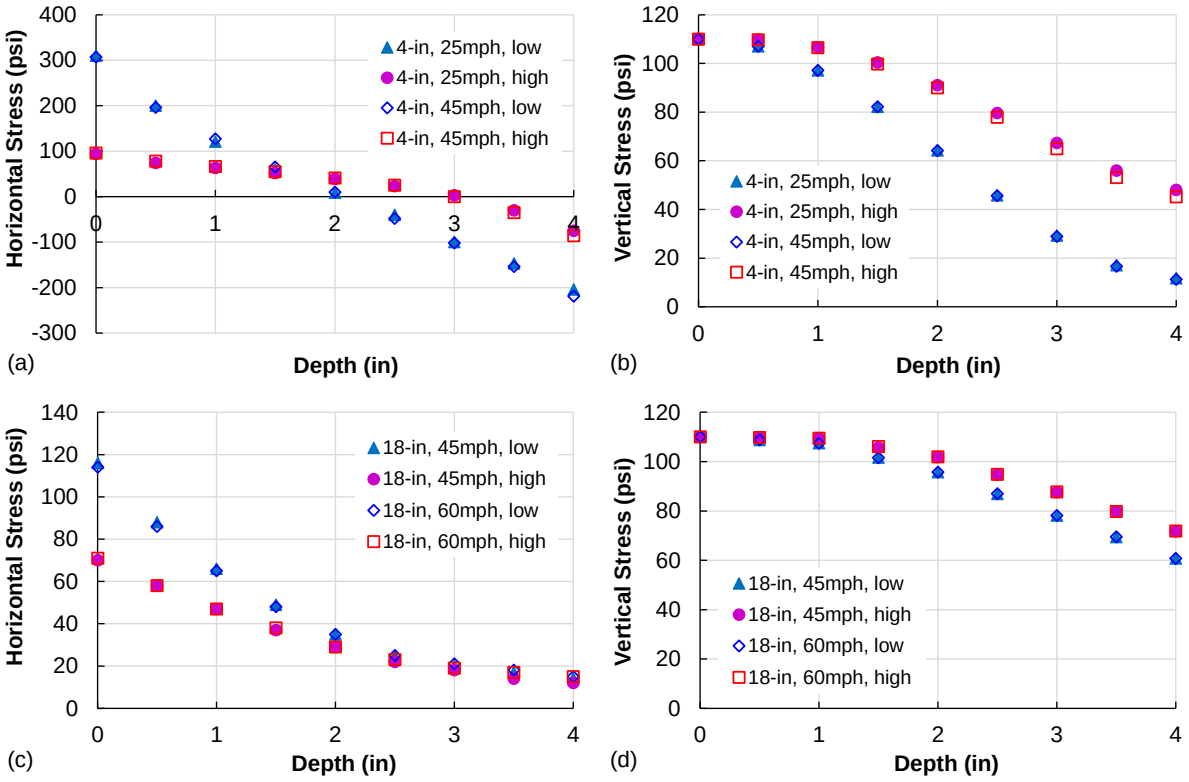

Figure 3-5 Horizontal and vertical stresses calculated with different vehicle speeds and temperature profiles for: (a) and (b) a thin 4-in. pavement, and (c) and (d) a thick 18-in. pavement.

Obviously, the stresses vary significantly with depth and temperature, and depend on the total thickness of asphalt layers. In the meanwhile, however, the vehicle speed has clearly indiscernible affect. Low temperature is able to increase the horizontal stresses while it also helps to spread and thus reduce the vertical loads. The sign convention for stress is positive for compression and negative for tension. For the thin pavement, the top 4-in materials experience compression at top and tension at bottom. The horizontal tensile stresses would make the material more vulnerable to deformation. On the contrary, the top 4-in of the thick

pavement is immersed in a horizontally compressive stress environment which is more mechanically favored to resist the vertical load. At the pavement surface, both the vertical and horizontal stresses reach the maxima and then both decline along the depth. While vertical stress is the cause of material deformation the horizontal compressive stress helps to strengthen the material and thus it is hard to determine where the material is experiencing the least favorable stress state by observing the two separately. As an alternative view, we may examine the so-called stress ratio defined as the ratio of deviatoric stress to confining pressure. Roughly using the difference between vertical stress and horizontal stress to approximate the deviatoric stress and ignoring the negative results we ended up with the graphical relation shown in Figure 3-6.

We can observe that for the thick pavement cases, only positive confinement is present for the top 4 in and the resulting stress ratio is within 0 to 5. Despite an increasing trend of the stress ratio, the vertical stress beyond 4 in reduces to below 70 psi while the confining stress becomes less than 10 psi. This is pointed out here just for the conclusion that the thin pavement cases as worse scenarios are able to incorporate the thick ones in that the materials around 2 ~ 3 in for the thin cases undergo a uniaxial like stress state with a deviatoric stress ranging between 30 and 90 psi according to Figure 3-5(b). Therefore, the need of performing unconfined uniaxial test appears and for confined ones a test grid has to be formed. Note that the above observation does not consider the shear stress components and researchers have been using the stress invariants (see Equation (2.4.4)) in order for a comprehensive examination.

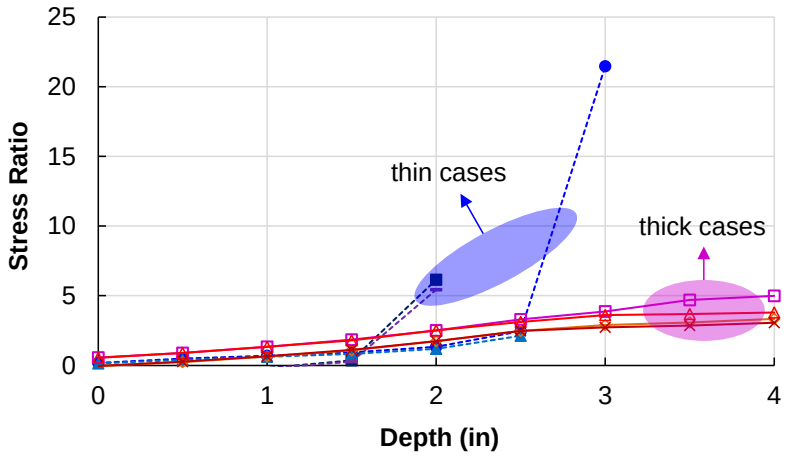

Figure 3-6 Stress ratio along the depth for thin and thick pavement cases.

With the six stress components at hand, the stress invariants expressed in Equation (2.4.4) can be calculated for each discretized nodes and then the deviatoric stress is plotted versus the confinement for 4 cases as shown in Figure 3-7. High deviatoric stress and confinement are expected to occur at the surface and bottom of the thin pavement for the low temperature profile. High confinement stiffens the material and makes it more rut resistant leaving no much necessity to perform the test; besides, the current lab device is able to handle only up to 30 psi confinement. On the other hand, negative confinement is out of consideration in the current study since the experimental simulation is too demanding. Consequently, experimentally we are only able to focus on a narrow confinement range (0 ~ 30 psi) where the corresponding deviatoric stress varies from 0 to 100 psi according to Figure 3-7.

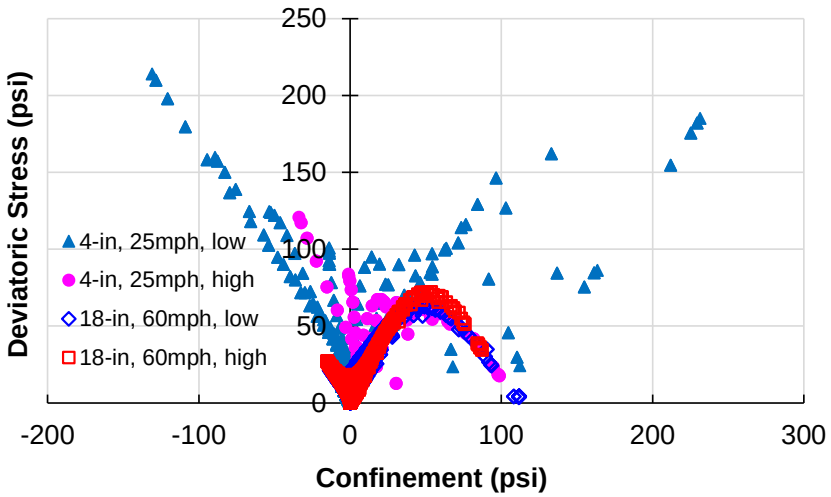

Figure 3-7 Deviatoric stress and confinement calculated from stress invariants.

Without a consensus on a presumably representative stress condition available in literature, Choi (2013) reviewed the numerical simulation work by von Quintus *et al.* (2007), Gibson *et al.* (2009), and Hajj *et al.* (2010) and concluded that the combination of 70 psi as the deviatoric stress and 10 psi as the confinement would be an appropriate choice. Starting from this point, to gain a clear idea of how the deviatoric and confining stress function competitively toward the deformation, a stress matrix is tentatively formulated including 4 confinements (0, 10, 20, 30 psi) and 3 deviatoric stresses (70, 100, 130 psi).

3.4.2 Test temperature

Test temperature should be specific to the location where the material is used. As briefly mentioned in the above, the EICM model is first used to generate the environment temperature and then compute the temperature profile within the pavement structure. Given the fact that high temperature contributes more to deformation but its occurrence is less frequent, Choi (2013) was able to develop an algorithm to approximate the relative share of different temperature ranges to the total deformation through certain assumptions regarding the traffic loading and plastic strain accumulation. The final result is a cumulative

distribution of the contributions of different temperatures to the total deformation as shown in Figure 3-8, from which we may determine three test temperatures: 48°C (100%), 28°C (70%), and 10°C (10%).

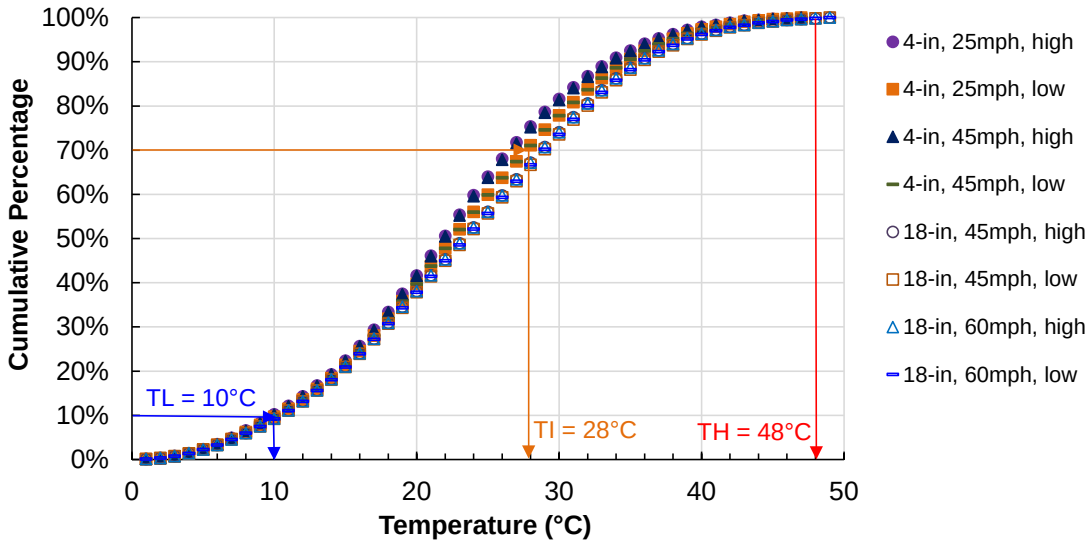

Figure 3-8 Cumulative distribution of temperature to total deformation throughout one year.

3.4.3 Pulse time and rest period

Through the finite element simulation, it is observed that the haversine curve resembles more closely than a square curve for the load pulse, and the pulse duration varies from 0.01 seconds to 0.1 seconds depending on the vehicle speed, depth, and temperature. Having a short pulse, however, may sacrifice the load accuracy due to machine limitation. Thus, from the modeling point of view, 0.4 seconds was chosen as the pulse duration for the haversine shape.

As for the rest period following the load pulse to complete one cycle, it is supposed to be long enough for the material in the specimen to fully relax so that at the end of the rest the total strain recorded becomes the irrecoverable plastic strain. Experimental experiences have

indicated that increasing the temperature helps to reduce the required rest time, yet here 100 seconds, which is usually deemed far beyond enough, was conservatively chosen as the rest period in this study.

CHAPTER 4 EXPERIMENTAL OBSERVATIONS AND PHENOMENOLOGICAL HYPOTHESES

4.1 Variation in Material Time Dependence

The general trend of variation in material properties under cyclic compressive loading can be relatively easily detected in a cyclic creep and recovery (CCR) test in which the load pulse takes a square shape. As a typical example, one CCR test done by Yun (2008) is now illustrated below with both input loading history (Figure 4-1) and the averaged strain collected at the end of the rest period in each cycle as permanent deformation history (Figure 4-2). A few cycles (#2, 10, 25, 75, as seen in Figure 4-2) have been selected for examining the averaged axial strain response (Figure 4-3). Here the square shape load pulse has a duration of 1.6 seconds and the subsequent rest period is 100 seconds in each cycle. The confining pressure and deviatoric stress are respectively 20 and 120 psi. The test was run at 55°C and was stopped without the advent of the tertiary flow stage.

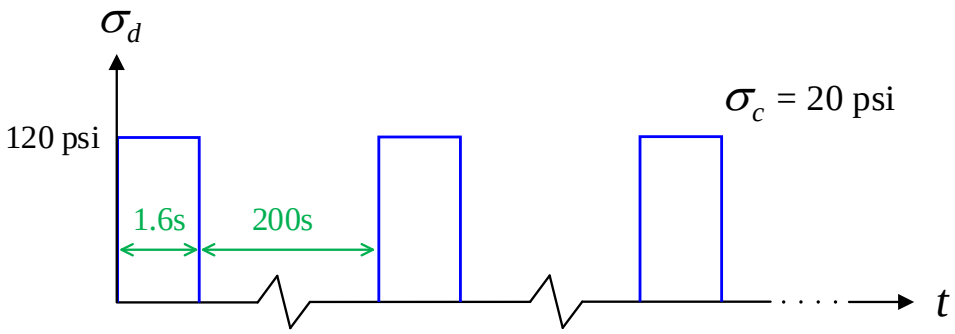

Figure 4-1 Load history used in a CCR test by Yun (2008).

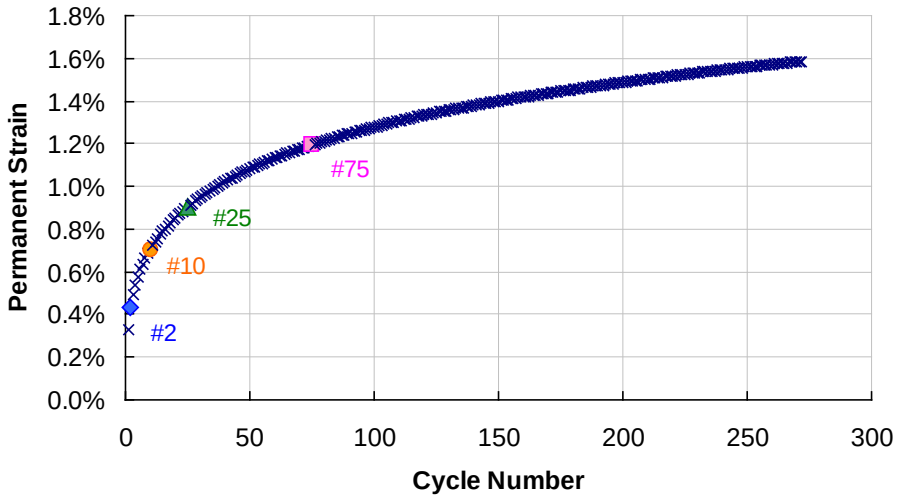

Figure 4-2 Permanent strain (axial strain collected at the end of rest period in each cycle) of the test corresponding to the loading history depicted in Figure 4-1 (Yun 2008).

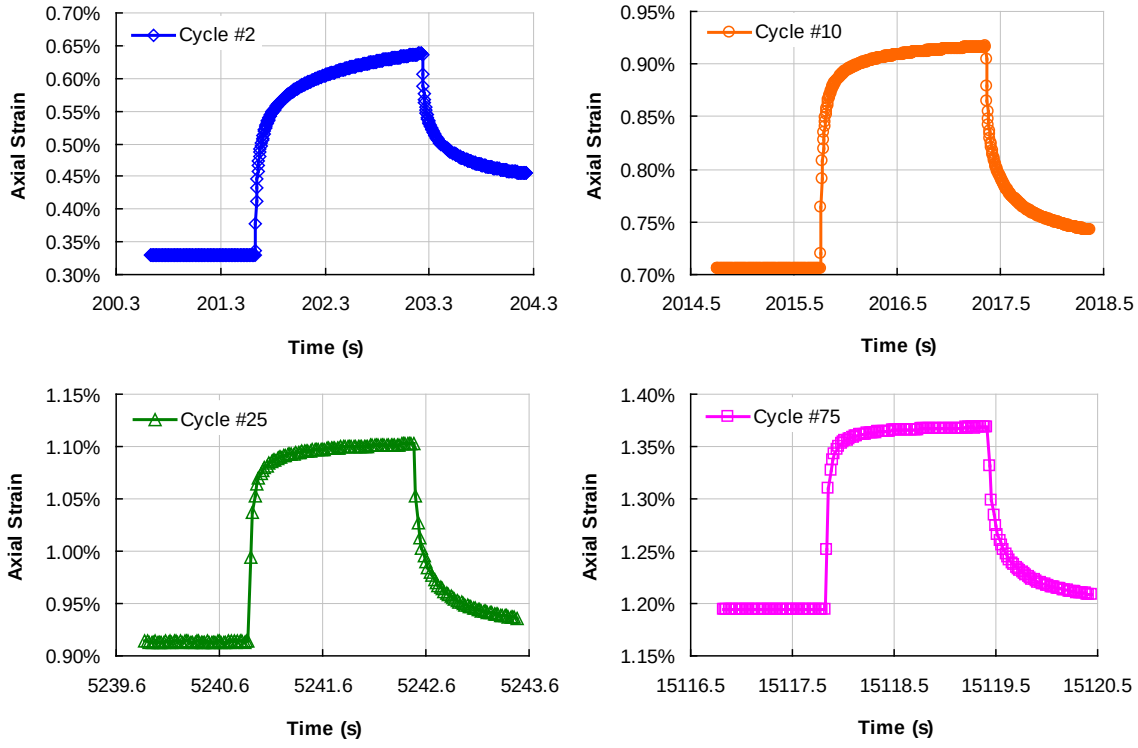

Figure 4-3 Averaged axial strain response for selected cycles (Yun 2008).

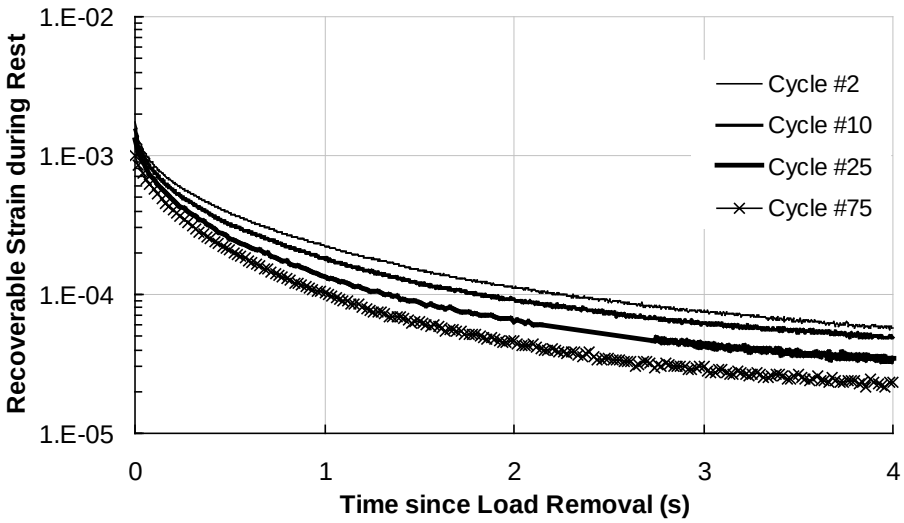

Figure 4-4 Recoverable axial strain for selected cycles (Yun 2008).

The axial strain response from a few selected cycles 2, 10, 25, and 75 are plotted in Figure 4-3 with the same length of time window but different scales for the strain for easy observations. Given the same loading history in each cycle, it is clear that the strain response becomes more instant with less delay as the cycle number increases. Note that after the deviatoric stress ramps up to the target value (here 120 psi) the slope of the strain curve decreases with cycle number. Also note that as times goes the percentage of the recovered strain in each cycle increases. These phenomena suggest a more elastic-like response and thus a reduction in the material time dependence. One more supporting argument can be made regarding the recoverable strain during the rest period as seen in Figure 4-4. The reversible strain during the recovery period for corresponding cycles are obtained by subtracting the strain value at the end of the rest period from the total strain. Obviously, in later cycles the material recovers in a quicker pace.

However, it is not fair to claim a continuous attenuation of time dependence throughout a whole loading history. A different test conducted by the author is presented here. The loading condition differs in that here the pulse takes a haversine shape with a duration of 0.4 seconds, rest period is 100 seconds, and the test temperature is 48°C. In order

to observe the tertiary flow, no confinement is exerted. The peak deviatoric stress is chosen as 100 psi. The test was run till the specimen deformation goes beyond the measured range which is typically 6~7% depending on the initial LVDT setting. The permanent strain history as well as the cyclic increment of the permanent strain is presented in Figure 4-5. As indicated in Figure 4-5, a few cycles are selected to check the recoverable strain during the rest period, and the results are shown in Figure 4-6.

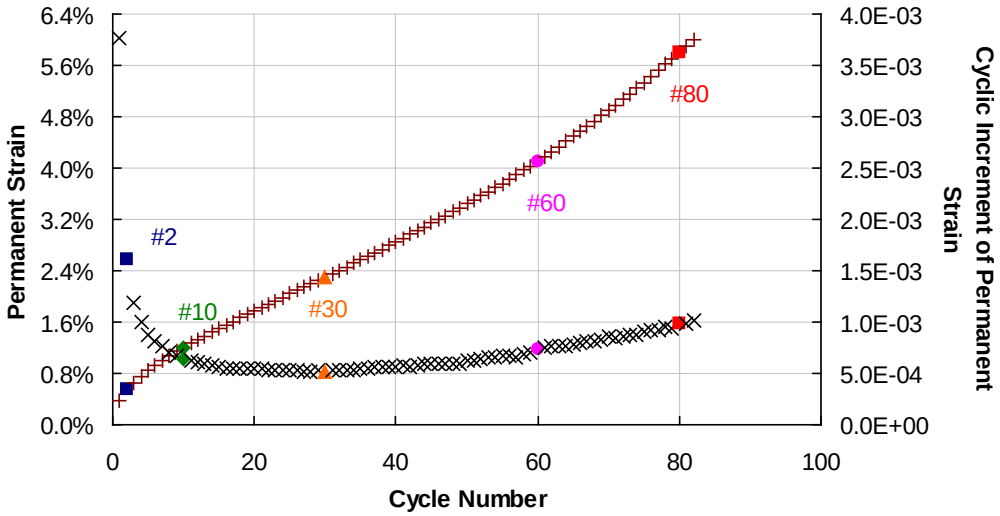

Figure 4-5 Permanent strain and the cyclic increment for an unconfined cyclic creep and recovery test (Test-38) with peak deviatoric stress of 100 psi and TH = 48°C.

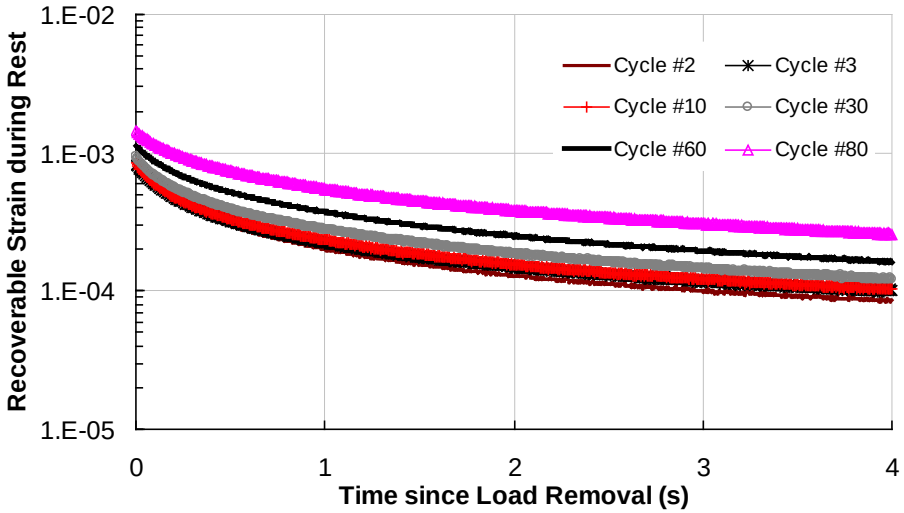

Figure 4-6 Recoverable axial strain for selected cycles in the unconfined creep and recovery test with haversine-shaped pulse.

According to Figure 4-5, the at cycle numbers #2, 3, and 10 the material is still in the primary stage, and at #60 and 80 the material is already having tertiary flow. Cycle # 30 is chosen from the secondary stage. The corresponding recoverable strain for these cycles as plotted in Figure 4-6 which however shows a different trend regarding the recovery speed than Figure 4-4. In fact the decrease in the recovery speed during the tertiary stage is expected since material softens due to microcracking (to be discussed in details below) in this region, and it is the microcracking damage that brings about the increase of material time dependence (Reese 1997).

Recall that in Figure 4-4 all the selected cycles are from the primary region and the material shows a consistent increase in the recovery speed. However, here in Figure 4-6 the recovery speed is quite similar between cycles in the primary region although a slight reduction can still be observed from cycle #2 to 3. This opposite trend is presumably attributed to the large strain and thus early microcracking damage in the unconfined test, and therefore more time dependence is present in the primary region. Another possibility is that the 100s rest period used in the test is perhaps not long enough to recover all the reversible

strains given the fact that the strain levels here especially in the tertiary stage are significantly higher than those in the confined test.

4.2 Hypotheses Regarding Hardening, Softening, and Recovery

It is believed that material hardens during the primary stage with a reduced hardening rate and when the tertiary stage comes the overall material state turns to softening. For the secondary stage which is characterized by a linear portion of the strain history curve, the cyclic contribution of permanent strain remains the same, which suggests a dynamic equilibrium between hardening and softening and thus a stable material state.

Before further discussion, some clarifications have to be made regarding hardening and softening here given the wide use of the terminologies in the literature for different materials and various phenomena. In the area of classical plasticity and viscoplasticity, hardening and softening during plastic deformation have been used to describe the geometrically the expansion/shrinkage or translation of the yield surface within which a material remains elastic. If the yield surface expands and/or moves toward the loading direction, material hardens. On the contrary, if the yield surface shrinks and/or moves opposite to the loading direction, the material is experiencing softening. Analytically, for the same amount of load increment in the same direction, the magnitude of the increment in the strain response diminishes due to hardening, which physically implies an increase in the material stiffness. Similarly, softening suggests a reduction in the material stiffness.

With the above discussion in mind, when applied to typical creep and CCR tests in asphalt concrete it can be perceived that hardening dominates the primary stage, during which the cyclic maximum total net strain as well as the residual or permanent net strain decreases with cycles. Likewise, softening governs the material behavior during the tertiary stage in which the cyclic contribution to the total strain and permanent strain rises.

In this dissertation research spring loaded LVDT have been employed to measure the radial deformation of cylinder specimens with or without confinement. Although a comparatively inferior degree of accuracy associated with these radial measurements should

be admitted, their availability helps to examine the volumetric deformation history which is critical for all the pressure dependent materials. Here one set of test results are provided to better understand the hardening and softening mechanisms. This test set was run at 4 different confinement levels (0, 10, 20, 30 psi) and one deviatoric stress which is 100 psi. As previously mentioned, pulse time and rest period are fixed respectively at 0.4 and 100 seconds. The test temperature is TH = 48°C. For each of these 8 conditions, two replicates were used. The volumetric strain history for each test condition are now presented in Figure 4-7. Note that compressive stress and strain are dealt with as positive while tensile stress and strain are negative. Accordingly, negative volumetric strain indicates a volume expansion while positive means a volume contraction as compared to the original undeformed specimen.

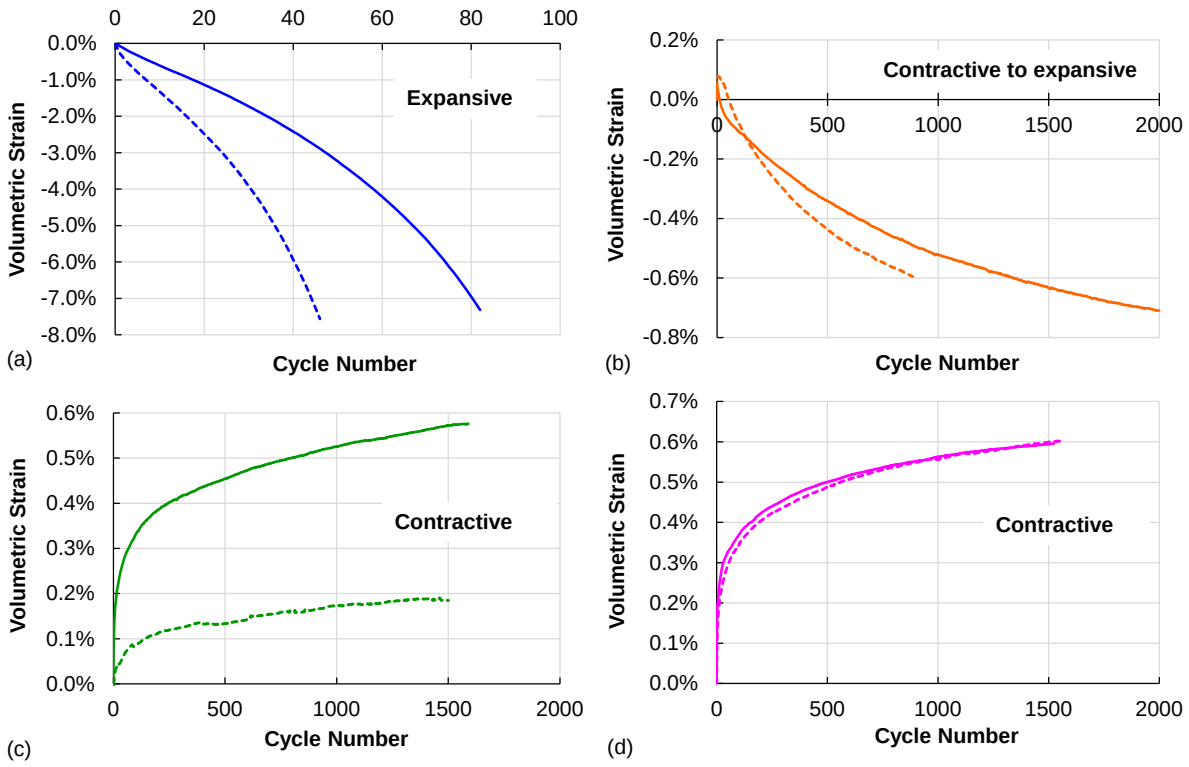

Figure 4-7 Volumetric deformation history for two replicates at different confinement levels: (a) 0 psi, (b) 10 psi, (c) 20 psi, and (d) 30 psi, with one deviatoric stress of 100psi.

Obviously, for the unconfined test the specimen starts to dilate from the beginning of the loading. At 10 psi confinement for the first few cycles the specimen contracts and then dilative behavior starts to dominate. When the pressure goes higher up to 20 and 30 psi, no volumetric dilation can be observed. So a general statement can be made here that depending on material state and the mechanical and environmental conditions, material may exhibit dilative or contractive behavior or a transition from contraction to dilatation in typical CCR tests.

It is believed, as supported by field observation, that material densification due to reduction in the air void content is generally present under all loading and environmental conditions when dealing with permanent deformation. Intuitively, the reduction in the air content will densify and stiffen the material, and therefore a macroscopic hardening can be observed in material response. In addition to the macroscopic densification, another local mechanisms involving asphalt binder can also be used to approach hardening. Under loading the aggregate structure changes and the binder is also deformed under confinement due to its surrounding aggregate particles. When the external load is removed, binder and the aggregate structure start to recover. The energy stored in the binder starts to release in the process of pushing away its surrounding particles. Nevertheless, the original aggregate structure cannot be restored due to permanent deformation and thus asphalt binder is not able to fully relax. Therefore, as confined in the void of aggregate structure the binder preserves certain amount of energy and this energy helps to resist further deformation.

To account for the material dilative behavior, other mechanisms have to exist. Starting from the compaction process of an asphalt mixture, the cohesive force of asphalt binder is able to conglutinate all the aggregate under compaction just as the water suction uniting the soil particles to form a soil specimen. After the compaction, an aggregate structure is generated with the void in the mineral aggregate (VMA) filled with air and effective binder (the binder portion that is not absorbed by aggregate). While asphalt binder and aggregate are incompressible, and the reduction in air content stiffens the material and causes contraction, and the only remaining explanatory mechanism behind dilation and softening is the change in the aggregate structure. One may argue that the air content

reduction cannot be achieved without the aggregate structure change. While this statement is true, it is thought that the change in the aggregate structure due to aggregate relative movement can also lead to the aggregate particle sliding and rotation, and the formation of microcracks. While particle sliding gives rise to material dilation (see Section 6.3 for deeper discussions), microcracks introduce air void back into the material, which may or may not balance out the densification depending on the loading condition and temperature. In the least favorable conditions with low confining levels and high temperatures, particle sliding and microcracks may initiate early in the deformation history and overwhelm the densification effect, which results into an overall dilative behavior as seen in the tests in Figure 4-7(a) and (b).

It should be pointed out here that the formation of microcracks may not immediately soften the material. In the tensile loading case cracks develop perpendicular to the load direction thus immediately reducing the effective load bearing area, and the tensile strength as well as material fatigue behavior depends on the weakest cross section with the least effective area. However, in the compressive loading case cracks usually form and propagate in the direction parallel to the load. Even though the overall volume of the randomly distributed microcracks may not be insignificant, the effective cross-sectional area can be negligibly affected, until the microcracks start to coalesce to form macrocracks and finally a shear zone starts to take shape.

As for the recovery after the load removal, it is intrinsically a delayed elastic behavior due to the existence of viscous binder in the aggregate structure. Without the presence of binder, recovery of the aggregate structure would be instantly elastic, and the existence of asphalt binder entitles the time dependence to the material recovery. During the recovery period asphalt binder pushes away its surrounding aggregate particles at a decreasing rate, and the remaining portion of deformation is accumulated with the loading history. Given a longer rest period, more reversible strain can be recovered, which usually provides the potential for the next load cycle to generate more deformation than the case with shorter rest period. Quantitatively, it still remains unclear that whether or not the effect of rest period on permanent deformation can be explained using viscoelasticity theory alone, although the

constant plastic deformation during recovery is usually deemed as an indication of a constant material state in plasticity or viscoplasticity models.

4.3 Viscoelastic Hardening due to Plastic Straining

In the attempt to model the viscoplastic behavior in asphalt concrete, researchers usually first calculate the viscoelastic responses using certain linear or nonlinear viscoelastic theories, and then obtain the viscoplastic strain by subtracting this viscoelastic strain from the total strain history. While this approach may work satisfactorily for modeling short period test with quasistatic loads, it usually fails when applied to long test especially when the load is intrinsically dynamic so that the material properties, reflected mathematically through the model parameters, change relatively fast. As a result, a model characterized by a certain period of data may usually yield poor predictions for another period. To be specific, this section is aimed to point out the changes in material viscoelastic properties with time or cycle number, or to be more accurate, with the viscoplastic deformation in typical CCR tests.

In the following trial analysis, the material total deformation is assumed to be decomposed into two parts: viscoelastic and viscoplastic strains. As just mentioned, viscoelastic strain is directly calculated and by subtracting the viscoelastic strain we obtain the viscoplastic strain. Here for the illustration purpose linear viscoelasticity is used. It is well known that linear viscoelasticity theory can be used to describe asphalt concrete behaviors when the deformation is small (e.g., < 100 $\mu\varepsilon$). However, the strain levels commonly dealt with in permanent deformation can go up to tens or hundreds of thousands of microstrain which is far beyond the linear range. Nevertheless, as long as we assume material viscoelastic properties remain the same with deformation history, we will arrive at the same conclusion regardless of the specific viscoelastic model to be used.

For this analysis, the data from one replicate of the unconfined test (Figure 4-7a) are used. Unconfined test is chosen because for the linear viscoelastic properties dynamic modulus test was done only without confinement for the mix VTa0%. For the first cycle, the stress and the total averaged axial strain are plotted in Figure 4-8. Also plotted there are the

linear viscoelastic strain and the recoverable strain during the rest period. The time window has a length of 0.7 seconds which covers the 0.4 second pulse and 0.3 second recovery.

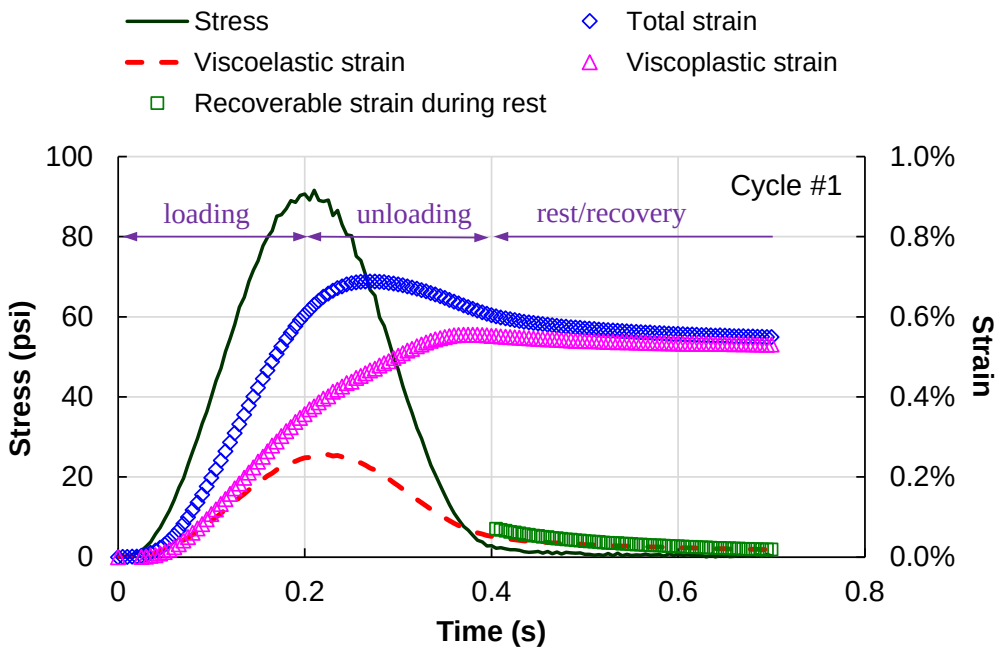

Figure 4-8 Strain decomposition for the first cycle in an unconfined creep and recovery test (Test-7) by the use of the linear viscoelasticity theory.

Note that in many researches unloading is used to denote the period when there is no external load. It is felt, however, that it is better in this study to use unloading to describe the second half of the pulse in which the load declines from peak to zero. The first half of the pulse is denoted as loading. Also note that even though the target value of the peak stress is 100 psi, the actual amount applied to the specimen is 90 psi for the first cycle. This is common in a dynamic experiment due to machine compliance and stability. As time goes, the peak stress will quickly increase up to the target value.

With enough description about the test itself, attention is now turned to the different strain components as shown in Figure 4-8. Despite the approximate nature, this strain

decomposition appears to be quite reasonable. First, the linear viscoelastic strain agrees well with the recoverable strain during the rest. Secondly, the viscoplastic strain increases during the loading half pulse, then continue its growth with a reduced rate during unloading half pulse, and finally when the load drops down to a certain small value the viscoplastic rate becomes zero giving a constant plastic strain which is close enough to the total strain during the rest period. All these behaviors are expected for a general viscoplastic material.

With the promising results seen for the first cycle, it is tempted to apply the same concept to later cycles. As shown in Figure 4-9, the same calculation has been done for cycle #3 and 10. Note that in these figures the initial strain at the beginning of each pulse has been shifted to zero so that all the strains plotted describe the net deformation in the corresponding cycle by assuming that 100 second rest period is long enough to recover all the reversible (viscoelastic) deformation. Since the material viscoelastic properties are deemed constant with deformation history, it naturally follows that the viscoelastic strain history takes the same shape and magnitude in each cycle. As shown in Figure 4-9, after the first cycle the calculated viscoelastic strain starts to deviate from the recoverable strain during the rest period, and as the cycle number increases this deviation enlarges, which indicates a reduced applicability of the linear viscoelastic model for the recoverable deformation. More importantly, during the loading half pulse the resulted viscoplastic strain surprisingly has a high slope under initial low stress level and a reduced or even negative slope when the stress increases to peak. And during the unloading half pulse the decreasing stress produces a faster development in the viscoplastic strain. All these characteristics of the viscoplastic strain curves does not follow the true material behaviors and this discrepancy is directly due to the assumption of constant viscoelastic properties which then leads to the overprediction of viscoelastic strain. The true viscoelastic strain should have lower peak values for larger cycle numbers. Hence, we can conclude that material viscoelastic properties change with plastic deformation, and these changes occur in a hardening way. This interaction can be denoted as viscoelastic-viscoplastic coupling as apparently the microstructural disturbance due to plastic straining is able to alter the viscoelastic response. This phenomenon also invalidates the use of any existing viscoelastic theories developed for purely viscoelastic materials since in their

framework the effect of plastic deformation is not incorporated. As a result, the analytical separation of viscoelastic strain and viscoplastic strain is not possible in a CCR test, which means we will not have a complete viscoplastic deformation history but rather a set of discrete points with one viscoplastic strain point for each cycle (see Figure 4-2 and Figure 4-5 for example).

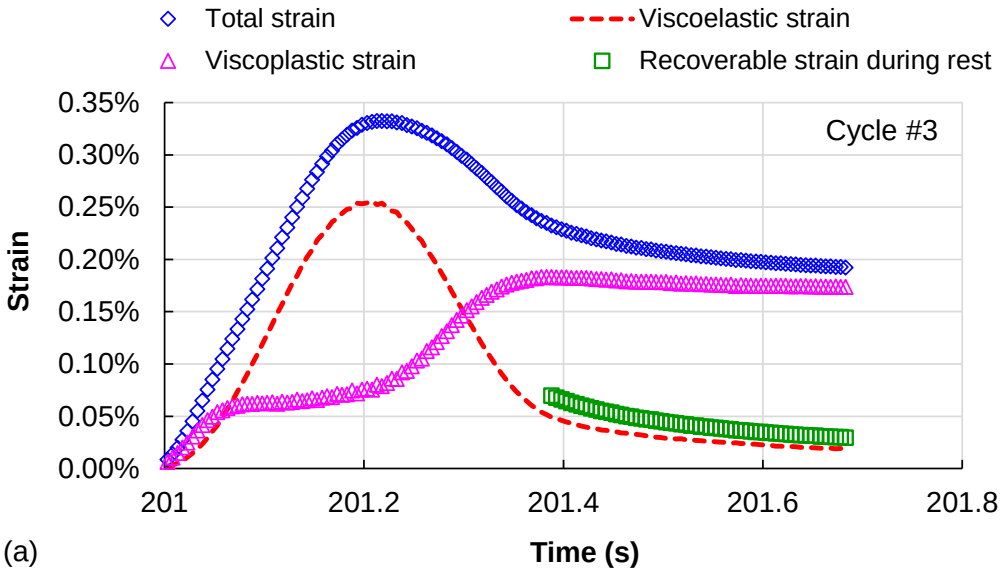

(a)

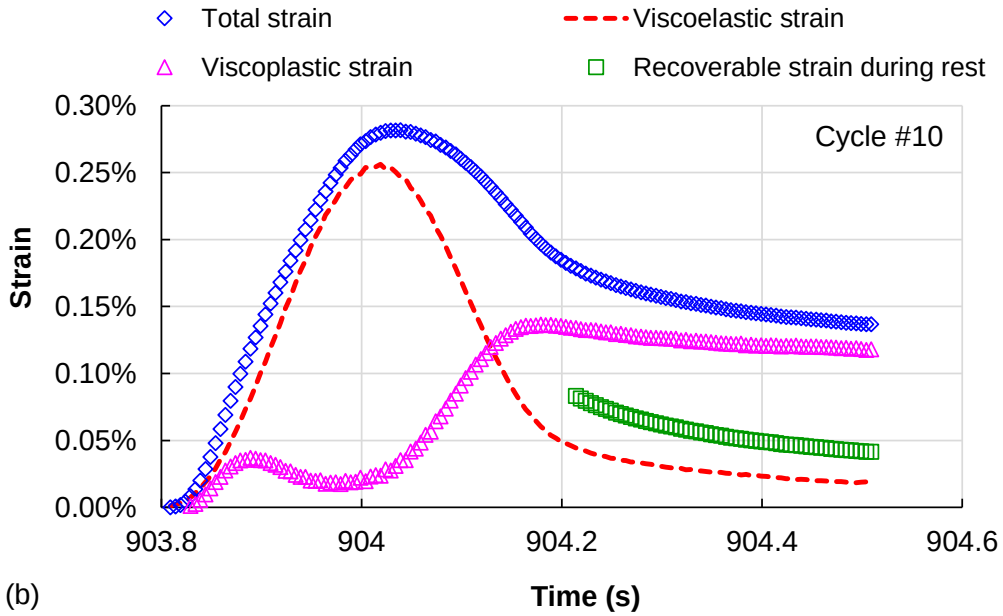

(b)

Figure 4-9 Strain decomposition in an unconfined creep and recovery test (Test-7) by the use of the linear viscoelasticity theory for (a) cycle #3, and (b) cycle #10; for both cycles the material remains in the primary deformation region.

4.4 Difficulties in Interpreting Tests with Large Deformations

In the experimental study on cyclic creep and recovery test, the pulse time (0.4 seconds), rest period (100 seconds), and temperature (TH = 48°C) were fixed while different combination of deviatoric stress and confining pressure were applied. Due to the limitation in the measurable strain range (6~7%) for the 75 mm gauge length used, some tests were terminated when all LVDTs readings went beyond the limit for the safety of equipment. For some confined tests with expansive volumetric strain, it is highly possible to see the tertiary flow at future cycles. All the unconfined tests are found to show a complete three stage permanent deformation history.

So far few researches have been devoted to the study on softening characterizations. It is understandable from a practical point of view since in the field whenever softening appears it then develops fast, and then material quickly loses its integrity and resistance to loads, and what leaves to engineers is to design and construct strong materials and structures to avoid the advent of softening during the design life. From another point of view, this reality also implies how great a challenge it is to understand and quantitatively capture softening mechanisms in different cases.

As far as the softening in asphalt concrete is concerned, using the three stage permanent deformation history as an example, piecewise or continuous empirical models have been explored early but they are only applicable to specific loading history and environmental conditions. In order to gain insight into the effect of complex traffic loading, phenomenological models have to be established and implemented into the structure analysis package, which presents a tremendous challenge. Usually in these types of model several internal state variables are required to track the material hardening/softening status so that the resulting overall material state would be able to agree with the experimental observations. None of the internal variables can be directly measured in experiments and this in most cases brings about the so-called ill-posed problems (Friedrich *et al.* 1996). Besides, the presence of considerable microcracks and macrocracks may invalidate the commonly used continuum assumption. In addition, the appearance of shear zones would bring about intense strain

concentrations and displacement discontinuities which require more advanced structural and micromechanical techniques.

Another issue with current phenomenological constitutive models is that most of them use the relations derived from small strain theories in which the original undeformed configuration is used to calculate the stress and strain. However, in the case with large deformation such as a creep and recovery test with low confinement, for the sake of accuracy the updated configuration shall be adopted. The importance of this point can be illustrated in Figure 4-10.

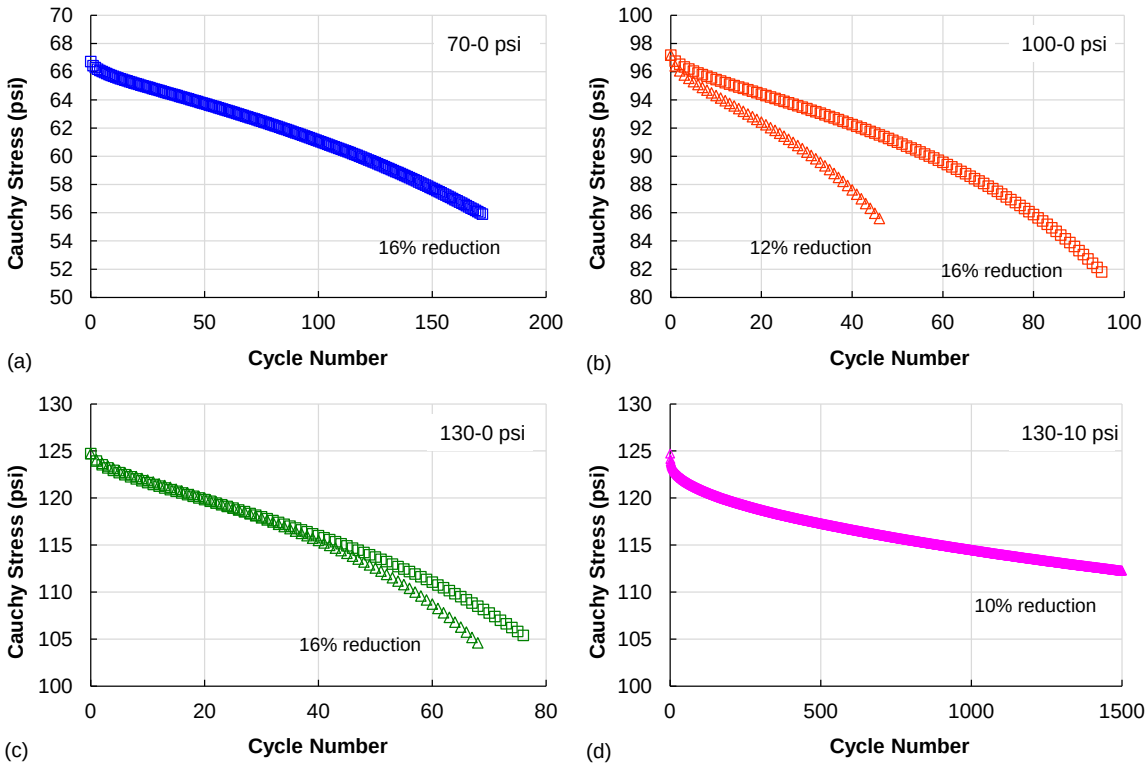

Figure 4-10 Significant reduction in Cauchy stress at the end of the test for several combinations of deviatoric stress and confinement: (a) 70-0 psi, (b) 100-0 psi, (c) 130-0 psi, and (d) 130-10 psi.

In Figure 4-10 the Cauchy stress is defined as the force divided by the deformed cross-section area. Apparently, the material dilation has caused considerable reduction in the normal stress actually felt by the material. If the tests were continued further, more reduction could be observed. This phenomenon should be taken into consideration when one attempts to simulate the large deformation in an asphalt mixture.

CHAPTER 5 ANALYTICAL INVESTIGATIONS

5.1 Evaluation of the Incremental Model

The empirical incremental model expressed in Equation (2.6.8) proposed by Subramanian (2011) are first evaluated using the confined CCR test data. As already demonstrated by Choi (2013), compared to other existing empirical relations the incremental model has the capability to fit both the primary and the secondary regions in individual tests very well. It is tempted to see how well the model behaves for the data with different confinement levels, and an attempt to correlate model coefficients to test conditions (here deviatoric and confining stresses) is then made. The fitting quality at all test conditions are now presented in Figure 5-1 ~ Figure 5-3 where both normal scales and semi-log scales have been utilized to check the fitness for initial cycles and the later part, respectively. Totally 9 different stress combinations each with 2 replicates are evaluated. Note that in all cases the model coefficient *A* has been set to zero. The optimized model coefficients for all the tests have been listed in Table 5-1.

As seen from the fitting results, the capability of the incremental model to fit both primary and secondary regions in individual test is well proven. The efforts are then devoted to seeking a quantitative relation between model parameters and test conditions, i.e., stress levels. As the biggest ambition of the current study is to consider the material pressure dependence explicitly, every parameter is first plotted against the confining pressure for each deviatoric stress as seen in Figure 5-4. A first glance of the scattering of the data points tells that the test variability between replicates enlarges when the deviatoric stress increases. It is further observed that the parameters *B* and *C* do not have a consistent trend with increase in the confinement. Comparatively, the parameter α appears to be least sensitive to test variability and shows a consistent trend among all three deviatoric stress levels. As mentioned before, α is directly related to the slope of the permanent strain history and thus is a phenomenological reflection of the material inherent nonlinearity. Therefore, based on the trend of α it can be concluded that at higher levels of deviatoric stresses the confining pressure has more nonlinear effect on the material response.

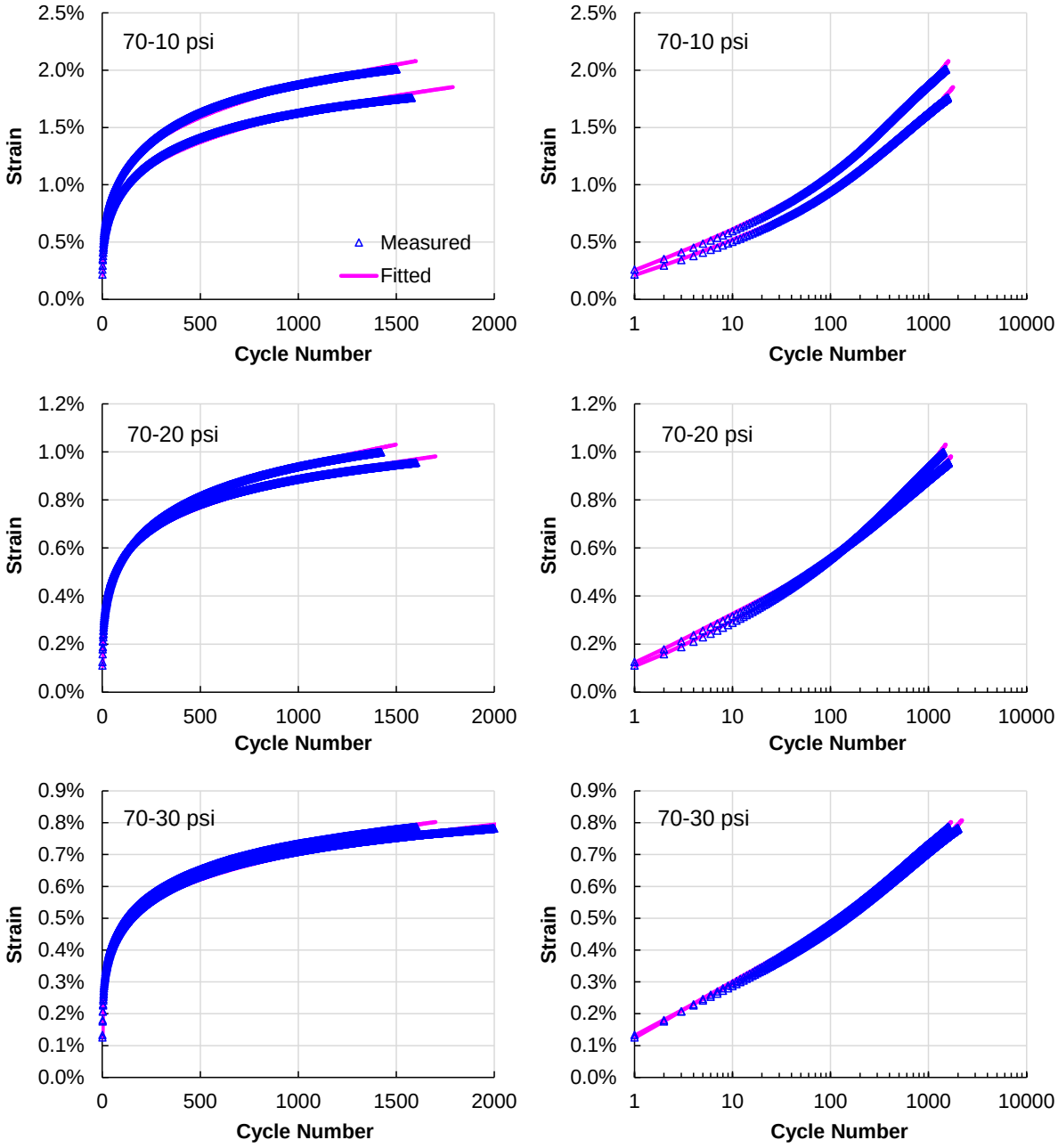

Figure 5-1 Application of the incremental model to CCR tests with 70 psi deviatoric stress and 3 confinement levels: 10, 20, and 30 psi.

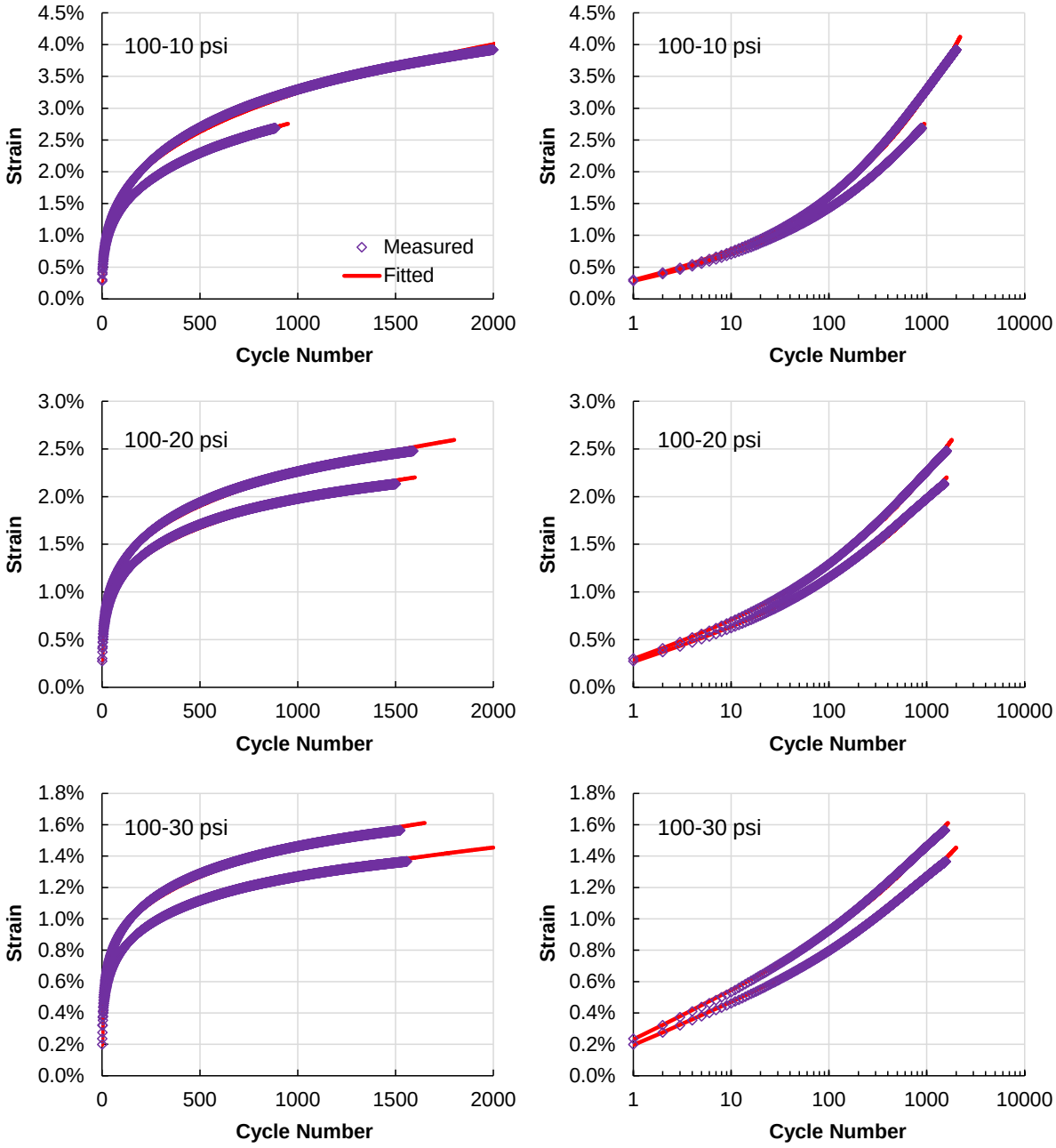

Figure 5-2 Application of the incremental model to CCR tests with 100 psi deviatoric stress and 3 confinement levels: 10, 20, and 30 psi.

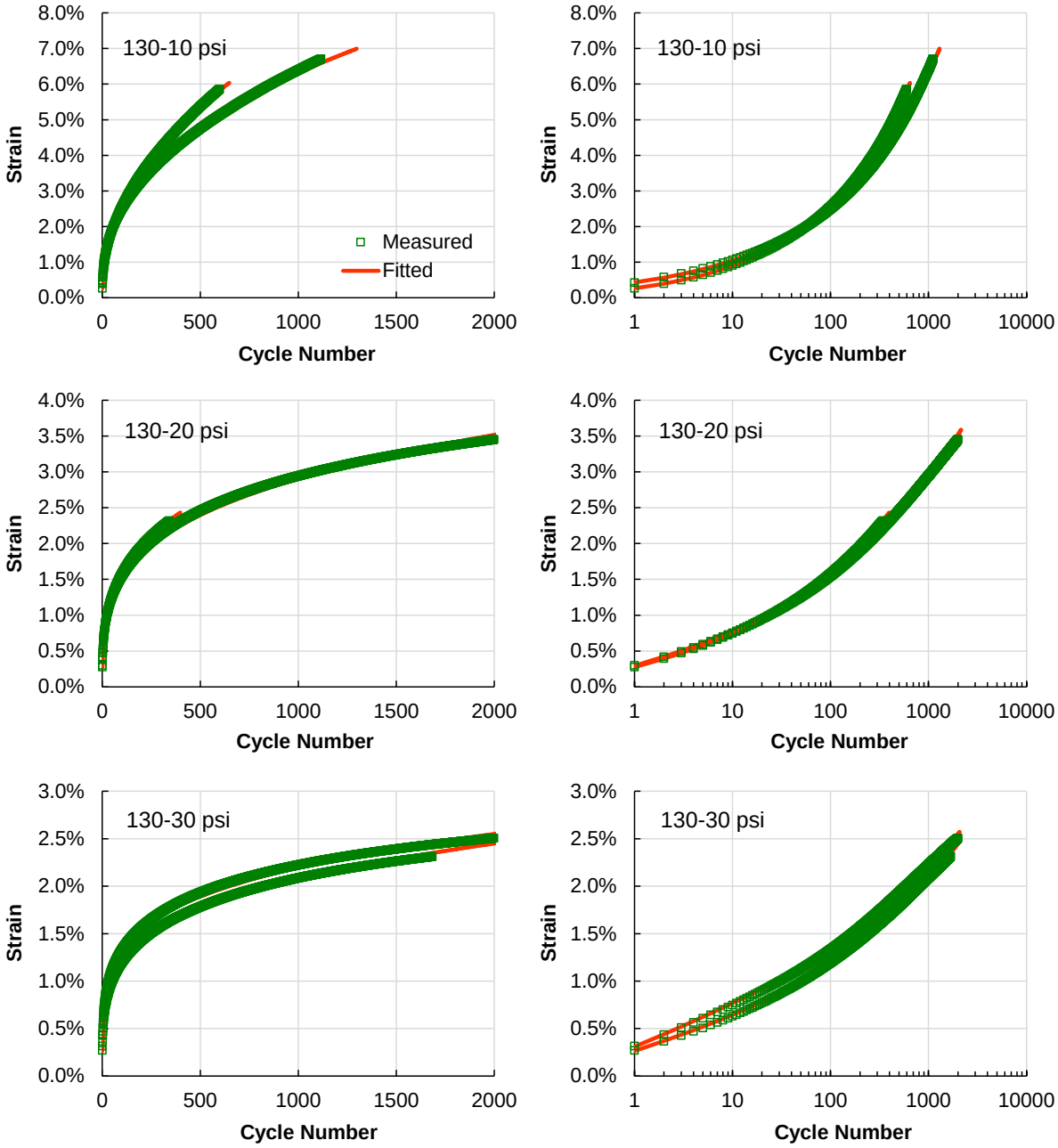

Figure 5-3 Application of the incremental model to CCR tests with 130 psi deviatoric stress and 3 confinement levels: 10, 20, and 30 psi.

Table 5-1 Optimized Coefficients of the Incremental Model for Different Stress Conditions

Stress Conditions (psi)		Replicate	Incremental Model Coefficients		
Deviatoric	Confinement		B	C	α
70	10	# 1	0.00377	0.671	0.769
		# 2	0.00319	0.709	0.765
70	20	# 1	0.00188	1.065	0.767
		# 2	0.00225	1.126	0.802
70	30	# 1	0.00216	0.966	0.824
		# 2	0.00208	0.753	0.824
100	10	# 1	0.00372	0.489	0.708
		# 2	0.00398	0.528	0.696
100	20	# 1	0.00387	0.615	0.764
		# 2	0.00424	0.604	0.758
100	30	# 1	0.00365	0.766	0.799
		# 2	0.00315	0.811	0.799
130	10	# 1	0.00324	0.491	0.548
		# 2	0.00430	0	0.611
130	20	# 1	0.00378	0.585	0.689
		# 2	0.00434	0.719	0.725
130	30	# 1	0.00499	0.847	0.785
		# 2	0.00386	0.656	0.757

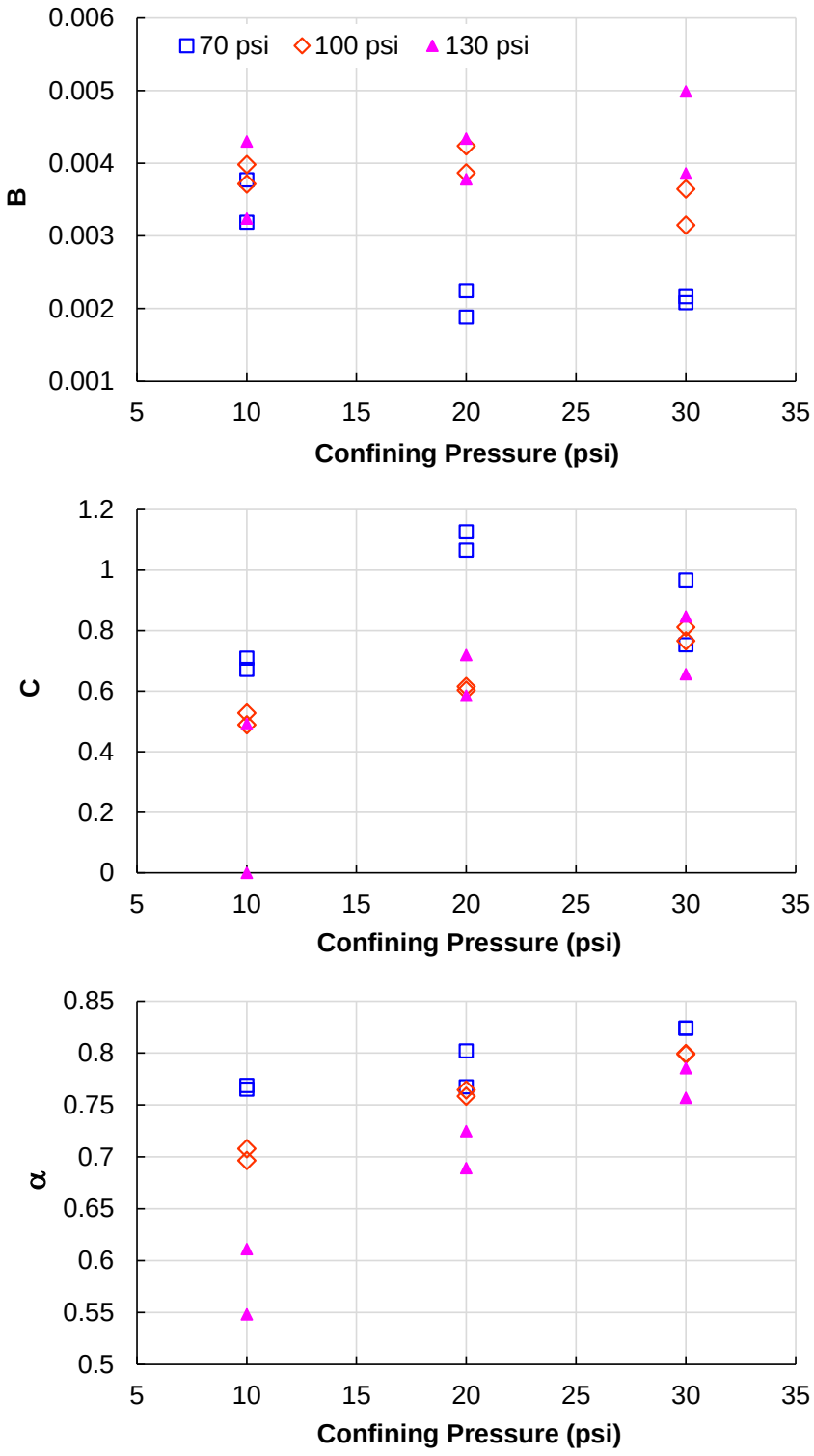

Figure 5-4 Relation between incremental model coefficients and confining pressure.

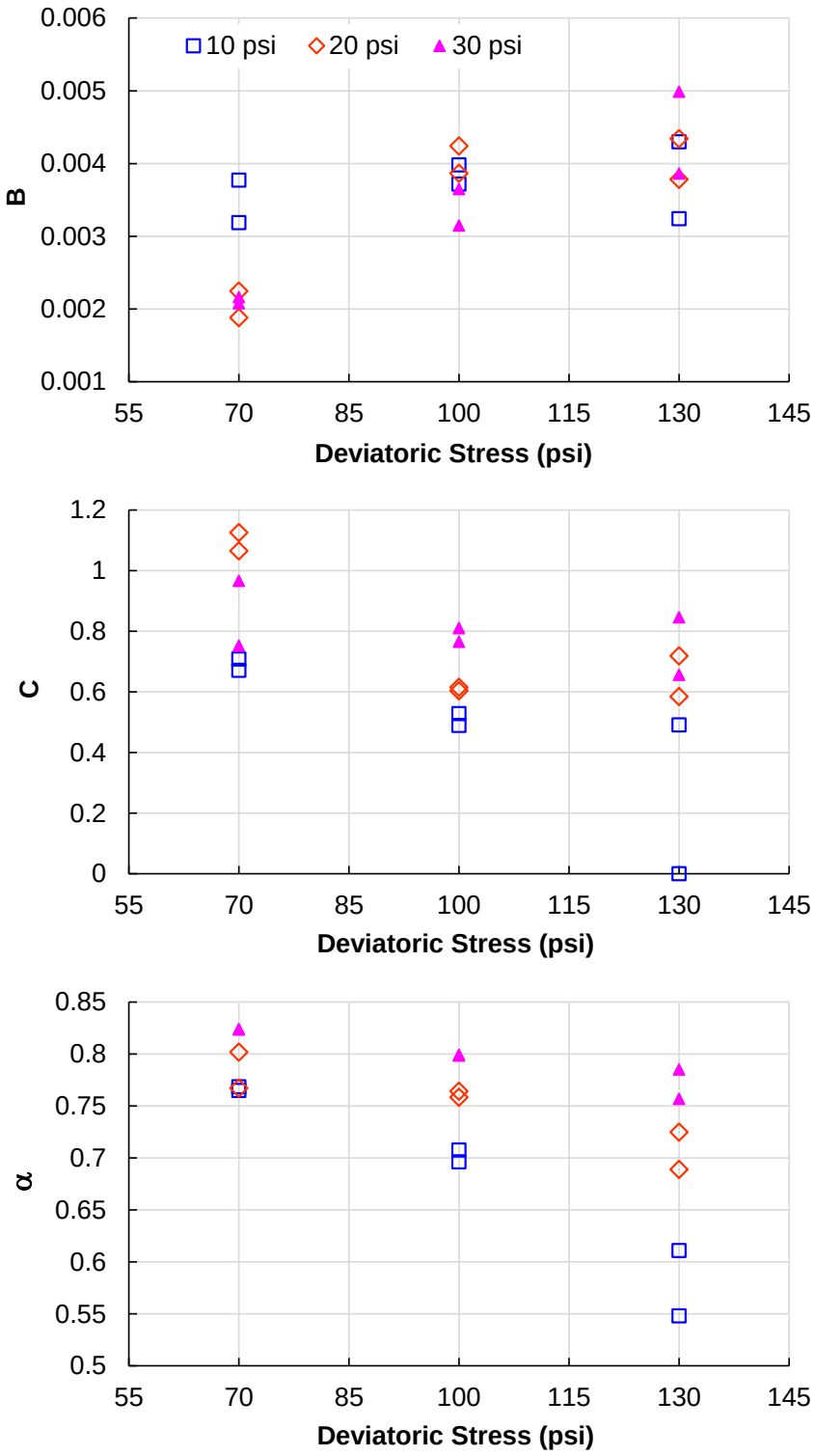

Figure 5-5 Relation between incremental model coefficients and deviatoric stress.

Then the model parameters are plotted versus deviatoric stresses for each confinement as shown in Figure 5-5. Again here possible functions relating the parameters *B*, *C* and deviatoric stress have been concealed by the experimental variability, and only α demonstrates a clear trend. Similarly, we can conclude that at lower confinement levels material exhibits more nonlinearity with deviatoric stress.

In summary, under high confining pressures and low deviatoric stresses materials show less nonlinear response while for low confinements and high deviatoric stresses materials see an increase in nonlinearity. Consider that in continuum stress theories the confining pressure is commonly represented by the mean stress σ_m, and the deviatoric stress by the von Mises equivalent stress as expressed in Equation (2.4.4). It is then felt that a third variable may be proposed to relate the two by weighting their respective contribution on the material nonlinearity. Thus here the triaxiality ratio which is simply defined as the ratio of the mean stress to the von Mises equivalent stress as shown in Equation (2.4.3) is examined. It is hoped that by fitting the parameter α the experimental variability can be somewhat eliminated. Then by using the fitted α values to optimize the remaining parameters *B* and *C* it is possible that better trends of these two can be revealed. Different functions have been tried and an exponential form seems to best represent (1-α). The data points and the fitting curve regarding (1-α) are presented in Figure 5-6.

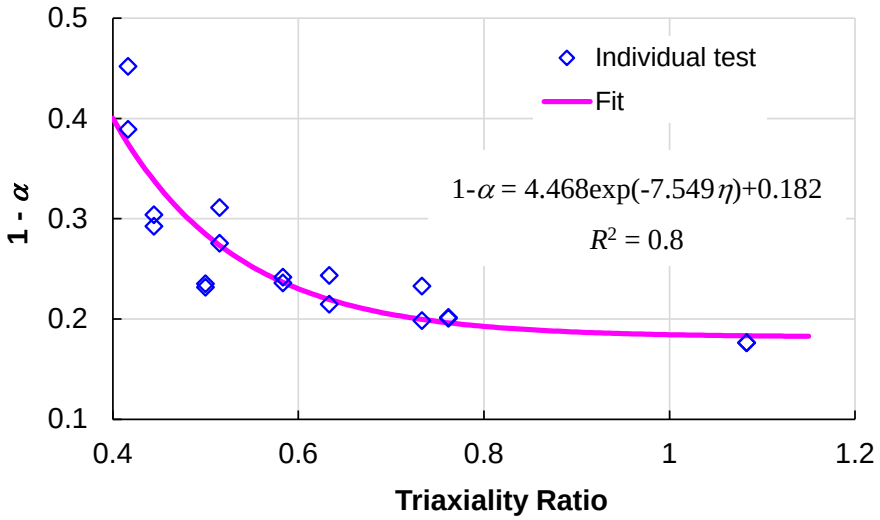

Figure 5-6 Relation between (1-α) and the triaxiality ratio.

Again in Figure 5-6 it can be observed that as the triaxiality ratio increases material nonlinearity reduces which brings less test variability. In other words, the test variability is strongly affected by the degree of material nonlinearity. With the fitted α values the parameters *B* and *C* are re-optimized. Unfortunately, again resulting trends of *B* and *C* with confining pressure or deviatoric stress are still not consistent.

5.2 Extension of the Incremental-Shift Model

5.2.1 Extended model form and experimental protocol

The failure of the attempt trying to correlate the incremental model parameters with stress conditions is presumably attributed to not only the test variability and the empirical nature of the model, but also the interdependence among all three parameters (*B*, *C*, α) in that a variation in one parameter will bring about the change in the other two. Attention is then turned to the incremental-shift model which is composed of an incremental function and shift factor functions. The advantage of the incremental-shift model is that in the incremental function all parameters are constant and determined from the reference test, while the

nonlinear effect due to the deviatoric stress is all reflected through only one variable, N_{red}. Apparently, here dealing with the relation of one variable (N_{red}) with stress conditions is potentially much more feasible than the relation of three parameters with stress conditions as in the incremental model.

Before further investigation, it is important to point out here that after the initial presentation in Choi (2013), the reduced pulse time shift factor in the incremental-shift model has been changed internally in the research group at NCSU from the original power law function to the current logarithmic function. The improved incremental-shift model is now presented for later use:

$$\varepsilon_{vp} = \frac{A + B \cdot N_{red}}{\left(C + N_{red}\right)^{\alpha}} \quad \text{with} \quad N_{red} = N \times 10^{a_{total}}$$

$$a_{total} = a_{\xi_p} + a_{\sigma_v} \quad \text{with} \quad a_{\xi_p} = p_1 \log\left(\xi_p\right) + p_2 \quad \text{and} \quad a_{\sigma_d} = b_1 \left(\frac{\sigma_v}{P_a}\right)^{b_2} + b_3 \tag{5.2.1}$$

This change is aimed to improve the extrapolation regarding the reduced load time beyond the range used in model calibration so that unrealistic results are avoided.

As the incremental-shift model is initially developed under a single confinement level (10 psi), variation in model coefficients are expected when applied to different confining pressures. How each coefficient varies with deviatoric stress and confinement should be investigated and this requires additional experimental work using the TSS test protocol proposed by Choi (2013). Basically, the TSS test profile is composed of several loading blocks with varying peak deviatoric stresses. The stress history in each block is similar to the CCR test. That is, the haversine shaped load pulse has a duration of 0.4s, followed by a rest period of 10s, and this pulse and rest constitute one cycle. In the current study, totally 6 loading blocks were used in the experiments and the sequence of the peak deviatoric stresses are 70, 100, 130, 150, 170, 190 psi. Two hundred cycles were applied in each block. Three confinement levels (10, 20, 30 psi) were used while in each test the confinement was maintained the same throughout. Three different temperatures (28°, 38°, 48°C) were chosen to investigate the effect of temperature and the (physical) pulse time, or the reduced pulse time.

Before the analysis methodology was finalized, different approaches were explored with the goal of better model predictive capability and less experimental requirements. First, originally the incremental-shift model needs a reference test which should be conducted at the same confinement level as the TSS tests. Now that we have three confinement levels, three reference curves are required for the model calibration. Since the peak deviatoric stress should be kept the same among the reference tests, here we used the CCR tests with 100 psi deviatoric stress and 10, 20, 30 psi confinement to generate the reference curves. Afterwards the total shift factor a_{total} can be calculated for each loading block. Then the remaining task is to find a function to express a_{total} in terms of test variables: peak vertical stress σ_v, confinement σ_c, and reduced pulse time ξ_p.

Originally the total shift factor was assumed additively separable into two components, reduced load time shift factor and vertical stress shift factor. See Equation (2.6.9). Since now the third variable (σ_c) is introduced it is expected that additional terms regarding the confinement should be present in the total shift factor function. Besides, it is also observed that the parameters in the reduced pulse time shift factor vary with confinement, and the parameters in the vertical stress shift factor change with both confinement and temperature. And more importantly the vertical stress shift factors appear to follow a linear function instead of the original power law function. Therefore, the total shift factor under a given confinement can be written as

$$a_{total} = C_1 \cdot \ln(\xi_p) + C_2 \cdot \sigma_v + C_3 \tag{5.2.2}$$

As just mentioned, C_1 varies with confinement while C_2 and C_3 change with reduced pulse time and confinement. To consider this variability, the simplest case in which these parameters are expressed linearly by respective variables are first tried, i.e.,

$$\begin{aligned} C_1 &= C_4 \cdot \sigma_c + C_5 \\ C_2 &= C_6 \cdot \ln(\xi_p) + C_7 \cdot \sigma_c + C_8 \\ C_3 &= C_9 \cdot \ln(\xi_p) + C_{10} \cdot \sigma_c + C_{11} \end{aligned} \tag{5.2.3}$$

Substitution of (5.2.3) into (5.2.2) results into the following after arrangements:

$$a_{total} = f \cdot \sigma_c + g \cdot \sigma_v + h \cdot \ln(\xi_p) + m \cdot (\sigma_c \times \sigma_v) + n \cdot \left[\ln(\xi_p) \times \sigma_v\right] + q \cdot \left[\ln(\xi_p) \times \sigma_c\right] + C \tag{5.2.4}$$

Note that compared to Equation (5.2.2) the confinement effects are introduced in a linear fashion just like the deviatoric stress, and the interaction terms expressed as the variable multiplications are also included. Note that in the original total shift factor function Equation (2.6.9) the vertical stress appears in a power law relation and thus here for consistency and additional flexibility, the linear terms of both vertical stress and confinement in Equation (5.2.4) can also be replaced by power functions:

$$a_{total} = f \cdot \sigma_c^{\lambda} + g \cdot \sigma_v^{\gamma} + h \cdot \ln(\xi_p) + m \cdot (\sigma_c \times \sigma_v) + n \cdot \left[\ln(\xi_p) \times \sigma_v \right] + q \cdot \left[\ln(\xi_p) \times \sigma_c \right] + C \quad (5.2.5)$$

When applied to the experimental data it was found that both Equation (5.2.4) and (5.2.5) fit very well the whole pool of calculated shift factors or its subsets. However, a retrospect reveals that this approach requiring individual reference curves has two major drawbacks: first several reference tests are needed in addition to the TSS tests, and besides a functional form should be sought for the spectrum of reference curves in terms of confinement. In order to reduce these experimental and mathematical complexities, the second approach was tried without the use of separate reference test results. For this purpose, only one reference curve is used for all TSS tests regardless of the temperatures and confinement levels. This reference curve is obtained from the strain history of the first loading block in 48°C TSS tests with 10 psi confinement. The reference data from two replicates and the incremental model fit are plotted in Figure 5-7 in both arithmetic and semi-log scales.

Since the reference curves have changed from the first approach, the total shift factors should be re-calculated. And again, as in the above the pool of shift factors using all the TSS data are first used to check the applicability of Equation (5.2.4) and (5.2.5). The fitted total shift factors are plotted versus the calculated ones in Figure 5-8. It is shown that the data points scatter closely around the line of equality in both cases and the difference between the two functional forms are indiscernible. Given this, it is comfortable to use either one of the two forms for the total shift factor. With the observed high fitting quality it is then attempted to check whether a subset of the shift factors is able to calibrate the model without sacrificing much accuracy.

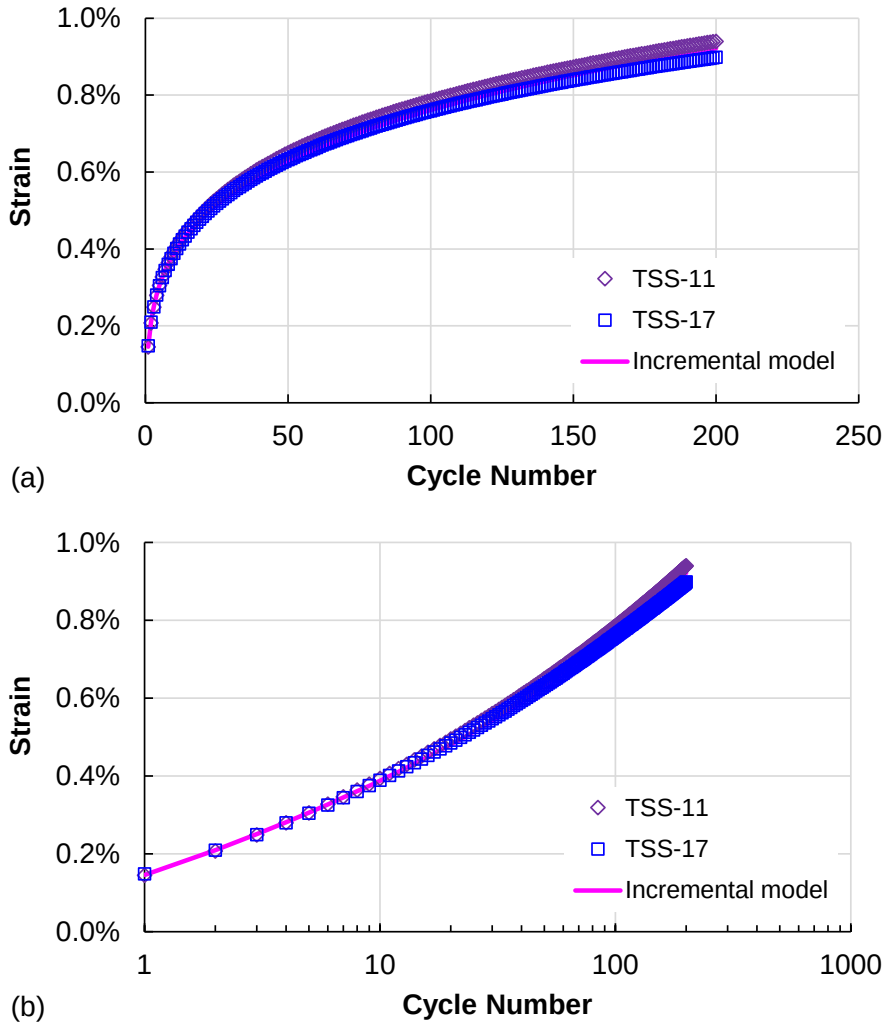

Figure 5-7 Reference tests and the incremental model fit using the first block of TSS tests at 48°C and 10 psi confinement.

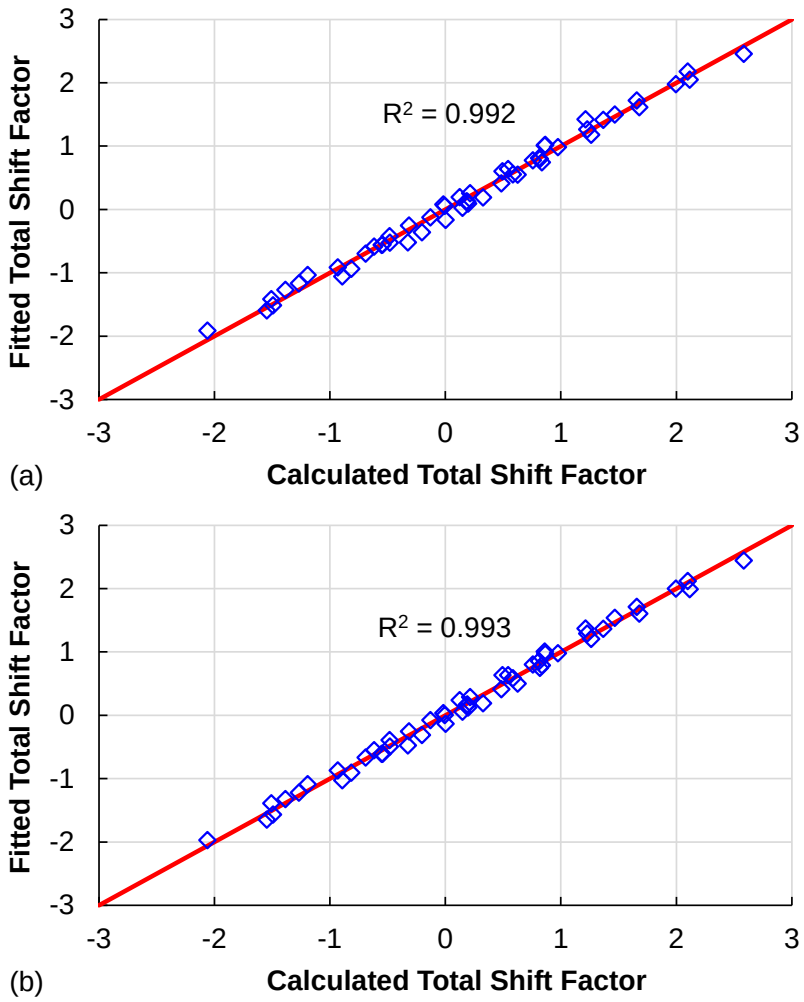

Figure 5-8 Fitted total shift factors versus the calculated ones from all TSS data with 6 blocks: (a) with the linear terms of deviatoric stress and confinement in the total shift factor function Equation (5.2.4), and (b) with the power-law terms Equation (5.2.5).

In the reduced experimental program, at least two temperatures and two confinement levels should be present. For the number of loading blocks, three (i.e., 70, 100, 130 psi) may be sufficient since it is generally deemed and also verified through finite element analysis (e.g., Figure 3-5) that the vertical stress in the field pavement depends on the tire-pavement contact pressure and is usually within 130 psi. The fourth block with 150 psi deviatoric stress can be used as a verification. After trying different combinations with the data at hand, it is

found that the following 4 combinations yield the best model capability: 28° and 48°C each with 10 and 30 psi confinement. These combinations are fairly expected as they produce the widest range in test conditions. Other options with 4 or even 3 combinations have been tried and proved less satisfactory, and several examples are presented in APPENDIX C for comparisons.

The predicted TSS strain curves using the calibrated parameters are shown in Figure 5-9 ~ Figure 5-11 along with the test replicates for each condition. The final model form are rewritten in Equation (5.2.6) below and the calibrated model parameters using the 4 combinations of test conditions are listed in Table 5-2. Note that in the final model form for the total shift factor the exponent of the first confinement term in Equation (5.2.5) has been dropped considering the insensitivity of the exponents on the model capability in fitting the experimental data and more importantly the presence of negative confinement in pavement structural simulations.

$$\varepsilon_{vp} = \frac{A + B \cdot N_{red}}{\left(C + N_{red}\right)^{\alpha}} \quad \text{with} \quad N_{red} = N \times 10^{a_{total}}$$
$$a_{total} = f \cdot \sigma_c + g \cdot \sigma_v^{\gamma} + h \cdot \ln(\xi_p) + m \cdot \left(\sigma_c \times \sigma_v\right) + n \cdot \left[\ln(\xi_p) \times \sigma_v\right] + q \cdot \left[\ln(\xi_p) \times \sigma_c\right] + C_0 \tag{5.2.6}$$

Table 5-2 Calibrated Parameters of the Extended Incremental-Shift Model

Incremental Model Function							
A		B		C		α	
0		0.00218		0.735		0.727	
Total Shift Factor Function (psi for stress)							
f	g	γ	h	m	n	q	C_0
-0.0942	0.165	0.684	0.259	1.009E-5	9.262E-4	-5.998E-3	-2.148
Total Shift Factor Function (kPa for stress)							
f	g	γ	h	m	n	q	C_0
-0.0139	0.0821	0.607	0.259	5.474E-7	1.342E-4	-8.698E-4	-2.624

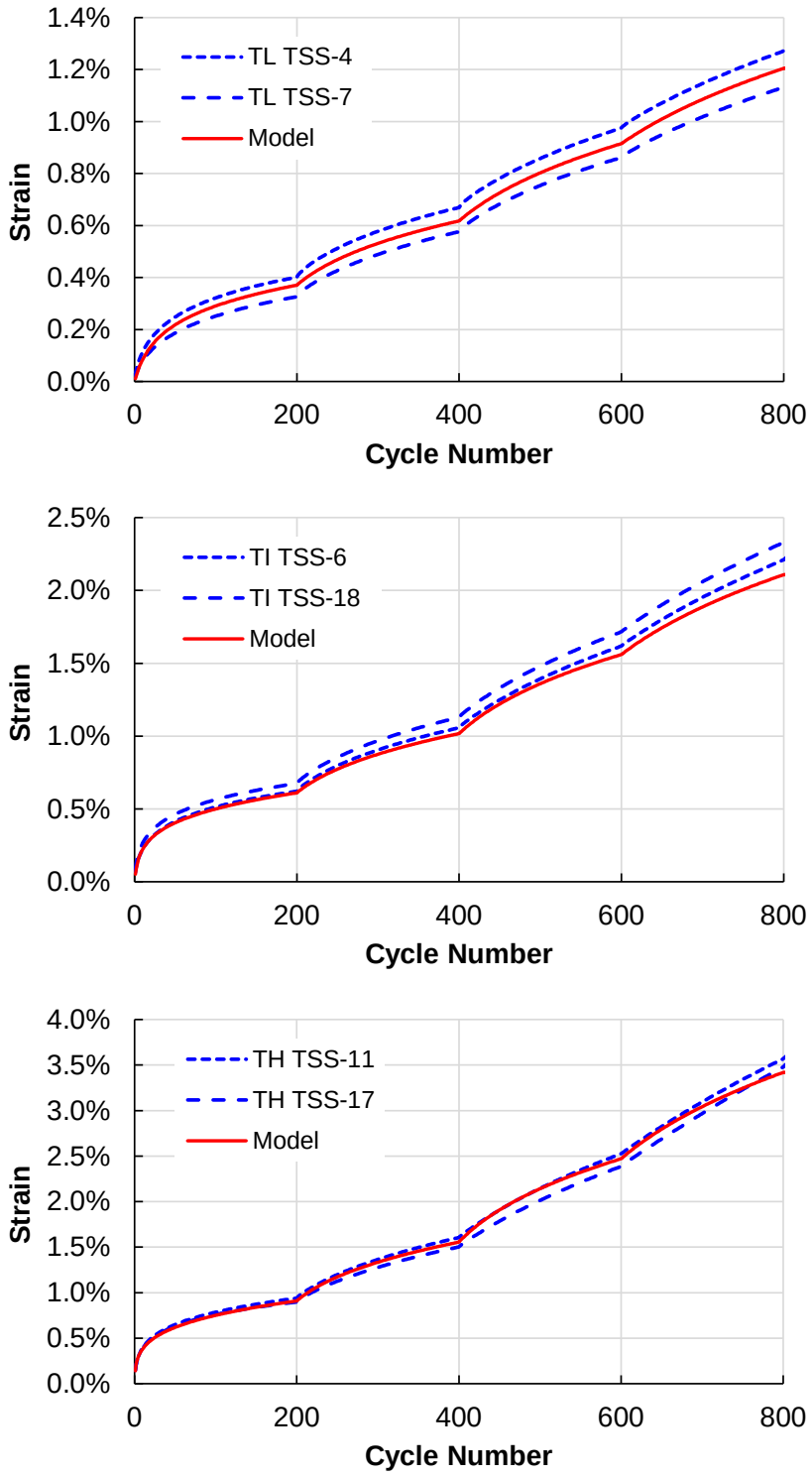

Figure 5-9 Predicted strain histories for TSS tests at 10 psi confinement (TL = 28°C, TI = 38°C, and TH = 48°C).

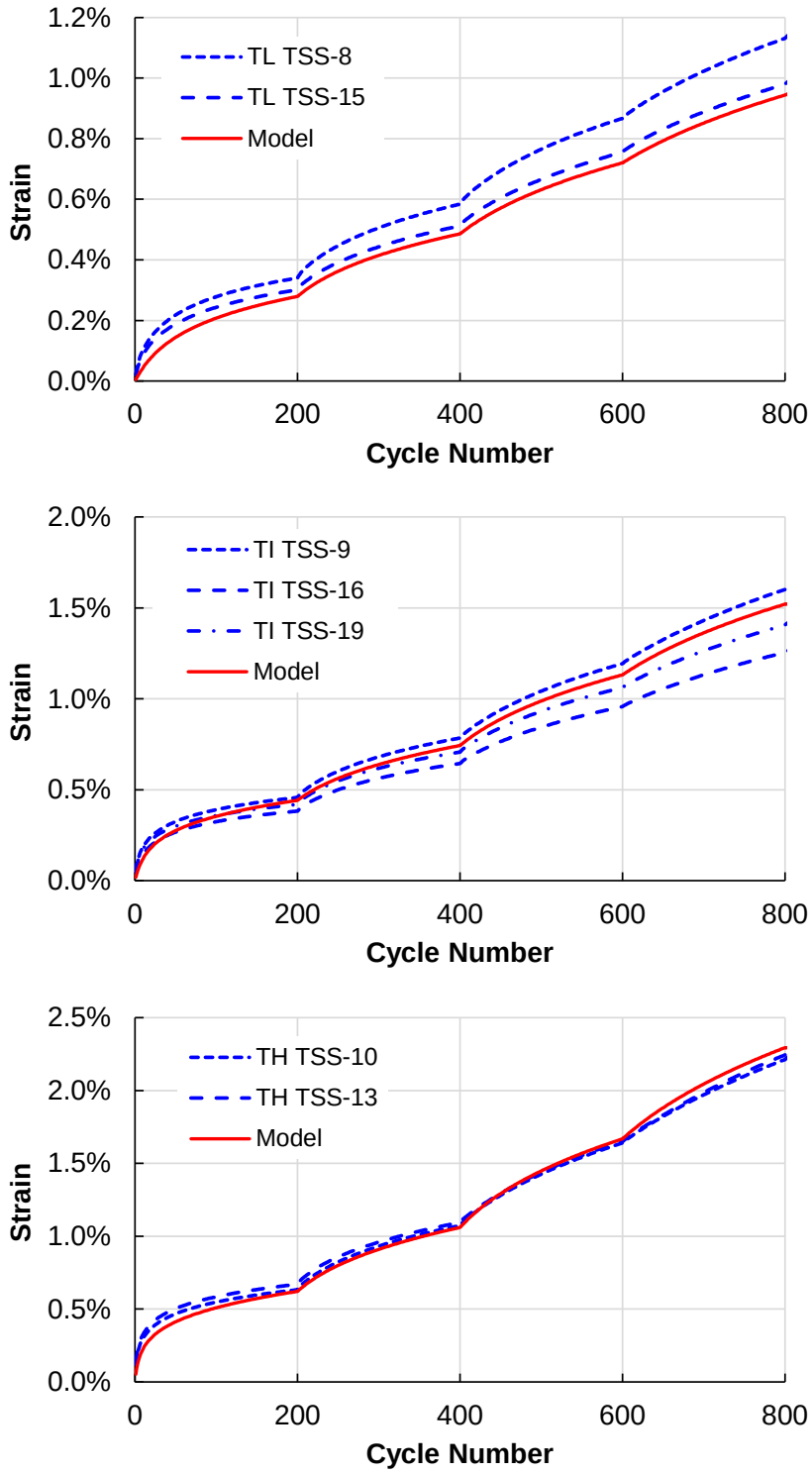

Figure 5-10 Predicted strain histories for TSS tests at 20 psi confinement (TL = 28°C, TI = 38°C, and TH = 48°C).

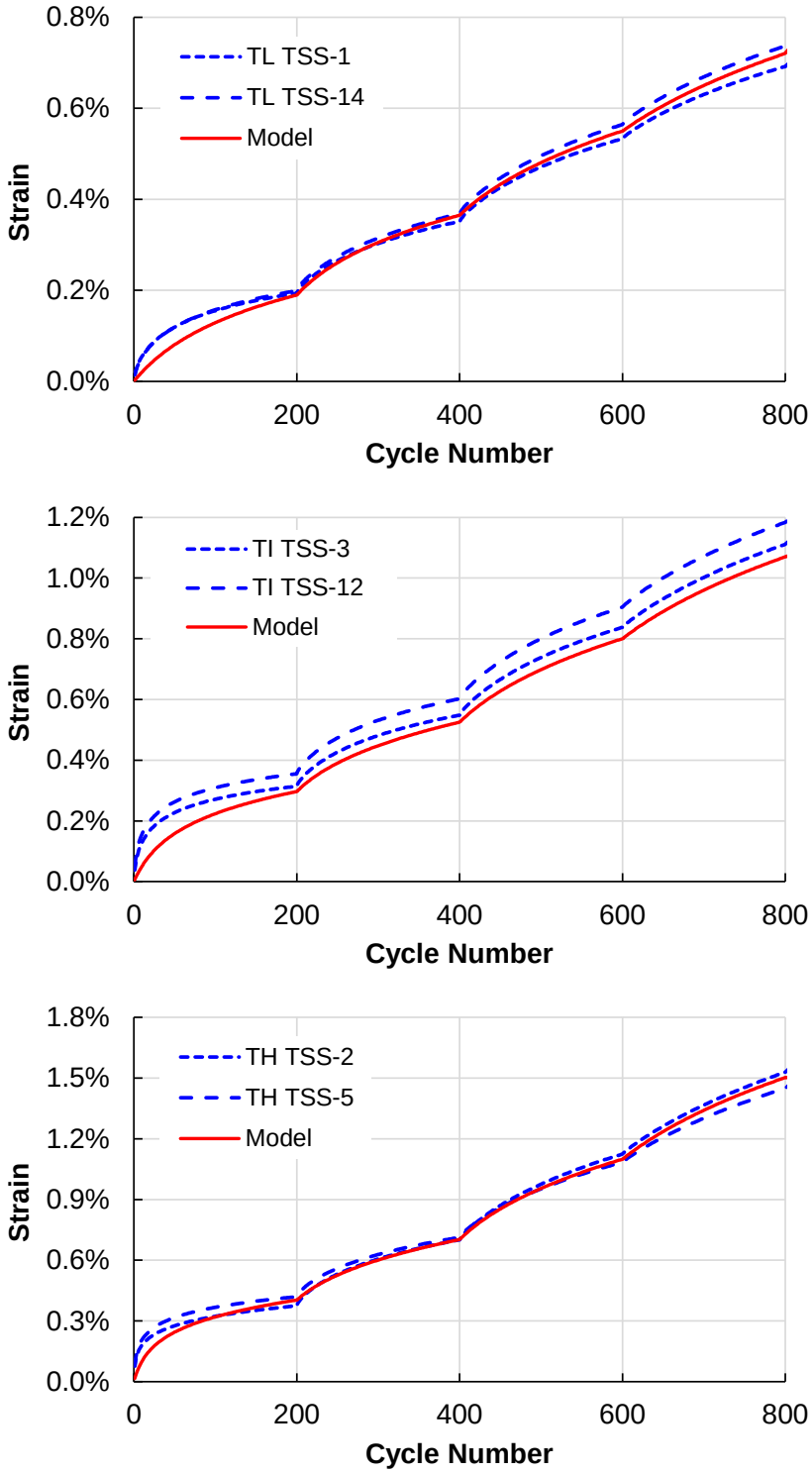

Figure 5-11 Predicted strain histories for TSS tests at 30 psi confinement (TL = 28°C, TI = 38°C, and TH = 48°C).

5.2.2 Verification using the random loading test

The calibrated incremental-shift model is finally verified by the random loading tests. Two tests were performed with the following combination of temperature and confinement: 43°C-15psi, and 33°C-25psi. In both the same random stress history was applied (Figure 5-12). Both the pulse time and peak deviatoric stress level varies among the totally 1500 cycles while the rest period is maintained as 10s. The measured and the predicted strain are presented in Figure 5-13 for both tests. The model capability is verified by the good agreement observed between the measurements and predictions.

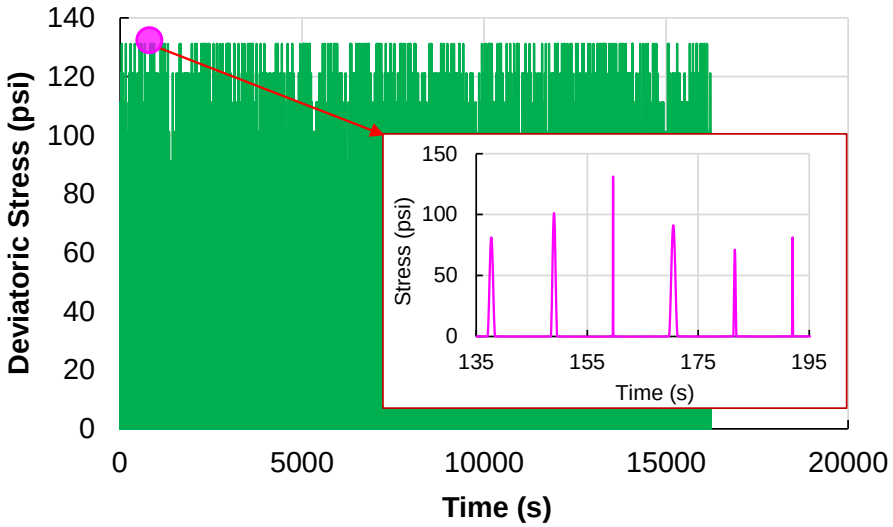

Figure 5-12 Stress history used in the random loading tests for model verification.

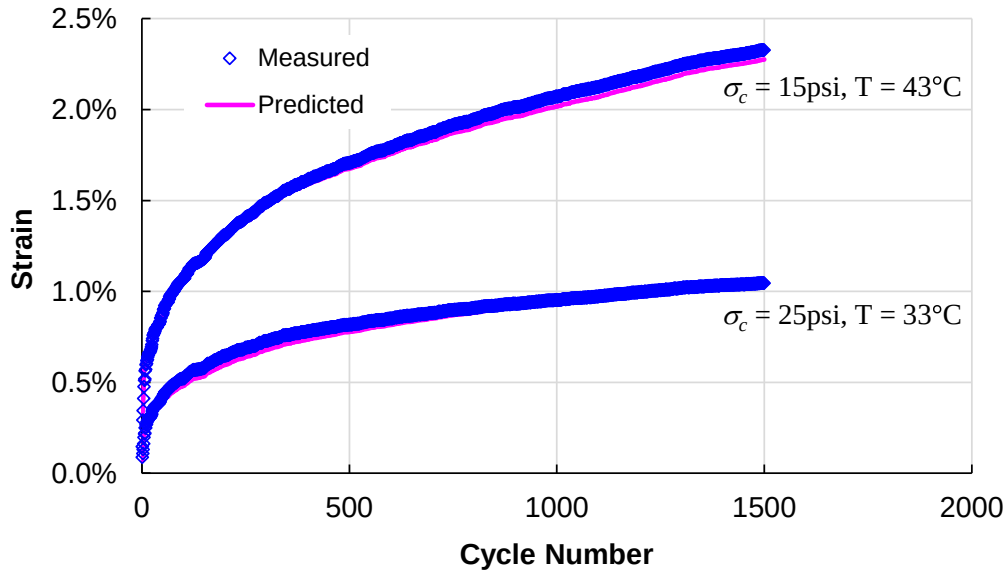

Figure 5-13 Measured and predicted strain histories by the extended incremental-shift model for random loading tests.

5.3 Improvement on the Convolution-type Viscoplastic Model

Beholding the incompetence of the incremental model to consistently capture the nonlinear effect due to confinement, its more rigorous form, as already introduced in Equation (2.6.5) and now re-presented below, which features two convolution integrals, is then evaluated against the experimental data. The model capability of fitting individual test has been validated using the available CCR data at different deviatoric stress and confinement levels.

$$H(t) = H_0 + \left\langle \int_{0^-}^{t} D_2(t-\tau)\frac{d\sigma(\tau)_H}{d\tau}d\tau \right\rangle$$
$$\varepsilon_{vp}(t) = \left\langle \int_{0^-}^{t} D_1(t-\tau)\frac{d\sigma(\tau)_{vp}}{d\tau}d\tau \right\rangle \qquad (5.3.1)$$

However, during the model calibration process, tremendous difficulties have been encountered. First, the model expression is intrinsically one convolution integral (for hardening) nested inside the other convolution integral (for viscoplastic strain). And, during

the unloading and rest period back calculation is required in both integrals. These complexities make the numerical computation extremely time consuming and thus the convergence speed in optimization is exceedingly slow. Secondly, in the model material hardening should be calculated as the first step in order to be substituted into the second integral to obtain the viscoplastic strain. Even though the hardening state is assumed to be expressed directly and explicitly using the deviatoric stress history, it is only a modeling concept and cannot be practically measured during a test. Therefore, all model parameters in both the outer and inner convolution integrals cannot be directly related to material responses or known properties; they can only be obtained through optimization. Another consequence is that initial parameter guesses basically can only be provided through trial and error, and the optimized parameters are very sensitive to the initial guesses. All these remarkable obstacles associated with the practical implementation motivated the attempt at simplification and improvement.

5.3.1 Improvement on the compliance-like functions

Before further discussion, even though the model form resembles the Boltzmann superposition principle, it should be first clarified that the two compliance-like functions D_1 and D_2 should not be treated as material functions like the viscoelastic compliance function, and thus cannot be directly measured from experiments. Yet similarly D_1 and D_2 are still expressed in terms of Prony series for convenient numerical considerations, and originally only two Prony terms for each were used by Subramanian (2011) in order to minimize the total number of model parameters to be identified. However, this may bring the criticism that since only two retardation times are considered the material instant or long-time viscous behavior may not be properly captured. Therefore, it is felt that if more Prony terms can be added then the model may be enhanced and perhaps certain other parameters can be dropped without sacrificing the accuracy. Nevertheless, simply adding Prony terms will only introduce more parameters, and so other schemes have to be sought.

Recall that instead of occurring at a single characteristic time, material time dependent behaviors can span over several decades. Thus it is usually believed there exist a

relaxation/retardation time spectrum for viscous materials. Theoretically, if this time distribution function can be obtained, then the material time dependent properties can be fully comprehended with reasonable number of unknowns. Yet, the biggest challenge is that this material function can never be directly measured but only numerically converted from other material functions, such as creep compliance and dynamic modulus in the domain of linear viscoelasticity, through certain assumptions. The second difficulty comes from the computational side in that in most cases the obtained distribution function is too numerically inconvenient to be implemented. As a compromise, in the current research the following scheme is adopted so that all retardation times are incorporated without introducing too many parameters or sacrificing the numerical efficiency.

As previously mentioned, owing to its simplicity and clear geometrical significance of model parameters, the log-normal function has been used to model the time distribution of relaxation/retardation in viscoelastic materials. The linear viscoelastic retardation distribution of the mix VTa0% has been obtained from dynamic modulus data and is now presented in Figure 5-14, where a log-normal function has been fitted against the experimental data points. In the conversion process the creep compliance is expressed in terms of Prony series with retardation times separated by one decade. The reference temperature used in analysis is 48°C, same as the temperature for the CCR tests. It can be seen that although the experimental data distribution is slightly skewed, the log-normal function fits the data points very well. Given the fitness in the case of linear viscoelasticity, the log-normal function is then tried for the viscoplastic model.

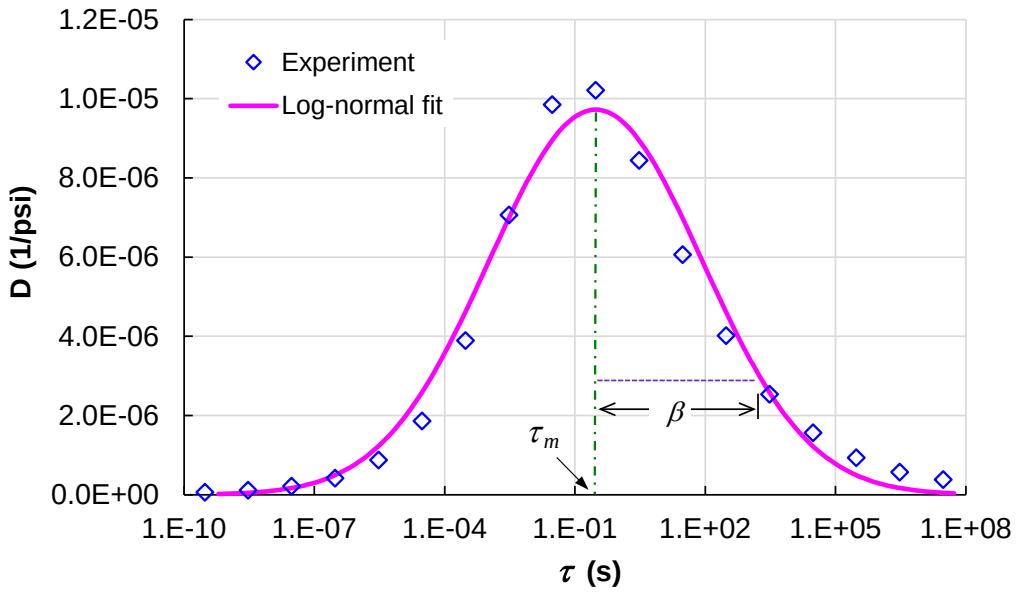

Figure 5-14 The linear viscoelastic retardation time distribution of mix VTa0% from experiments and the log-normal fitting function.

The log-normal function has been introduced in Section 2.2 and is now rewritten in Equation (5.3.2):

$$D(z) = \Delta D \cdot \Phi(z) = \Delta D \cdot \frac{1}{\beta\sqrt{\pi}} e^{-(z/\beta)^2} \quad \text{with} \quad z = \ln(\tau / \tau_m) \tag{5.3.2}$$

where $\Phi(z)$ is the standard log-normal function, and ΔD acts as a scaling factor. The geometrical significance of the parameters β and τ_m can be graphically perceived in Figure 5-14. Basically, τ_m denotes the average retardation time and β measures the distribution width as previously described.

The log-normal function is not analytically integrable, and thus it cannot be directly used to represent the two compliance-like functions. Thus a compromise is made by selecting as many as necessary points along the log-normal curve. For example, in this study one point is chosen at the mean time τ_m, and 16 points are selected at each side of τ_m with one decade interval. See Figure 5-15 for the illustration. This way, the functions D_1 and D_2 can still be expressed through Prony terms so that the computational advantage is preserved. In the

meanwhile, the full range of the retardation times can now be incorporated with only 3 parameters.

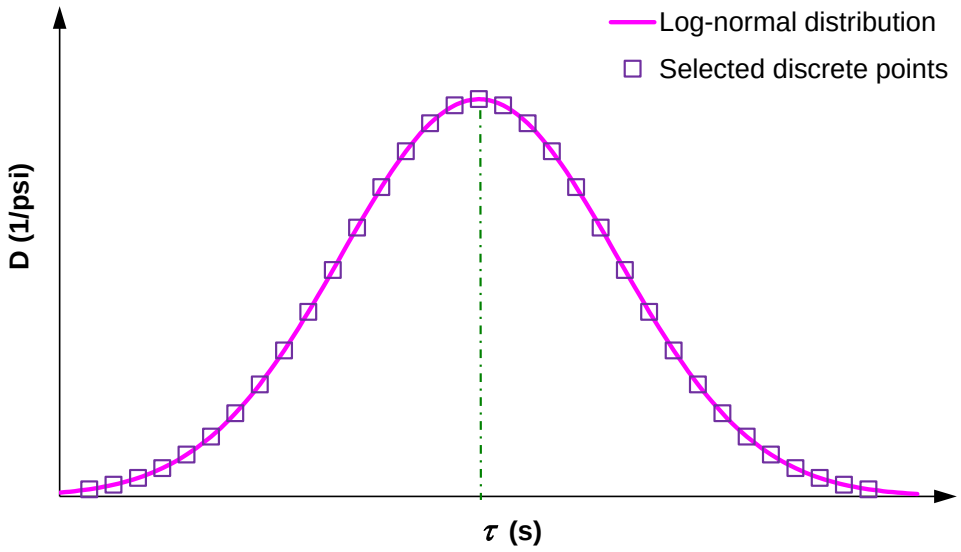

Figure 5-15 Discrete points selected from the continuous log-normal distribution of retardation for the compliance-like functions.

After the extension on the two compliance-like functions, the total number of model parameters remains the same, but the fitting quality has seen an improvement for individual experiments.

5.3.2 Simplification on the stress terms and hardening

In the two stress terms as shown in Equation (5.3.3), power law functions are selected to modify the actual deviatoric stress and as a result 7 parameters are required. Efforts have been devoted to simplifying the stress functions.

$$\begin{aligned} \sigma(t)_H &= H_1\left(\sigma(t)\right)^q \\ \sigma(t)_{vp} &= \frac{\left(G_1\sigma(t)\right)^{p_1} + \left(G_2\sigma(t)\right)^{p_2}}{H(t)^\alpha} \end{aligned} \tag{5.3.3}$$

As the first step, one or two parameters were selected to be fixed, and then the model capability was checked by fitting all experimental data individually. It is found that the model is quite flexible in that in all cases the fitting quality is satisfactory. In addition, it is also discovered that the parameter H_0 in Equation (5.3.1) has no effect on the fitting quality; it essentially is a measure of the internal scale of the model. When H_0 assumes a different value, all other optimized parameters change. Besides, the two compliance-like functions can be the same. Moreover, it is also realized that the hardening $H(t)$ can be set to any positive constant without sacrificing the model fitting capability. All these observations are believed to imply a redundancy of model parameters.

In addition, the material hardening state being explicitly expressed through the stress history brings both computational and practical inconveniences. First, the convolution integral for hardening is nested in the convolution integral for deformation, and this results to fairly expensive numerical computation. Secondly, as a pure mechanical concept, material hardening status can never be measured and therefore the parameters in the hardening function (although explicitly specified) can only be obtained through minimizing the error of the viscoplastic deformation rather than the hardening, and this leads to a very slow convergence in optimization.

Besides, as already illustrated in Figure 2-12, both convolution integrals in Equation (5.3.1) exhibit reduced cyclic increments due to the evolution of respective back stresses. Based on this analytical feature it is speculated that, if we consider only the second convolution for viscoplastic deformation, then the material hardening (or softening) may be qualitatively described by the evolution of the back stress, which is a concept similar to that used by Yun (2008). That is, the back stress here is comparable to the yield stress used in Yun's model. The difference is that Yun assumed evolution laws for both the increase ("hardening" by Yun) and decrease ("softening" by Yun) of the yield stress, whereas here only how the back stress descends during unloading and rest period is specified. With this in mind, it is hypothesized that only using the convolution integral for the viscoplastic strain should be sufficient to simulate the whole deformation history for a CCR test.

With all the above considerations, the original model is reduced into the following:

$$\varepsilon_{vp}(t) = \left\langle \int_{0^-}^{t} D(t-\tau)\frac{d\sigma(\tau)}{d\tau}d\tau \right\rangle \tag{5.3.4}$$

which is essentially the single integral linear viscoelastic model enclosed in the Macaulay brackets. In the reduced expression the actual deviatoric stress is used, yet the viscoplastic strain is still nonlinear with the deviatoric stress because of the existence of the Macaulay brackets and the resulting evolution of the back stress. For the completeness and a better understanding of the model the numerical algorithm of implementing the improved model Equation (5.3.4) has been attached in APPENDIX B.

5.4 Understanding the Improved Model

With the improved convolution-type model shown in Equation (5.3.4), the 4 model parameters are all inside the compliance-like function $D(t)$:

$$D(t) = D_0 + \sum_{j=1}^{M} D_j \left(1 - e^{-\frac{t}{\tau_j}} \right) \tag{5.4.1}$$

where D_0 is the elastic-like compliance, and the D_j-τ_j pairs are specified by the log-normal function expressed in Equation (5.3.2). Due to the extreme resemblance of the improved viscoplastic model to the classical single integral viscoelastic model, it is felt more appropriate to first investigate how the parameter would affect the material linear viscoelastic behavior with the use of the log-normal function for the retardation spectrum.

5.4.1 Parameter analysis for the linear viscoelastic model

When the Macaulay brackets are taken off, the resulting linear viscoelastic function will certainly predicts a decreasing strain response after the peak stress only with a certain delay time. Now the 4 parameters, D_0, ΔD, β, and τ_m, are to be varied to examine the sensitivity of the viscoelastic strain response. In this analysis, a haversine-shaped load pulse with 0.4s duration followed by 0.4s rest period is used as the stress input (Figure 5-16). The strain output is first generated by using a set of “original” parameters (listed in Table 5-3) which

are obtained by fitting the experimental retardation spectrum of mix VTa0% at 48°C as shown in Figure 5-14. Then every parameter is varied by a certain amount with all others kept unchanged to observe the sensitivity of the resulting change in strain.

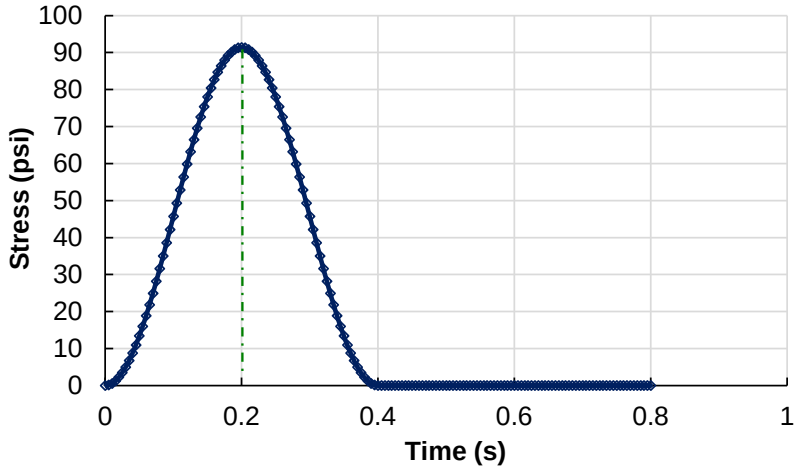

Figure 5-16 Stress input for the sensitivity analysis.

Table 5-3 Parameters of the Compliance Function Used in Sensitivity Analysis

D_0 (1/psi)	ΔD (1/psi)	$\ln(\tau_m)$	β
3.92E-07	1.38E-04	-1.2	8.0

5.4.1.1 Sensitivity with D_0

If only D_0 is varied, the material viscosity is not altered and then only the elastic portion of the strain response is affected. As demonstrated in Figure 5-17, the elastic compliance has a significant influence on the overall response, which is indeed expected. What should be additionally pointed out here is that with the increased weight of the elastic portion in the total strain, the material time dependence manifested by the delay between stress and strain is slightly reduced although the effect is minimal as seen below. It is also obvious that at high

temperatures (in this case 48°C) for a realistic linear viscoelastic material the strain response is mostly viscous with very limited elastic portion.

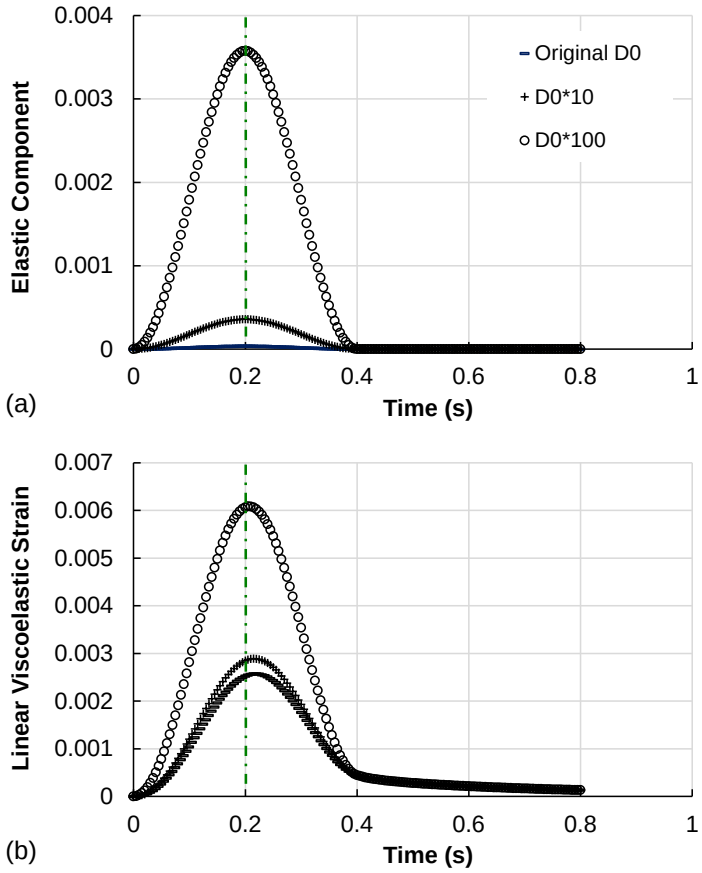

Figure 5-17 Change of the linear viscoelastic strain response with variation in D_0: (a) the elastic component, and (b) the total viscoelastic strain.

5.4.1.2 Sensitivity with ΔD

As can be seen from Equation (5.3.2), ΔD is a factor used to linearly scale the retardation spectrum and thus is expected to directly determine the material overall viscous response. Since ΔD only adjusts the magnitude of the spectrum and has no effect regarding the horizontal location (which is determined by τ_m), the viscous component of the strain is

linearly scaled by it (Figure 5-18). It is not obvious from the figure but it can still be confirmed that, when ΔD decreases to certain levels so that the resulting viscous component is comparable to the elastic component the delay time between stress and strain is slightly affected by varying ΔD.

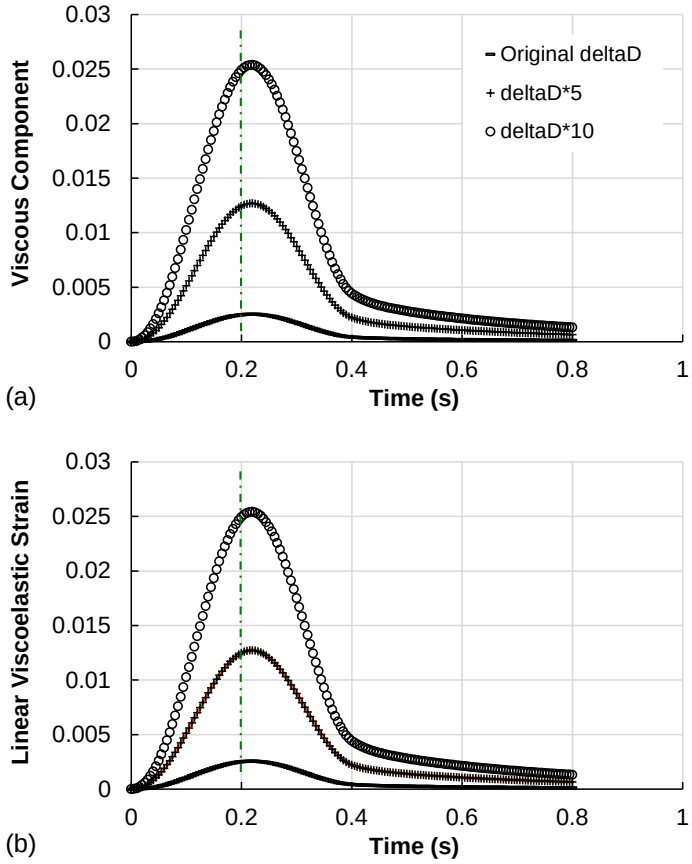

Figure 5-18 Change of the linear viscoelastic strain response with variation in ΔD: (a) the viscous component, and (b) the total viscoelastic strain.

5.4.1.3 Sensitivity with β

The parameter β is used to control the width of the log-normal distribution. As β increases, the retardation spectrum covers wider time ranges. The influence of β can be grasped from Figure 5-19 below. Through fitting the log-normal function to experimental curves of retardation spectrum from several mixes including VTa0%, it is found that β varies between 6 and 9. Hence here β is varied by adding and subtracting 2 from the original value 8. As β reduces the spectrum becomes higher and narrower and thus more weight is given around the mean retardation time and thus material tends to creep at narrower ranges of characteristic times with the limiting case of a single time (for which the compliance is mathematically expressed by one Prony term). The less focus on shorter times with reduction in β brings materials more time dependence although the influence is observed very limited below.

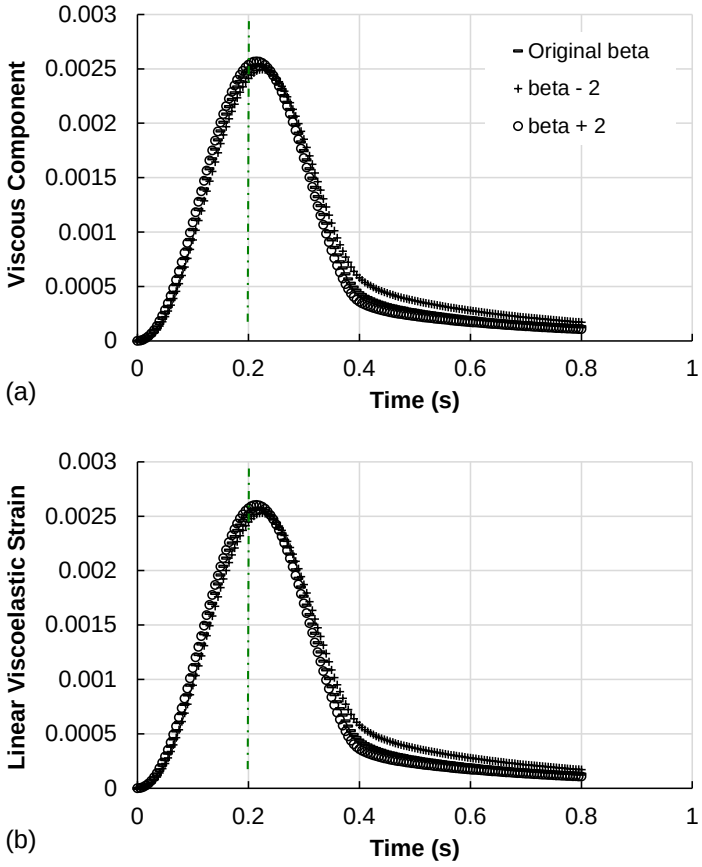

Figure 5-19 Change of the linear viscoelastic strain response with variation in β: (a) the viscous component, and (b) the total viscoelastic strain.

5.4.1.4 Sensitivity with τ_m

The mean retardation time τ_m represent, as the name indicates, the statistically average characteristic time of the material response in a creep loading. Therefore as illustrated in Figure 5-20 it is expected that a small value of τ_m would make instant responses and thus less delay between the stress and strain. As a result, the parameter τ_m can be deemed as the critical parameter influencing the material time dependence. Note that in the figure below the mean retardation time is changed in terms of its logarithmic value since it is $\ln(\tau_m)$ that is utilized in expressing the retardation spectrum in Equation (5.3.2). Also note that when the

retardation spectrum moves to larger times while its shape is maintained, the calculated viscoelastic strain also reduces. The reason is that when the retardation spectrum shifts to the right, it moves away from the time range of the stress input, which leaves less and less impact on the material response and thus the viscous component of the total strain decreases.

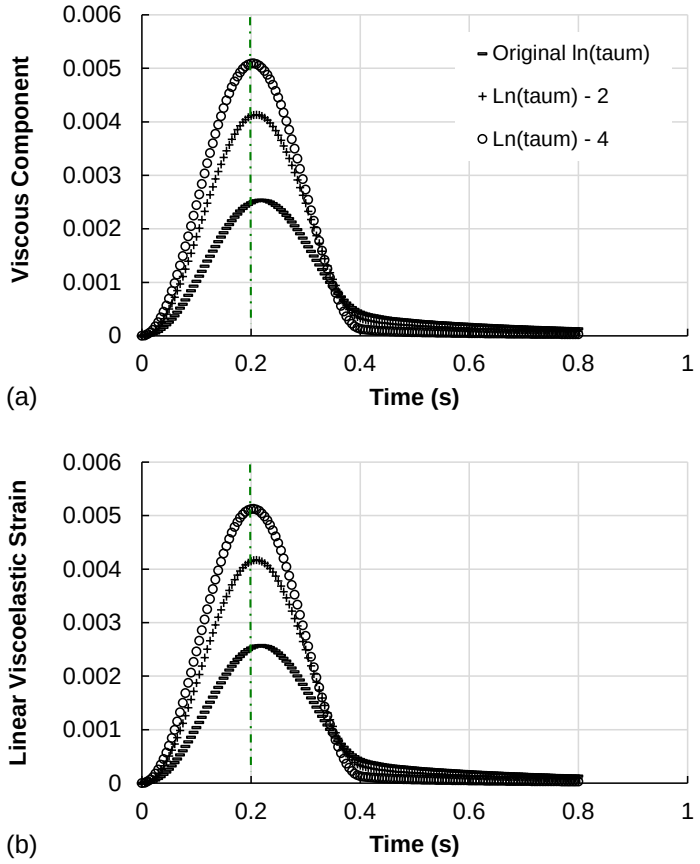

Figure 5-20 Change of the linear viscoelastic strain response with variation in ln(τ_m): (a) the viscous component, and (b) the total viscoelastic strain.

5.4.1.5 Summary

In the total viscoelastic strain, the elastic component is linearly scaled by D_0 whereas the viscous component is proportional to ΔD. The increase in D_0 yields a more fraction of the

elastic portion and thus the material is observed to be less time dependent. Similarly, the increase in ΔD pushes the weight toward the viscous part and thus more time dependence will be seen. The other two parameters β and τ_m also exert influence through changing the width and horizontal location of the retardation spectrum, respectively. Usually β varies in a narrow range and thus has a limited effect. Yet τ_m is the critical parameter controlling how fast the material responses due to loading. For smaller τ_m values the material exhibits more elastic-like behaviors.

5.4.2 Parameter analysis for the improved viscoplastic model

With the previous analysis regarding how the 4 parameters in $D(t)$ affect the material linear viscoelastic response in magnitude and time dependence, it is now more comfortable and prepared to investigate the analytical characteristics of the improved viscoplastic model. Obviously, the major complexity newly introduced comes from the addition of the Macaulay brackets which dictate non-decreasing results from the convolution integral. As a result, the additional variable, the back stress, appears and serves as the internal variable to indicate the change of material status with loading/deformation history.

In the following, both viscoplastic strain and back stress will be investigated with variations in the model parameters. The deviatoric stress input is similar to one of the loading histories in CCR tests: a haversine-shaped pulse with 100 psi peak value and 0.4 second duration followed by a 100 second rest period in each cycle. The permanent strain is collected from the end of the rest period in each cycle. For the sake of convenience and consistence with the terminology used in linear viscoelasticity theory, the compliance function shown in Equation (5.4.1) is called the viscoplastic compliance, while the two terms in its expression at the right hand side are termed plastic compliance and viscous compliance, respectively. Their contribution to the total viscoplastic strain is therefore named plastic component (instantaneous and thus time independent) and viscous component (delayed and thus time dependent), respectively. The numerical algorithms are detailed in APPENDIX B.

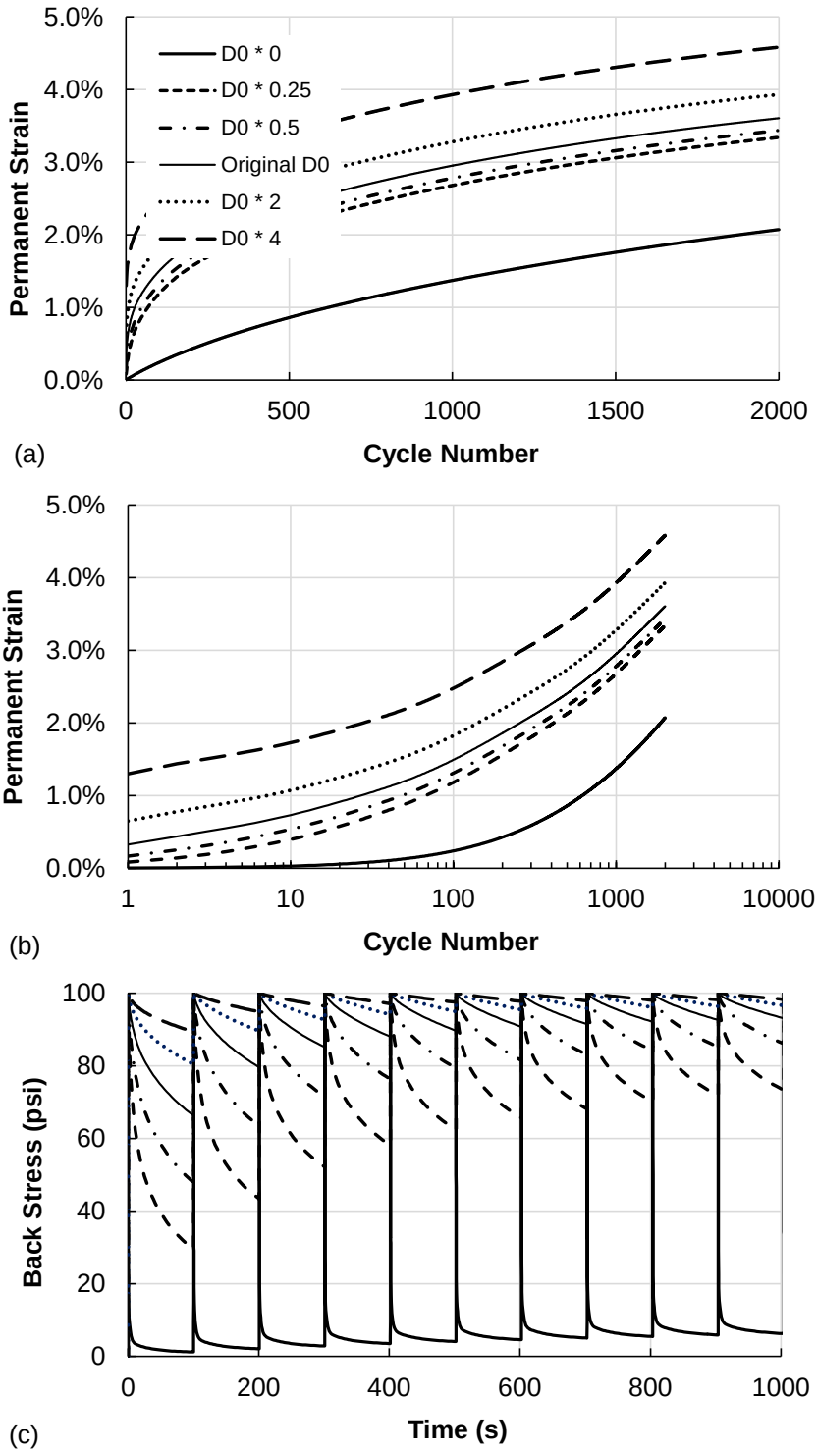

Figure 5-21 Change in permanent strain and back stress with variations in D_0: (a) permanent strain in normal scale, (b) permanent strain in semi-log scale, and (c) back stress evolution.

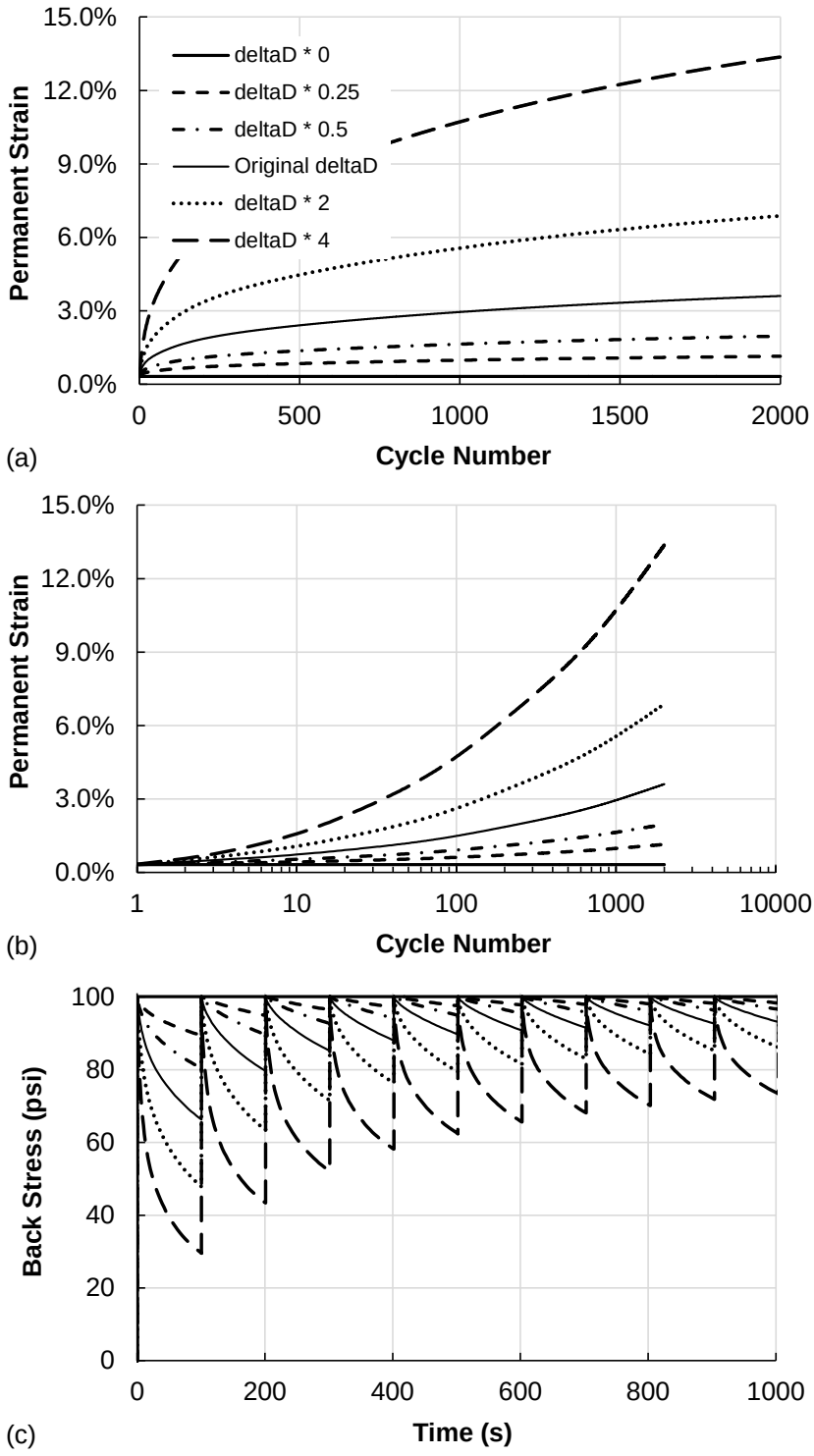

Figure 5-22 Change in permanent strain and back stress with variations in ΔD: (a) permanent strain in normal scale, (b) permanent strain in semi-log scale, and (c) back stress evolution.

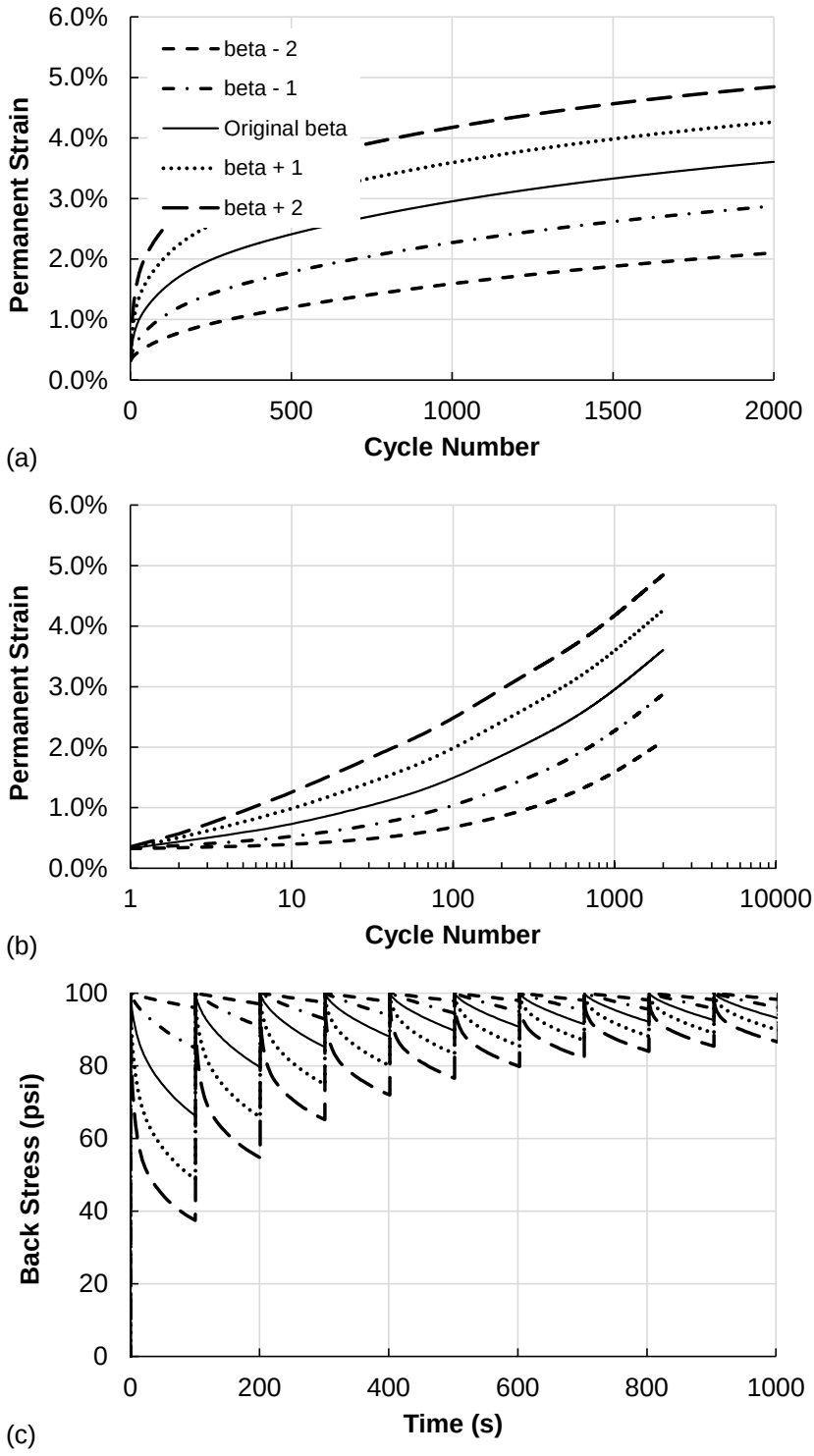

Figure 5-23 Change in permanent strain and back stress with variations in β: (a) permanent strain in normal scale, (b) permanent strain in semi-log scale, and (c) back stress evolution.

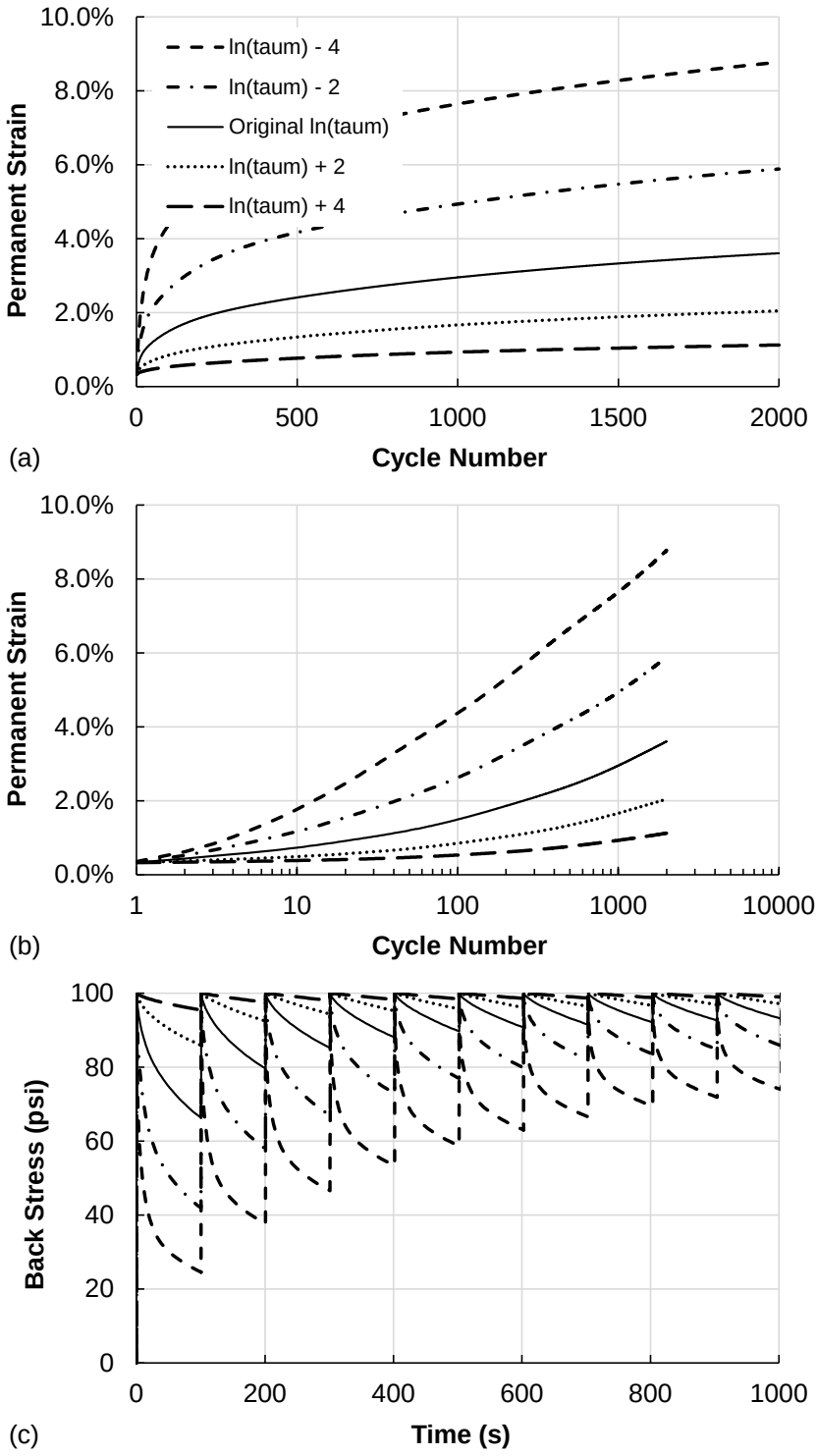

Figure 5-24 Change in permanent strain and back stress with variations in ln(τ_m): (a) permanent strain in normal scale, (b) permanent strain in semi-log scale, and (c) back stress.

The model sensitivity with respect to D_0 has been shown in Figure 5-21. It shows that an increase in D_0 has the ability to increase the strain level in both primary and secondary regions and thus the whole strain curve is raised up. Compared to large cycle numbers, the variation in D_0 has more impact on the relative changes in strains at small cycles. These effects become even more pronounced as D_0 increases. Conversely, with the reduction in D_0 the model tends to approximate a certain lower asymptote with $D_0 = 0$, which is the viscous strain history generated by time dependent mechanisms alone.

In Figure 5-22, the parameter ΔD, which controls the material overall viscous behavior, is also observed to have a nonlinear relation with the total viscoplastic deformation. As shown there, variation in ΔD has negligible influence on the first few cycles. But with the cycle number increases, the impact due to increase of ΔD on the strain level grows rapidly. Conversely, when ΔD decreases the strain curves exhibit less curvature indicating reduced time dependence and viscosity. In the limiting case with $\Delta D = 0$ the material becomes purely plastic without any time dependence, and thus the permanent strain can only be generated in the first cycle and remains the same throughout the rest loading history.

As for the parameter β, it usually varies within a narrow range regardless of the stress condition. It can be seen from Figure 5-23 that the variation in β seems to have a nearly linear effect on the permanent strain after the first few hundreds of cycles whereas for the first few cycles the impact can be neglected. The reduction in permanent strain with the decrease in β is attributed to the reduced coverage of material characteristic times due to the shrinkage of the viscous retardation spectrum.

Regarding the parameter τ_m, as previously discussed, it basically controls how fast a material will deform under external loading. As obvious in Figure 5-24 with the increase in τ_m, the material accumulates the permanent strain in a slower rate.

In sum, all 4 parameters in the improved convolution-type viscoplastic model have nonlinear effects on the permanent strain history. D_0 dominates the permanent strain generated by the first cycle, and is fully responsible for the time independent strain component. The other three parameters control the viscous (time dependent, or delayed)

portion of the permanent deformation by defining the size and location of the viscous retardation spectrum.

After finishing the observation on permanent deformation, focus is now turned to the evolution of back stress. As shown in the above 4 figures and discussed previously in Figure 2-12, the back stress decreases during unloading and rest period with a reduced rate with cycle number, and this leaves a less portion of the load pulse to generate permanent deformation. The way the back stress evolves can be explained in Figure 5-25 below. For a given stress level (denoted as σ_a) in the unloading or rest period, the difference between the back stress and this actual stress increases with cycle, which indicates that the actual stress should be raised higher in order to maintain the viscoplastic strain. Consider the model form in Equation (5.3.4), which is mathematically equivalent to the reduction in material viscoplastic compliance, or the increase in the viscoplastic relaxation modulus and thus a material hardening. With this in mind, it is now easy to understand that with the material viscosity increases (for example, when D_0 decreases or ΔD increases), the back stress reduces at a higher rate than in other scenarios since the actual stress during unloading or rest should only be raised by smaller amount to maintain the viscoplastic strain due to the increased delay in response. In the analytical sense, if the actual stress is used for the unloading and rest period, the convolution integral without the Macaulay brackets will reduce at lower rates for materials with high viscosities, and thus less additional stress is required to add to the actual stress to bring the results back to the peak value in the cycle. The back stress behavior with respect to β and τ_m can be similarly explained.

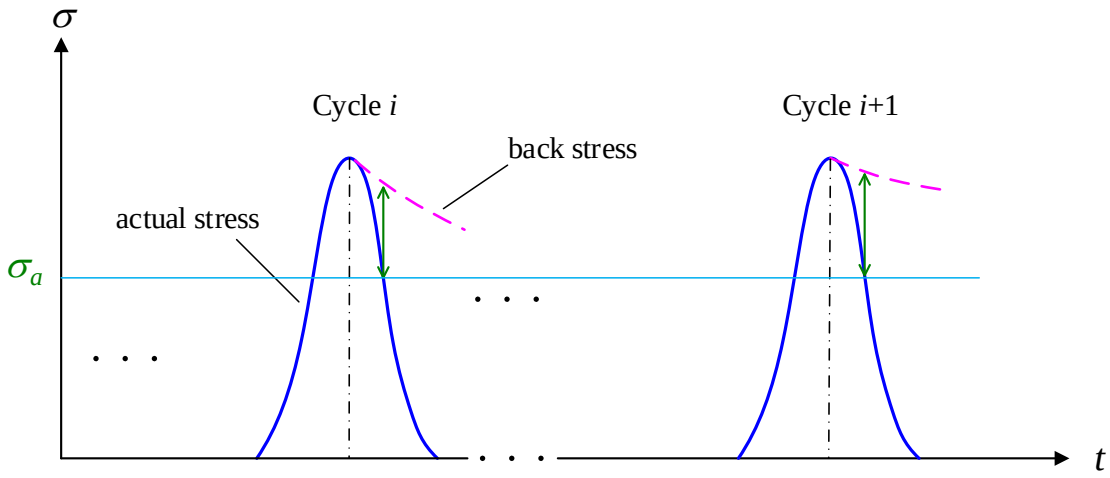

Figure 5-25 Illustration of the mechanisms behind the evolution of back stress.

5.5 Evaluation of the Improved Model

With the understanding from the parameter analysis, the improved convolution-type viscoplastic model is now applied to all the CCR tests with 9 different combinations of deviatoric stress and confining pressure. In the optimization process, the viscoplastic strain history is first calculated using the same loading condition as the tests, and then the strain at the end of the rest period in each cycle is collected to form the measured permanent strain (ε_{mea}). For each data point of the measured permanent strain, the absolute value of relative error is used and then summed over all cycles. The final error function is defined as the average cyclic relative error defined as

$$ERR = \frac{1}{N_{total}} \sum_{i=1}^{N_{total}} \frac{\left|\varepsilon_{mea}^{i} - \varepsilon_{pre}^{i}\right|}{\varepsilon_{mea}^{i}} \tag{5.5.1}$$

where N_{total} is the total number of cycles from the experimental data, and ε_{mea} and ε_{pre} denote the measured and predicted permanent strain in each cycle, respectively.

As expected the improved model is found to be able to fit each individual test and replicate very well. For the optimized model parameters, D_0 is plotted in Figure 5-26, and ΔD, β, and τ_m are presented in terms of the retardation spectrum in Figure 5-27 for each

deviatoric stress level and in Figure 5-28 for each confinement level. The linear viscoelastic retardation spectrum (at 48°C, same as the CCR test temperature, and unconfined) has also been added for easy comparison. Note that due to difficulties in finding proper initial guesses for the stress condition with 130 psi deviatoric stress and 10 psi confinement, the fitting quality for this case is not satisfactory and thus not shown here.

As indicated by Figure 5-26, it is still unfortunate that the optimized parameter D_0 does not follow a clear and consistent trend with confinement at any deviatoric stress level. However, if we look at the retardation spectrum in Figure 5-27 and Figure 5-28, its amplitude consistently increases with the reduction in confinement and increase in the deviatoric stress. Another observation is that in some cases the center of the spectrum does not change with deviatoric stresses or confinements but in other cases it does. A closer examination reveals that this phenomenon may be related to the degree of material nonlinearity since under low deviatoric stress (70 psi) and high confinement (30 psi) material exhibits least nonlinearity and in these two cases the retardation spectra happen to have approximately the same location of the center. For the other cases, in Figure 5-27, under the same deviatoric stress as the confinement level reduces, material nonlinearity increases and meanwhile the retardation spectrum shifts to right, i.e., material is characterized by a larger mean retardation time. Likewise, in Figure 5-28 under the same confinement level as the deviatoric stress increases the degree of material nonlinearity increases and in the meantime the mean retardation time also increases. Thus in sum, the mean retardation can be used as an indicator of the degree of material nonlinearity.

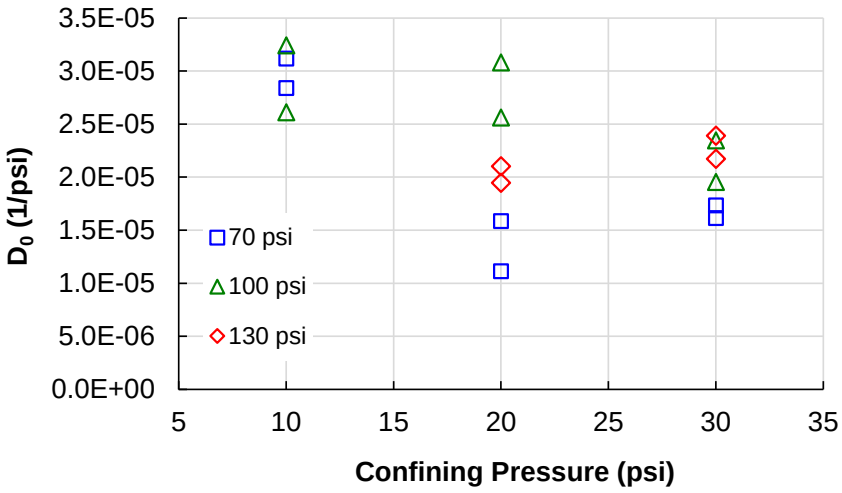

Figure 5-26 The optimized parameter D_0 of the improved model with respect to confining pressure at different deviatoric stress levels.

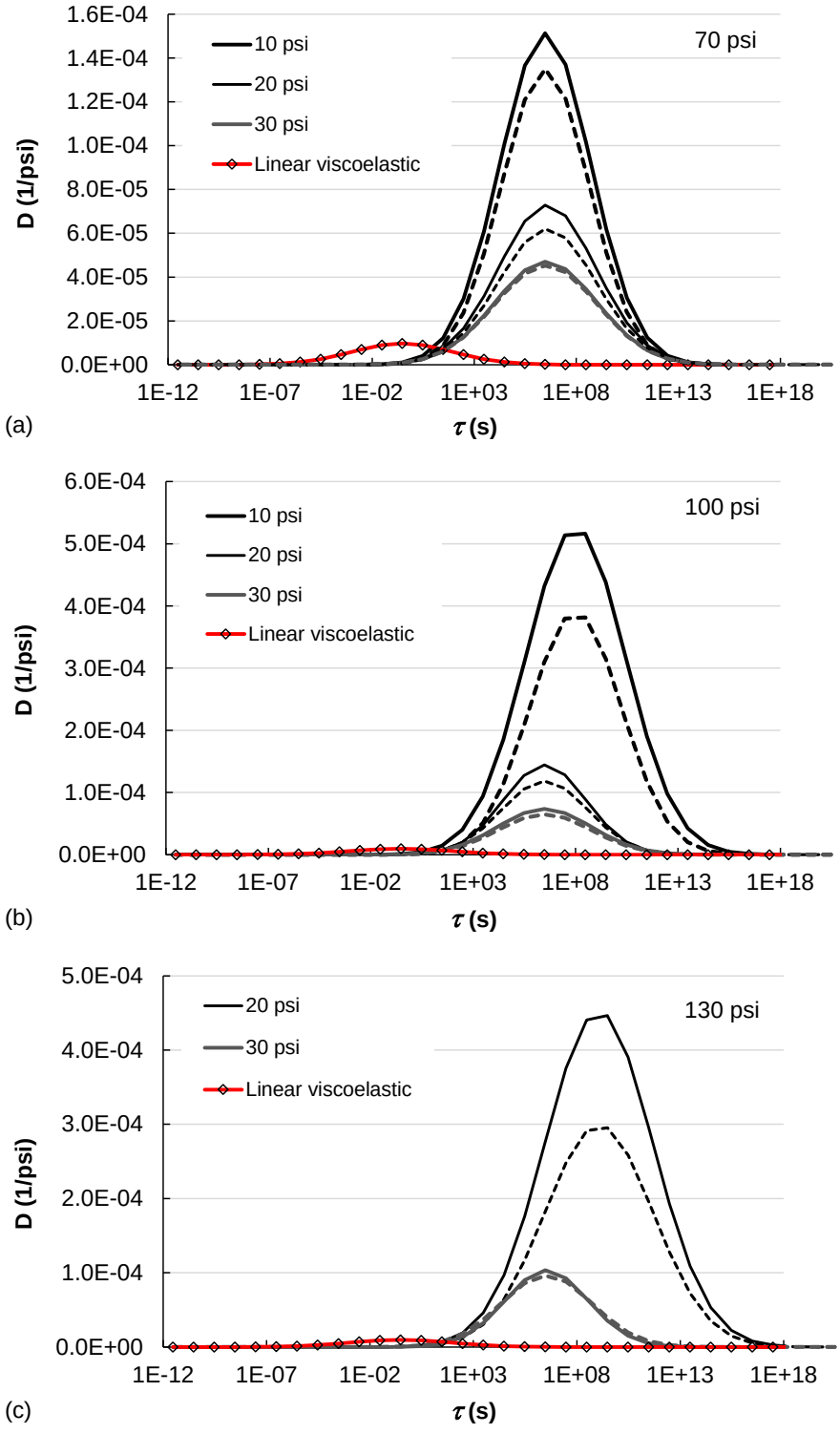

Figure 5-27 The optimized retardation spectrum for the improved model at different deviatoric stress levels: (a) 70 psi, (b) 100 psi, and (c) 130 psi.

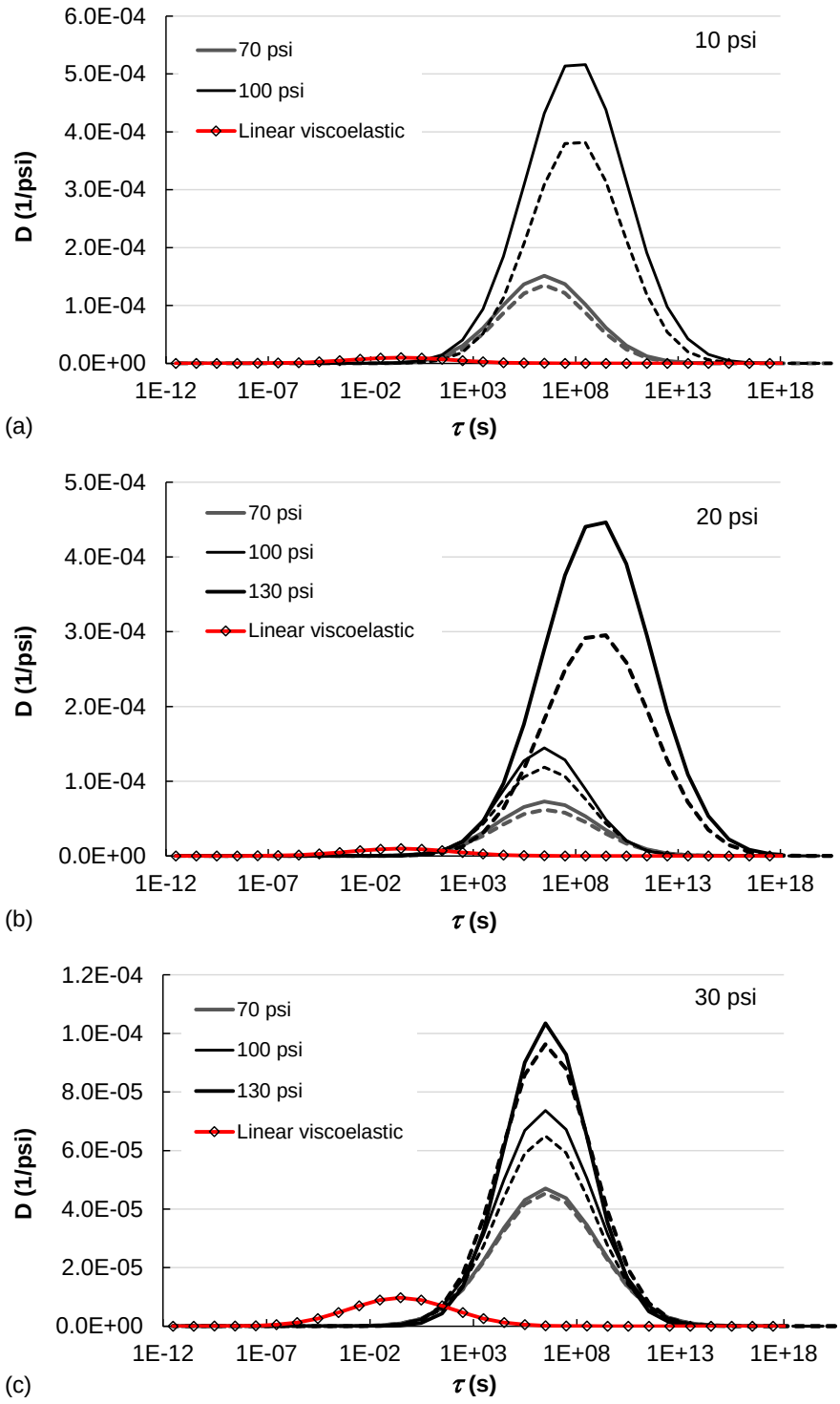

Figure 5-28 The optimized retardation spectrum for the improved model at different confinement levels: (a) 10 psi, (b) 20 psi, and (c) 30 psi.

The same challenge remains in the attempt to correlate each of the model parameters to stress conditions. As always the case, the accuracy of model parameters are subjected to experimental errors. A high fitting quality with an experimental curve might also suggest a poor set of optimized parameters if the experimental data actually deviate considerably from the truth. On the other hand, it can also be expected that the mathematically optimized parameters may not be the most physically or mechanically desired in that they may demonstrate unreasonable characteristics that are not expected based on test conditions and material known properties. Conversely, an optimum set of parameters may sacrifice certain degrees of accuracy in fitting experimental data but they may be more easily correlated to existing knowledge about the material and thus are more favored for practical purposes.

With the above realization in mind, it is encouraged to further investigate the model manipulations. Recall that in Section 2.4 it is mentioned that in the viscoelastic domain material relaxation spectra share approximately the same size and shape regardless of the confinement level as seen in several asphalt mixtures. As the relaxation spectrum remains nearly unchanged, its counterpart the retardation spectrum is meant to vary due to the difference in the material long-term equilibrium modulus. With this observation in mind, it is motivated to check the distribution of the viscoplastic relaxation spectra through converting the available retardation spectra.

5.5.1 Conversion of the retardation spectra to relaxation spectra

The interconversion between viscoelastic relaxation modulus and creep compliance functions has been well documented in the literature with both numerical techniques and analytical methods available (Park and Schapery 1999, Schapery and Park 1999). Here the conversion algorithm using the Prony representation is re-derived just for the sake of completeness.

In the linear viscoelasticity theory, the exact relationship between relaxation modulus $E(t)$, and creep compliance $D(t)$, in time domain is given by the following integrals:

$$\int_{o^-}^{t} D(t-\tau)\frac{dE(\tau)}{d\tau}d\tau = 1 \tag{5.5.2}$$

And the relaxation and compliance functions are represented using Prony series respectively:

$$E(t) = E_\infty + \sum_{i=1}^{M} E_i e^{-\frac{t}{\rho_i}} = \left(E_\infty + \sum_{i=1}^{M} E_i \right) + \sum_{i=1}^{M} E_i \left[\exp(-t/\rho_i) - 1 \right] \tag{5.5.3}$$

$$D(t) = D_0 + \sum_{j=1}^{N} D_j \left[1 - \exp(-t/\tau_j) \right] \tag{5.5.4}$$

where E_∞ is the long-term equilibrium modulus, D_0 is the instantaneous elastic compliance, E_i, ρ_i are the parameters in the i-th Maxwell element, and D_j, τ_j are the parameters defining the j-th Voigt element. Rewrite the relaxation function using Heaviside function as

$$E(t) = \left(E_\infty + \sum_{i=1}^{M} E_i \right) H(t) + \sum_{i=1}^{M} E_i \left[\exp(-t/\rho_i) - 1 \right] \tag{5.5.5}$$

where $H(t)$ is the Heaviside function defined by

$$H(t) = \begin{cases} 0, & t < 0 \\ 1, & t \geq 0 \end{cases} \tag{5.5.6}$$

Note that the reason why the relaxation function is written in the way shown in Equation (5.5.3) is that at $t = 0$, the instantaneous relaxation modulus is $E_\infty + \sum_{i=1}^{M} E_i$, not E_∞.

Substituting Equation (5.5.4) and (5.5.5) into (5.5.2) and using the Dirac delta function we arrive at

$$\int_{0^-}^{t} \left(E_\infty + \sum_{i=1}^{M} E_i e^{-\frac{t-\tau}{\rho_i}} \right) \left[D_0 \delta(\tau) + \sum_{j=1}^{N} \frac{D_j}{\tau_j} e^{-\frac{\tau}{\tau_j}} \right] d\tau = 1 \tag{5.5.7}$$

The left hand side of the above equality can be expanded into 4 terms and can be simplified by using the sifting property of the Dirac delta function:

$$\int_0^t D_0\left(E_\infty+\sum_{i=1}^{M}E_i\right)\delta(\tau)d\tau = D_0\left(E_\infty+\sum_{i=1}^{M}E_i\right)$$

$$\int_0^t \sum_{j=1}^{N} D_j\left(1-e^{-\frac{t-\tau}{\tau_j}}\right)\left(E_\infty+\sum_{i=1}^{M}E_i\right)\delta(\tau)d\tau = \sum_{j=1}^{N} D_j\left(1-e^{-t/\tau_j}\right)\left(E_\infty+\sum_{i=1}^{M}E_i\right)$$

$$-\int_0^t D_0\sum_{i=1}^{M}\frac{E_i}{\rho_i}e^{-\frac{\tau}{\rho_i}}d\tau = -D_0\sum_{i=1}^{M}E_i\left(1-e^{-t/\rho_i}\right)$$

$$-\int_0^t \sum_{j=1}^{N} D_j\left(1-e^{-\frac{t-\tau}{\tau_j}}\right)\sum_{i=1}^{M}\frac{E_i}{\rho_i}e^{-\frac{\tau}{\rho_i}}d\tau = -\sum_{j=1}^{N} D_j\sum_{i=1}^{M}\frac{E_i}{\rho_i}\int_0^t\left(e^{-\frac{\tau}{\rho_i}}-e^{-\frac{t}{\tau_j}+\frac{\tau}{\tau_j}-\frac{\tau}{\rho_i}}\right)d\tau$$

Denote and note that

$$\varphi_{ij} \equiv \int_0^t\left(e^{-\frac{\tau}{\rho_i}}-e^{-\frac{t}{\tau_j}+\frac{\tau}{\tau_j}-\frac{\tau}{\rho_i}}\right)d\tau = \rho_i\left(1-e^{-\frac{t}{\rho_i}}\right)-e^{-\frac{t}{\tau_j}}\frac{\rho_i\tau_j}{\rho_i-\tau_j}\left[\exp\left(t/\tau_j-t/\rho_i\right)-1\right]$$

$$= \rho_i\left[1-\exp\left(-t/\rho_i\right)\right]+\frac{\rho_i\tau_j}{\rho_i-\tau_j}\left[\exp(-t/\tau_j)-\exp\left(-t/\rho_i\right)\right]$$

$$= \rho_i+\frac{\rho_i\tau_j}{\rho_i-\tau_j}\exp(-t/\tau_j)-\frac{\rho_i^{\,2}}{\rho_i-\tau_j}\exp\left(-t/\rho_i\right)>0 \quad \text{for } \rho_i\neq\tau_j$$

and

$$\varphi_{ij} \equiv \int_0^t\left(e^{-\frac{\tau}{\rho_i}}-e^{-\frac{t}{\tau_j}+\frac{\tau}{\tau_j}-\frac{\tau}{\rho_i}}\right)d\tau = \rho_i\left(1-e^{-\frac{t}{\rho_i}}\right)-e^{-\frac{t}{\tau_j}}t>0 \quad \text{for } \rho_i=\tau_j$$

We then obtain

$$\varphi_{ij}=\begin{cases}\rho_i+\dfrac{\rho_i\tau_j}{\rho_i-\tau_j}\exp(-t/\tau_j)-\dfrac{\rho_i^{\,2}}{\rho_i-\tau_j}\exp\left(-t/\rho_i\right)>0 & \text{when } \rho_i\neq\tau_j\\ \rho_i\left(1-e^{-\frac{t}{\rho_i}}\right)-e^{-\frac{t}{\tau_j}}t>0 & \text{when } \rho_i=\tau_j\end{cases} \tag{5.5.8}$$

Putting the above together we can have

$$\sum_{i=1}^{M}\left[\sum_{j=1}^{N} D_j\left(1-e^{-t/\tau_j}-\frac{\varphi_{ij}}{\rho_i}\right)+D_0e^{-t/\rho_i}\right]E_i = 1-\left[D_0+\sum_{j=1}^{N} D_j\left(1-e^{-t/\tau_j}\right)\right]E_\infty \tag{5.5.9}$$

Equation (5.5.9) has to be satisfied for any $t \in (0, \infty)$, approximations can be made by choosing a number (p) of specific time instants so that the above equality holds. If the number p is equal to the number of unknowns (M), then a system of linear equations can be constructed and solved to obtain exactly a unique solution of E_i. If p is larger than M, i.e. the number of equations are greater than the number of unknowns, then minimization techniques (e.g. least squares) are to be employed to find the optimum solution. This problem-solving technique is called the collocation method. It generally works well even though in some scenarios one or two coefficients are negative. Note that for the unknown E_i, the ρ_j are pre-specified and thus φ_{ij} are known constants. Written in matrix form, the resulting linear equations are

$$A_{ki}E_i = R_k \tag{5.5.10}$$

where

$$A_{ki} = \sum_{j=1}^{N} D_j \left(1 - e^{-\frac{t_k}{\tau_j}} - \frac{\varphi_{ij}}{\rho_i} \right) + D_0 e^{-\frac{t_k}{\rho_i}} > 0 \tag{5.5.11}$$

$$R_k = 1 - \left[D_0 + \sum_{j=1}^{N} D_j \left(1 - e^{-\frac{t_k}{\tau_j}} \right) \right] E_\infty > 0 \tag{5.5.12}$$

The retardation spectra plotted in Figure 5-27 with the parameter D_0 are now converted to corresponding relaxation spectra. The resulting parameters E_∞ are shown in Figure 5-29, and the relaxation spectra are all plotted together in Figure 5-30 to check the similarity. As shown in Figure 5-29 that the converted equilibrium modulus exhibit a clear and consistent decreasing trend with increase in deviatoric stress and decrease in the confinement. As for the converted relaxation spectra, from Figure 5-30 it can be seen that except the replicate denoted by “70-20 #1” all the other spectra seem to have the same size and shape. Note that even though the retardation spectrum is assumed to follow the log-normal distribution, the relaxation spectrum from conversion usually does not. Thus, given the large test variability usually seen in CCR tests, it is believed feasible and much more convenient to use a single relaxation spectrum and stress condition dependent equilibrium moduli to describe the material viscoplastic properties.

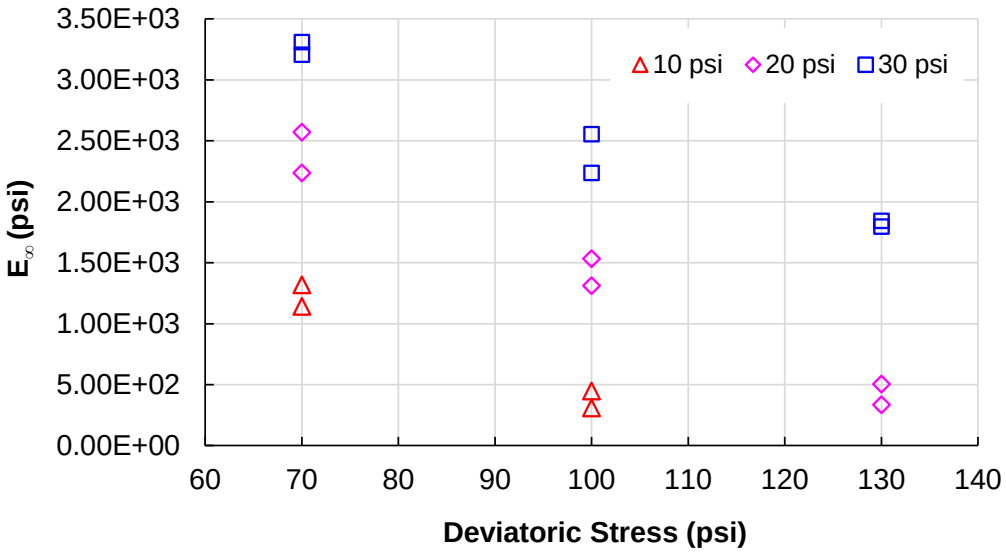

Figure 5-29 Converted long-term modulus from the optimized viscoplastic compliance functions for all stress conditions.

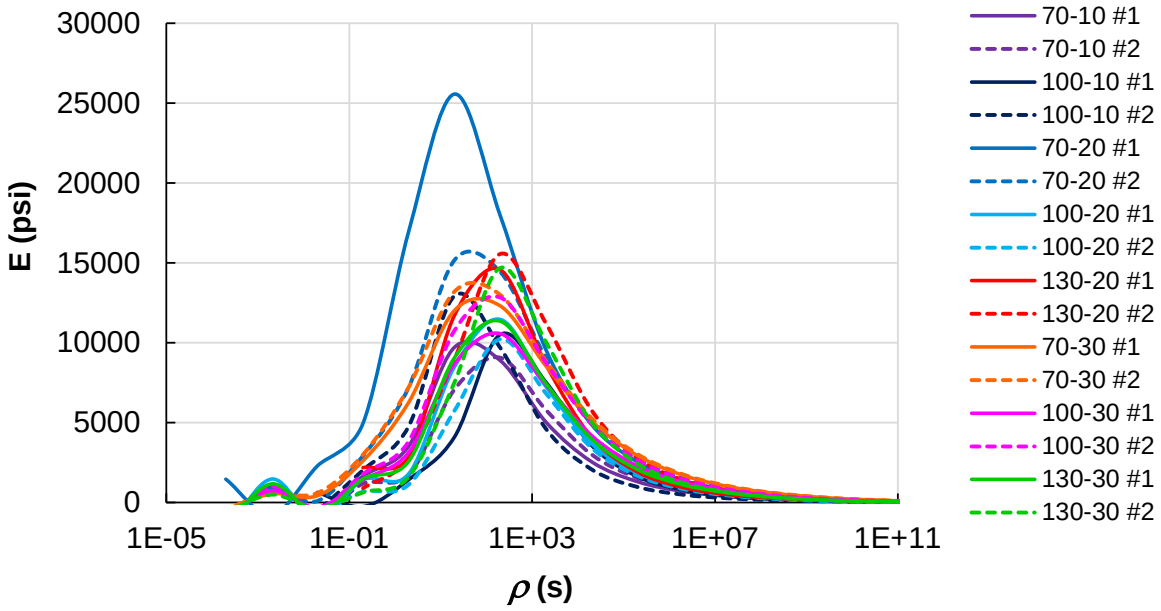

Figure 5-30 Converted relaxation spectra from the optimized viscoplastic compliance functions for all stress conditions (70-10 #1 indicates 70 psi deviatoric stress, 10 psi confinement, and replicate #1).

5.5.2 Final model form

Based on the above observations, the new model form and the computation procedures are now summarized in the following. The viscoplastic strain is obtained from the convolution-type model as presented in Equation (5.3.4):

$$\varepsilon_{vp}(t) = \left\langle \int_{0^-}^{t} D(t-\tau)\frac{d\sigma_d(\tau)}{d\tau}d\tau \right\rangle \tag{5.5.13}$$

Note that the subscript "*d*" has been added to the stress term explicitly indicating the use of the deviatoric stress. The compliance function $D(t)$ takes the Prony representation as usual:

$$D(t) = D_0 + \sum_{j=1}^{M} D_j \left(1 - e^{-\frac{t}{\tau_j}}\right) \tag{5.5.14}$$

Here, unlike the previous assumption of a log-normal function regarding the distribution of retardation times, the model parameters are now switched to those for the relaxation spectrum, i.e., E_∞ and E_i. Again, in order to reduce the number of unknowns the relaxation spectrum is assumed to follow another log-normal distribution:

$$E(x) = \Delta E \cdot \Psi(x) = \Delta E \cdot \frac{1}{\theta\sqrt{\pi}} e^{-(x/\theta)^2} \quad \text{with } x = \ln(\rho / \rho_m) \tag{5.5.15}$$

where $\Psi(x)$ is the standard log-normal function, ΔE acts as a scaling factor, ρ_m denotes the mean relaxation time, and θ measures the distribution width. Basically all these parameters share very similar significances as their counterparts for the retardation function in Equation (5.3.2). The viscoplastic behaviors of asphalt mixtures can now be fully characterized by a single viscoplastic relaxation spectrum and an equilibrium modulus which is dependent on the stress condition.

Once the model parameters (E_∞, ΔE, ρ_m, θ) are given, the relaxation function Equation (5.5.3) is then determined. And the compliance function Equation (5.5.14) can then be found by converting the relaxation spectrum to the retardation spectrum. Note that here a reversed conversion is required as compared to the steps presented in Section 5.5.1. The detailed procedures are listed in APPENDIX D.

5.6 Parameter Calibration of the Improved Viscoplastic Model

With the final model form all the CCR test data are utilized to calibrate the parameters: ΔE, ρ_m, θ, and E_∞. It should be pointed out that the first three, ΔE, ρ_m, θ, remain the same while only E_∞ changes with the stress state. That is to say, the viscoplastic relaxation spectrum is assumed as a material intrinsic property irrespective of the mechanical condition; the effect of stress condition (deviatoric stress and confinement) is reflected through E_∞ alone. The data of two replicates are first averaged for each stress condition and then the resulting 9 sets of strain histories (combination of 3 deviatoric stresses and 3 confining pressures) participate in the numerical optimization simultaneously. The optimized values are listed in Table 5-4 for the first three parameters, and in Table 5-5 for E_∞ at each stress condition.

Table 5-4 Calibrated Parameters for All Stress Conditions

ΔE (psi)	$\ln(\rho_m)$	θ
2.003E+05	1.558	6.606

Table 5-5 Calibrated Parameter E_∞ for Each Stress Condition

σ_d (psi)	σ_c (psi)	E_∞ (psi)
70	10	2291
70	20	6130
70	30	7996
100	10	1293
100	20	3310
100	30	6082
130	10	0
130	20	2710
130	30	4437

The combined effect of the deviatoric stress and confinement is reflected through E_∞ and thus the relationship between E_∞ and the stress conditions remains to be sought, and for this purpose the data list in Table 5-5 are explored. Fortunately, the following consistency can be observed: for the same deviatoric stress level E_∞ increases with the confinement, and for the same confinement level E_∞ decreases with the increase in deviatoric stress. This relation agrees with common experimental trends. Increase in E_∞ causes shrinkage in the retardation spectrum thus generating less viscoplastic strain according to the model, while increase in confinement and/or decrease in deviatoric stress will also lead to reduction in permanent strain in experiments.

Various function forms have been tried with the following conception born in mind. First, analytically it can be easily seen that reduction in confinement is equivalent to increase in deviatoric stress in terms of the amount of the permanent strain generated, which should be demonstrated via the E_∞ expression. Secondly, for the purpose of scalability and potential use in three-dimensional pavement structure analysis, the deviatoric stress and confinement are better to be expressed in the form of stress invariants. It is finally discovered that E_∞ can be well characterized by the ratio of the two stress invariants (similar to the previously mentioned triaxiality ratio): I_1 and σ_{vM} as expressed in Equation (2.4.4). As illustrated in Figure 5-31 below, a logarithmic function is capable to fit E_∞ for all the stress conditions.

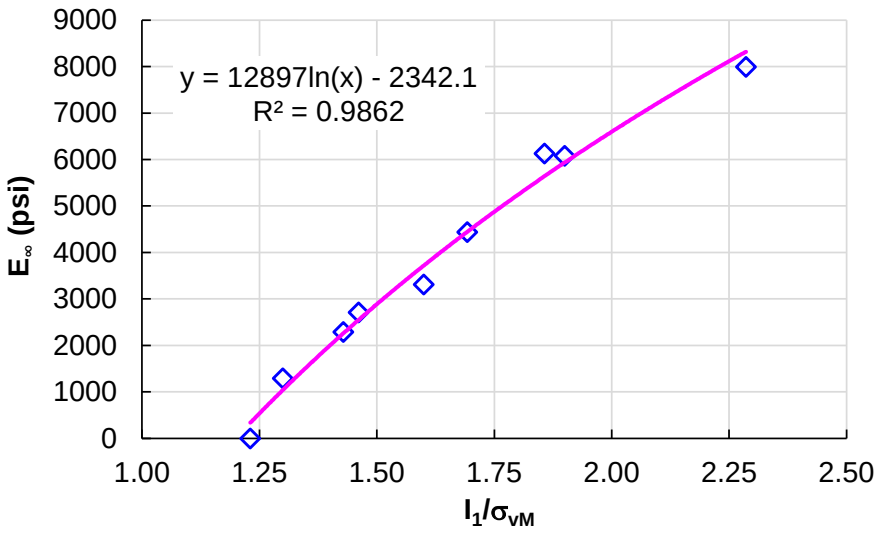

Figure 5-31 Relation of E_∞ versus the ratio of first stress invariant and von Mises stress for all stress conditions.

5.7 Verification of the Convolution-type Viscoplastic Model

The calibrated improved convolution-type viscoplastic model is finally verified via random loading tests. The deviatoric stress history is the same as that used to verify the extended incremental-shift model. Since the viscoplastic model is calibrated at only a single temperature (48°C) and thus the verification tests are supposed to be run at the same temperature as the model parameters are inherently temperature dependent. Two random loading tests are performed at different confinement levels: 15 and 25 psi.

Since the model assumes that the variation in material viscoplastic property is fully described by E_∞ which is dependent on the stress state, each cycle in the verification test should have its own E_∞ value as the peak deviatoric stress varies even though the confinement is kept the same throughout. Therefore, in the numerical implementation the material property is allowed to update in a cyclic manner instead of at each time increment or computation step, which is expected to endow the model with higher efficiency and reasonable accuracy. Another important point should be made regarding the translation of E_∞ between cycles. Note that E_∞ is not changed immediately upon the beginning of the next

loading cycle. Rather, the translation of E_∞ in a cycle occurs right at the moment when the applied deviatoric stress is greater than the corresponding back stress (recall Figure 2-12).

The experimental permanent strain histories as well as the predicted histories from the viscoplastic model are shown in Figure 5-32 below. Despite the presence of some numerical noises due to computational complexities, the predicted deformation history agrees very well with the experimental data under each confinement level.

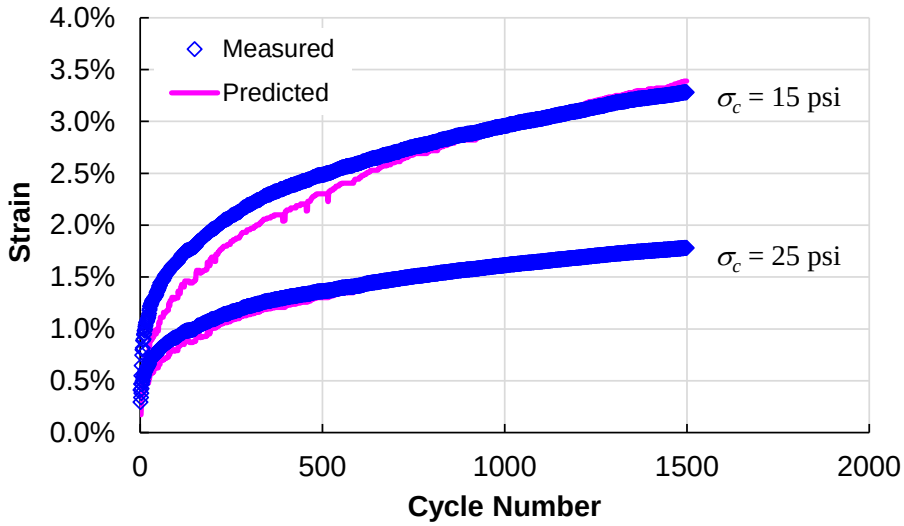

Figure 5-32 Measured and predicted strain history by the improved convolution-type viscoplastic model for random loading tests at 48°C.

5.7.1 Model Calibration and Verification on a Different Mix

After the successful application on the VT0% mix, the model is then tested on a second mix, which is the Control mixture used in the FHWA ALF project (see Section 6.2 for project overview). The CCR tests with three different pulse times (0.1, 0.4, 1.6 seconds), three deviatoric stress levels (90, 120, 150 psi), and 100 second rest period as well as the random loading tests have been respectively used in developing and validating the original convolution-type viscoplastic model by Subramanian (2011). The confinement level is 20 psi

for all the tests, and the testing temperature is 54°C. Compared to the VT0% mix, the FHWA ALF Control mix has a higher high temperature PG grade (PG 70-22) and a coarser aggregate gradation (Figure 5-33). In the following, the CCR tests with 0.4 second pulse duration and different deviatoric stresses are employed for the model calibration, while the random loading tests are used for verification and the other CCR tests with 0.1 and 1.6 second pulse durations are used to examine the pulse time effect on the model behavior.

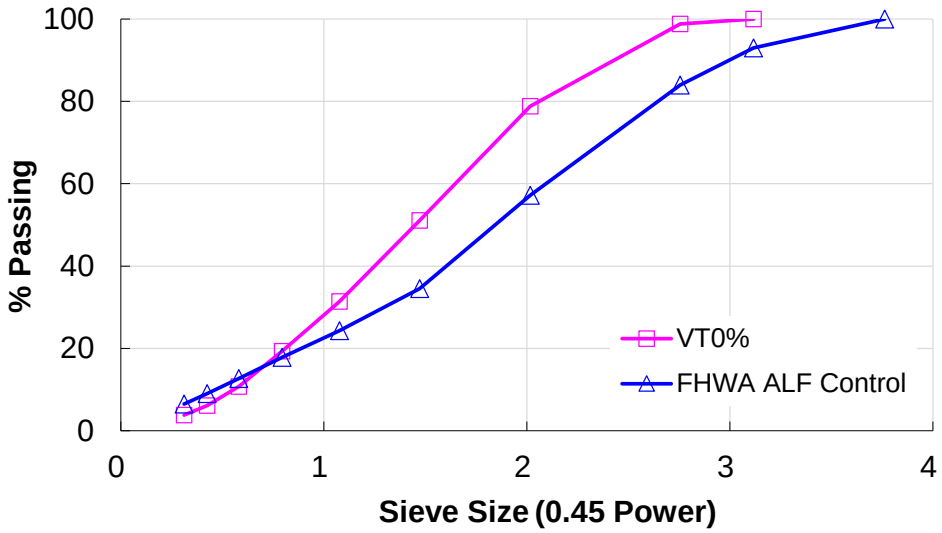

Figure 5-33 Aggregate gradation of the FHWA ALF Control mix compared to the VT0% mix.

The test data with 0.4 second pulse duration and the model fits are presented in Figure 5-34. The calibrated model is then applied to predict the strain histories in other CCR tests with 0.1 and 1.6 second pulse durations. See Figure 5-35 for the measured and predicted strains. As the pulse time differs, the strains are plotted against the cumulative load time instead of the cycle number. In the original model, the effect of pulse time is captured through the use of two stress functions (Equation (2.6.7)) and two convolution integrals (Equation (2.6.5)). However, as shown in Figure 5-35 a general overprediction is observed

for the tests with 0.1 second pulse time and underprediction for 1.6 second pulse time. Therefore, it is implied that in the improved model the parameters are inherently dependent on the pulse duration.

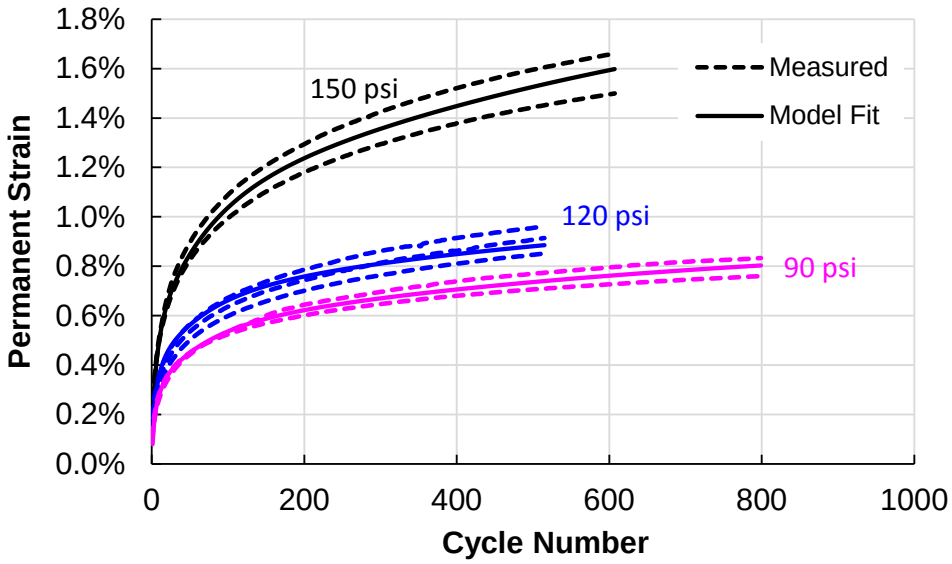

Figure 5-34 Model calibration on the FHWA ALF Control mix using CCR test data at 54C and 20 psi confinement with different deviatoric stress levels.

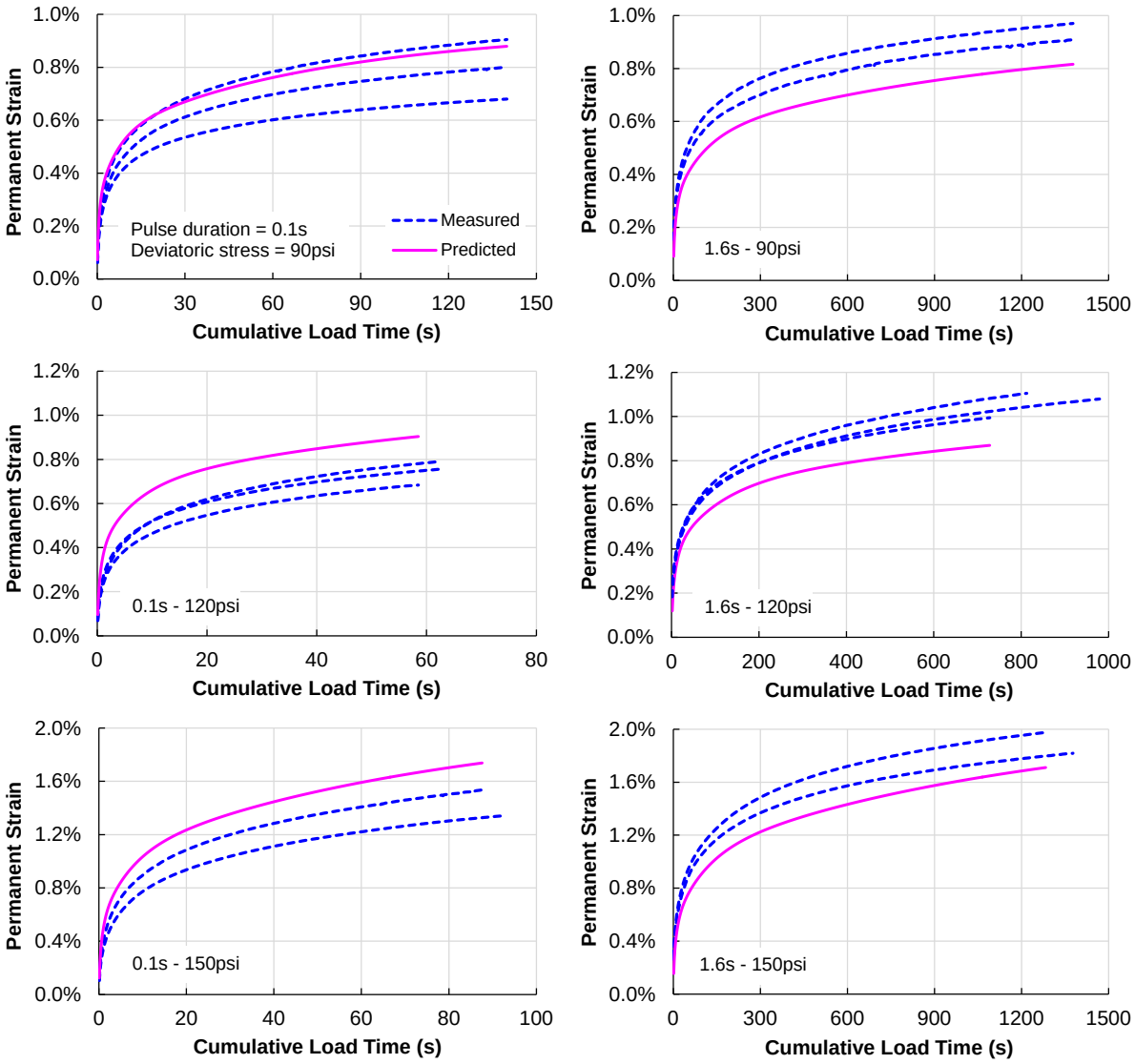

Figure 5-35 Measured and predicted strain histories of CCR tests on FHWA ALF Control mix with 0.1s and 1.6s pulse durations at different deviatoric stress levels.

In the next step, the calibrated model is used to predict the strains in the random loading test as a further verification. As mentioned in the above, the random loading test is conducted at the same confinement (20 psi) and temperature (54°C) with the CCR tests. The deviatoric stress history is different than that used previously for the verifications on the VTa0% mix. Here, in the random loading test three pulse times (0.1, 0.4, 1.6s) and three

deviatoric stress levels (90, 120, 150 psi) are randomly combined and then assigned to each cycle. The frequency of occurrence of each condition is illustrated in Figure 5-36. The predicted strain history is plotted in Figure 5-37 with the measured data from the two replicates. The prediction matches the measurements very well and has a slight improvement compared to the original model. Compared to the model predictions in the CCR tests with fixed pulse times (Figure 5-35), the random loading test appears to be more tolerant to the variation in pulse time. This reduced sensitivity helps to blur the effect of pulse duration and thus a satisfactory agreement can still be observed in the random loading test despite that the model is calibrated at a single pulse time. As the random loading test simulates the real traffic loading more closely than the CCR test, it is reasonable to conclude that the successful applications on both VT0% and FHWA ALF Control mixes have demonstrated the model capability on predicting the permanent deformation behavior in asphalt concrete.

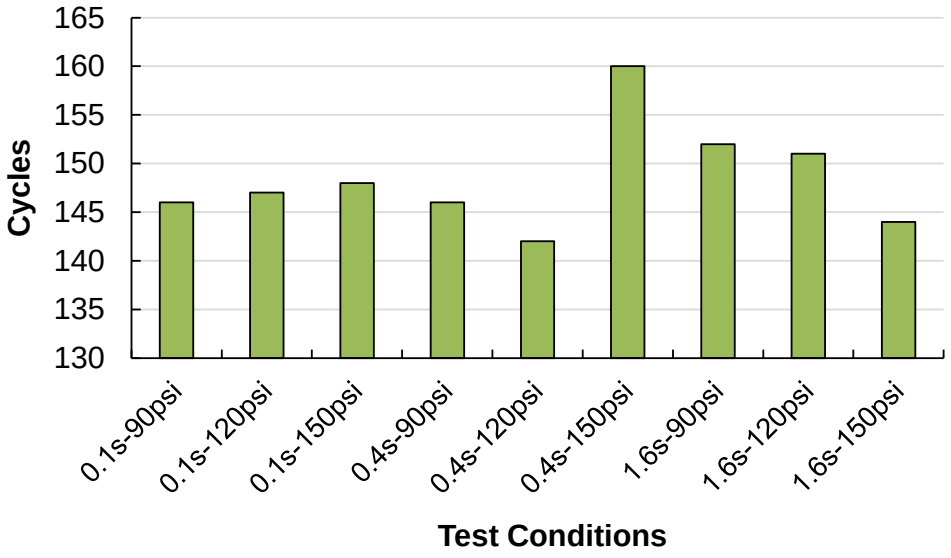

Figure 5-36 Frequency of occurrence of test conditions in the random loading test on the FHWA ALF Control mix.

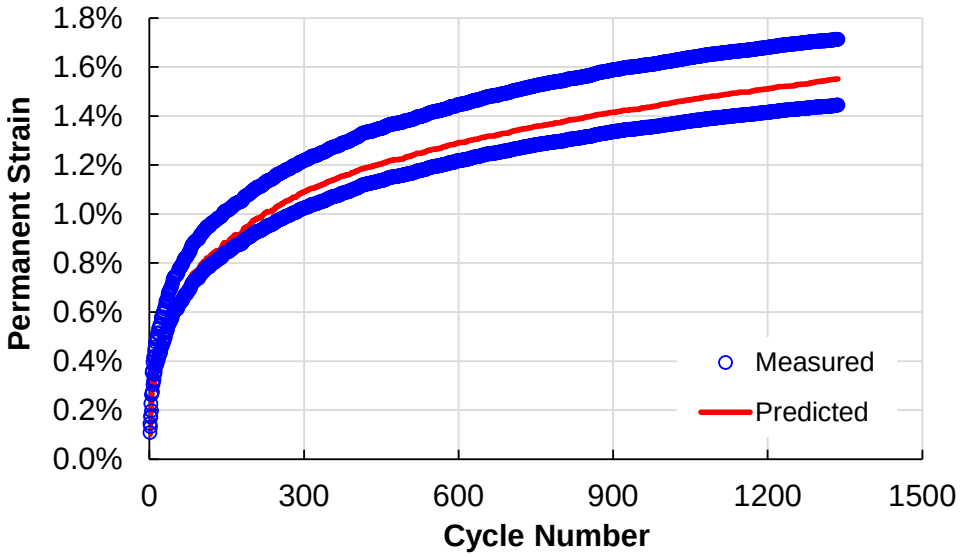

Figure 5-37 Measured and predicted strain histories in the random loading tests on the FHWA ALF Control mix.

CHAPTER 6 SHEAR RELATED TRANSFER FUNCTION AND FIELD PREDICTION IMPROVEMENTS

6.1 Finite Element Implementation and Numerical Examples

6.1.1 Implementation of rigorous viscoplastic models

Finite element analysis requires first the discretization of the pavement structure so that the material constitutive relation can be applied at each material node to calculate stress and strain responses at each step. For linear viscoelastic materials, even though history dependence is involved, the nodal responses at each time step can be directly updated via the previously mentioned state variable method (Simo and Hughes 1998) with satisfactory accuracy so that the time-consuming iteration process is avoided. However, once the material should be considered as viscoplastic the whole situation becomes much worse. First, due to the model inherent complexity iteration at each time step is required for solving stresses and strains. Secondly, given the common vehicle speed a small time increment (especially for highway simulations) should be chosen to guarantee an accurate computation under traffic loading. And finally, unlike viscoelastic materials in the case of pavement simulation where material property can be approximated as unchanged and deformation fully recovered after the rest period between the pass of two vehicles, viscoplastic materials will accumulate the deformation as well as the irreversible property changes. A direct consequence is that the analysis time period will be as long as the design life of the pavement which can be 15 to 20 years. Therefore, if a pavement cross section is to be analyzed, the combined effort required for tens of thousands of material nodes, literally countless small time increments, and the numerical iteration at every time increment would be daunting and prohibitively expensive. It is thus believed that for the time being any rigorous viscoplastic model attempting to simulate the cyclic and discontinuous traffic loading should be developed with the prior aim to understand the material behavioral characteristics under different mechanical and environmental loading conditions. And there is still a long journey lying in front of us before we can directly implement such constitutive relationships into finite element pavement analyses for permanent deformation.

6.1.2 Implementation of the extended incremental-shift model

The following simulation scheme has been widely adopted as a compromise but feasible solution. By excluding the viscoplasticity materials are now treated as elastic or viscoelastic. Consequently, response analysis does not suffice; the performance analysis as a second step is called for. The extended incremental-shift model is implemented into LVECD and takes the viscoelastic stresses and strains from the first step response analysis as model inputs to make predictions on the time history of viscoplastic strain at each material node.

In order to check the model performance, two typical pavement structures with different thicknesses are tested. The base and subgrade inputs are the same for the two structures: 10 in. aggregate base with Young's modulus as 40000 psi, and 255 in. subgrade with a modulus of 10000 psi. The thin pavement has 4 in. asphalt layer and for the thick case it is 15 in. The parameters for the time-temperature shift factor function and the Prony series are listed in Table 6-1 and Table 6-2, respectively. The extended incremental-shift model as well as the calibrated parameters have been presented in Section 5.2 (see Equation (5.2.6) and Table 5-2). The original incremental-shift model is expressed by Equation (2.6.9) and the calibrated model parameters using TSS test data at 10 psi confinement are listed in Table 6-3. The same temperature profiles as used in determining the stress conditions for CCR tests in Section 3.4 are employed here. See Figure 3-3 for the pavement surface temperature for a perception of the climate condition used.

Table 6-1 Time-Temperature Shift Factor Function and Parameters for VTa0% (SI)

Reference Temperature	Function Form	a_1	a_2	a_3
5°C	$\log(a_T) = a_1 T^2 + a_2 T + a_3$	7.479E-4	-0.168	0.820

Table 6-2 Parameters of the Prony Series for VTa0% (SI)

E_∞ (kPa)	145000						
E_i (kPa)	2E+10	2E+9	2E+8	2E+7	2E+6	2E+5	2E+4
τ_i (s)	6720	4800	8340	14700	26700	49900	97900
E_i (kPa)	2E+3	2E+2	2E+1	2E+0	2E-1	2E-2	2E-3
τ_i (s)	202000	430000	896000	1710000	2580000	3000000	2750000
E_i (kPa)	2E-4	2E-5	2E-6	2E-7	2E-8	2E-9	2E-10
τ_i (s)	2110000	1440000	917000	555000	329000	192000	256000

Table 6-3 Calibrated Parameters of the Original Incremental-Shift Model (SI)

Incremental Model Function					
A	B	C	α		
0	0.00218	0.735	0.727		
Shift Factor Functions					
p_1	p_2	b_1	b_2	b_3	p_a (kPa)
0.684	1.070	-34.745	-0.0827	29.453	101.325

The major limitation with the two incremental-shift models lies in the narrow range of confinement used in model calibration. The original form is strictly applicable to only 10 psi confinement, while the extended form can be used for 10 ~ 30 psi confining levels. In the actual pavement, however, the horizontal compressive stresses can be very low or even negative (i.e. tensile) especially at the bottom of asphalt layer for thin pavements. As an example, the horizontal stresses (σ_{xx} and σ_{yy}) serving as the approximation to confinement for the 4 and 15 in. asphalt pavements are obtained for a relatively warm temperature profile under 110 psi (758 kPa) tire-pavement contact pressure, and are now plotted along depth together with corresponding vertical stresses in Figure 6-1. It is seen that extreme horizontal

stresses (around ±218 psi or ±1500 kPa) are present on the top and bottom of the 4 in. asphalt layer. Comparatively, the stresses for the thick pavement are rather moderate, ranging from 102 psi (700 kPa) at the top to -16 psi (-110 kPa) at the bottom. It is worth mentioning that for colder temperature profiles the horizontal stresses are expected to be more extreme.

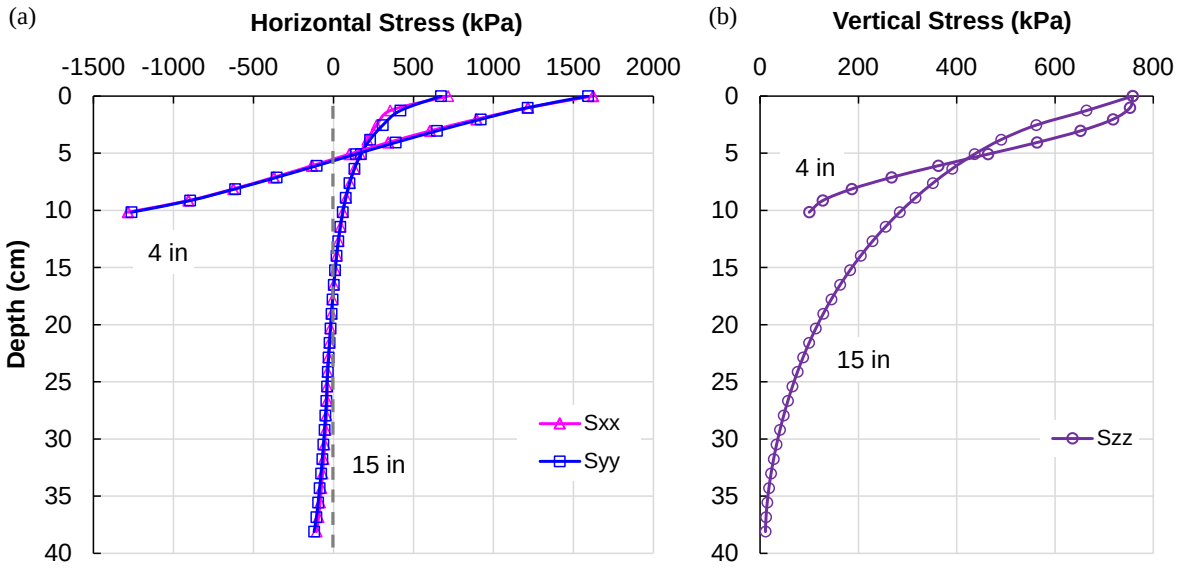

Figure 6-1 Normal stresses calculated from LVECD for the 4 and 15 in. asphalt pavements (compressive treated as positive): (a) horizontal stresses, and (b) vertical stress.

Inside LVECD, when the original incremental-shift model is activated, it is assumed that viscoplastic strain vanishes for material nodes with zero or negative confinement whereas for nodes with positive confinement, the model is applied to calculate viscoplastic deformation. As negatively confined materials tend to be more susceptible to deformation, certain errors are expected with this simplification especially in the thin pavement case. When the extended model is activated, two options are attempted. First, the calculated confinement is directly plugged into the model for the permanent strain calculation. Secondly, for nodes with negative confinement, 0 psi is used instead of the calculated

confinement. The above three methods are applied to both pavements and the rut depth evolution histories for 5 years are presented in Figure 6-2.

Obviously, the rut depth calculation using the extended model gives an unrealistic history for the thin pavement; there is a jump at the tenth month of every year, the time corresponding to the coldest month in the year according to Figure 3-3. Conversely, the rut evolution history for the thick pavement appears to be reasonable for both model forms. The consistent jump of rut depth at every coldest month as shown in Figure 6-2(a) first suggests the possible inappropriateness of extrapolating the model for the extreme confinements at the surface and bottom of the thin asphalt layer.

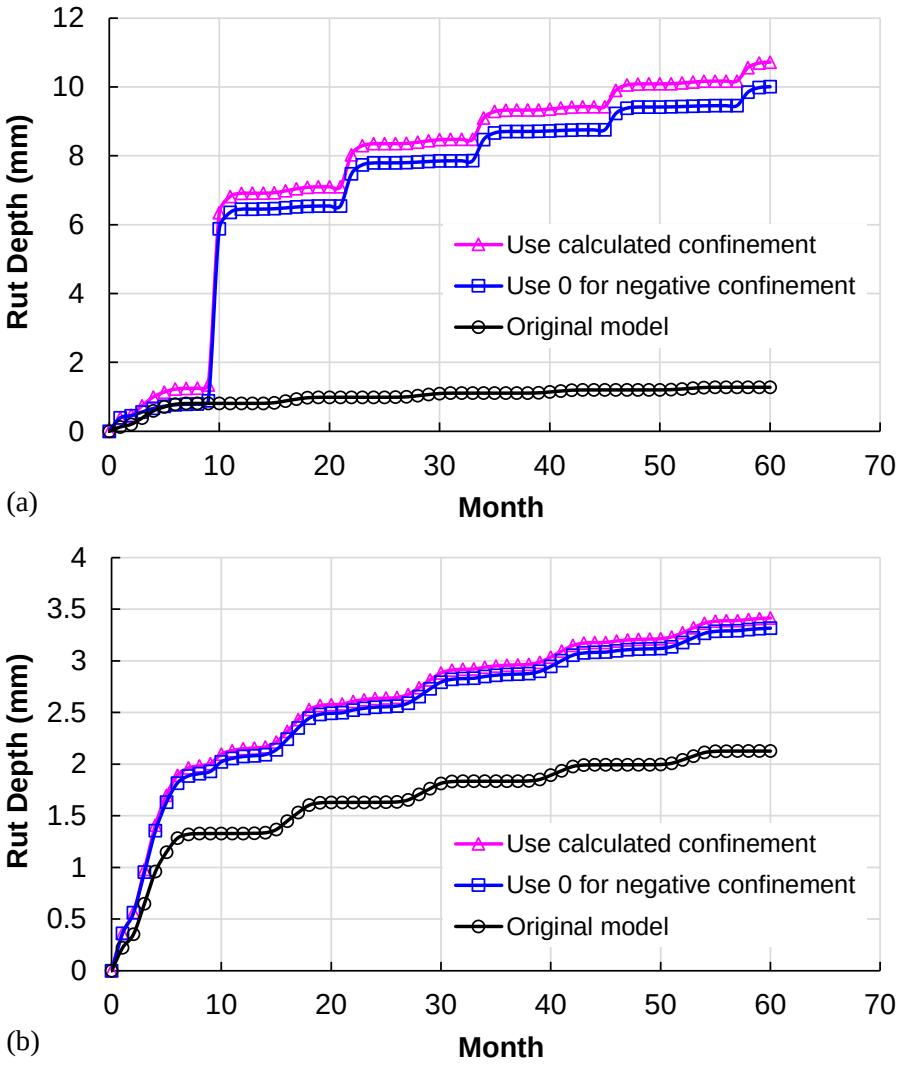

Figure 6-2 Rut depth evolutions in the asphalt layer using three methods for the two cases investigated: (a) 4 in., and (b) 15 in.

Also note that when 0 psi is used for all the negatively confined material nodes, the resulting rut depth history is rather similar to the case when the calculated confinement is directly used. This observation indicates the insensitivity of the extended model to negative confinement and that the jump in the rut depth may actually contributed by the materials with positive confinement. Yet, in both cases the extended model gives higher rut values than the

original one, which is believed as due to a more realistic characterization of the effects from positive confinements especially the low confining levels.

The remaining part of this section is devoted to the investigations of the jump in the predicted rut depth with the extended model. As will be detailed in Section 6.5, in LVECD the temperature input is processed so that a constant temperature profile is generated for each time segment. The segment is the basic analysis period and the default setting is that every month is decomposed into three segments with the same length. So for a one-year analysis we should expect 36 data points of stress/strain responses or permanent strain for each material node. Thus, we first extract the time histories of the reduced pulse time, deviatoric stress, and confinement for the material nodes beneath the tire center as these three are the independent variables in the extended function of a_{total}. In the current analysis, the 4 in. asphalt layer is divided into 10 sublayers. The histories of a_{total} and the three variables are now presented in Figure 6-3 for the selected nodes beneath the tire center.

As can be seen in Figure 6-3(a) the upper portion of the asphalt layer is responsible for the jump in the rut depth, which explains the insensitivity of the model to the negative confinements as shown in Figure 6-2. This jump is accompanied with the abrupt drop in the reduced pulse time and increase in confining pressure at Month 10. In addition, certain extrapolations have been used in the pavement simulation. For example, the extended model is calibrated using the TSS data with reduced pulse time ranging from 1E-6 to 1E-1 seconds, whereas from the pavement response analysis the obtained reduced time range is [1E-10, 1E-4] seconds. Likewise, for the confinement, the extrapolation is also required from the range of [10, 30] psi to [-218, 290] psi for the confinement. It is therefore speculated that the reduced pulse time and the confinement should be the reason for the abrupt rut depth jump. To check this inference the first six terms at the right hand side of the equal sign in the total shift factor function in Equation (5.2.6) are calculated for the material node at pavement surface beneath the tire center and are shown in Figure 6-4. It is obvious that the term #6 is the source of the abrupt increase in the total shift factor as it is proportional to the multiplication of the confinement and the logarithm of reduced pulse time. Comparatively, when the improved incremental-shift model is used, the total shift factor for the same

material point together with the contributions from the vertical stress and reduced pulse time is plotted in Figure 6-5. Clearly, in this case the reduced pulse time dominates the behavior of the incremental-shift model and thus the rut depth prediction. The calculated history of the total shift factor follows the same trend as the reduced pulse time while this trend is consistent with the temperature history used in the analysis. As a result, at high temperatures the rut depth increases quickly whereas during low temperatures the rut barely evolves.

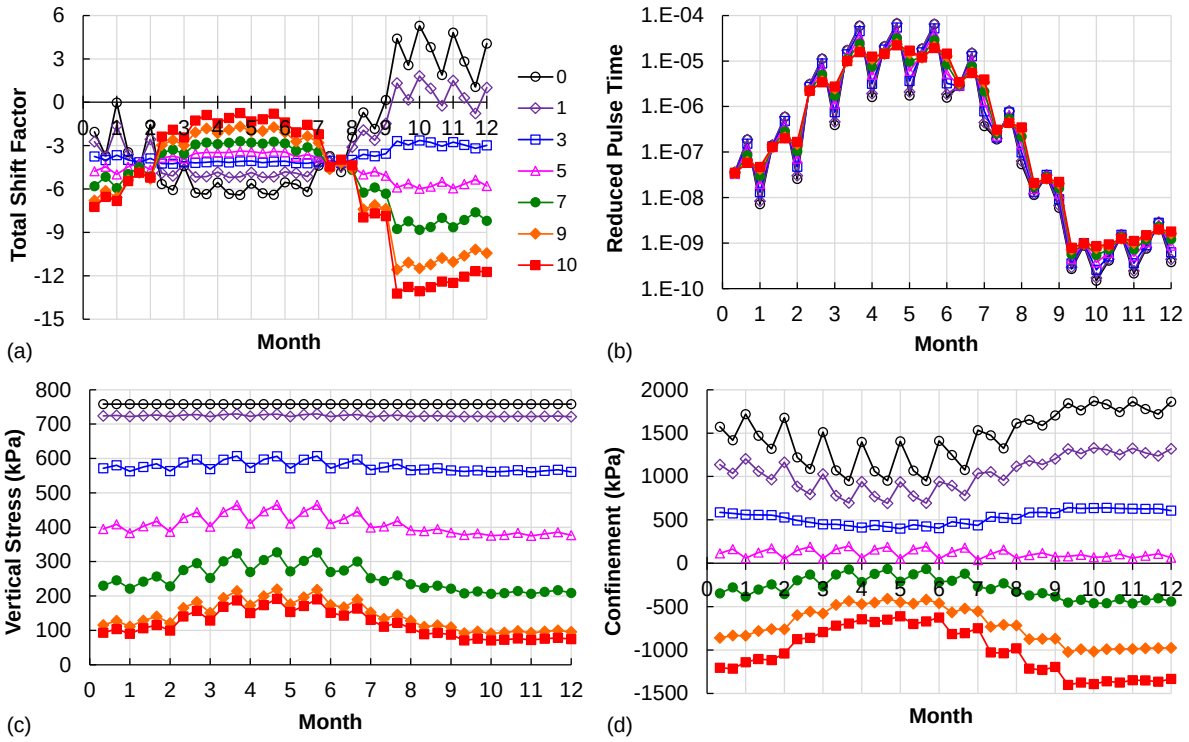

Figure 6-3 Variables calculated for the 4 in. pavement at selected depths (cm) for: (a) total shift factor, (b) reduced pulse time, (c) vertical stress, and (d) confinement.

Attempts such as dropping this term in the total shift factor function have been proved to be helpless as in the process of model parameter optimization more weight of confining pressure and reduced pulse time will be transferred to other terms involving each when term #6 is eliminated, and the resulting function will still predict a jump in the shift factor at the

coldest month. In fact, the laboratory test data present a linear relationship between the total shift factor and the confining pressure within the investigated range (10 ~ 30 psi) for a given reduced pulse time and deviatoric stress level. However, based on previous observations within the full range of confinement in the real pavement the total shift factor is supposed to be nonlinear with respect to the confinement. As for the limited range of the available laboratory data any assumed nonlinear functional form lacks a sound reason, further improvement on the extended model would require additional data with wider ranges of reduced pulse time and confining pressure.

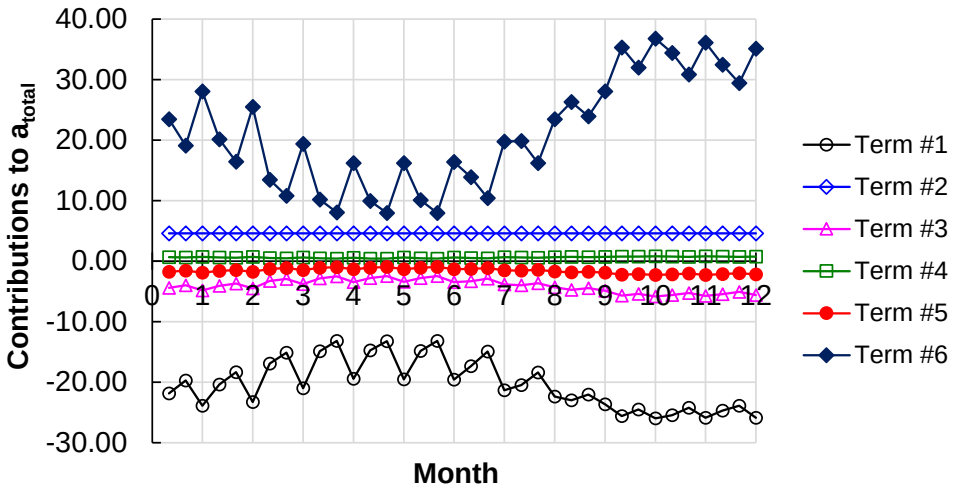

Figure 6-4 Individual contributions to the total shift factor at pavement surface from the first six terms in the extended function expressed in Equation (5.2.6).

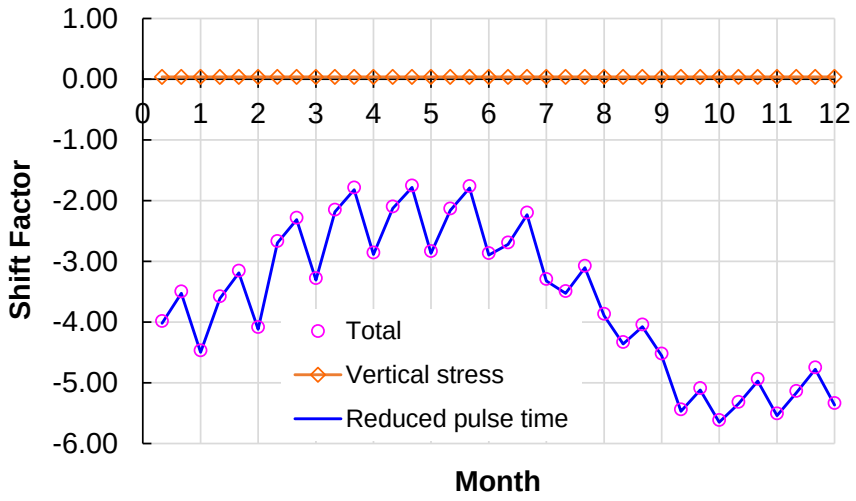

Figure 6-5 The total shift factor at pavement surface and the individual contributions from the vertical stress and reduced pulse time in the improved function in Equation (5.2.1).

In order to expand the laboratory data range and minimize the extrapolations, lower test temperatures with shorter pulse times can be adopted to arrive at lower reduced pulse times. As for the positive confinement, higher pressures will bring about challenges to the rigidity of the triaxial cell. On the other hand, to achieve the negative confinement a new triaxial cell equipped with a vacuum pump has to be developed, or the triaxial extension test can be performed as a possible circumvention. More importantly, with low or negative confinement the specimen can easily enter the tertiary flow stage with large and instable deformation, which invalidates the incremental model form that is suitable only for the primary and secondary stage and serves as the cornerstone of the incremental-shift model. Another aspect on the model improvement lies in the introduction of material strength or modulus into the modeling framework. Currently, the incremental-shift model is based on the stress alone without the presence of strain or material strength/modulus, which is also responsible for the jump in rut depth at the coldest time since low temperature produces higher stress responses. Given the current situation, compromise is again employed and the incremental-shift model with the improved total shift factor function is retained in LVECD for rut depth predictions.

6.2 LVECD Rut Predictions on Field Sections

The finite element program LVECD with the original incremental-shift model is now applied to the two full scale test sections denoted as FHWA ALF and NCAT. The material characterization and rut prediction for the two projects have been accomplished respectively by Choi (2013) and LaCroix (2013) in their dissertation researches. The motivation of re-running the rut simulation first lies in the change of the function form for the reduced load time shift factor (compare Equation (5.2.1) to (2.6.9)). The second rational involves the attempt to improve the current prediction by empirically incorporating the contribution from shear deformation, which will be presented in subsequent sections. In this section, the two projects are briefly reviewed and then the rut depth predictions with the current form of the incremental-shift model are produced. Detailed information regarding materials, pavement structures, environmental and traffic loading conditions can be found in the dissertations by Choi (2013) and LaCroix (2013).

6.2.1 FHWA ALF test sections

6.2.1.1 Project overview

The FHWA ALF (Federal Highway Administration Accelerated Loading Facility) project contains six different asphalt mixtures (without RAP), among which the aggregate type and gradation are maintained the same with the binder type being the only variable. Totally four types of binder, denoted as Control (base asphalt, unmodified PG 70-22), SBS-LG (base asphalt modified by linearly grafted SBS), CR-TB (modified by crumb rubber, terminal blended), and Terpolymer (modified by reactive Terpolymer), are used in the study at NCSU. For each mix, both thin (100 mm) and thick (150 mm) pavement structures are constructed on top of unbound dense-graded crushed aggregate base over the uniformly compacted subgrade. The tire-pavement contact pressure is 100 psi (689 kPa) and the pavement temperature (45°, 64°, 74°C) is kept constant during testing. Traffic wander is not present in the field rutting test. Rut depth is measured at certain time intervals as the downward displacement from the original pavement level with lateral upheaval excluded.

In the following analysis some test sections are not involved. First, all the field tests at 74°C are excluded because all 74°C sections are naturally aged for over 3 years before testing compared to 0.3 ~ 1.5 years of aging for 64°C sections. This extended aging life for 74°C sections directly yields a consistent lower rut depth than their 64°C counterparts with the same structure design and materials (Gibson *et al*. 2011). Given that aging effect characterization is beyond the scope of the present research, the data for tests at 74°C are not used. Note that even though some of the 45°C sections are naturally aged for 3.9 years, the data are still included in the analysis assuming the aging effect is less significant for this lower temperature. Secondly, the data for all the Terpolymer sections with 100 mm thickness are deemed as unreliable due to abnormally greater water absorption (Gibson *et al*. 2011). Thus, the selected test sections with valid data are summarized below in Table 6-4.

Table 6-4 Selected FHWA ALF Test Sections for LVECD Rut Simulations

	Control	SBS-LG	CR-TB	Terpolymer
Thickness (mm) – Temperature (°C)	100-64 150-64 150-45	100-64 150-64 150-45	100-64	150-64

6.2.1.2 LVECD predictions

The TSS laboratory test on FHWA ALF mixes at field measured air void contents are re-analyzed to calibrate the current incremental-shift model. Then the model parameters are entered into LVECD along with other material coefficients and traffic and environmental information. The resulting LVECD predictions as well as the field measurements are plotted with respect to the number of wheel passes in Figure 6-6 and Figure 6-7.

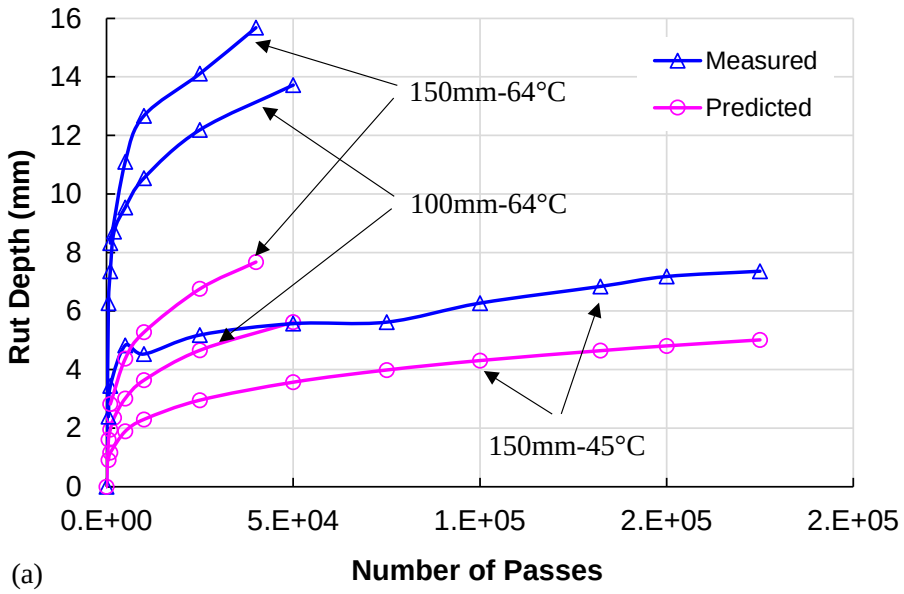

(a)

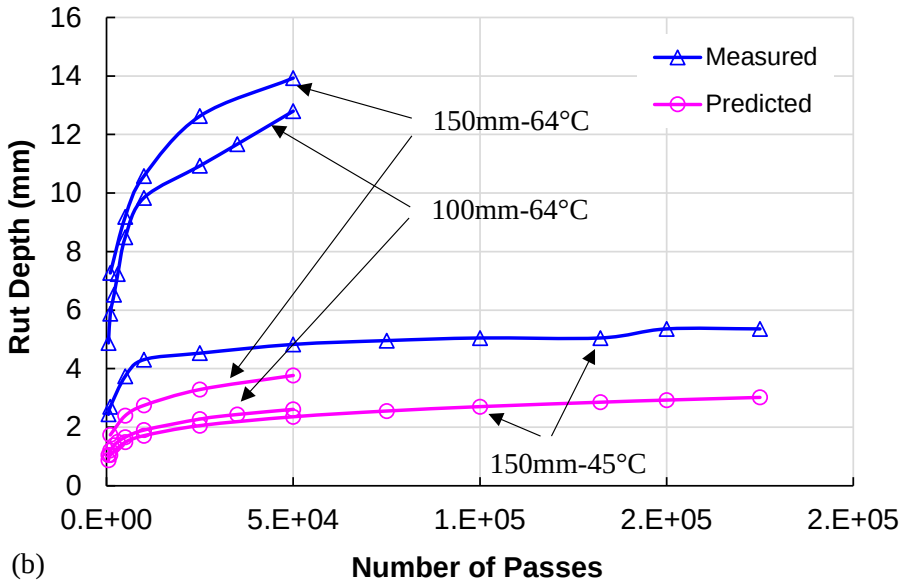

(b)

Figure 6-6 LVECD predicted and field measured rut depth in asphalt layers for FHWA ALF mixes: (a) Control, and (b) SBS-LG.

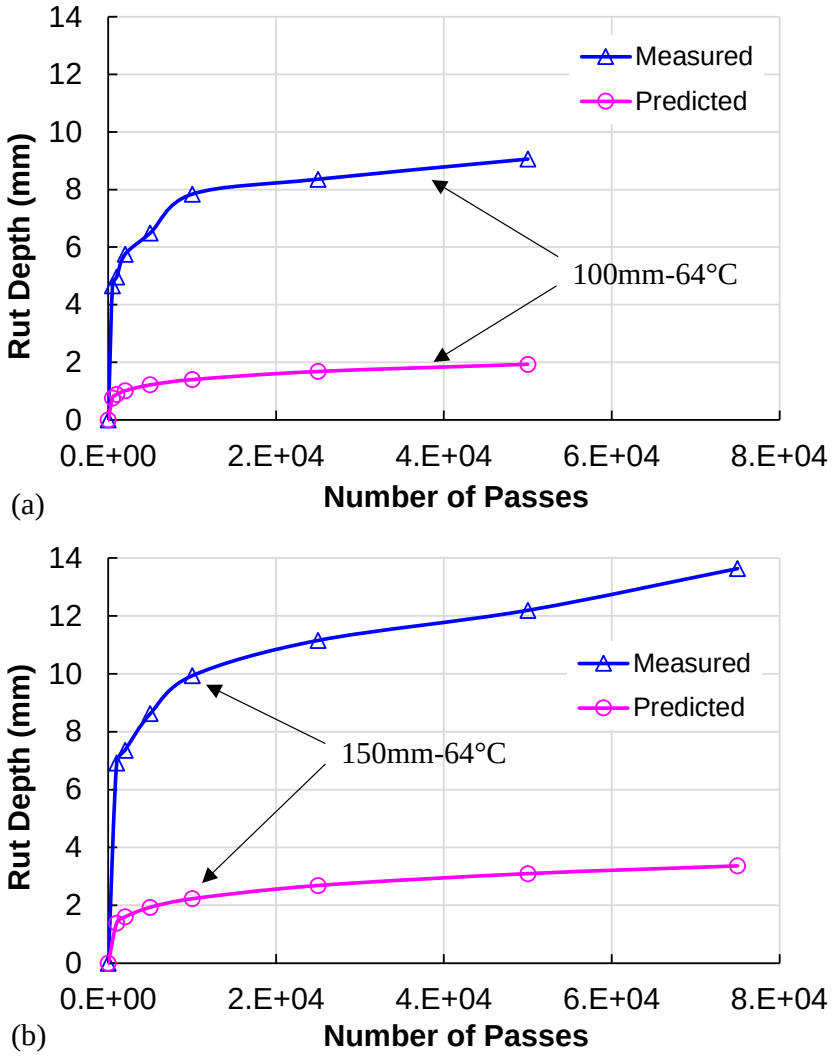

Figure 6-7 LVECD predicted and field measured rut depth in asphalt layers for FHWA ALF mixes: (a) CR-TB, and (b) Terpolymer.

Compared to the predictions with the previous model form, no significant difference in predicted rutting history is observed for each mix. Obviously, in all the test sections the rut histories are seriously underpredicted. In fact, in the field significant lateral upheaval is observed for all the sections considered in the above. Even though in the field rut measurements the upheaval portion is not included, the formation of the upheaval is able to accelerate the downward rutting. However, this part of contribution has been missing in the

modeling scheme and thus the LVECD simulation. Lateral upheaval is understood as being caused by the shear stress especially beneath the tire edge so that the materials are shoved to sides and upward, and then appear as humps beside the wheel track. This process is expedited by the increase in temperature and loading levels, and the reduction in vehicle speed. Nevertheless, the role of the shear deformation is absent in the incremental-shift model which takes the vertical normal stress alone and is capable of only the primary and secondary stages in permanent deformation. Despite the inadequacy in matching the magnitude, however, the incremental-shift model and the LVECD simulation produce the same ranking in rutting performance with the field measurements: CR-TB, Terpolymer, SBS-LG, and Control from superior to inferior.

6.2.2 NCAT test sections

6.2.2.1 Project overview

The NCAT test track is also a full scale pavement, and is constructed with the goal to evaluate the structural response and performance of pavements with 1) warm-mix asphalt (WMA) technologies, 2) high percentage of RAP, 3) the combination of WMA and high RAP, and 4) a porous open-graded friction course (OGFC) (LaCroix 2013). Totally six test sections are employed in this study with different mixes but the same structure. For each section, three layers of asphalt mixtures (1.25 in. surface, 2.75 in. intermediate, and 3 in. base) are paved on top of a 5.5 in. dense graded aggregate base over the local subgrade. See Table 6-5 for the section descriptions.

Table 6-5 Description of NCAT Test Sections (LaCroix 2013)

Label	Description
C	Control
O	OGFC surface with control intermediate and base
FW	Control mixtures using foamed asphalt WMA
AW	Control mixtures using Advera additive WMA
R	Control with 50% RAP mixture
RW	Control with 50% RAP mixture using foamed asphalt WMA

The test track is loaded intensively by five trucks systematically so that at the end of two years the pavements have experienced the equivalent of 10.14 million equivalent single-axle loadings (ESALs). Wheel wander is incorporated in the field testing to mimic the transverse variation in actual traffic loading. Unlike the FHWA ALF sections with fully controlled pavement temperatures, NCAT sections are totally exposed to the natural environment. The test track is located in central Alabama where the climate is quite mild. The weather station at Montgomery, Alabama is selected to generate the pavement temperature profile via EICM. The pavement surface temperature for the two year analysis period is presented in Figure 6-8. The rut depth histories are not provided; only the information at the end of two years testing is available at NCSU. Contrary to FHWA ALF sections, field observation reveals the absence of lateral upheavals in NCAT pavements, which can be explained as the result of traffic wander and much less extreme environmental conditions. It is thus expected from simulations that compared to densification the contribution from the shear mechanism should be small or negligible.

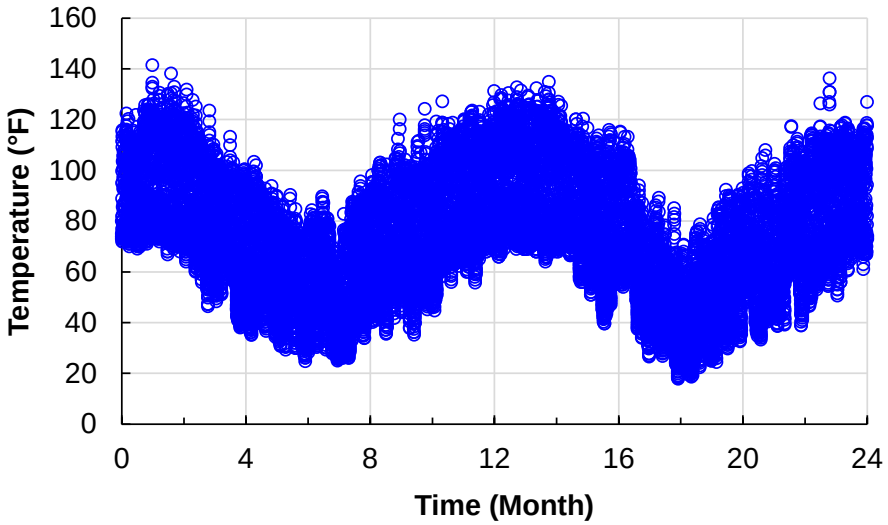

Figure 6-8 The two year temperature history at pavement surface used in NCAT test track simulation.

6.2.2.2 LVECD predictions

The current form of the incremental-shift model is calibrated using the TSS laboratory test at the field measured air void content for each mix. As for the pavement structure, even though the design is the same across all the six sections the averages of measured layer thicknesses after construction for each suggest a maximum variability of 0.5 in., and thus in LVECD simulation the measured thickness for each layer is used instead of the designed value. As traffic wander is present in the field test, according to MEPGD a reducing factor of 0.8 has been applied on the daily traffic input (ESAL) in LVECD. The temperature profile is generated from EICM for each section. The final rut depth at the end of two years for each section is predicted and shown in Figure 6-9 along with corresponding measurement.

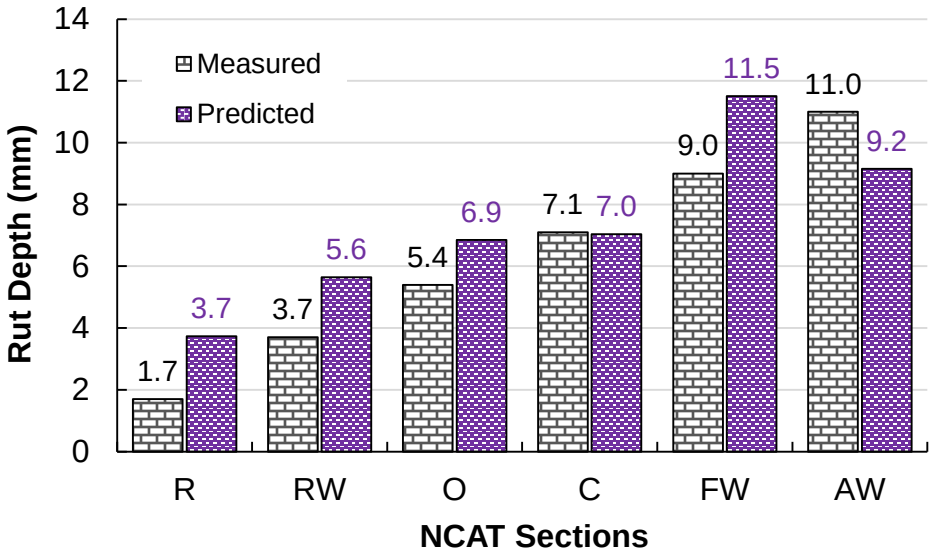

Figure 6-9 LVECD predicted (with the improved form of the original incremental-shift model) and field measured rut depth in asphalt layers after two years for NCAT sections.

In LaCroix's work (2013), the predictions with the old model form give a consistent overprediction for every section. Yet here a noticeable underprediction is observed for the AW section. The current predictions are generally smaller than those by the old model form and yet closer to the field measurements. Besides, in terms of ranking the current prediction corrects the ranking between RW and O sections. The underprediction in NCAT sections has been presumably attributed to the aging effect (LaCroix 2013). And if the shear effect is to be somehow added, its contribution is expected to be significantly small compared to the current LVECD prediction.

6.2.3 Summary

In this section both the FHWA ALF and NCAT test tracks are simulated in LVECD using the latest form of the incremental-shift model. In the FHWA ALF test sections, extreme (constant and high) temperatures are maintained during the field testing and the actual rut depths are all underpredicted. The lack of the incorporation of shear contribution is believed as responsible for this underprediction since significant lateral upheavals are observed at the

sides of wheel paths in the field. For NCAT pavements, the rut depths for most sections are overpredicted, which is assumed as a result of the aging effects and the complexities involving the real-world climate change and traffic. The shear effect, however, is believed to be small or negligible as no lateral upheaval is discerned in the field. In sum, despite of the neglect of aging and shear effect, and the assumptions regarding the 10 psi confinement used in modeling and finite element simulation, the current framework produces predictions matching the field ranking quite well for both test tracks. In the remainder of this chapter, efforts are devoted to understanding the shear mechanisms in permanent deformation and seeking an approach to approximately quantify the contribution of shear effects.

6.3 Understanding the Shear Behavior of Asphalt Concrete

6.3.1 General Deformation Mechanisms of Granular Materials

Granular materials, such as soils, rock, concrete, and asphalt mixtures, are usually subject to compressive stresses during service. One of the most salient features of granular materials that set them apart from metallic materials is the volumetric expansion or dilation under plastic deformation, and this is owing to their granular nature. From the traditional point of view, the Mohr-Coulomb theory gives the constitutive origin of material strength: the cohesive stress and the internal friction. While the internal friction between particles is ubiquitous in all granular materials depending on the particle shape, angularity, and surface texture, the cohesion force is zero for cohesionless soils like sand and gravel. As far as asphalt concrete is concerned, the asphalt acts like cement binding all aggregate particles together, thus providing a non-vanishing cohesion force.

As mentioned in the above, volume changes accompany the plastic deformation for all geomaterials. The behavior of a common viscousless granular material in a monotonic test is first described here before introducing the asphalt concrete which brings about an added viscous complexity. With the absence of viscosity, the stress-strain curve in a monotonic test (either with or without confinement) can usually be broken down into three parts: the initial elastic region with a linear slope (Region I in Figure 6-10), the hardening region with a

monotonously decreasing slope (Region II in Figure 6-10), and the final post-peak softening region with a negative slope (Region III in Figure 6-10).

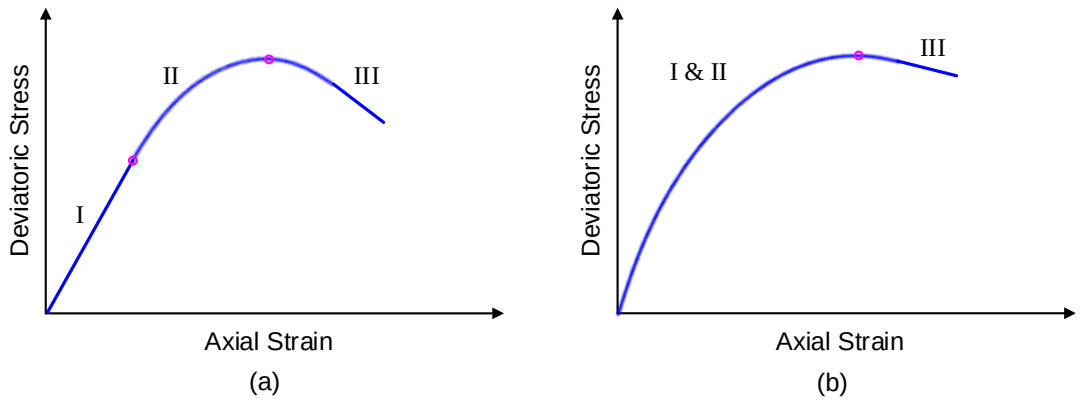

Figure 6-10 Representative stress and strain relations in monotonic tests for: (a) viscousless materials, and (b) viscous materials.

In the first elastic region, all the deformations can be instantly recovered upon unloading and there are negligible energy dissipative processes occurring within the material, which indicates that there are literally no particle rearrangement in a soil sample and hardly any presence of microcracking in cemented materials like concrete and rock (Vermeer and *de* Borst 1984) (i.e., no microstructural change). When the hardening behavior is initiated, plasticity comes into the picture as a result of energy dissipative mechanisms like particle sliding in soils and microcracking in concrete and rock. At this stage, material dilation takes place and this is due to the presence of microcracks and/or caused by frictional sliding either between particles or along the microcracks. The advent of the softening regime is marked by the peak in the stress strain curve, although it may be not visually pronounced but very smooth in the case of loose sands and for concrete and rock under high confinement. It is generally considered that the shear bands are largely responsible for the marked peak for sand tests with a low density, while for concrete and rock tested at low confinement the situation is further complicated because of the appearance of axial tensile fractures.

Now attention is turned onto geomaterials with viscosity (e.g. asphalt concrete) under monotonic loading as illustrated in Figure 6-10(b). Clearly the time-dependent viscoelasticity renders a nonlinear relation from the very beginning of the loading and thus now it becomes extremely challenging, if not impossible, to distinguish between the viscoelastic region and the plastic hardening region. By analogy with the viscousless materials, within the viscoelastic region the material experiences small deformation with negligible presence of microcracks and meanwhile the aggregate particles have not been mobilized for rearrangement. As deformation goes, more particle contacts are realized, and then either one or both of microcracks and particle rearrangement initiate depending on the confining state. Under high pressures the microcracking is suppressed and thus particle sliding is predominant, whereas for low pressures the tensile fracture transverse to the loading direction becomes easier to take place. The softening region is relatively easy to define based on the stress peak.

Combined with the analyses and hypotheses presented in previous chapters, the deformation phenomenon and mechanisms of asphalt concrete under general compressive loading conditions can now be complemented and described as follows. Inside the domain of elasticity and viscoelasticity the material is experiencing slight volumetric contraction as the apparent Poisson's ratio is smaller than 0.5. Within this region the material microstructure remains intact and unchanged. Under further loading the material may enter plasticity domain which is symbolized by the microstructural change in terms of overall densification, and internal particle sliding and rotation. If the initial material is loose enough under certain temperature and confinement, the material will first experience contraction and then dilation. Otherwise dilation will take place as soon as plastic deformation is present. Densification occurs because material is able to arrive at a denser state to attain a stiffer structure under loading by particle sliding and overriding and thus deforming the asphalt binder and squeezing out the air void among particles, whereas dilation happens since at the given material state and mechanical condition the material fails to reach a denser state either because the material is currently at the corresponding optimum density or has gone beyond that state.

While it is apparent to see the decisive role of material shear resistance in a shear test, it is not straightforward to perceive how shear is involved when the material is loaded axially by a compressive force as in the traditional triaxial test. For granular materials, an aggregate structure is formed by particle contacting and interlocking with each other, thus providing the resisting force against the external loading. Under small loading or deformation, this aggregate structure is in the static equilibrium. At this stage, the particle strength and static friction of the particle surface control the aggregate macroscopic strength. When the material is further loaded, the static equilibrium is lost and particles are mobilized and start to slide and rotate. At this stage, it is the particle strength as well as the dynamic friction that dominates the material strength. If no particle is to be crushed under the contact forces, then the frictional force between particles stands out as the decisive factor on the material resisting force. Therefore, without considering particle breakage we can conclude that granular materials will always deform in the shear mode microscopically regardless of the macroscopic loading type (either shear or normal loading). Asphalt concrete is no exception as asphalt binder filling the void of aggregate structure also deforms in the shear mode.

As in the shear deformation particle sliding is the predominant causer and contributor to axial contraction and transverse dilation, the classical concept of uniaxial shear strength in soil mechanics as well as the angle of dilation which relates the axial and volumetric deformation, are deemed as capable to fulfill the role as an indicator of material shear resistance. In order to observe significant dilation, asphalt concrete is usually tested at high temperatures, and in this situation asphalt binder becomes soft and more adhesive so that under axial compression the transverse microcracking can be quickly and largely healed especially when the rest period is applied, or may even not initiate at all. The absence of microcracking in the region where the angle of dilation is determined helps to guarantee that the particle overriding is the only or at least the major source of dilation as the contribution from microcracks is minimized. In the next section both the dilation angle and the familiar angle of internal friction are introduced.

6.3.2 Determination of Angle of Internal Friction and Angle of Dilation

As already discussed in the above, the cohesive stress and the internal friction as two intrinsic material properties constitute the failure resistance of granular materials in the context of the Mohr-Coulomb theory. The two material parameters can usually be determined by two types of laboratory tests: direct shear test and triaxial test.

In the direct shear test a soil sample is placed in the metal shear box which can be split horizontally into two halves. A constant normal force is applied on the sample while the top half is pulled until the sample fails. By repeating the test at multiple levels of the normal force, the normal-shear stress pairs are recorded and plotted in the space of shear stress versus normal stress. And finally a straight line is used to fit the data points with the intercept being the cohesive stress and the slope being equal to the tangent of the angle of internal friction.

Similarly, the triaxial compression test can be repeated with various cell pressures and the pressure-axial stress pairs are recorded at the moment of sample failure. Afterwards each stress pair is marked on the horizontal normal stress axis and a circle is drawn through the two points with the stress difference being used as the diameter. Then a straight line is drawn approximately tangent to all the circles. The cohesive stress and the angle of internal friction can then be found again via the intercept and slope. Note that in the above two approaches the straight line obtained is named the Mohr-Coulomb failure envelope, and material failure is signified by the peak of the stress-strain curve.

The concept of the angle of dilation (ψ) is utilized to quantify the ratio of two plastic strain rates, i.e., the rate of plastic volumetric strain and the rate of plastic distortional strain (Vermeer and *de* Borst 1984):

$$\sin\psi = \frac{\dot{\varepsilon}_V^{pl}}{\dot{\gamma}^{pl}} \tag{6.2.1}$$

where the plastic distortional strain rate is given by

$$\dot{\gamma}^{pl} = \frac{1}{\sqrt{2}}\sqrt{(\sigma_{11}-\sigma_{22})^2+(\sigma_{11}-\sigma_{33})^2+(\sigma_{22}-\sigma_{33})^2+6(\sigma_{12}^2+\sigma_{13}^2+\sigma_{23}^2)} \tag{6.2.2}$$

For the cases of direct shear test and triaxial compression test, Equation (6.2.1) can be reduced to

$$\sin\psi = \frac{\dot{\varepsilon}_V^{pl}}{-2\dot{\varepsilon}_1^{pl} + \dot{\varepsilon}_V^{pl}} \tag{6.2.3}$$

Bolton (1986) calculated the angle of dilation using the data around the peak stress in the direct shear test by arguing that in this region the normal stress hardly increases which gives an almost zero elastic strain rate and thus all the measured strain increments are plastic. And then a linear relation can be observed between the volumetric strain rate and the axial strain rate. In calculating the dilation angle, the data at and beyond the stress peak are generally used despite of the formation of shear bands and bulging of specimens (Schanz and Vermeer 1996). The strain rate ratio is not strongly sensitive to the inhomogeneous deformation even though the strain increments may suffer from inaccurate measurements (Vermeer and *de* Borst 1984). In fact, to minimize the effect of the fluctuation in the measured strain, Equation (6.2.3) is not directly applied but rather rearranged into the following form:

$$\frac{\dot{\varepsilon}_V^{pl}}{\dot{\varepsilon}_1^{pl}} = \frac{2\sin\psi}{\sin\psi - 1} \tag{6.2.4}$$

Note that in the equation above compressive strain is treated as positive while the expansive volumetric strain is considered negative. The dilation angle can then be found from the slope of the linear portion in the plot of volumetric strain versus axial strain as illustrated in Figure 6-11.

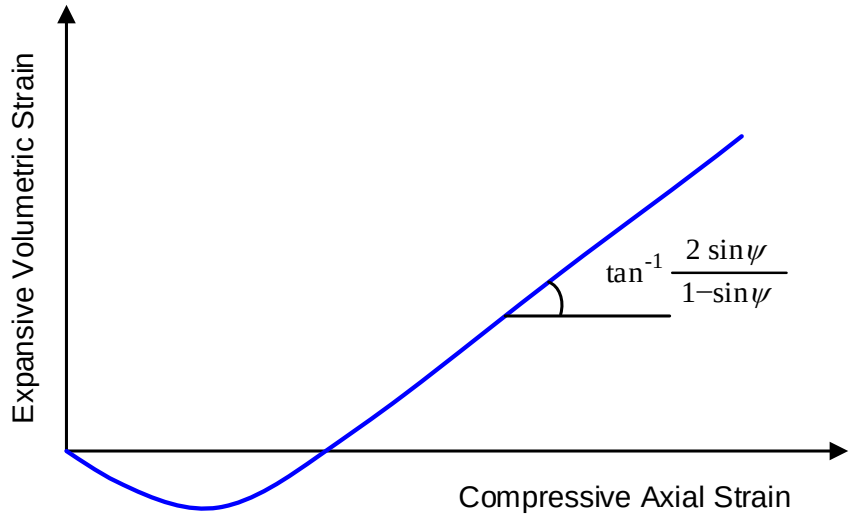

Figure 6-11 Calculation of the dilation angle based on the relation between volumetric strain and axial strain.

Experimental results on soils, rock and concrete have demonstrated that the observed friction angle is generally much larger than the angle of dilation. Various empirical relations have been established to relate the two (see Houlsby 1991 for a brief review). It is also worth mentioning that materials will not dilate forever. For cohesionless granular materials, at the later stage of deformation the volumetric strain will level out yielding a constant-volume shearing, which is the so-called critical state. In other cases, the dilation may not occur at all as it has been reported in literature that dilation vanishes at high confining pressures for soils, rock and concrete. So it should be understood that unlike the angle of internal friction as a material property, the dilation angle depends on the pressure for general granular materials. In the case of asphalt concrete, temperature should be included as an additional affecting factor for both angles.

6.3.3 Application to CCR and TSS Tests

As the angle of dilation is originally proposed for direct shear test and monotonic triaxial test on cylindrical specimens, the same concept can also be applied to the triaxial test with

complex loading histories like those in the CCR and TSS tests. As already mentioned, for a given asphalt concrete, the material dilation characteristics are expected to be dependent on the temperature, confinement level, and presumably the loading rate. The relations between volumetric strain and axial strain from the CCR tests on VTa0% mix at 48°C with 130 psi deviatoric stress and various confinement (0, 10, 20, 30 psi) have been presented in Figure 6-12, and those for the TSS tests on the same mix at different temperatures with 10 psi confinement are shown in Figure 6-13.

Unlike monotonic loading there is no stress peaks in the cyclic tests, which makes it indefinite to use what portion of the curves to calculate the angle of dilation. Despite this, some general conclusions can still be drawn. Figure 6-12 demonstrates the fact that material dilation can be substantially suppressed by the confinement and when the confining level is high enough contraction or negative angle of dilation emerges. Similarly, the effect of temperature can be perceived from Figure 6-13 that lower temperatures also help to suppress the dilation. Naturally, under high temperatures asphalt binder has a reduced adhesive force providing less restraint for particle rearrangement, while in the meantime it also acts like a lubricant promoting the particle sliding and overriding, and thus more dilation is caused.

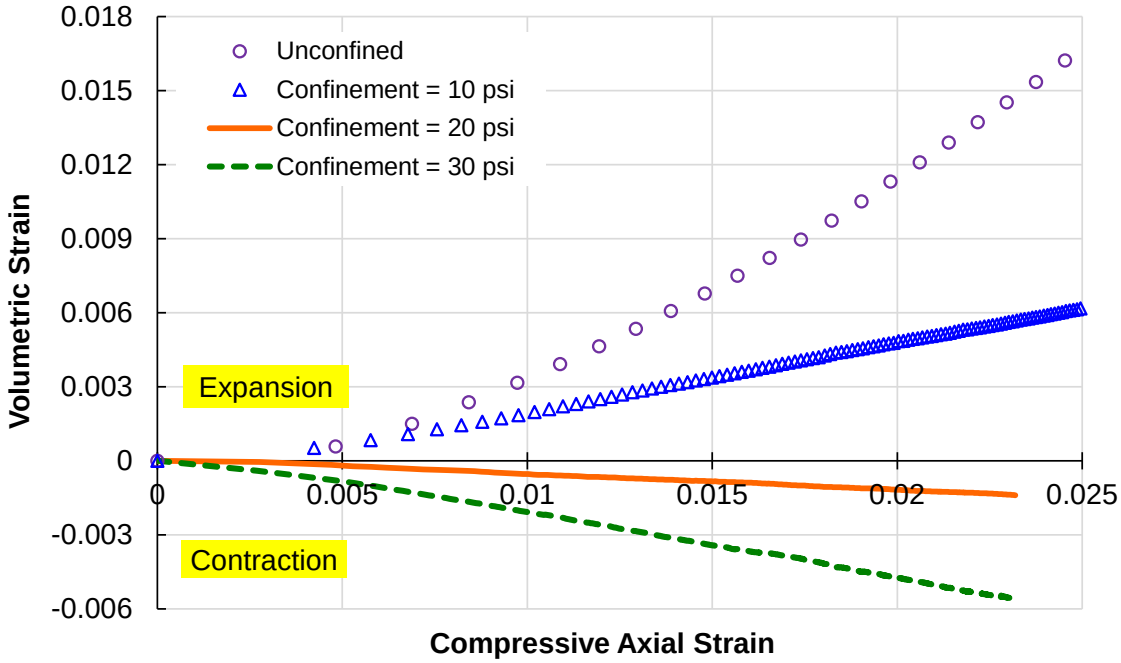

Figure 6-12 Relations of volumetric strain versus axial strain for CCR tests on VTa0% mix at 48°C and 130 psi deviatoric stress with various confinement levels.

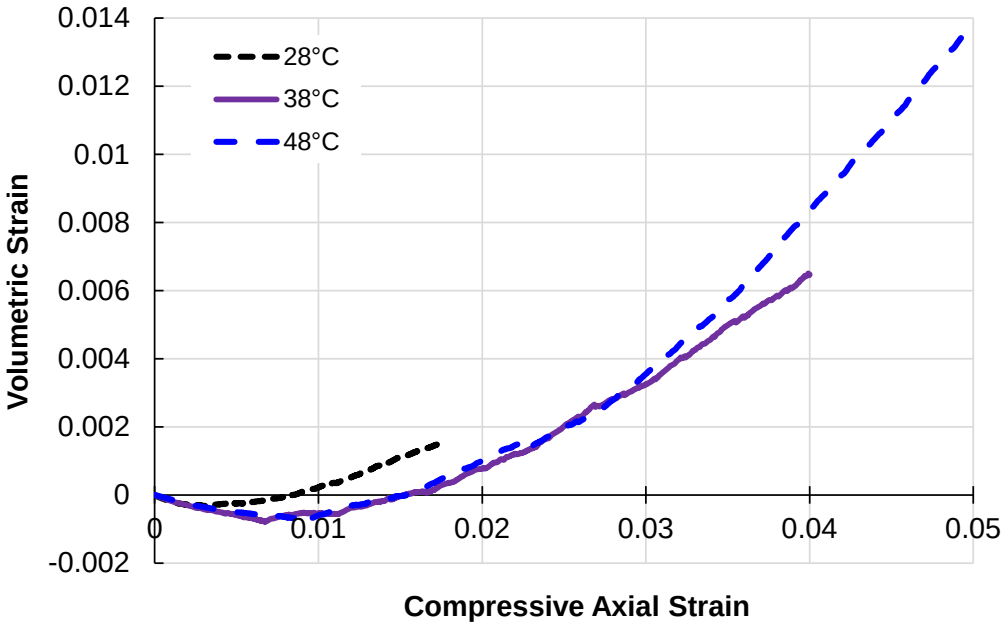

Figure 6-13 Relations of volumetric strain versus axial strain for TSS tests on VTa0% mix at 10 psi confinement with various test temperatures.

6.3.4 Comparative Study: Application to Monotonic Compression Tests

In order to verify the applicability of the dilation angle to the quantification of degree of dilation and thus the shear resistance, two different mixes are used here in the comparative study. The test type for this purpose has been chosen to be the monotonic compression test. Zero confinement is adopted with the aim to observe the maximum radial dilation while minimizing the possibility of particle crushing. The test temperature is set to be 48°C so that the material behavior will be dominated by aggregate particle interlocking and sliding. For the safety of test equipment the displacement control mode is utilized and the displacement rate is set as 1 mm/min (equivalent to a strain rate of 1.1E-4 $m/m \cdot s^{-1}$) for all the specimens and at this rate the loading is considered as quasi-static and thus the rate effect from asphalt binder can be minimized. Another practical consideration is that if the loading rate is set too high the specimen may move horizontally during testing which causes the non-uniform axial loading and also the failure of radial measurement.

The first mix is the control mix used in the Federal Highway Administration Accelerated Load Facility (FHWA ALF) pavements (Kim *et al*. 2005). The asphalt binder is unmodified and has a PG grade of 70 and -22. The aggregate has a nominal maximum aggregate size of 9.5 mm and the gradation curve is shown in Figure 6-14.

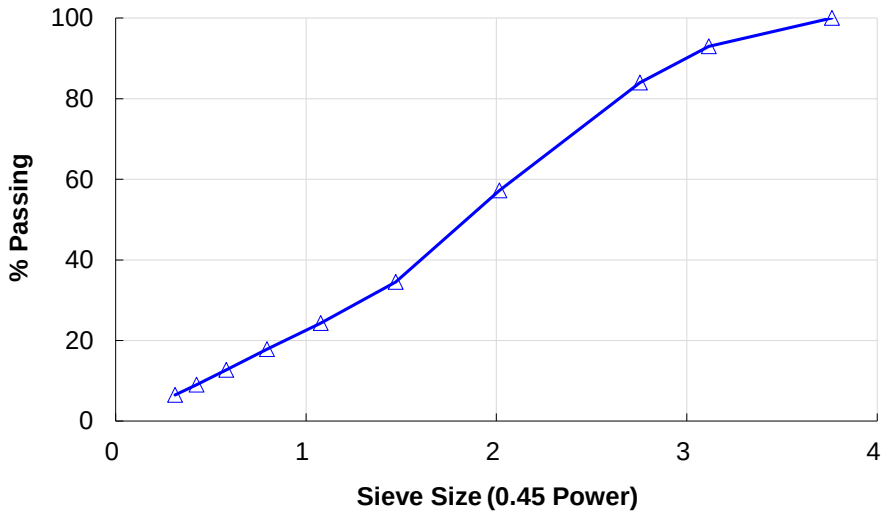

Figure 6-14 Aggregate gradation curve of the FHWA ALF mix.

To design the second mix in this comparative study, a few considerations have to be made. First, as reported in the literature, aggregate shape and angularity are the primary factor influencing the dilation characteristics and thus an appreciably different aggregate with rounded shape and less angularity should be used in the second mix. Secondly, to isolate the aggregate shape and angularity as the only independent variable, other affecting factors should be kept the same between the two mixes. For the first consideration, natural river gravel was chosen and they were purchased from the pet store Petsmart®. These gravels are originally sold for aquarium tanks rather than for construction or paving, and therefore their strength remains to be checked in specimen compaction and testing as particle breakage is not favored and should be ruled out of the energy dissipative mechanisms when the mix is

subject to loading. For the second consideration, the aggregate gradation and air void of test specimens are kept the same between the two mixes. Theoretically, for the fine aggregate (passing #8 sieve size or smaller than 2.38 mm) natural sand is supposed to be used while in practice it is very hard and time consuming to match the fine gradation especially to obtain a considerable amount of sand finer than 0.075 mm. On the other hand, it is believed in the present case study that the effect of particle shape and angularity is dictated by coarse aggregate. Hence, here the same fine aggregate as used in FHWA ALF mix is employed in the second mix with the anticipation that compared to the FHWA ALF mix the replacement of coarse aggregate is able to bring about significant differences in material dilation.

Before fabricating specimens for the second mix (designated as River Gravel), bulk specific gravities of aggregate have to be found based on AASHTO specifications (T-84 for fine aggregate and T-85 for coarse aggregate), and optimum binder content has to be determined according to Superpave mix design method (Asphalt Institute 2001). The optimum binder content is found to be 3.63% as compared to 5.3% for the FHWA ALF mix. It should be pointed out that this optimum value corresponds to the 4% air void content, and due to the use of the special aggregate and the enforcement of the same gradation some of the other requirements (VMA and the ratio of dust to effective binder content) are not satisfied. Figure 6-15 presents one batch of the total aggregate for half of a River Gravel specimen. Obviously, the coarse aggregate is more rounded with less angularity. In Figure 6-16 the test specimens are demonstrated for both mixes and again it is clear to observe that the River Gravel mix has more rounded aggregate than the FHWA ALF mix. All test specimens are targeted at 3.5% air void content in order to skip over the initial densification stage as present for specimens with higher air void contents. It is aimed to observe dilation at early stages of deformation as practically the LVDT has a maximum measurable range of around 6% for axial strain. During specimen fabrication no particle breakage was observed for either mix.

Figure 6-15 One batch of the total aggregate (including lime) for half a specimen.

Figure 6-16 Test specimens for the River Gravel mix (left) and FHWA ALF mix (right).

As mentioned in the above, monotonic compression tests without confinement at the same high temperature (48°C) were performed for all the specimens at the same displacement rate (1 mm/min) with the only independent variable being the difference in particle shape and angularity of coarse aggregate between the two mixes. The test results are presented in Figure 6-17 and Figure 6-18, and the angle of dilation calculated based on Equation (6.2.4) and Figure 6-11 are listed in Table 6-6. Note that two replicates are used for each mix. When the measurements from one opposite pair of LVDT go beyond the range the test is stopped. Specimens were fractured at the end of test as shown in Figure 6-19. Again, no particle breakage was found at the fracture surfaces of any specimen after test.

Obviously during the loading the volumetric strain grows at an increasing rate for each test as opposed to the typical curve for granular soils for which the volumetric strain increases at a relatively constant rate as shown in Figure 6-11 before leveling out and reaching the critical state where material is sheared at a constant volume. This difference is attributed to the evolving tensile fractures in asphalt concrete specimens and finally the material will collapse providing a vanishing resistance rather than attaining a residual strength.

Even though significant fracture is present at the end of test, the angle of dilation is calculated in the region corresponding to the peak stress as marked by the bars in the volumetric-axial strain curves in Figure 6-17(b) and Figure 6-18(b), and in this region the radial expansion is quite limited (< 1.5% for FHWA ALF mix, < 1% for River Gravel mix) and cracks were not observed on the specimen surface where they would most likely occur due to lack of confinement from surrounding materials. As mentioned previously, the absence of cracks is the guarantee to an accurate measure of the angle of dilation.

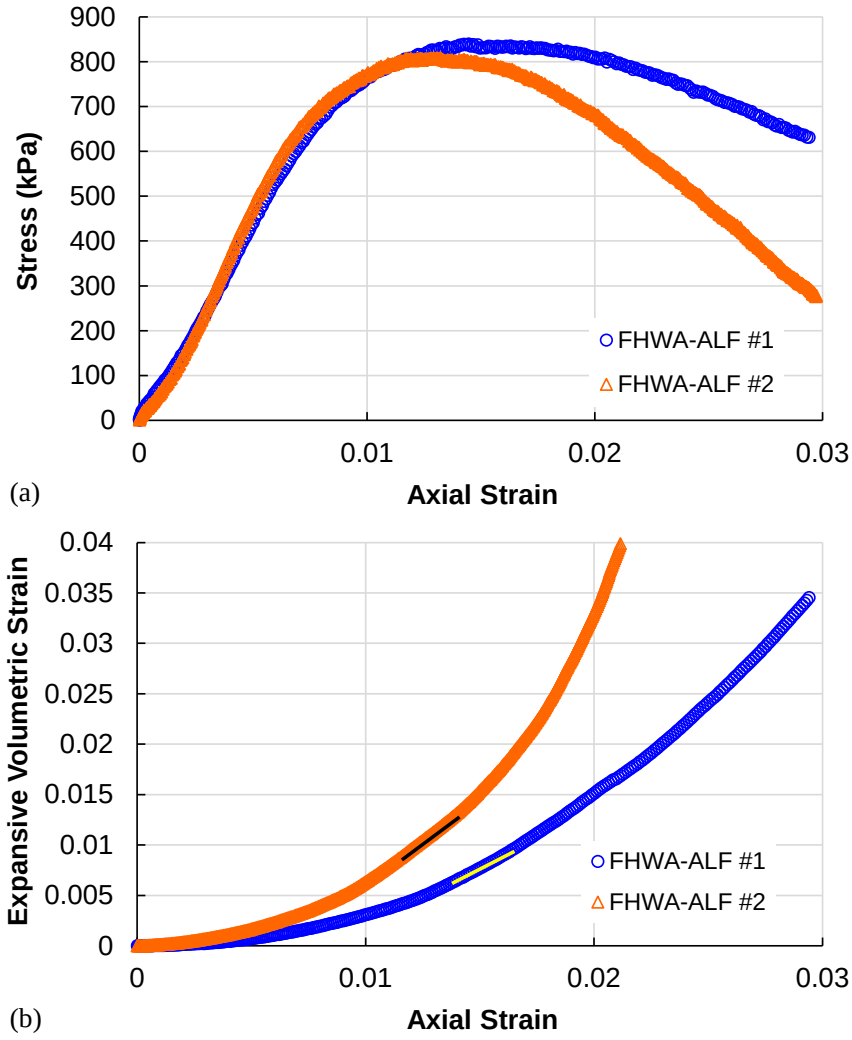

Figure 6-17 Monotonic compression test results for FHWA ALF mix: (a) stress versus axial strain, and (b) expansive volumetric strain versus axial strain.

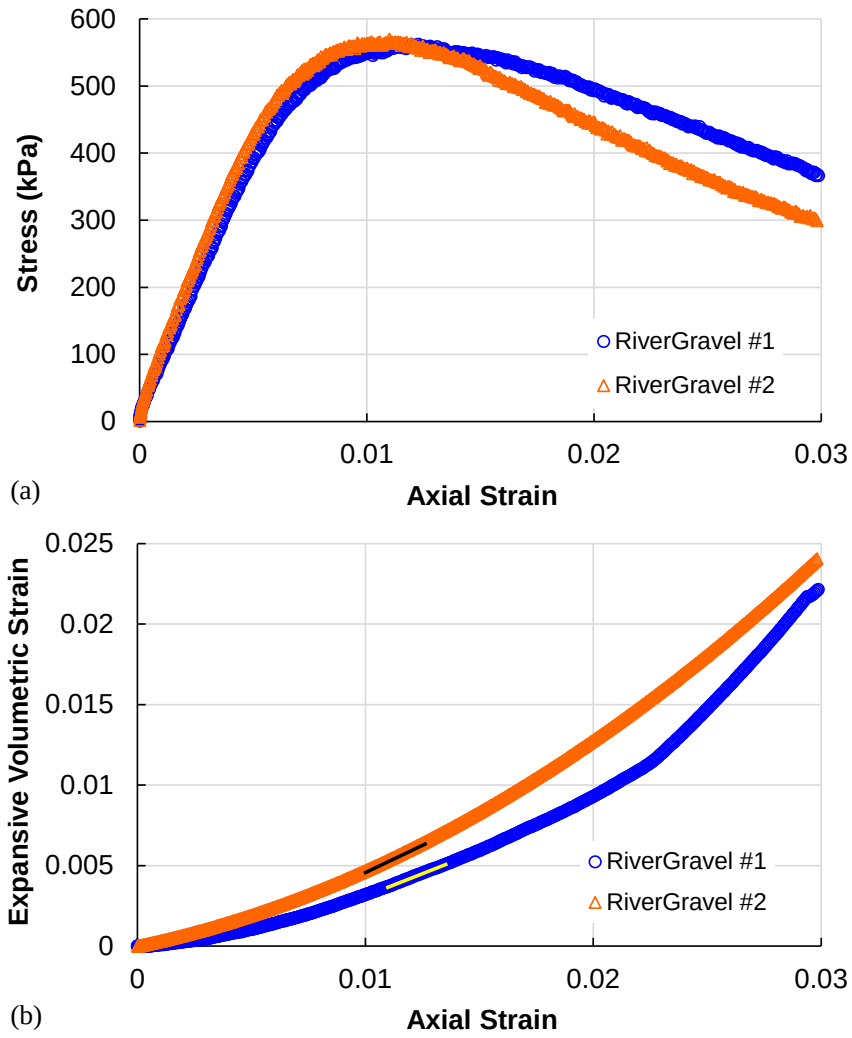

Figure 6-18 Monotonic compression test results for River Gravel mix: (a) stress versus axial strain, and (b) expansive volumetric strain versus axial strain.

Table 6-6 Angle of Dilation for All Monotonic Compression Tests

Mix	Replicate	Angle of Dilation (degree)
FHWA ALF	# 1	24.3
	# 2	28.1
River Gravel	# 1	12.5
	# 2	14.4

Figure 6-19 Specimens fractured after the monotonic compression tests.

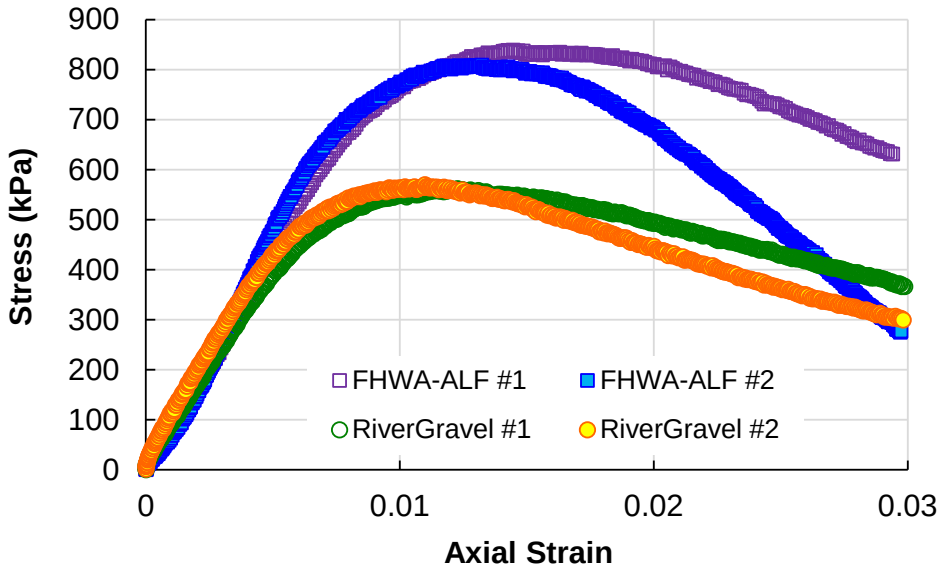

Figure 6-20 Stress and strain relations for all the monotonic compression tests.

It is first seen that the River Gravel mix exhibit a lower uniaxial strength (Figure 6-20) as well as a smaller angle of dilation (Table 6-6) under the same test condition, which is expected and consistent with general observations in other granular materials like soil and sands. In the present comparative study, asphalt binder and fine aggregate are kept the same between the two mixes, and thus in the context of Mohr-Coulomb theory the cohesion stress provided by asphalt or FAM (fine aggregate matrix) are supposedly the same. It then follows that the material strength is now purely dependent on the angle of internal friction of aggregate. As particles with high angularity tend to be more easily assembled into an interlocked aggregate structure, the FHWA ALF mix is expected to demonstrate a higher shear strength.

In addition to the internal interparticle friction, dilation can be treated as another source of the material shear resistance (Guo and Su 2007). When aggregate interlocking is broken and particles are mobilized under loading, particles start to rotate or slide over each other. As particle rotation plays an insignificant role in shear strength as well as material dilation, particle sliding helps to resist further loading while generating volumetric dilation. (Therefore, dilation can be used as a reasonable measure of the proportion of particle sliding in the total particle arrangement.) On the macroscopic level, the particle sliding will also lead to an increased apparent (mobilized) friction angle (Taylor 1948, Rowe 1962) compared to the internal interparticle friction.

As aggregate with higher angularity is able to provide greater shear resistance, it also gives more constraint to particle rotation and thus particle sliding occurs to a greater extent, which results in more considerable dilation than that for aggregate with lower angularity. The same observation has been made on laboratory experiments (Mair *et al*. 2002, Guo and Su 2007) and through numerical simulations using discrete element method (DEM) (Mirghasemi *et al*. 2002, Pena *et al*. 2006). In sum, regarding the two mixes it can be concluded that for the FHWA ALF Control mix more particle sliding and less rotation are present at failure, whereas for the River Gravel mix its lower shear strength and dilation angle are attributed to the prevalence of particle rotation over sliding.

A secondary yet interesting finding can be made with regard to Figure 6-20. As shown in the beginning of the loading the stress-strain curves of the two mixes collapse, which implies that particle shape is not a significant factor in the viscoelastic behavior of asphalt concrete. Particle shape and angularity start to exert influence once the material enters the plastic state through affecting how the aggregate structure changes.

6.3.5 Summary

In this section the macroscopic material behavior and the local particle movements are investigated. It is realized that for all granular materials it is the contacts and shearing among aggregate particles that constitute the main source of material resistance. Particle rotation plays an insignificant role in material strength and dilation, and it dominates the local mechanisms in the shear band. Particle sliding, on the other hand, helps to explain the hardening phenomenon as well as material dilation.

The difference in material shear deformations between traditional triaxial tests and field pavements is admitted. It is believed that the shear deformation in laboratory tests due to particle sliding occurs to a much less extent than would be observed in real pavements with lateral upheavals. In laboratory tests particle shearing helps to further resist external loading but as microcracks start to develop the number of particle contacts and thus particle sliding are reduced. The microcracking develops irreversibly and finally the material fails due to fracture. However, in the field the dilated materials are shoved to sides largely by the shear stress beneath the tire edge. The reduction in field material resistance is not primarily due to cracking but instead is caused by the particle rotation and/or loss of particle contact in the shear flow process. Therefore, to account for the contribution of shear mechanisms to rut evolution, models based on triaxial tests are inadequate. A supplementary shear based model is called for, and for this purpose a few transfer functions are reviewed in next section.

6.4 Review of Shear Based Transfer Functions

Traditionally, the vertical compressive strain on the top of subgrade is computed in pavement simulation and minimized in structure design, whereas the shear resistance is considered only in the mix design procedures via the Marshal method. Early rutting models are attempted to relate the field performance to traffic (number of load cycles), temperature, and material properties (such as air void and viscosity). Compared to these purely empirical models which are limited to similar materials, structures, traffic and environmental conditions used for the model development, certain mechanistic-empirical models, known as transfer functions or performance equations, have extensive applicability by expressing the permanent strain in terms of the calculated stress and strain responses in the pavement structure. This way, the effect of material, structure, mechanical and environmental conditions are more rigorously and systematically considered.

Given the apparent inadequacy of considering only densification under the centerline of wheel path especially in the cases under extreme traffic and climate circumstances, the incorporation of shear effect in modeling field rutting has been drawing an increasing amount of attention. Since in the current LVECD predictions only the densification effect is included, to match the field performance a multiplier or the so-called correction factor can be introduced as commonly used in the mechanistic-empirical modeling scheme. However, since the disagreement between simulations and measurements are primarily attributed to the lack of consideration of the shear effect, which is inherently different from the densification, it is felt more reasonable to separately quantify the shear deformation and then sum up the two portions as the final rut predictions. Afterwards, a correction factor can be sought if a sufficient amount of data required is available.

In the remainder of this section, several transfer functions based on pavement shear responses are reviewed, and then the WesTrack transfer function is selected for an exploratory application to the FHWA ALF and NCAT test sections in the section that follows.

6.4.1 Simple power law by Selvaraj

With the access to the database of NCAT test sections, Selvaraj (2007) was able to develop a shear strain based rut depth predictive model in the form of a power law:

$$RD_i = RD_{i-1} + \lambda_0 N_i^{\lambda_1 \cdot \gamma_i} \tag{6.2.5}$$

where γ_i is the maximum shear strain beneath the tire edge at the analysis time period i, N_i is the number of wheel passes during the period, RD_{i-1} is the rut depth at the end of previous period i-1, RD_i is the rut depth at the end of period i, and λ_0, λ_1 are regression coefficients. The pavement strain response was calculated by assuming a multilayered linear elastic pavement system. The model was calibrated using the field measured rutting history for each NCAT section individually. Recently the model has been slightly extended to account for the variation in traffic loading by incorporating a second power term so that the contribution from single and tandem axles can be considered separately (Hossain *et al*. 2013). In Selvaraj's work, the capability of the model has been demonstrated by reasonably fitting the NCAT field data, and yet the possibilities of calibrating the model with laboratory material tests were not investigated as field data are usually not available to be used for model calibration.

6.4.2 WesTrack transfer function

The WesTrack shear based transfer function was developed using the field data generated from the WesTrack project (Epps *et al*. 2000). In its framework the material densification is totally excluded and thus pavement rutting is assumed to be controlled only by shear deformations. Accordingly, in the project for the 150 mm asphalt pavements the shear stress and strain were calculated at a depth of 50 mm (2 in.) beneath the tire edge and used for estimating the permanent deformation. The predictive model is expressed as

$$\gamma_p = ae^{b\tau}\gamma N^c \tag{6.2.6}$$

where γ, τ, and γ_p are respectively the resilient or elastic shear strain, shear stress, and the corresponding predicted permanent shear strain, all at a depth of 2 in. beneath the tire edge; N is the number of axle load repetitions; and a, b, c are regression coefficients. The model is

required to be calibrated using the experimental data of repeated simple shear test at constant height (RSS-CH) at multiple temperatures. For each mixture, the exponent *c* from all tests at different temperatures were averaged and then this average value was used to determine *a* and *b*. The final rut depth within the asphalt layer was calculated as

$$RD = K\gamma_p \tag{6.2.7}$$

where the multiplier *K* is a function of layer thickness as listed in Table 6-7.

Table 6-7 *K*-values for the WesTrack Transfer Function

Asphalt Layer Thickness (in.)	*K*-value
5 ~ 7	5.5
7 ~ 9	7.0
9 ~ 12	8.5
> 12	10.0

6.4.3 Transfer function based on shear stress to strength ratio by Li *et al*.

With the belief that shear flow was the dominating contributor to permanent deformation in asphalt layers, Li *et al*. (2011) proposed a rut predictive model based on the ratio of shear stress to shear strength:

$$\varepsilon_p = c_1 e^{c_2 N} e^{c_3 \frac{\tau}{\tau_f} N^{c_4}} t^{c_5} \tag{6.2.8}$$

where *N* is the number of load repetitions, *t* is the pulse duration in each load cycle, τ is the shear stress response, τ_f is the shear strength, and c_1-c_4 are regression coefficients. The material shear strength, in terms of cohesion (*c*) and internal angle of friction (ϕ), at a given temperature can be determined via triaxial compressive strength test at multiple confinement levels, or the combination of indirect tension test and unconfined compressive strength test as suggested by Christensen and Bonaquist (2002).

The model was calibrated by the results from CCR tests conducted at multiple temperatures, deviatoric stresses, and confinement levels with a ratio of pulse time to rest period as 1 to 9. Given the conventional triaxial stress state in CCR tests, the shear stress to strength ratio can be calculated as follows for a specific confining pressure:

$$\frac{\tau}{\tau_f} = \frac{(\sigma_1 - \sigma_3)(\tan\phi \sin\phi + \cos\phi - \tan\phi)}{2(c + \sigma_3 \tan\phi)} \tag{6.2.9}$$

where σ_1 and σ_3 are maximum and minimum principal stresses, respectively. Obviously, when calibrating the model using CCR test results the material shear properties c and ϕ should be obtained from corresponding tests at the same temperature as they are sensitive to temperature variations. The predictive model in Equation (6.2.8) was found to be applicable to various temperatures and stress conditions in the CCR tests.

For rut depth simulations on a pavement, the asphalt layer is divided into sublayers; at the center of each sublayer beneath the tire edge the elastic principal stresses were calculated. The pulse duration was obtained as a function of depth, vehicle speed and frequency based on the work by Brown (1973). When finally applied to the data from the full scale accelerated pavement testing (APT), a correction factor of 3.1 was determined to account for the differences in material properties and testing conditions between laboratory tests and APT as well as potential errors involved in rut measurements.

6.5 Implementation of the WesTrack Shear Based Transfer Function

6.5.1 Maximum shear stress and strain

Before the application of the WesTrack transfer function to the two full-scale test tracks, the reason why this function is selected should be stated. First, it is better if the selected model is based on strain, or if the stress variable is present then strain or material modulus/strength variables should be included. This can generally help to minimize the possibility of unrealistic results in the cases with extreme stress responses under low temperatures. Secondly, in order for the model to have material specific parameters, it should be able to be calibrated by laboratory material tests. In this scenario, a correction factor is usually

necessary when applying the model to predict rutting performance of real pavement structures. In addition, as for the laboratory characterization test the specimens are better to be loaded in the shear mode as the in the compression mode there exists negligible material flow due to shear.

As a mechanical-empirical model, the WesTrack transfer function provides a basis for extending the WesTrack findings to different traffic and environmental conditions. As already described in the above, the WesTrack model is based on the shear stress and shear strain at a depth of 2 in. beneath the outer edge of the tire (Figure 6-21). It is reasonable to speculate that the underlying rational for choosing this position is that the calculated elastic shear stress and strain reach maxima at this location. If the same coordinate system as in LVECD is used here, the shear stress and strain employed in the WesTrack project can be denoted as σ_{zx} and ε_{zx}, respectively. To check the above speculation regarding the maximum shear stress and strain, here the LVECD program is again resorted to for the FHWA ALF and NCAT sections. Note that in the FHWA ALF project two structures with different asphalt layer thicknesses (100 mm and 150 mm) are constructed, and thus designated as FHWA-4 in. and FHWA-6 in. The NCAT sections are designed with only one structure and thus denoted as NCAT-7 in. The use of different materials and temperature profiles (for the NCAT case) in a given structure has been realized to have little effect on the pattern of stress and strain distribution. Therefore, control mixes have been used in all cases. The resulting contours of shear stress σ_{zx} and strain ε_{zx} for all three structures are given in Figure 6-22 to Figure 6-24.

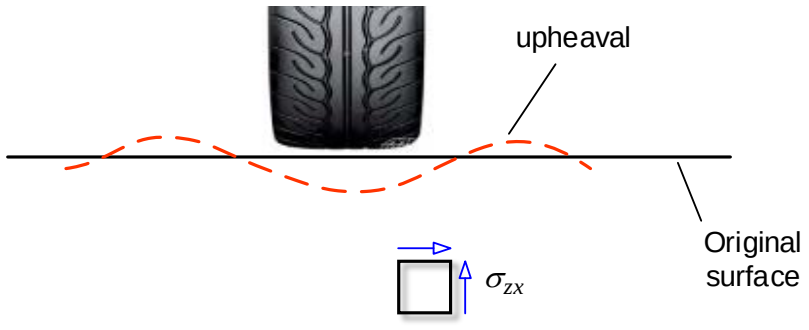

Figure 6-21 Shear stress and strain beneath the tire edge responsible for the lateral upheavals.

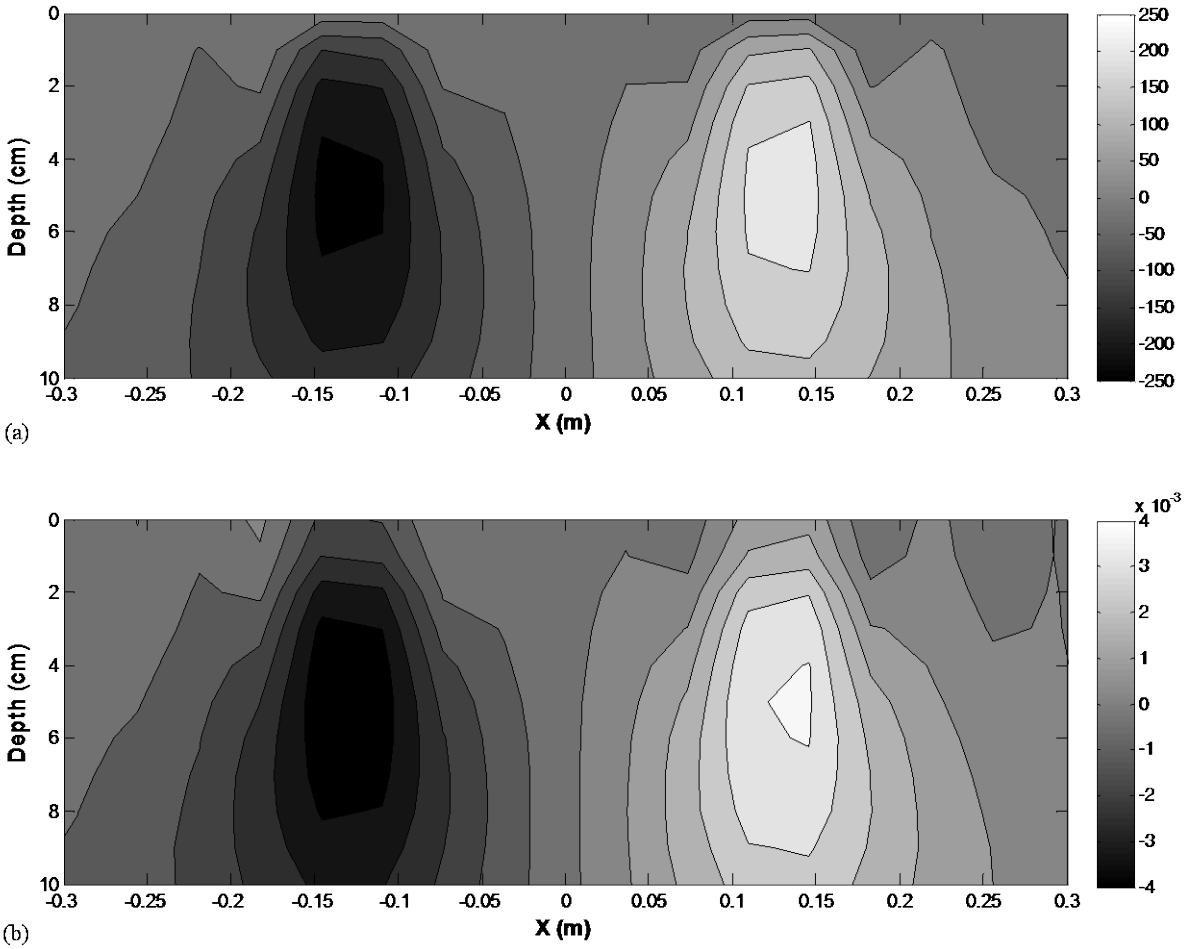

Figure 6-22 Shear response under wheel loading for FHWA-4 in. structure: (a) shear stress σ_{zx} in kPa, and (b) shear strain ε_{zx}.

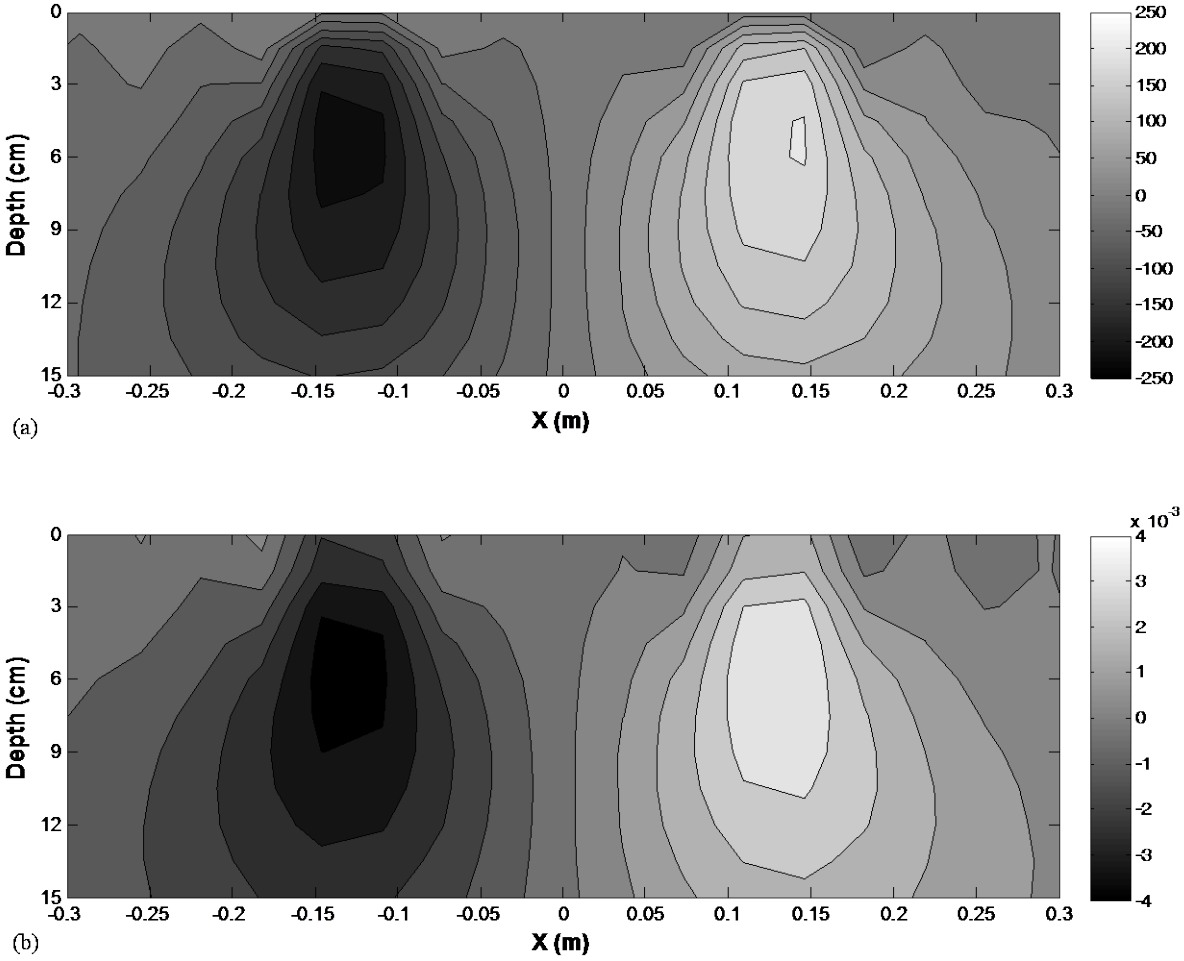

Figure 6-23 Shear response under wheel loading for FHWA-6 in. structure: (a) shear stress σ_{zx} in kPa, and (b) shear strain ε_{zx}.

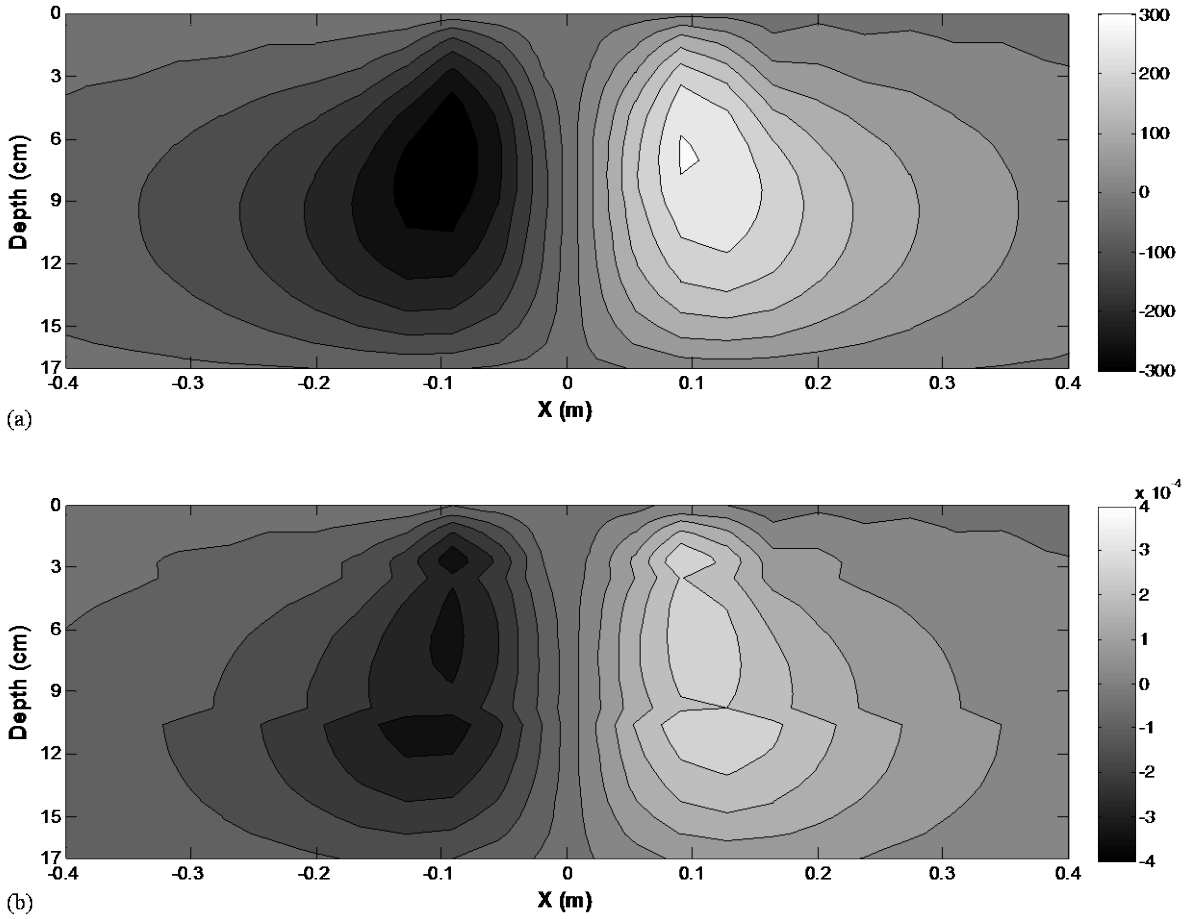

Figure 6-24 Shear response under wheel loading for NCAT-7 in. structure: (a) shear stress σ_{zx} in kPa, and (b) shear strain ε_{zx}.

In order to attain the field wheel load and contact pressure, in the FHWA ALF sections the tire width used in analysis is 0.253 m and thus the half width is 0.126 m. And in the case of NCAT, the half width of the tire is 0.092 m. In all simulations a single wheel is placed at the center of the lane. It is clear that the maximum shear stress and strain both occur beneath the tire edge. In the FHWA ALF sections, only one layer of asphalt concrete is paved. For the 10 cm layer (Figure 6-22), the maxima show up at a depth of 5 cm or 2 in. which is the same location used in WesTrack analysis. For the 15 cm layer (Figure 6-23), the maxima move downward to a depth of about 6 cm (2.4 in.). In fact the WesTrack project has the same 15 cm asphalt layer thickness but considerable difference in shear responses is not

expected between depths of 5 cm and 6 cm according to the contour shown here. In NCAT test sections, three asphalt layers are constructed and the layer interface can be easily located in the shear strain contour in Figure 6-24(b), where a maximum shear strain can be discerned in each asphalt layer. Given that these maxima have approximately the same magnitude, we can conclude that for the three layer asphalt pavement, the maximum shear responses can be found at a depth of about 7.5 cm. Hence, at this point it can be summarized that if the WesTrack transfer function is to be used, what should be entered are the maximum shear stress and strain, and they can be located at a certain depth beneath the tire edge.

There are at least two benefits that can be acknowledged by the use of the shear response component σ_{zx} and ε_{zx}. First, the shear stress σ_{zx} pair (and also ε_{zx} pair) beneath the tire edge on a material element (Figure 6-21) acts in a way that the materials are pushed sideward and upward, which exactly corresponds to the material flowing trajectory to develop the lateral upheavals. Compared to σ_{zx}, other shear stress components are inconsiderable and not directly responsible for the side humps. The second benefit is related to the convenience of using this stress component in computation. In LVECD the traction continuity has been prescribed as one of the boundary conditions which enforce the continuity of shear stresses in horizontal planes (Cao 2012). As a result, the stress σ_{zx} is continuous across different asphalt layers, which raises the possibility of using single stress and strain terms as representative for multilayered pavement structures.

In the following, the WesTrack transfer function is applied to both the FHWA ALF and NCAT test tracks. With the attempt for better predictions, the maximum shear stress and strain are located and extracted from response analysis via LVECD for each individual section rather than from the same location for all cases. As proposed in the WesTrack research, the shear based transfer function is calibrated by the RSST-CH tests. Since the required test data are not available for FHWA ALF and NCAT materials, the following technique is adopted. The FHWA ALF field rutting data and the previous LVECD predictions are used to optimize the parameters in the transfer function and the same function is then applied to NCAT test tracks. The FHWA ALF data are chosen for the function calibration simply because the rut evolution histories are available only for this field

experiment. In this exploratory approach the possible effects of temperature and material differences on the transfer function are ignored, and for the *K*-value the asphalt layer thickness (SI unit) is used. For this analysis, the major intention has been placed on assessing the concept and potential of introducing the shear contribution into the existing modeling framework.

6.5.2 Application on FHWA ALF test sections

Recall in Figure 6-6 and Figure 6-7 that in all the selected sections the rutting histories are underpredicted, especially the 64°C sections with a minimum underprediction of 50%. The rising difference between measurements and predictions with temperature implies an increasing need of incorporating the shear effect in addition to the existing scheme where only densification is considered. The input for the transfer function are the maximum shear stress σ_{zx} and strain ε_{zx}, and thus are first extracted from LVECD response analysis for each section as provided in Table 6-8. The coefficients in the transfer function are identified by minimizing the error between the field rutting histories and the sum of LVECD predictions and the results from the transfer function for all FHWA ALF sections, and are listed in Table 6-9.

Table 6-8 Maximum Shear Stresses and Strains Extracted for FHWA ALF Sections

Mix	Thickness (mm)-Temperature (°C)	Maximum σ_{zx} (kPa)	Maximum ε_{zx}
Control	100-64	213.3	3.72E-3
	150-64	197.4	3.50E-3
	150-45	254.2	1.40E-3
SBS-LG	100-64	225.4	3.10E-3
	150-64	207.1	2.90E-3
	150-45	241.0	1.70E-3
CR-TB	100-64	238.7	2.77E-3
Terpolymer	150-64	196.9	3.54E-3

Table 6-9 The Optimized Coefficients of the Transfer Function for FHWA ALF Sections

a	*b*	*c*
7.697	4.459E-4	7.491E-2

A few observations can be quickly made regarding Table 6-8. The maximum shear stress and strain decrease as the layer thickness increases. Besides, temperature is found to have significant effect on structure responses. As temperature reduces, the stress increases while the strain decreases due to the enhancement in material stiffness. The final calculated rutting histories are plotted against the field measurements in Figure 6-25 for Control and SBS-LG sections and in Figure 6-26 for CR-TB and Terpolymer sections.

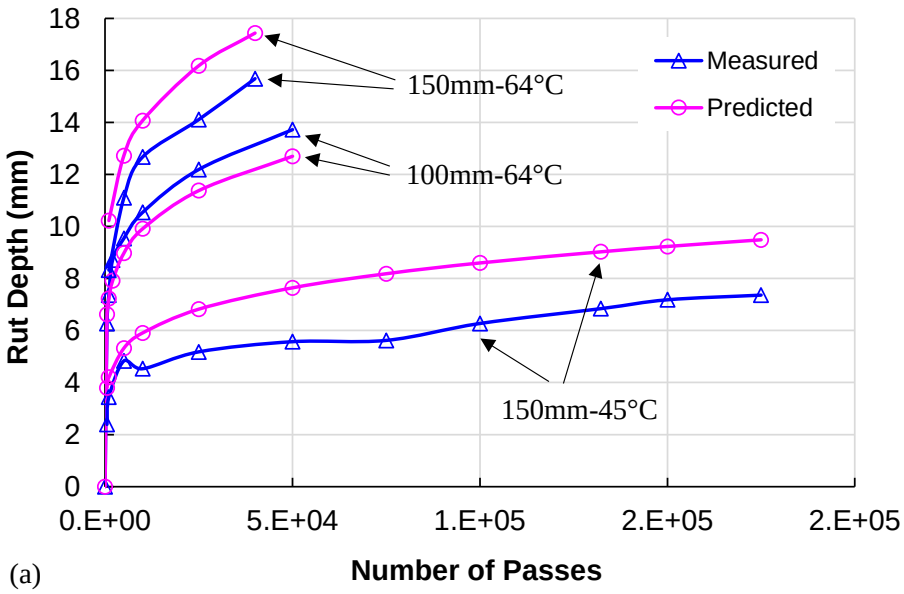

(a)

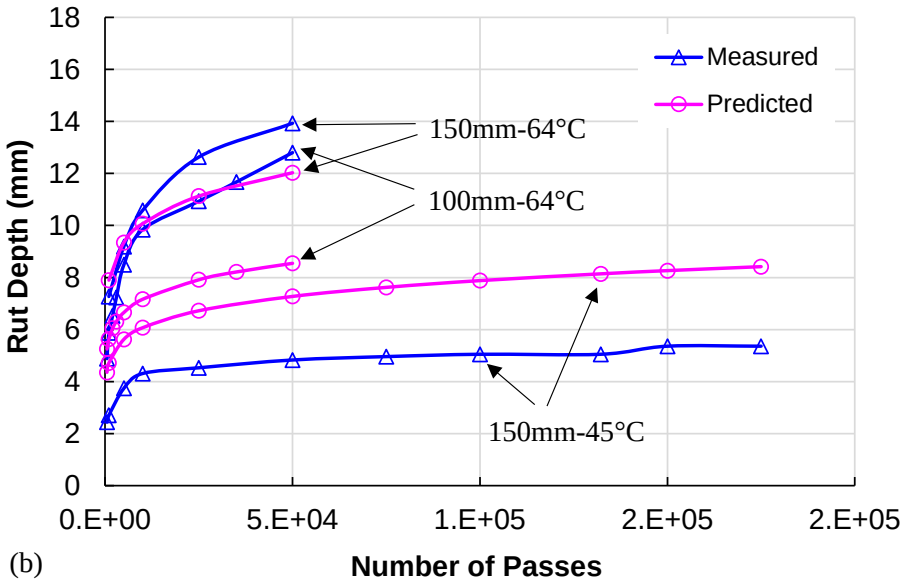

(b)

Figure 6-25 Calculated and field measured rutting histories for FHWA ALF sections with: (a) Control mix, and (b) SBS-LG mix.

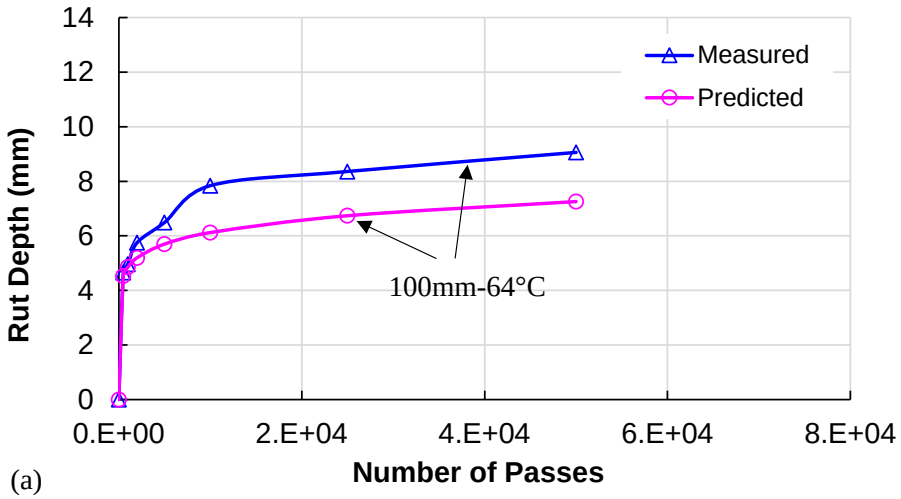

(a)

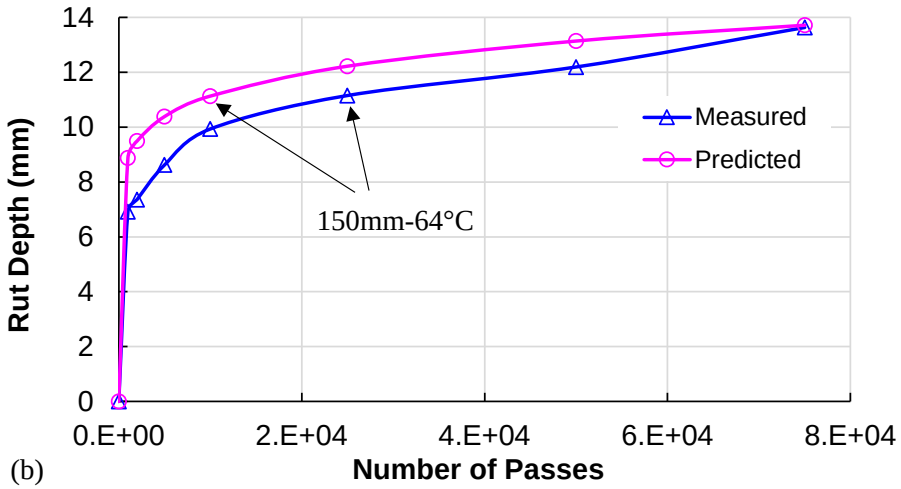

(b)

Figure 6-26 Calculated and field measured rutting histories for FHWA ALF sections with: (a) CR-TB mix, and (b) Terpolymer mix.

As seen in the above two figures, the two 45°C sections are now overpredicted, while both overprediction and underprediction exist for 64°C sections. The ranking among the four mixes are CR-TB, SBS-LG, Terpolymer, and Control from superior to inferior. Compared to the previous LVECD predictions and field data the positions of SBS-LG and Terpolymer are switched. However, the current calculations are much closer to the field measurements by adding the shear contributions. From both the simulation and field observation on the FHWA ALF sections it is obvious that the contribution to rutting from shear deformation is more

than or at least equally as important as densification. It is believed that better rut prediction can be promised by calibrating the transfer function using laboratory material tests and enhancing the model for consideration of wider temperature ranges.

6.5.3 Application on NCAT test sections

Contrary to the FHWA ALF sections under constant testing temperature, the NCAT test track is subject to the natural environment and thus the temperature fluctuation brings about an additional complexity regarding the variation in the computed maximum shear stress and strain with time in the pavement structure. As already indicated in Table 6-8 for the FHWA ALF sections, temperature exerts a remarkable amount of influence on the pavement responses and thus cannot be oversimplified in simulations.

Currently in the LVECD program the hourly temperature profile for the structure is required for input, but in order to reduce the computation time the given temperature data is first processed before subsequent calculations. LVECD uses 30 days for a month and every month is divided into, for example, three segments each with an equivalent of 10 days, which yields totally 36 segments for a year. The division among the segments for a month is based on the time period in a day. For example, the user can choose to assign the 5AM-12PM as the first segment, 12PM-7PM as the second segment, and 7PM-5AM as the third segment for each month. Within each segment, the temperature profile is assumed constant and is obtained by averaging all the temperature data for the month within the corresponding time period. For instance, for the first segment the temperature data of the first month falling within the 5AM-12PM time range are extracted and averaged to generate one single temperature profile, and then LVECD uses this temperature profile to compute the responses and performance results for this segment. LVECD provides users with the option to choose the number of segments from 1 to 24 for a month. For the present study, the default option is used: 3 segments divided as 5AM-12PM, 12PM-7PM, 7PM-5AM. The variations in the calculated maximum shear stress and strain are illustrated in Figure 6-27 for the NCAT C section as an example.

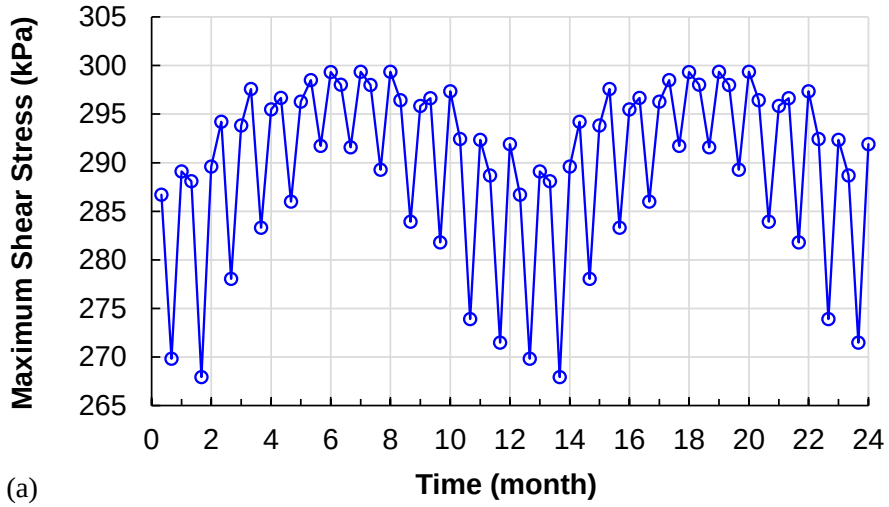

(a)

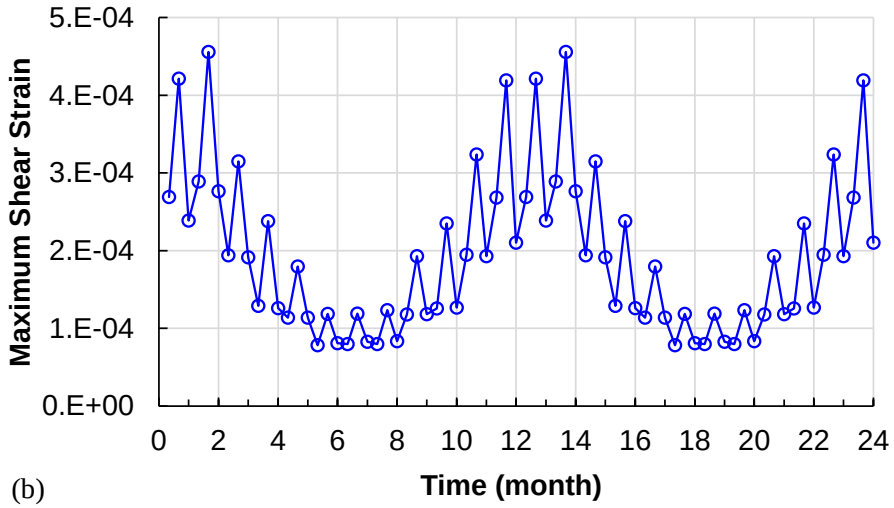

(b)

Figure 6-27 The two year histories of maximum shear responses as a result of temperature fluctuation for the NCAT C section: (a) shear stress, and (b) shear strain.

As a result of the variation in maximum shear stress and strain with time, the transfer function cannot be directly applied; it has to be rewritten in the incremental form in order to compute the rut depth for the second segment and so forth (Epps *et al*. 2000):

$$\gamma_{p,1} = \eta_1 \left(\Delta N_1\right)^c$$
$$\gamma_{p,i} = \eta_i \left[\left(\frac{\gamma_{p,i-1}}{\eta_i} \right)^{\frac{1}{c}} + \Delta N_i \right]^c \quad \text{where} \quad \eta_i = ae^{b\tau_i}\gamma_i \quad \text{with} \quad i = 2,3,... \tag{6.2.10}$$

where ΔN_i is the number of load applications during the *i*-th segment, and τ_i and γ_i are the calculated viscoelastic shear stress and strain in the segment, respectively. The final predictions considering both densification and shear, and the shear deformation alone are presented in Figure 6-28 along with the measurements.

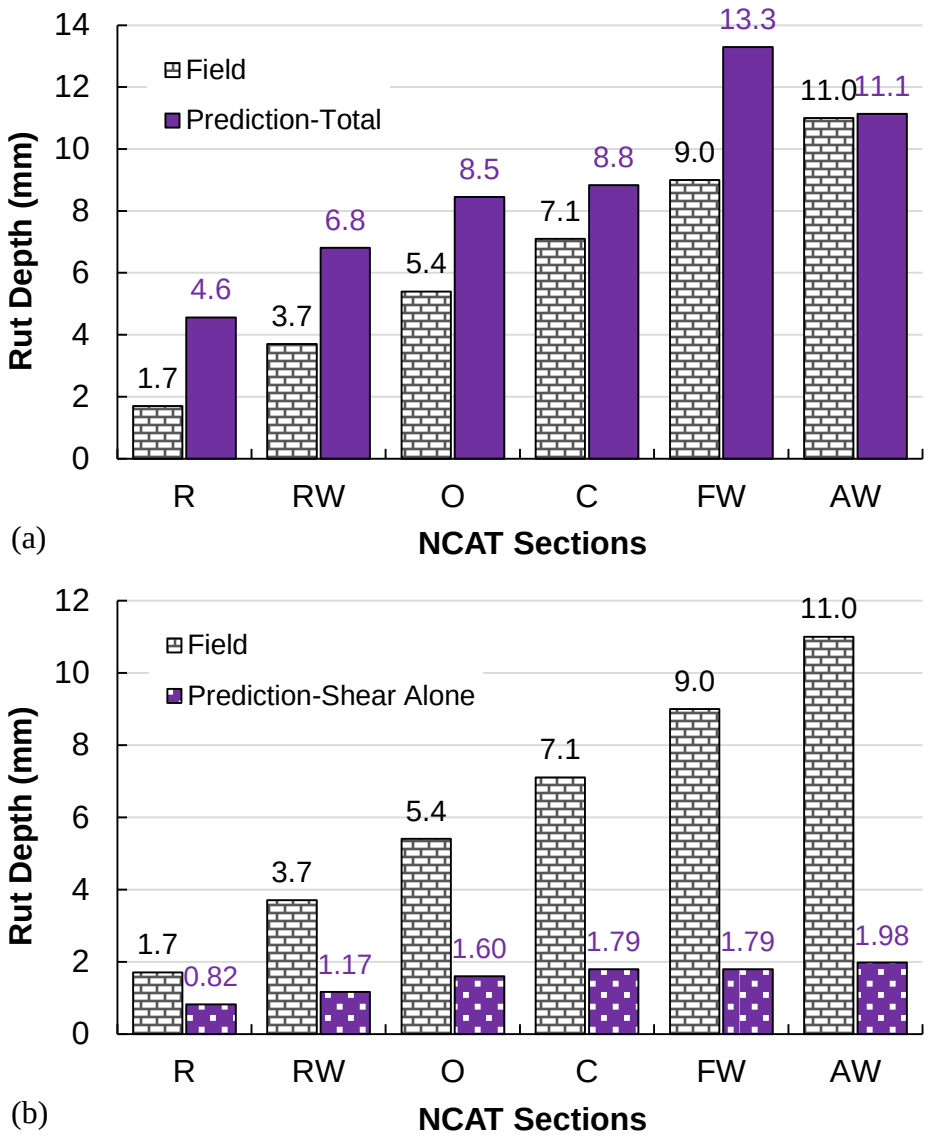

Figure 6-28 Measured and predicted rut depths for NCAT test sections after two years: (a) simulation considering both densification and shear effects, and (b) prediction from the shear transfer function alone.

As shown in Figure 6-28(b), unlike in the FHWA ALF sections, the calculated rut depth due to shear deformation is much smaller than that due to densification (as already presented in Figure 6-9) for each NCAT section. This agreement with field observation should be primarily attributed to the low values of the calculated maximum shear strain

(Figure 6-27) compared to the FHWA ALF sections (Table 6-8) even though the same transfer function are used for both. In addition, recall that in the previous LVECD prediction the ranking between FW and AW does not match the field data. But in Figure 6-28(b) where only shear deformation is compared the AW section has been correctly ranked as the one with the worst rutting resistance. In sum, the analysis on the NCAT test track further enhances the confidence of including the shear effect in predicting permanent deformation of asphalt pavement.

Finally, it is worth mentioning that to further improve the rutting prediction a more realistic and systematic consideration of traffic wander can be a promising starting point. In the present analysis, as already mentioned in Section 6.2 a single factor of 0.8 is used to reduce the traffic volume. The resulting rut depth has been found to be around 10% less than would be without considering traffic wander in LVECD. However, in the field the wheel wander is better described as a normal or Laplace distribution (Blab and Litzka 1995). Besides, the suppressing effect of traffic wander on the formation and evolution of upheavals has not been accounted for in the current analysis. This restraint on material flow should help to further reduce the magnitude of rut depth. Therefore, we can conclude that the reducing effect of traffic wander on rutting can be much greater as it has both effects on alleviating the densification and suppressing the upheaval. As an example, in the laboratory simulation using the heavy vehicle simulator (HVS) Wu and Harvey (2008) consistently observed an approximate reduction of 56% in rut depth in the pavement structure used in their study by allowing the traffic loading to wander.

CHAPTER 7 SUMMARY AND RECOMENDATIONS

7.1 Summary

This dissertation research is mainly focused on understanding and phenomenologically characterizing the underlying mechanisms behind permanent deformation or rutting in asphalt pavement. On the aspect of experimental investigations, cyclic creep and recovery tests were conducted on cylindrical specimens at high temperature with various deviatoric stress and confinement levels. The following material modeling complexities are perceived:

- Material time dependence varies with the deformation stage. In the primary and secondary regions the cyclic response becomes more elastic like due to material hardening, while in the tertiary region material time dependence increases as a result of microcracking damage;
- The viscoelastic and viscoplastic deformations are coupled. Material structural change due to plastic straining brings about the hardening in viscoelastic properties;
- Material experiences significant stress reductions in tests with large deformations. In general modeling schemes the original undeformed configuration is used whereas the updated configuration is required for the cases with large volumetric dilation.

In the aspect of phenomenological modeling, the viscoplastic model proposed by Subramanian (2011) was first simplified through analytical investigations combined with experimental observations. And then the variable of confining pressure was successfully introduced so that the material permanent deformation can be fully characterized by a single viscoplastic relaxation spectrum and a stress state dependent parameter. The improved model presented a convenient and reliable approach to the characterization of permanent deformation. However, due to inherent computational complexities in common rigorous viscoplastic models, the proposed model has not been implemented into finite element structure analysis. The incremental-shift model proposed by Choi (2013) was also extended by incorporating the effects of confining pressure. The extended model was characterized by TSS tests conducted at various confining pressures and verified by the random loading tests.

Both the improved viscoplastic model and the extended incremental-shift model are found to be applicable to material states with only positive confinements.

Finally, the inadequacy of LVECD predictions on the rut depths of FHWA ALF field test sections motivated further examination of the role of shear deformation in rutting. Under the assumption that the total rut depth is additively contributed from material densification and shear deformation, a few shear based transfer functions were reviewed and then an exploratory study was conducted. The WesTrack transfer function was selected and calibrated using the FHWA ALF field data, and then applied to the NCAT sections. The accurate quantification of the relative contributions from densification and shear deformation in both cases emphasized the necessity and enhanced the confidence of incorporating the shear contribution in predicting rutting performance of asphalt pavement.

7.2 Recommendations for Future Work

With an appreciation of the material complexities and the model limitations, potential future research directions are recommended in the following:

- On the material level, the proposed improved viscoplastic model and the extended incremental-shift model are currently limited to densification modeling with positive confinement. When very low positive or negative confinement is present, numerical errors may emerge in the viscoplastic model. As for the extended incremental-shift model, as its basis the incremental model determines the applicability to only the primary and secondary permanent deformation regions. In order to reasonably account for material behaviors under low or negative confinement, new experimental devices and protocols have to be developed. In addition, the two models will have to be further extended and enhanced. For the improved viscoplastic model, regularization techniques may be required to avoid numerical errors in computation. The temperature dependence of model parameters should also be investigated. For the extended incremental-shift model, material strength/modulus and/or strain variables are suggested to be introduced into the model expression. Or, as a second option to circumvent these experimental and

theoretical difficulties, the relative contributions from the top and bottom part of the asphalt layer in thin pavement can be somehow quantified in field test sections since even though the bottom portion is negatively confined it is also subject to much less harsh vertical compressive stresses. The research direction may be redefined if the contribution from the bottom part is found to be much less than that of the top part for thin asphalt layers in real pavements.

- The consideration of shear deformation is necessary in addition to densification especially for the pavements with significant upheavals observed beside wheel paths. Analogous to modeling the densification effect, the maximum viscoelastic shear stress and strain obtained beneath the tire edge can be utilized. The WesTrack mechanistic-empirical model is deemed as a promising starting point. As for the model calibration, laboratory material test conducted in the shear mode is suggested to simulate the material flow or particle rotation as in the formation of field upheaval humps. As an enhancement to this preliminary framework, certain flow models for the cohesionless granular materials may be adapted to study the particle rearrangement behaviors, and for this purpose the discrete element analysis may be required on the structural level.
- The role of traffic wander in predicting rutting performance in field pavements should be emphasized and quantified. The wander in traffic loading helps to alleviate densification and suppress the upheavals. Its effect in reducing the rut depth predicted from channelized loading is much more considerable than what is considered in the present modeling scheme. Compared to the single reducing factor in traffic volume, a systematic consideration of wander, for example, in terms of the normal and/or Laplace distribution, in the prediction of field rutting performance is preferred.

REFERENCES

AASHTO. (2008). Standard Method of Test for Specific Gravity and Absorption of Coarse Aggregate. T 85. Washington D.C.

AASHTO. (2008). Standard Method of Test for Specific Gravity and Absorption of Fine Aggregate. T 84. Washington D.C.

Abbo, A. J., & Sloan, S. W. (1995). A Smooth Hyperbolic Approximation to the Mohr-Coulomb Yield Criterion. *Computers and Structures, 54*(3), 427-441.

Adeyeri, J. B., Krizek, R. J., & Achenbach, J. D. (1970). Multiple Integral Description of the Nonlinear Viscoelastic Behavior of A Clay Soil. *Transactions of The Society of Rheology, 14*(3), 375-392.

Adolfsson, K., Enelund, M., & Olsson, P. (2005). On the Fractional Order Model of Viscoelasticity, Mechanics of Time-Dependent Materials. *Mechanics of Time-Dependent Materials, 9*(1), 15-34.

Aklonis, J. J., & MacKnight, W. J. (1972). *Introduction to Polymer Viscoelasticity* (2 ed.). New York: John Wiley & Sons, Inc.

Anderson, D. A., Christensen, D. W., Bahia, H. U., Dongre, R., Sharma, M. G., Antle, C. E., & Button, J. (1994). *Binder Characterization and Evaluation, Vol 3: Physical Characterization.* SHRP-A-369, National Research Council, Washington, D.C.

Ashouri, M. (2014). *Modeling Microdamage Healing in Asphalt Pavements Using Continuum Damage Theory.* Ph.D. Dissertation, North Carolina State University, Raleigh, N.C.

Asphalt Institute. (2001). *Superpave Mix Design: Superpave Series No. 2* (3 ed.).

Bagley, R. L., & Torvik, P. J. (1983). A Theoretical Basis for the Application of Fractional Calculus to Viscoelasticity. *Journal of Rheology, 27*(3), 201-210.

Bhattacharjee, S., Swamy, A. K., & Daniel, J. S. (2012). Continuous Relaxation and Retardation Spectrum Method for Viscoelastic Characterization of Asphalt Concrete. *Mechanics of Time-Dependent Materials, 16*(3), 287-305.

Blab, R., & Litzka, J. (1995). Measurements of the Lateral Distribution of Heavy Vehicles and Its Effects on the Design of Road Pavements. *Road Transport Technology*, 389-395.

Bolton, M. D. (1986). The Strength and Dilatancy of Sands. *Geotechnique, 36*(1), 65-78.

Brodnyan, J. G., Gaskins, F. H., Philippoff, W., & Thelen, E. (1960). The Rheology of Asphalt. III. Dynamic Mechanical Properties of Asphalt. *Transactions of The Society of Rheology, 4*(1), 279-296.

Brown, S. F. (1973). Determination of Young's Modulus for Bituminous Materials in Pavement Design. *Highway Research Record 431*, 38-49.

Cao, W., Eslaminia, M., & Kim, Y. R. (2012). Fatigue Performance Modeling of Binzhou Perpetual Pavements Using Viscoelastic Continuum Damage Finite Element Program. Nanjing: International Sociery for Asphalt Pavements.

Caputo, M. (1967). Linear Model of Dissipation Whose Q Is almost Frequency Independent-II. *Geophysical Journal of the Royal Astronomical Society, 13*(5), 529-539.

Choi, Y. (2013). *Development of a Mechanistic Prediction Model and Test Protocol for the Permanent Deformation of Asphalt Concrete.* Ph.D. Dissertation, North Carolina State University, Raleigh, NC.

Christensen, D. W., & Anderson, D. A. (1992). Interpretation of Dynamic Mechanical Test Data for Paving Grade Asphalt Cements. *Proceedings of Association of Asphalt Paving Technologists, 61*, 67-116.

Christensen, D. W., & Bonaquist, R. (2002). Use of Strength Tests for Evaluating the Rut Resistance of Asphalt Concrete. *Journal of the Association of Asphalt Paving Technologists, 71*, 692-711.

Dickinson, E. J., & Witt, H. P. (1974). The Dynamic Shear Modulus of Paving Asphalts as a Function of Frequency. *Transactions of The Society of Rheology, 18*(4), 591-606.

Epps, J. A., Hand, A., Seeds, S., Scholz, T., Alavi, S., Ashmore, C., & Monismith, C. L. (2000). *NCHRP Report 455: Recommended Performance Related Specification for Hot-Mix Asphalt Construction. Part II: Performance Related Specification.* Washington, D.C.: TRB, National Research Council.

Erdélyi, A., Magnus, W., Oberheltinger, F., & Tricomi, F. G. (1954). *Higher Transcendental Functions, Vol. 3.* New York: McGraw-Hill.

Eslaminia, M., Thirunavukkarasu, S., Guddati, M. N., & Kim, Y. R. (2012). Accelerated Pavement Performance Modeling Using Layered Viscoelastic Analysis. In A. Scarpas, N. Kringos, I. Al-Qadi, & A. Loizos (Eds.), *7th RILEM International Conference on Cracking in Pavements* (pp. 497-506). Springer Netherlands.

Ferry, J. D., Landel, R. F., & Williams, M. L. (1955). Extensions of the Rouse Theory of Viscoelastic Properties to Undiluted Linear Polymers. *Journal of Applied Physics, 26*, 359-362.

Findley, W. N., Lai, J. S., & Onaran, K. (1976). *Creep and Relaxation of Nonlinear Viscoelastic Materials.* NY: Dover.

Friedrich, C., Honerkamp, J., & Weese, J. (1996). New Ill-Posed Problems in Rheology. *Rheologica Acta, 35*(2), 186-193.

Fung, Y. C. (1972). Stress Strain History Relaxations of Soft Tissues in Simple Elongation . In Y. C. Fung, N. Perrone, & M. Anliker (Eds.), *Biomechanics, Its Foundations and Objectives.* Englewood Cliffs, NJ: Prentice Hall.

Fung, Y. C. (1993). *Biomechanics, Mechanical Properties of Living Tissues* (2 ed.). New York: Springer-Verlag.

Gibson, N. H., Kutay, M. E., Keramat, D., & Youtcheff, J. (2009). Multiaxial Strain Response of Asphalt Concrete Measured During Flow Number Performance Test. *Journal of the Association of Asphalt Paving Technologists, 79*, 25-66.

Gibson, N., Qi, X., Shenoy, A., Al-Khateeb, G., & Kutay, M. E. (2011). *Full-Scale Accelerated Performance Testing for Superpave and Structural Validation.* FHWA, U.S. Department of Transportation.

Gross, B. (1953). *Mathematical Structure of the Theories of Viscoelasticity.* Hermann and et Cie.

Guo, P., & Su, X. (2007). Shear Strength, Interparticle Locking, and Dilatancy of Granular Materials. *Canadian Geotechnical Journal, 44*(5), 579-591.

Ha, K., & Schapery, R. A. (1998). A Three-Dimensional Viscoelastic Constitutive Model for Particulate Composites with Growing Damage and Its Experimental Validation. *International Journal of Solids and Structures, 35*, 3497-3517.

Hajj, E. Y., Ulloa, A., Siddharthan, R., & Sebaaly, P. E. (2010). Estimation of Stress Conditions for the Flow Number Simple Performance Test. *Journal of the Transportation Research Board, 2181*, 67-78.

Heymans, N., & Bauwens, J. C. (1994). Fractal Rheological Models and Fractional Differential Equations for Viscoelastic Behavior. *Rheologica Acta, 33*, 210-219.

Honerkamp, J., & Weese, J. (1989). Determination of the Relaxation Spectrum by a Regularization Method. *Macromolecules, 22*(11), 4372-4377.

Hossain, N., Solanki, P., Zaman, M., Muraleetharan, K. K., & Singh, D. (2013). Development of Field Rut Prediction Models from an Instrumented Test Section on Interstate-35. Submitted to the Transportation Research Board.

Houlsby, G. T. (1991). How the Dilatancy of Soils Affects Their Behaviour. *10th European Conference on Soil Mechanics and Foundation Engineering. 4*, pp. 1189-1202. Florence, Italy: Associazione Geotecnica Italiana.

Hu, K., & Zhu, K. (2009). Mechanical Analogies of Fractional Elements. *Chinese Physical Society, 26*(10).

Jongepier, R., Kuilman, B., Schimidt, R. J., Puzinauskas, V. P., & Rostler, F. S. (1969). Characteristics of the Rheology of Bitumens. *Proceedings of Association of Asphalt Paving Technologists, 38*, 98-122.

Katicha, S. W., & Flintsch, G. W. (2011). Use of Fractional Order Viscoelastic Models to Characterize Asphalt Concrete. *Transportation and Development Institute Congress*, (pp. 677-687). Chicago, Illinois.

Kim, Y. R., Guddati, M. N., S., U. B., Yun, T. Y., Subramanian, V., & Savadatti, S. (2009). *Development of a Multiaxial Viscoelastic Continuum Damage Model for Asphalt Mixtures.* FHWA, U.S. Department of Transportation.

Kim, Y. R., Guddati, M. N., Underwood, B. S., Yun, T. Y., Subramanian, V., & Heidari, A. H. (2005). *Characterization of ALF Mixtures Using the Viscoelastoplastic Continuum Damage Model.* Final report to FHWA.

Koeller, R. C. (1984). Application of Fractional Calculus to the Theory of Viscoelasticity. *Journal of Applied Mechanics, 51,* 299-307.

Lacroix, A. T. (2013). *Performance Prediction of the NCAT Test Track Pavements Using Mechanistic Models.* Ph.D. Dissertation, North Carolina University, Raleigh, NC.

Lacroix, A., Underwood, B. S., & Kim, Y. R. (2011). Reduced Testing Protocol for Measuring the Confined Dynamic Modulus of Asphalt Mixtures. *Transportation Research Record: Journal of the Transportation Research Board, 2210*, 20-29.

Lai, J., & Bakker, A. (1995). An Integral Constitutive Equation for Nonlinear Plasto-Viscoelastic Behavior of High-Density Polyethylene. *Polymer Engineering and Science, 35*, 1339-1347.

Lakes, R. S., & Vanderby, R. (1999). Interrelation of Creep and Relaxation: A Modeling Approach for Ligaments. *Journal of Biomechanical Engineering, 121*(6), 612-615.

Lewis, B. A. (2004). *Manual for LS-DYNA Soil Material Model 147.* Federal Highway Administration, FHWA-HRT-04-095, McLean, VA.

Lytton, R. L., Uzan, J., Fernando, E. J., Roque, R., Hiltunen, D., & M., S. S. (1993). *SHRP-A-357: Development and Validation of Performance Prediction Models and Specifications for Asphalt Binder and Paving Mixes.* National Research Council, Washington, D.C.

Mair, K., Frye, K. M., & Marone, C. (2002). Influence of Grain Characteristics on the Friction of Granular Shear Zones. *Journal of Geophysical Research, 107*(B10), ECV 4-1 - ECV 4-9.

Marasteanu, M. O., & Anderson, D. A. (1999). Improved Model for Bitumen Rheological Characterization. *Proceedings of the Eurobitume Workshop on Performance Related Properties for Bituminous Binders*, (pp. 1-4). Brussels.

Mirghasemi, A. A., Rothenburg, L., & Matyas, E. L. (2002). Influence of Particle Shape on Engineering Properties of Assemblies of Two Dimensional Polygon-Shaped Particles. *Geotechnique, 52*(3), 209-217.

Monismith, C. L., Alexander, R. L., & Secor, K. E. (1966). Rheological Behavior of Asphalt Concrete. *Proceedings of the Association of Asphalt Paving Technologists, 35*, 400-450.

Nowick, A. S., & Berry, B. S. (1961). Lognormal Distribution Function for Describing Anelastic and Other Relaxation Processes I. Theory and Numerical Computations. *IBM Journal of Research and Development, 5*(4), 297-311.

Oeser, M., Pellinen, T., Scarpas, T., & Kasbergen, C. (2008). Studies on Creep and Recovery of Rheological Bodies Based upon Conventional and Fractional Formulations and Their Application on Asphalt Mixture. *International Journal of Pavement Engineering, 9*(5), 373-386.

Onaran, K., & Findley, W. N. (1965). Combined Stress-Creep Experiments on a Nonlinear Viscoelastic Material to Determine the Kernel Functions for a Multiple Integral Representation of Creep. *Transactions of The Society of Rheology, 9*(2), 299-327.

Oza, A., Vanderby, R., & Lakes, R. S. (2003). Interrelation of Creep and Relaxation for Nonlinearly Viscoelastic Materials: Application to Ligament and Metal. *Rheologica Acta, 42*(6), 557-568.

Papoulia, K. D., Panaskaltsis, V. P., Kurup, N. V., & Korovajchuk, I. (2010). Rheological Representation of Fractional Order Viscoelastic Material Models. *Rheologica Acta, 49*, 381-400.

Park, S. W., & Kim, Y. R. (2001). Fitting Prony-Series Viscoelastic Models with Power-Law Presmoothing. *Journal of Materials in Civil Engineering, 13*(1), 26-32.

Park, S. W., & Schapery, R. A. (1999). Methods of Interconversion between Linear Viscoelastic Material Functions. Part I – A Numerical Method Based on Prony Series. *International Journal of Solids and Structures, 36*(11), 1653-1675.

Pellinen, T. K., & Witczak, M. W. (2002). Stress Dependent Master Curve Construction for Dynamic (Complex) Modulus. *Journal of the Association of Asphalt Paving Technologists, 71*, 281-309.

Pena, A. A., Garcia-Rojo, R., & Herrmann, H. J. (2007). Influence of Particle Shape on Sheared Dense Granular Media. *Granular Matter, 9*, 279-291.

Provenzano, P. P., Lakes, R. S., Corr, D. T., & Vanderby, R. (2002). Application of Nonlinear Viscoelastic Models to Describe Ligament Behavior. *Biomech Model Mechanobiol, 1*(1), 45-57.

Provenzano, P., Lakes, R., Keenan, T., & Vanderby, R. (2001). Nonlinear Ligament Viscoelasticity. *Annals of Biomedical Engineering, 29*(10), 908-914.

Rahmani, E., Darabi, M. K., Abu Al-Rub, R. K., Kassem, E., Masad, E. A., & Little, D. N. (2013). Effect of Confinement Pressure on the Nonlinear-Viscoelastic Response of Asphalt Concrete at High Temperatures. *Construction and Building Materials, 47*, 779-788.

Reese, R. (1997). Properties of Aged Asphalt Binder Related to Asphalt Concrete Fatigue Life. *Journal of the Association of Asphalt Paving Technologists, 66*, 604-632.

Rouse, P. E. (1953). A theory of the Linear Viscoelastic Properties of Dilute Solutions of Coiling Polymers. *Journal of Chemical Physics, 21*(7), 1272-1280.

Rowe, P. W. (1962). The Stress-Dilatancy Relation for Static Equilibrium of an Assembly of Particles in Contact. *Proceedings of the Royal Society of London*, (pp. 500-527). London.

Schanz, T., & Vermeer, P. A. (1996). Angle of Friction and Dilatancy of Sand. *Geotechnique, 46*(1), 145-151.

Schapery, R. A. (1966). A Theory of Non-linear Thermoviscoelasticity Based on Irreversible Thermodynamics. *Proceedings of the 5th U.S. National Congress of Applied Mechanics* (pp. 511-530). Minneapolis, Minnesota: American Society of Mechanical Engineers.

Schapery, R. A. (1969). *Further Development of A Thermodynamic Constitutive Theory: Stress Formulation.* Lafayette, Indiana: Purdue University School of Aeronautics, Astronautics and Engineering Sciences.

Schapery, R. A. (2000). Nonlinear Viscoelastic Solids. *International Journal of Solids and Structures, 37*, 359-366.

Schapery, R. A., & Park, S. W. (1999). Methods of Interconversion between Linear Viscoelastic Material Functions. Part II - An Approximate Analytical Method. *International Journal of Solids and Structures, 36*(11), 1677-1699.

Schiessel, H., & Bluemen, A. (1993). Hierarchical Analogues to Fractional Relaxation Equations. *Journal of Physics A: Mathematical and General, 26*, 5057-5069.

Schiessel, H., & Bluemen, A. (1995). Mesoscopic Pictures of the Sol-Gel Transition: Ladder Models and Fractional Networks. *Macromolecules, 28*, 4013-4019.

Schiessel, H., Metzler, R., Bluemen, A., & Nonnenmacher, T. F. (1995). Generalized Viscoelastic Models: Their Fractional Equations with Solutions. *Journal of Physics A: Mathematical and General, 28*, 6567-6584.

Selvaraj, S. I. (2007). *Development of Flexible Pavement Rut Prediction Models from the NCAT Test Track Structural Study Sections Data.* Ph.D. Dissertation, Auburn University, Auburn, AL.

Simo, J. C., & Hughes, T. J. (1998). *Computational Inelasticity.* New York: Springer-Verlag.

Sloan, S. W., & Booker, J. R. (1986). Removal of Singularities in Tresca and Mohr–Coulomb Yield Functions. *Communications in Applied Numerical Methods, 2*(2), 173-179.

Subramanian, V. (2011). *A Viscoplastic Model with Rate-Dependent Hardening for Asphalt Concrete in Compression.* Ph.D. Dissertation, North Carolina State University, Raleigh, NC.

Taylor, D. W. (1948). *Fundamentals of Soil Mechanics.* New York: John Wiley & Sons Inc.

Thornton, G. M., Oliynyk, A., Frank, C. B., & Shrive, N. G. (1997). Ligament Creep Cannot Be Predicted from Stress Relaxation at Low Stress: A Biomechanical Study of the Rabbit Medial Collateral Ligament. *Journal of Orthopaedic Research, 15*(5), 652-656.

Tschoegl, N. W. (1989). *The Phenomenological Theory of Linear Viscoelastic Behavior: An Introduction.* Springer Berlin Heidelberg.

Underwood, B. S., Yun, T., & Kim, Y. R. (2011). Experimental Investigations of the Viscoelastic and Damage Behaviors of Hot-Mix Asphalt in Compression. *Journal of Materials in Civil Engineering, 23*(4), 459-466.

Vermeer, P. A., & de Borst, R. (1984). Non-associated Plasticity for Soils, Concrete and Rock. *HERON, 29*(3), 1-64.

Von Quintus, H. L., Mallela, J., Bonaquist, R., Schwartz, C. W., & Carvalho, R. L. (2007). Calibration of Rutting Models for HMA Structural and Mix Design. NCHRP 9-30A

Quarterly Report (Apr. 2007 ~ Jun. 2007). *Transportation Research Record: Journal of the Transportation Research Board*.

Welch, S. J., Rorrer, R. L., & Duren, R. G. (1999). Application of Time-Based Fractional Calculus Methods to Viscoelastic Creep and Stress Relaxation of Materials. *Mechanics of Time-Dependent Materials*, *3*(3), 279-303.

Witczak, M. W., & Uzan, J. (1988). *The Universal Airport Pavement Design System - Report I of IV: Granular Material Characterization.* Department of Civil Engineering, University of Maryland at College Park, MD.

Wu, R., & Harvey, J. T. (2008). Evaluation of the Effect of Wander on Rutting Performance in HVS Tests. Madrid, Spain: Proceedings of the 3rd International Conference on Accelerated Pavement Testing.

Yun, T. (2008). *Development of a Viscoplastic Constitutive Model Using a Rate-Dependent Yield Criterion for HMA in Compression.* Ph.D. Dissertation, North Carolina State University, Raleigh, NC.

Zhao, Y., Liu, H., & Liu, W. (2013). Characterization of Linear Viscoelastic Properties of Asphalt Concrete Subjected to Confining Pressure. *Mechanics of Time-Dependent Materials*, *17*(3), 449-463.

APPENDICES

APPENDIX A. Proof of the Cauchy Formula

The proof of the Cauchy formula for repeated integration, Equation (2.2.25), can be given by mathematical induction. The base case for Equation (2.2.25) is produced when *n* assumes 1, which yields

$$If(x) = \int_a^x f(t)dt \tag{A.1}$$

which is exactly the definition of the operator as in Equation (2.2.23). Now suppose Equation (2.2.25) is true for any positive integer *n*, the following proves it for *n*+1.

$$\begin{aligned} I^{n+1} f(x) &= \int_a^x \int_a^{x_1} \cdots \int_a^{x_n} f(x_{n+1}) dx_{n+1} \cdots dx_2 dx_1 \\ &= \frac{1}{(n-1)!} \int_a^x \int_a^{x_1} (x_1 - t)^{n-1} f(t) dt dx_1 \\ &= \frac{1}{(n-1)!} \int_a^x \int_a^{x_1} (x_1 - t)^{n-1} f(t) dx_1 dt \\ &= \frac{1}{n!} \int_a^x (x-t)^n f(t) dt \end{aligned} \tag{A.2}$$

Hence Equation (2.2.25) is proved.

APPENDIX B. Numerical Implementation of the Improved Convolution-type Viscoplastic Model

The improved convolution-type viscoplastic model is now rewritten in Equation (B.1) below at time step *n*:

$$\varepsilon_{vp}^{n} \equiv \left\langle I^{n} \right\rangle \quad \text{with} \quad I^{n} \equiv \int_{0^{-}}^{t^{n}} D(t^{n}-\tau)\dot{\sigma}(\tau)d\tau \tag{B.1}$$

As usual, the use of the Prony representation of the compliance function $D(t)$ facilitates the numerical computation:

$$D(t) = D_0 + \sum_{j=1}^{M} D_j \left(1 - e^{-\frac{t}{\tau_j}}\right) \tag{B.2}$$

The numerical algorithms for the convolution-type model is not fully explained in the dissertation by Subramanian (2011) and thus they are now comprehensively described here for better understanding the model. For this purpose, three case scenarios categorized by the status of deviatoric stress are presented.

Loading at the first cycle

As already mentioned, loading means physically the applied stress does not decrease and here mathematically is also characterized by an increasing ε_{vp} calculated from Equation (B.1). Admittedly, there is certain delay between the strain response and stress, which renders a slight difference between the previous two definitions of loading. But practically this difference is rather negligible and thus by loading either or both definitions are implied.

It is assumed that at beginning of the loading we have $t = 0$, $\sigma(0) = 0$, $\varepsilon_{vp}(0) = 0$. During the loading duration, assuming the viscoplastic strain is known at time step *n*, then Equation (B.1) reduces to the standard linear viscoelastic convolution integral since the stress is increasing giving $I^{n+1} > I^{n}$, and the viscoplastic strain at time step $n+1$ is obtained as

$$
\begin{aligned}
\varepsilon_{vp}^{n+1} = I^{n+1} &\equiv \int_{0^-}^{t^{n+1}} D\left(t^{n+1}-\tau\right)\dot{\sigma}(\tau)d\tau = \int_{0^-}^{t^{n+1}} D\left(t^{n+1}-\tau\right)d\sigma(\tau) \\
&= \int_{0^-}^{t^{n+1}} \left[D_0 + \sum_{j=1}^{M} D_j \left(1-e^{-\frac{t^{n+1}-\tau}{\tau_j}} \right) \right] d\sigma(\tau) \\
&= \int_{0^-}^{t^{n+1}} D_0 d\sigma(\tau) + \sum_{j=1}^{M} D_j \int_{0^-}^{t^{n+1}} \left(1-e^{-\frac{t^{n+1}-\tau}{\tau_j}} \right) d\sigma(\tau) \\
&= D_0\sigma^{n+1} + \sum_{j=1}^{M} I_j^{n+1}
\end{aligned}
\tag{B.3}
$$

where σ^{n+1} is the applied deviatoric stress at time step n+1, and

$$
I_j^{n+1} = D_j \int_{0^-}^{t^{n+1}} \left(1-e^{-\frac{t^{n+1}-\tau}{\tau_j}} \right) d\sigma(\tau) \tag{B.4}
$$

The state variable method (Simo and Hughes, 1998) is used to update I_j^{n+1}, and before that, Equation (B.4) has to be rearranged in the following form:

$$
\begin{aligned}
I_j^{n+1} &= D_j \int_{0^-}^{t^{n+1}} \left(1-e^{-\frac{t^{n+1}-\tau}{\tau_j}} \right) d\sigma(\tau) = D_j \int_{0^-}^{t^{n+1}} d\sigma(\tau) - D_j \int_{0^-}^{t^{n+1}} e^{-\frac{t^{n+1}-\tau}{\tau_j}} d\sigma(\tau) \\
&= D_j\sigma^{n+1} - D_j L_j^{n+1}
\end{aligned}
\tag{B.5}
$$

where

$$
\begin{aligned}
L_j^{n+1} &= \int_{0^-}^{t^{n+1}} e^{-\frac{t^{n+1}-\tau}{\tau_j}} d\sigma(\tau) = \int_{0^-}^{t^{n}} e^{-\frac{t^{n+1}-\tau}{\tau_j}} d\sigma(\tau) + \int_{t^n}^{t^{n+1}} e^{-\frac{t^{n+1}-\tau}{\tau_j}} d\sigma(\tau) \\
&= \int_{0^-}^{t^{n}} e^{-\frac{t^{n}-\tau+\Delta t^{n+1}}{\tau_j}} d\sigma(\tau) + \int_{t^n}^{t^{n+1}} e^{-\frac{t^{n+1}-\tau}{\tau_j}} d\sigma(\tau) \\
&= e^{-\frac{\Delta t^{n+1}}{\tau_j}} \int_{0^-}^{t^{n}} e^{-\frac{t^{n}-\tau}{\tau_j}} d\sigma(\tau) + e^{-\frac{t^{n+1}}{\tau_j}} \int_{t^n}^{t^{n+1}} e^{\frac{\tau}{\tau_j}} d\sigma(\tau) \\
&= e^{-\frac{\Delta t^{n+1}}{\tau_j}} L_j^{n} + e^{-\frac{t^{n+1}}{\tau_j}} \int_{t^n}^{t^{n+1}} e^{\frac{\tau}{\tau_j}} d\sigma(\tau)
\end{aligned}
\tag{B.6}
$$

The integral at the right hand side of the last equal sign can be simplified using the first mean value theorem as

$$\int_{t^n}^{t^{n+1}} e^{\frac{\tau}{\tau_j}} d\sigma(\tau) = \dot{\sigma}(x) \int_{t^n}^{t^{n+1}} e^{\frac{\tau}{\tau_j}} d\tau = \dot{\sigma}(x)\tau_j \left(e^{\frac{t^{n+1}}{\tau_j}} - e^{\frac{t^n}{\tau_j}} \right) \quad \text{with } x \in \left[t^n, t^{n+1} \right] \tag{B.7}$$

Since usually the time step size is small, the stress slope within a step can be well approximated by the mean slope:

$$\dot{\sigma}(x) = \frac{\Delta\sigma^{n+1}}{\Delta t^{n+1}} \quad \text{with } \Delta\sigma^{n+1} = \sigma^{n+1} - \sigma^n, \text{ and } \Delta t^{n+1} = t^{n+1} - t^n \tag{B.8}$$

Substitution of Equation (B.7) and (B.8) into (B.6) yields

$$L_j^{n+1} = e^{-\frac{\Delta t^{n+1}}{\tau_j}} L_j^n + \frac{\Delta\sigma^{n+1}}{\Delta t^{n+1}} \tau_j \left(1 - e^{-\frac{\Delta t^{n+1}}{\tau_j}} \right) \tag{B.9}$$

Substitute Equation (B.5) into (B.3) and we can finally arrive at

$$\varepsilon_{vp}^{n+1} = \left(D_0 + \sum_{j=1}^{M} D_j \right) \sigma^{n+1} - \sum_{j=1}^{M} D_j L_j^{n+1} \tag{B.10}$$

with the state variable L_j^{n+1} being updated using Equation (B.9) and the initial condition at the beginning of loading $L_j^0 = 0$.

Unloading and rest period

During unloading, the applied stress decreases causing a reduction in the convolution integral, i.e., $I^{n+1} < I^n$. While a reduction in the viscoplastic strain is forbidden by the Macaulay brackets (that is, $\varepsilon_{vp}^{n+1} = \varepsilon_{vp}^n$), a new stress named back stress is to be sought and calculated as if it is applied to the material so that the strain response remains unchanged during unloading and rest period. The numerical procedures are as follows.

Assuming I^n is known with the back stress σ_b^n already calculated at step n, then for time step n+1 an increment in the back stress, $\Delta\sigma_b^{n+1}$, should be calculated in order for $\varepsilon_{vp}^{n+1} = \varepsilon_{vp}^{n}$ to hold. From Equation (B.9) and (B.10) we can write

$$\begin{aligned}\varepsilon_{vp}^{n+1} &= \left(D_0 + \sum_{j=1}^{M} D_j\right)\sigma_b^{n+1} - \sum_{j=1}^{M} D_j L_j^{n+1} \\ &= \left(D_0 + \sum_{j=1}^{M} D_j\right)\left(\sigma_b^n + \Delta\sigma_b^{n+1}\right) \\ &\quad - \sum_{j=1}^{M} D_j \left\{\exp\left(-\Delta t^{n+1}/\tau_j\right) L_j^n + \frac{\Delta\sigma_b^{n+1}}{\Delta t^{n+1}}\tau_j\left[1-\exp\left(-\Delta t^{n+1}/\tau_j\right)\right]\right\}\end{aligned} \tag{B.11}$$

Rearranging by factoring the back stress increment term out we can have

$$\begin{aligned}\varepsilon_{vp}^{n+1} &= \left(D_0 + \sum_{j=1}^{M} D_j\right)\sigma_b^n - \sum_{j=1}^{M} D_j \exp\left(-\Delta t^{n+1}/\tau_j\right) L_j^n \\ &\quad + \left\{\left(D_0 + \sum_{j=1}^{M} D_j\right) - \sum_{j=1}^{M} D_j \frac{1-\exp\left(-\Delta t^{n+1}/\tau_j\right)}{\Delta t^{n+1}/\tau_j}\right\}\Delta\sigma_b^{n+1}\end{aligned} \tag{B.12}$$

Since we are forcing $\varepsilon_{vp}^{n+1} = \varepsilon_{vp}^{n}$, we then will obtain

$$\Delta\sigma_b^{n+1} = \frac{\varepsilon_{vp}^n - \left(D_0 + \sum_{j=1}^{M} D_j\right)\sigma_b^n + \sum_{j=1}^{M} D_j \exp\left(-\Delta t^{n+1}/\tau_j\right) L_j^n}{\left(D_0 + \sum_{j=1}^{M} D_j\right) - \sum_{j=1}^{M} D_j \frac{1-\exp\left(-\Delta t^{n+1}/\tau_j\right)}{\Delta t^{n+1}/\tau_j}} \tag{B.13}$$

Then the updated back stress for time step n+1 is

$$\sigma_b^{n+1} = \sigma_b^n + \Delta\sigma_b^{n+1} \tag{B.14}$$

The updated state variable is

$$L_j^{n+1} = e^{-\frac{\Delta t^{n+1}}{\tau_j}} L_j^n + \frac{\Delta\sigma_b^{n+1}}{\Delta t^{n+1}}\tau_j\left(1 - e^{-\frac{\Delta t^{n+1}}{\tau_j}}\right) \tag{B.15}$$

And as a verification, the following equality should hold true:

$$\varepsilon_{vp}^{n} = \left(D_0 + \sum_{j=1}^{M} D_j \right) \sigma_b^{n+1} - \sum_{j=1}^{M} D_j L_j^{n+1} \tag{B.16}$$

Loading after the first cycle

As demonstrated in Figure 2-13, the back stress acts like the yield surface in classical plasticity and viscoplasticity theories. Therefore, when the load is initiated again after the first cycle, no further permanent deformation is generated when the applied stress is smaller than the back stress at the same time. After the actual stress increases beyond the back stress, the viscoplastic strain starts to develop following the convolution integral. The algorithms are details below.

If at time step n and n+1, all variables at step n are known and the following are satisfied:

$$\sigma^{n} \le \sigma_b^{n} \quad \text{and} \quad \sigma^{n+1} > \sigma_b^{n+1} \tag{B.17}$$

then, the viscoplastic strain at time step n+1 is given by

$$\varepsilon_{vp}^{n+1} = \left(D_0 + \sum_{j=1}^{M} D_j \right) \sigma^{n+1} - \sum_{j=1}^{M} D_j L_j^{n+1} \tag{B.18}$$

with the state variable

$$L_j^{n+1} = e^{-\frac{\Delta t^{n+1}}{\tau_j}} L_j^{n} + \frac{\sigma^{n+1} - \sigma_b^{n}}{\Delta t^{n+1}} \tau_j \left(1 - e^{-\frac{\Delta t^{n+1}}{\tau_j}} \right) \tag{B.19}$$

After step n+1, the subsequent steps during loading follow the same procedures as those for the loading portion of the first cycle.

APPENDIX C. Calibration of the Extended Incremental-Shift Model using Other Temperature-Confinement Combinations

In the following, different combinations of test temperature and confinement levels are tried to calibrate the function for the total shift factor, Equation (5.2.5). The same reference curve from the first block of 48°C-10psi test has been used throughout all attempts.

Trial-1 Four Combinations (1)

Here the following combinations are tried for the total shift factor calibration: 28°C-10psi, 48°C-10psi, 28°C-20psi, and 48°C-30psi. Figure C-1 shows the relation between the calculated shift factors based on TSS test data and the predicted ones using the calibrated function. It is obvious that the four points from 20°C-30psi deviate from the line of equality and thus a poor prediction at this condition is expected as seen in Figure C-2.

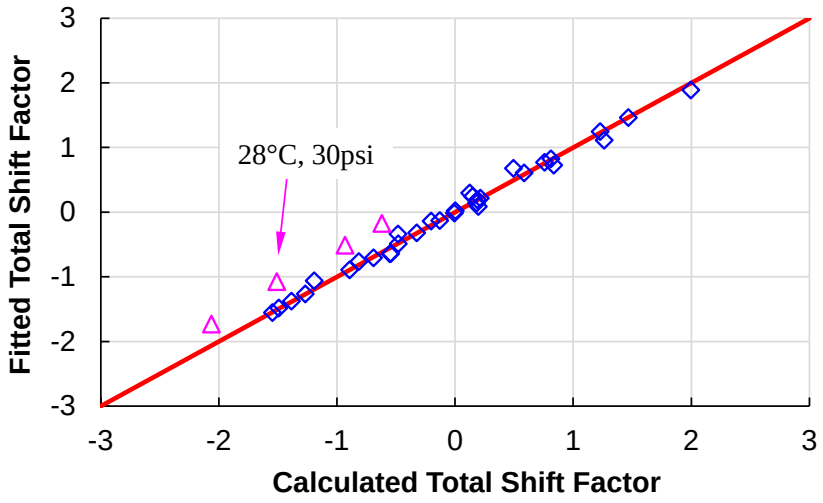

Figure C-1 Fitted versus calculated total shift factors for 4 blocks using the following TSS test temperature-confinement combinations for calibration: 28°C-10psi, 48°C-10psi, 28°C-20psi, and 48°C-30psi.

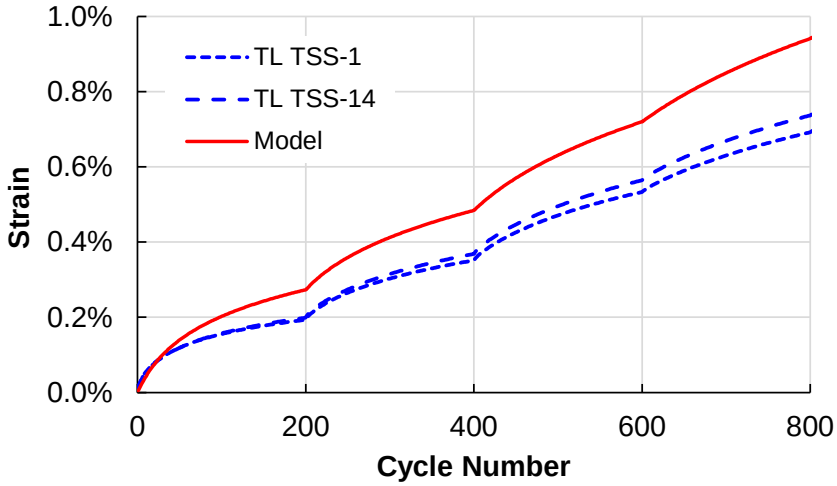

Figure C-2 Measured and predicted strains in the TSS test at 28°C-30psi.

Trial-2 Four Combinations (2)

In this second trial the following combinations are used: 38°C-10psi, 48°C-10psi, 28°C-20psi, 28°C-30psi. Figure C-3 presents the fitted versus the calculated total shift factors, and it shows that except those used in calibration all other conditions cannot be represented by the calibrated total shift factor function.

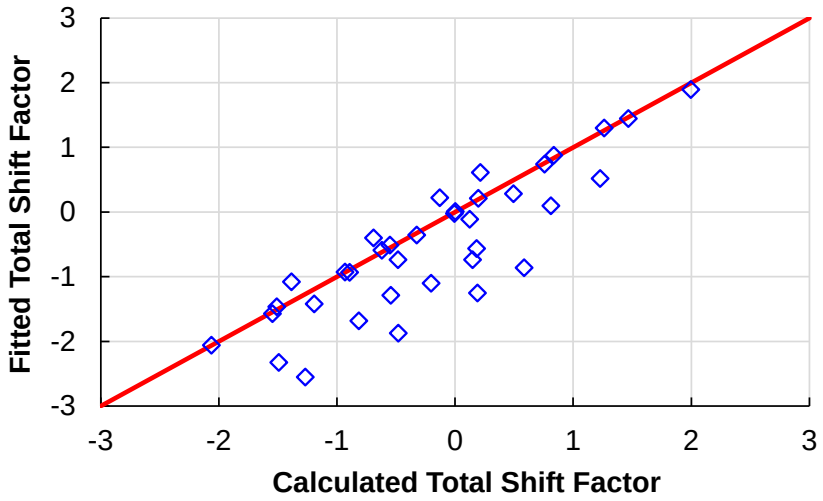

Figure C-3 Fitted versus calculated total shift factors for 4 blocks using the following TSS test temperature-confinement combinations for calibration: 38°C-10psi, 48°C-10psi, 28°C-20psi, and 28°C-30psi.

Trial-3 Three Combinations

Here the following combinations are used: 28°C-10psi, 48°C-10psi, 28°C-30psi. Compared to the final choice described in Section 5.2 only 48°C-30psi is eliminated. The resulting predicted versus the calculated total shift factor is plotted in Figure C-4.

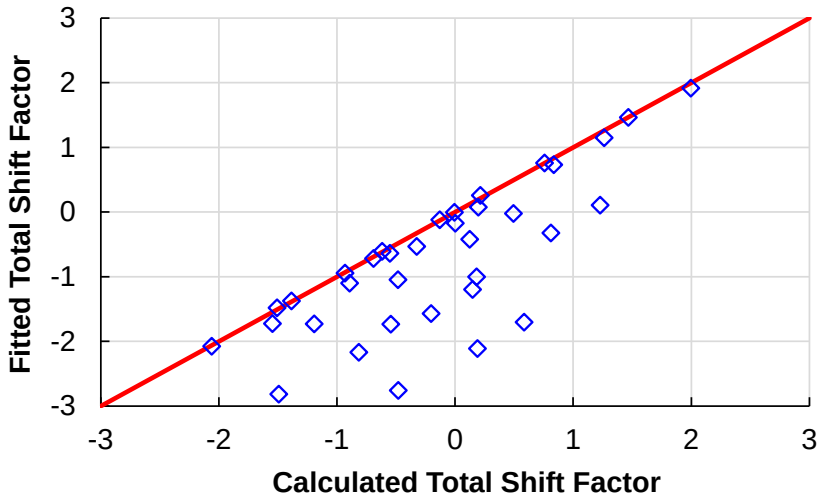

Figure C-4 Fitted versus calculated total shift factors for 4 blocks using the following TSS test temperature-confinement combinations for calibration: 28°C-10psi, 48°C-10psi, and 28°C-30psi.

APPENDIX D. Conversion of the Relaxation Spectra to Retardation Spectra

The conversion from the relaxation spectrum to retardation spectrum requires the use of the following exact relation in linear viscoelasticity theory:

$$\int_0^t E(t-\tau)\frac{dD(\tau)}{d\tau}d\tau = 1 \tag{D.1}$$

Both $E(t)$ and $D(t)$ are expressed via Prony series as usual:

$$E(t) = E_\infty + \sum_{i=1}^{M} E_i \exp(-t/\rho_i) \tag{D.2}$$

$$D(t) = D_0 + \sum_{j=1}^{N} D_j \left[1 - \exp(-t/\tau_j)\right] \tag{D.3}$$

Rewrite the compliance function using the Heaviside function $H(t)$ (see Equation (5.5.6)) as

$$D(t) = D_0 H(t) + \sum_{j=1}^{N} D_j \left[1 - \exp(-t/\tau_j)\right] \tag{D.4}$$

The time derivative of $D(t)$ can then be found as

$$\frac{dD(t)}{dt} = D_0\delta(t) + \sum_{j=1}^{N} \frac{D_j}{\tau_j} e^{-\frac{t}{\tau_j}} \tag{D.5}$$

where $\delta(t)$ is the Dirac delta function which is the time derivative of the Heaviside function. Substitution of Equations (D.2) and (D.5) into (D.1) yields

$$\int_0^t \left(E_\infty + \sum_{i=1}^{M} E_i e^{-\frac{t-\tau}{\rho_i}} \right) \left[D_0\delta(\tau) + \sum_{j=1}^{N} \frac{D_j}{\tau_j} e^{-\frac{\tau}{\tau_j}} \right] d\tau = 1 \tag{D.6}$$

which can be expanded into

$$\int_{0^-}^t \left[E_\infty D_0\delta(\tau) + \sum_{i=1}^{M} E_i e^{-\frac{t-\tau}{\rho_i}} D_0\delta(\tau) + E_\infty \sum_{j=1}^{N} \frac{D_j}{\tau_j} e^{-\frac{\tau}{\tau_j}} + \left(\sum_{i=1}^{M} E_i e^{-\frac{t-\tau}{\rho_i}} \right) \left(\sum_{j=1}^{N} \frac{D_j}{\tau_j} e^{-\frac{\tau}{\tau_j}} \right) \right] d\tau = 1 \tag{D.7}$$

Each of the four terms in the integral can be simplified as follows

$$\int_0^t E_\infty D_0\delta(\tau)d\tau = E_\infty D_0$$

$$\int_0^t \sum_{i=1}^{M} E_i e^{-\frac{t-\tau}{\rho_i}} D_0 \delta(\tau) d\tau = D_0 \sum_{i=1}^{M} E_i e^{-\frac{t}{\rho_i}}$$

$$\int_0^t E_\infty D_0 \delta(\tau) d\tau = E_\infty D_0$$

$$\int_0^t \left(\sum_{i=1}^{M} E_i e^{-\frac{t-\tau}{\rho_i}} \right) \left(\sum_{j=1}^{N} \frac{D_j}{\tau_j} e^{-\frac{\tau}{\tau_j}} \right) d\tau = \sum_{i=1}^{M} \sum_{j=1}^{N} E_i \frac{D_j}{\tau_j} e^{-\frac{t}{\rho_i}} \int_0^t e^{\frac{\tau}{\rho_i} - \frac{\tau}{\tau_j}} d\tau$$

Denote and note that

$$\psi_{ij} \equiv e^{-\frac{t}{\rho_i}} \int_0^t e^{\frac{\tau}{\rho_i} - \frac{\tau}{\tau_j}} d\tau = \begin{cases} \dfrac{\rho_i \tau_j}{\rho_i - \tau_j} \left[\exp\left(-t/\rho_i\right) - \exp\left(-t/\tau_j\right) \right] > 0 & \text{when } \rho_i \neq \tau_j \\ \exp\left(-t/\rho_i\right) t > 0 & \text{when } \rho_i = \tau_j \end{cases} \quad \text{(D.8)}$$

Putting the above together we can obtain

$$\sum_{j=1}^{N} \left[\sum_{i=1}^{M} \frac{E_i}{\tau_j} \psi_{ij} + E_\infty \left(1 - e^{-\frac{t}{\tau_j}} \right) \right] D_j = 1 - D_0 \left(E_\infty + \sum_{i=1}^{M} E_i e^{-\frac{t}{\rho_i}} \right) \quad \text{(D.9)}$$

Collocation method is employed to solve for all the D_j while τ_j are pre-specified and thus ψ_{ij} are known constants. Written in matrix form, the resulting linear equations are

$$\int_0^t E_\infty D_0 \delta(\tau) d\tau = E_\infty D_0 \quad \text{(D.10)}$$

$$B_{kj} = \sum_{i=1}^{M} \frac{E_i}{\tau_j} \psi_{ij} + E_\infty \left(1 - e^{-\frac{t_k}{\tau_j}} \right) > 0 \quad \text{(D.11)}$$

$$F_k = 1 - D_0 \left(E_\infty + \sum_{i=1}^{M} E_i e^{-\frac{t_k}{\rho_i}} \right) > 0 \quad \text{(D.12)}$$

where $i = 1 \ldots M$, $j = 1 \ldots N$, and $k = 1 \ldots p$ in which p is the number of time instants selected in the collocation method. Note that D_0 can be easily calculated by setting $t = 0^+$ in Equation (D.7) as

$$D_0 = \frac{1}{E_\infty + \sum_{i=1}^{M} E_i} \quad \text{(D.13)}$$